ADDITION AND INFLUENCE OF NANO-PARTICLES IN THE MANUFACTURE OF CAST STEEL

Ana Kračun

Doctoral Dissertation
Jožef Stefan International Postgraduate School
Ljubljana, Slovenia

Supervisor: Prof. Dr. Bojan Podgornik, Institute of Metals and Technology, Lepi pot 11, Ljubljana, Slovenia

Evaluation Board:
Prof. Dr. Monika Jenko, Chair, Jožef Stefan International Postgraduate School and Institute of Metals and Technology, Lepi pot 11, Ljubljana, Slovenia
Assoc. Prof. Dr. Uroš Cvelbar, Member, Jožef Stefan International Postgraduate School and Jožef Stefan Institute, Jamova 39, 1000 Ljubljana, Slovenia
Prof. Dr. Walter R. Tuckart, Member, Universidad Nacional del Sur – UNS, Bahia Blanca, Argentina

MEDNARODNA PODIPLOMSKA ŠOLA JOŽEFA STEFANA
JOŽEF STEFAN INTERNATIONAL POSTGRADUATE SCHOOL

Ana Kračun

ADDITION AND INFLUENCE OF NANO-PARTICLES IN THE MANUFACTURE OF CAST STEEL

Doctoral Dissertation

DODAJANJE IN VPLIV NANODELCEV PRI IZDELAVI JEKLA S POSTOPKOM LITJA

Doktorska disertacija

Supervisor: Prof. Dr. Bojan Podgornik

Ljubljana, Slovenia, January 2019

To all members of my family, especially to my mother Ana Kračun and my father Roman Kračun. This dissertation is dedicated to my boyfriend, who encouraged me to pursue my dreams and finish my dissertation.

Acknowledgments

The research work was conducted at the Institute of Metals and Technology in the frame of the research program P2-0050, which is financed by the Slovenian Research Agency.

I would like to express my gratitude to my supervisor Prof. Dr. Bojan Podgornik for the opportunity to work in the Department of Metallic Materials and Technology, his guidance and valuable comments to improve my thesis.

This thesis would not have been completed without those who helped and supported me the whole time. I would especially like to thank:

- Dr. Franc Tehovnik for discussions and guidance during experiments preparations and production of the samples,
- Dr. Franci Vode, mag. Boštjan Arh, Simon Malej mag. inž. metal. mat., Zdenko Majer, Robert Lampe, Luka Snoj for assistance with the preparations and production of the samples,
- Jekla Kovač for chemical analysis of the samples,
- Nataša Lipovšek for discussions and guidance during preparations of the samples for LM and SEM observation,
- Dr. Fevzi Kafexhiu for SEM investigations and help with constructive discussions about the results,
- Dr. Francisco Ruiz Zepeda and Dr. Darja Jenko for TEM investigations and help with constructive discussions about the results,
- Dr. Borut Žužek and Rok Rezar for mechanical properties testing,
- Dr. Marko Sedlaček for guidance during fatigue testing and everyday motivational speeches,
- Prof. Dr. Borivoj Šuštaršic and Božo Skela mag. inž. metal. mat. for help and constructive discussion of thermodynamic calculations,
- Dr. Uroš Cvelbar and Andrea Jurov mag. fizike from the Jožef Stefan Institute Department of Surface Engineering and Optoelectronics (F4) for producing the plasma surface modified nano-particles.

In addition, I would like to thank all my co-workers who were available when needed and helped me during my PhD work.

Finally, I would like to thank my friends and family for constantly encouraging and supporting me.

Ana Kračun

Abstract

In recent decades, considerable efforts have been made in the production of steel and the modification of its microstructure in order to improve the mechanical properties through the incorporation of nano-particles. Nanotechnologies offer potential in the manufacture of nano-engineered steels. While typical production methods for Metal Matrix nano-Composites (MMnCs) are difficult and expensive, the main drawback of the casting method is the agglomeration of the nano-particles and a poor interface between the nano-particles and the metal matrix. Therefore, the aim of this doctoral thesis was to investigate the potential of different nano-particle additions as reinforcement elements in the conventional liquid-metal casting process, which cannot be obtained or at least not easily through precipitation and to study their effect on the microstructure, mechanical properties and wear behavior. The investigation was focused on the various approaches to the production, modification and addition of nano-particles, as well as the influence of the type, concentration, size and surface modification of nano-particles added to a steel matrix on the homogeneity and distribution. The right combination of mentioned factors can provide superior mechanical strength, while maintaining or even improving other properties, such as toughness, damping capacity, wear resistance, creep behavior as well as electrical and thermal properties. The results show that also in the case of the conventional casting process, it is possible to produce reinforced steel-matrix nano-composites with a homogeneous distribution of the nano-particles in the matrix, resulting in improved properties. The identification and interface between the nano-particles and the steel matrix is highlighted and the properties evaluated on the example of austenitic stainless steel (AISI 316L type), used due to its simple two-phase microstructure. The properties were found to depend on the type and distribution of the reinforcing nano-particles, with the best results shown by Al_2O_3, Y_2O_3 and TiB_2 nano-particles when mixed with a dispersive medium. When the nano-particles were used with a dispersive medium, a more uniform distribution of the nano-particles was achieved, leading to improved hardness, fatigue and wear resistance, while maintaining the yield and ultimate tensile strength of the reference non-modified steel. On the other hand, nano-particle reinforcement in general resulted in a reduced high-temperature creep resistance, evaluated at 650 °C. However, the main reason lies in the precipitation of the σ phase, starting above 600 °C, with the incorporated nano-particles acting as nucleation sites. A higher fraction of the σ phase is therefore present in the nano-particle-reinforced material, thus having a detrimental effect on the high-temperature properties of the investigated steel.

Povzetek

V zadnjih desetletjih narašča zanimanje za izdelavo jekel in modifikacijo njihove mikrostrukture z dodajanjem nano-delcev in sicer z namenom izboljšanja mehanskih lastnosti.Nanotehnologije predstavljajo velik potencial v proizvodnji nano-konstruiranih jekel. Medtem ko so tipične metode izdelave nano-kompozitov s kovinsko osnovo (MMnCs) težavne in drage, je glavna pomanjkljivost procesa litja, aglomeracija nano-delcev in slaba mejna površina med nanodelci in kovinsko matrico. Namen doktorskega dela je bila raziskava možnosti uporabe različnih nano-delcev kot armaturnih elementov v jekleni matrici dodanih pri postopku konvencionalnega litja kovin, ki jih drugače ni moč oz. jih je zelo težko dobiti s termodinamskim procesom izločanja in njihovega vpliva na mikrostrukturo, mehanske in protiobrabne lastnosti. Delo zajema različne metode dodajanja nano-delcev v procesu izdelave in učinek tipa, koncentracije, velikosti in površinske modifikacije nano-delcev, dodanih v jekleno matrico na homogenost mikrostrukture in porazdelitev nano-delcev. Prava kombinacija omenjenih faktorjev lahko zagotovi izboljšano mehansko trdnost, medtem ko se ohranijo ali celo izboljšajo druge lastnosti, kot so žilavost, zmogljivost dušenja, odpornost proti obrabi, obnašanje pri lezenju kot tudi električne in toplotne lastnosti. Rezultati kažejo, da je mogoče tudi s konvencionalnim postopkom litja izdelati nano-kompozit z armirano jekleno matrico in homogeno porazdelitvijo nanodelcev, kar ima za posledico izboljšanje lastnosti. S poudarkom na stabilnosti nano-delcev v jeklu, so obravnavani primerni ojačitveni elementi oz. armature in jeklene matrice. Delo je osredotočenotudi na analizo mejne površine in povezavo med nano-delci in jekleno matrico, pri čemer so bile raziskave, zaradi enostavne dvofazne mikrostrukture, izvedene na primeru nerjavnega avstenitnega jekla (tip AISI 316L). Ugotovili smo, da so lastnosti odvisne od vrste in porazdelitve ojačitvenih nano-delcev. Najboljše rezultate so pokazali nano-delci Al_2O_3, Y_2O_3 in TiB_2, zmešani z disperzijskim medijem. Pri dodajanju nano-delcev skupaj z disperzijskim sredstvom je bila dosežena bolj enakomerna porazdelitev v kovinski matrici, kar je posledično vplivalo na doseganje višje trdote, odpornosti proti utrujanju in odpornosti proti obrabi, medtem ko sta meja tečenja in natezna trdnost ostali na nivoju referenčnega nemodificiranega jekla. Po drugi strani, pa so armaturni nano-delci zmanjšali visokotemperaturno odpornost proti lezenju pri 650 °C. Glavni razlog tiči v tvorbi σ faze, ki se začne nad 600 °C, kjer imajo dodani nano-delci vlogo nukleacijskih mest za precipitacijo σ faze. Večji delež σ faze se tako pojavlja v materialu, kjer so bili dodani nano-delci, kar ima škodljiv vpliv na visokotemperaturne lastnosti preiskovanega jekla.

Contents

List of Figures

List of Tables

Abbreviations

AISI 316L . . . austenitic stainless-steel quality 316L
BCC . . . body-centered cubic structure (α – and/or δ – ferrite)
BSE . . . backscattered secondary electron
BF . . . bright-field imaging
CNT . . . carbon nanotubes
CTE . . . coefficient of thermal expansion
EDS . . . energy-dispersive X-ray spectroscopy
EM . . . elastic modulus
FCC . . . face-centered cubic structure(austenite)
FEG . . . field-emission gun
GNDs . . . geometrically necessary dislocations
HV . . . Vickers hardness
HAADF . . . high-angle annular dark-field
LCF . . . life-cycle fatigue
MMnCs . . . Metal Matrix nano-Composites
M_3C . . . cementite
M_6C . . . molybdenum-rich carbides
M_7C_3 . . . chromium-rich carbides
$M_{23}C_6$ . . . chromium-rich carbides
SEI . . . Secondary Electron Image
SEM . . . Scanning Electron Microscopy
STEM . . . Scanning transmission electron microscopy
PVD . . . Physical Vapor Deposition
TEM . . . Transmission electron microscopy
UHC . . . ultrahigh-cycle fatigue regime

Symbols

A . . . geometric constant (term relative to CTE mismatch)
B . . . coefficient related to Orowan effect
α . . . proportional constant
β . . . constant
b . . . Burger's vector
δ . . . ferrite
d . . . mean diagonal of indentation (mm)
d . . . average grain size
d_p . . . particle diameter
E . . . modulus of elasticity
G . . . matrix shear modulus
G_m . . . matrix shear modulus of the unreinforced matrix
ε . . . strain
F_N . . .normal load
N . . . number of cycles to failure
k_y . . . strengthening coefficient
l . . . size of the particulate parallel to the load direction
P . . . indentation load (kg)
ρ^{CTE} . . . density of thermal expansion
ρ^{EM}. . . density of elastic modulus
σ . . . sigma phase (chromium intermetallictetragonal phase)[1]
σ . . . stress
$\Delta\sigma_{LH-P}$ . . . Hall-Petch strengthening
σ_m . . .yield strength of the unreinforced matrix
σ_c . . . strength of the composite
$\Delta\sigma_{CTE+EM}$ . . . combined strengthening due to CTE and EM
$\Delta\sigma_i$ . . .single strengthening effects
$\Delta\sigma_{LT}$. . . load transfer
$\Delta\sigma_{OR}$. . . Orowan strengthening
s . . . sliding distance
S . . . stress amplitude
t . . . size of the particulate perpendicular to the load direction
v_p. . . volume fraction
W . . . wear volume
χ . . . chi phase

[1] In the engineering society σ is used as a symbol for both microstructure constituent sigma phase and as a symbol for stress.

Chapter 1

Introduction

Metal Matrix nano-Composites (MMnCs) are being investigated worldwide because of their promising properties, making them suitable for a large number of functional and structural applications. It has been shown that MMnCs can provide superior mechanical strength, while maintaining or even improving other important engineering properties, such as toughness, damping capacity, wear resistance, creep behavior as well as electrical and thermal properties. However, for optimal exploitation of the strengthening potential a homogeneous distribution of reinforcement nano-particles in the metal matrix needs to be obtained. For this reason, different production methods have been developed, mainly based on powder metallurgy. However, the high cost and complexity limit their use in the mass production of steel parts.

Developments in the field of nanotechnology and nano-particles production offer huge potential when it comes to modifying steel's properties through nano-particle incorporation. However, for the large-scale production of metal-matrix nano-composites, the main problem to be faced is the low wettability of the ceramic nano-particles in the molten metal, which does not allow the preparation of MMnCs by conventional casting processes, since the result would be an inhomogeneous distribution of the particles within the matrix. The high surface energy of nano-particles leads to the formation of clusters of nano-particles within the matrix, which are not effective in hindering the movement of dislocations and can hardly generate a physical-chemical bond with the matrix, thus significantly reducing the strengthening capability of the nano-particles and leading to an impairment of the properties. Several inconvenient methods have been proposed in order to overcome the wettability issue. However, the effect of the surface modification of the nano-particles, as well as the combined effect of the nano-particle type, size and concentration on their homogeneous distribution within the metal matrix when using conventional casting routes has not been reported. There is also a lack of knowledge about how, in this case, different nano-particles are bound in the metal matrix.

In this work we aimed to investigate the effect of the type, concentration, size and surface modification of the nano-particles added to a steel matrix on the homogeneity of the distribution and the development of the microstructure, mechanical, fatigue and creep properties, as well as the wear resistance. Therefore, the research was focused on various aspects of the production, modification and addition of nano-particles, with the investigation and characterization methods available at the Institute of Metals and Technology, the Institute Jožef Stefan and the National Institute of Chemistry. In the first phase thermodynamic calculations using ThermoCalc software were performed, with which the most stable nano-particle were selected, which were further plasma surface modified in a low-pressure plasma reactor. With the use of an induction melting furnace different techniques of adding nano-particles into the steel melt as well as the type, concentration and size of the added nano-particles were examined and the nano-particles-reinforced austenitic stainless-steel microstructure was characterized using light microscopy (LM), scanning electron microscopy (SEM), energy-dispersive X-ray spectroscopy (EDS) and transmission electron microscopy (TEM). Finally, the effect of the nano-particle addition and the method of introduction on the mechanical properties of the reinforced stainless

steel (AISI 316L type) was analyzed using hardness and impact toughness measurements, tensile, fatigue and high-temperature creep tests, as well as tribological testing.

Chapter 2

State of the Art

2.1 Metal Matrix Nano-Composites (MMnCs) Reinforced by Nano-Particles

During the past 30 years, materials design has shifted emphasis to pursue light weight, environment friendliness, low cost, quality and performance. In parallel with this trend Metal Matrix nano-Composites (MMnCs) have been attracting growing interest, owing to their promising properties, suitable for a large number of functional and structural applications. Metal matrix nano-Composite (MMnCs) is an engineered combination of a metal matrix and a hard-particles reinforcement to provide tailored properties.

For most of the particle-reinforced MMCs, the size of the reinforcing particles ranges from several to tens of microns, normally resulting in a considerable reduction in ductility and toughness. It is mainly due to the easy initiation and propagation of cracks in the ceramic particles or the interface. In order to enhance the mechanical properties, the particle size needs to be reduced to below the micrometer range [1].The reduced size of the reinforcement phase down to the nano-scale is such that the interaction of particles with dislocations becomes of significant importance and, when added to other strengthening effects typically found in conventional MMCs, results in a remarkable improvement of the physical and mechanical properties, e.g., tensile and compressive properties, creep, notch and wear resistance, density, thermal expansion and thermal density, etc. The material limitations are thermal fatigue, thermos-chemical compatibility and low transverse creep resistance. In general, the metallic matrix is expected to provide the high ductility and toughness of the MMnCs, while the particle reinforcements embedded in the metallic matrix are responsible for the high strength, elastic modulus, wear resistance, high melting point and low density. Different oxides, carbides, borides, nitrides and carbon nanotubes are incorporated into the metal matrix to produce MMnCs with superior physical, mechanical and wear properties. As such, in recent years, particulate-reinforced metal-matrix composites have attracted the attention of many researchers, engineers and designers as promising advanced engineering and structural material for automobile and advanced aerospace applications.

The production methods can be categorized into two major groups: ex situ and in situ. The first synthesis route consists of adding nano-reinforcements to the liquid or powdered metal, while in situ processes refer to those methods leading to the generation of ceramic nano-compounds by reaction during processing, for example, by using reactive gases. Several methods have been developed for the ex situ synthesis of MMnCs. In particular, different powder-metallurgy techniques were successfully employed.

On the other hand, the casting routes are considered to be the most suitable for the bulk production of MMnCs. In the production of MMnCs using the casting method there are several factors that need to be considered, especially when using nano-sized reinforcement particles. A homogeneous distribution of nano-particles in molten metals is extremely hard to achieve. Because of the low wettability of ceramic nano-particles with the molten metal, this does not allow the production of MMnCs by conventional casting processes. Furthermore, nano-sized particles tend to agglomerate and form clusters, losing

their capability to be homogeneously dispersed throughout the matrix for an optimal exploitation of the strengthening potential.

In the literature, different kinds of matrix metals have been coupled with several types of nano-metric phases. Ceramic compounds (SiC, Al_2O_3, etc.), intermetallic materials and carbon allotropes were used to reinforce Al, Mg, Cu and other metals and alloys. Particular importance is assigned to carbon nanotubes (CNTs), which are characterized by very high strength, stiffness and electrical conductivity. These properties confer higher mechanical strength, while improving the electrical and thermal properties of the base material [2]. Moreover, MMnCs can be made with other improved, interesting engineering properties, such as damping capacity [3], wear resistance [4] and creep behavior [5].

2.2 Nano-Particle Strengthened Alloys and Available Reinforcements

Metal Matrix nano-Composites (MMnCs) combine the properties of the reinforcements (nano-particles) and the metallic matrix. Different metallic materials have been considered as the matrix component for the preparation of MMnCs. Currently produced and applied in practice are composite materials based on light metal alloys. In particular, the most interesting metals for industrial applications are magnesium, aluminum, copper, titanium and their alloys. Different kinds of reinforcements are being used in the production of these MMnCs, such as oxides, carbides, borides, as well as nitrides and carbon nanotubes.

2.2.1 Selection of the matrix

The continuous phase of a composite material is referred to as the matrix. It carries the uniformly distributed reinforcement material. Metallic matrices' advantages compared to polymer-matrix materials are their higher tensile strength and shear modulus, high melting point, low coefficient of thermal expansion, resistance to moisture, dimensional stability, high ductility and toughness. Important physical and mechanical properties that should be considered when choosing the matrix material for a given application are characteristics such as density, strength, high-temperature strength, ductility and toughness. As matrix materials, Al, Ti, Mg, Cu and Fe have been generally used. Because of the light weight, high thermal conductivity, a unique combination of good corrosion resistance and excellent mechanical properties, the main focus is given to aluminum as a matrix material. Among all those properties, another important factor is the low cost of making the aluminum matrix, making it well suited for use as a matrix metal. Aluminum has a melting point high enough that the application requirements are being satisfied. It can also accommodate a variety of reinforcing agents, including continuous boron fibers, aluminum oxide fibers, SiC fibers, and graphite fibers as well as various particles, short fibers and whiskers [6].

2.2.2 Selection of reinforcements

The addition of a reinforcement into the matrix material increases the strength, stiffness and temperature-resistance capacities of MMnCs. The reinforcement may be in the shape of continuous fibers, whiskers or particles, the size of which can vary in the composite. Reinforcement in the matrix can be present in a continuous or discontinuous form. The first type, continuous fiber reinforcement, in comparison with the discontinuous type, has superior properties; however, it suffers from the disadvantage of anisotropic properties added to the need for adopting near-net-shape forming techniques. On the other hand, the discontinuous reinforcement offers isotropic properties and an amenability to be processed

by conventional secondary metal forming techniques. The most common and having the lowest cost are particulate reinforcement materials. The addition of particulates actually leads to a favorable effect on the properties, such as hardness, wear resistance and compressive strength. Aluminum-based reinforced MMnCs with SiC particulates have good potential for use as wear-resistant materials. Actually, particulates lead to a favorable effect on properties such as the hardness, wear resistance and compressive strength. The selection criteria for the ceramic reinforcement include factors like elastic modulus, tensile strength, density, melting temperature, thermal stability, compatibility with the matrix material and cost effectiveness [6].

2.2.3 Composite materials based on magnesium alloys

The physical properties of magnesium and its alloys and the combination of mechanical properties, Young's modulus and density make them very useful for application as the matrix of composite materials. Studies have shown that composite materials based on magnesium alloys reinforced by dispersion particles of silicon carbide (SiC) with a low density of 2.0–2.1 g/cm^3 have 30–40 % have better mechanical properties than unreinforced magnesium alloys [7]. Magnesium-based composite materials reinforced by dispersion particles are produced by mixing the dispersion particles in liquid magnesium alloy or by squeeze casting under pressure. When produced using melting processes, nano-particle-reinforced magnesium composites are expected to enjoy strengthening due to the grain refinement described in the Hall–Petch relation. When an isotropic distribution of nano-particles is achieved, the composites are additionally expected to be Orowan-strengthened. In the review of Dieringa [8] a variety of ceramic materials, such as SiC, Al_2O_3, Y_2O_3, SiO_2 and carbon nanotubes, were investigated for reinforcement in pure magnesium and different magnesium alloys. For the production method they chose both powder metallurgical (PM) and melting processes. The mechanical properties of the composites were generally enhanced, compared to an unreinforced alloy; not only at room temperature, but also at elevated temperatures. In some cases an increase in strength in combination with increased ductility was also identified.

2.2.4 Composite materials based on aluminum alloys

Aluminum-alloy-based metal-matrix composites have established themselves as a suitable wear-resistant material, especially for sliding-wear applications. Composite materials based on an aluminum-alloy matrix are manufactured by powder metallurgy, by applying the mechanical alloying process, dispersion of particles in atomized aluminum alloys using co-spray deposition process and squeeze-casting methods. The advantages of an aluminum alloy reinforced with 20 wt. % of SiC particles are a high wear resistance, good strength and relatively good heat conduction, resulting in their practical application as car brake discs, as reported by Dasgupta [9]. On the other hand, Crowet al. [10] determined a drop in mechanical properties in the case of the dispersion of µm-sized SiC particles in the aluminum alloy 7091, which was explained by the weak bonding at the matrix/reinforcement phases.

2.2.5 Composite materials based on copper alloys

Copper-matrix composites have been found to be the most promising engineering material for many applications within the electronics and manufacturing industries requiring components with a high electrical and thermal conductivity, a high corrosion and oxidation resistance as well as good mechanical properties. Currently, copper-based composite

materials are produced by powder-metallurgy methods, cold pressing and then hot-consolidation processes by forging or extrusion and by the mechanical blending of copper powders with dispersion powders [11]. As the reinforcements, mostly alumina and silicon carbides are used. However, poor wetting has been observed between the copper matrix and reinforced ceramic materials such as alumina and silicon carbides, which often result in poor adhesion and interface strength between the copper and the ceramic reinforcement [12]. Tungsten carbide particle-reinforced composites with a copper alloy as the matrix (Cu-alloy/WCp) are widely used in drill-bit applications, and this is for different reasons. First, the two materials have good compatibility with each other and show excellent wetting characteristics that can form a good interfacial bond between the matrix and the reinforcing phase [13]. Second, copper alloy-based composites exhibit substantial wear resistance when reinforced with hard ceramic particles, such as tungsten carbide [14]. Third, tungsten carbide has limited solubility in copper and does not form complex interfacial intermetallic layers with copper alloys [13]. Fourth, tungsten carbide retains its hardness up to 1400° C without any phase change [14].

2.2.6 Composite material based on titanium alloys

Titanium alloys show high specific mechanical properties up to high temperatures and a good corrosion resistance [15]. Composite materials based on titanium alloys are reinforced mainly with titanium borides (TiB) and carbides (TiC). Saito et al. [16]produced P/M titanium-based composite materials with 10 wt.% of titanium boride (TiB) and determined a considerable increase in the mechanical properties in comparison to reference sintered titanium. Furthermore, the high-temperature mechanical properties of titanium-based alloy composite materials were higher than those of heat-treated steels. Taking into account the relatively low density of titanium alloys, very high specific mechanical properties of titanium-based composite materials are achieved.

2.2.7 Composite material based on steel alloys

Steel MMnCs have demonstrated good mechanical, physical and wear properties in comparison to conventional steel. The efforts to produce high-performance materials with very high strength were directed towards the use in the specialized aerospace, automotive and wear industries [17]. Steel MMnCs are typically produced with a low volume fraction of reinforcements, ranging from 5 to 30 % for structural applications, otherwise the ductility and toughness may be lower than required [18]. Ceramic-reinforced steel MMnCs with a high volume fraction of reinforcements such as 50-80 % are in use for applications where a high hardness and wear resistance are required[18]. An increase in the properties of a composite material based on steel alloys such as hardness, wear and corrosion resistance depends on several processing and microstructural parameters. The microstructural parameters include the volume fraction of ceramic reinforcements, the shape and size of the reinforcements, the interface between the ceramic reinforcement and the matrix material, the composition of the steel matrix, the defects, cracks and the distribution of reinforcements in the steel matrix. There are several processing routes, such as powder metallurgy, spray deposition, mechanical alloying, infiltration and casting techniques. As-synthesized reinforcements, such as TiC, TiB_2, WC and TiCN, in the form of particulates, are added to the steel matrix by powder metallurgy. Haussainova [19] reported that it was possible to incorporate a low and high volume fraction of particulate ceramic reinforcements in the steel matrix and achieve a dense composite material by optimizing the sintering parameters. Liquid-phase processing routes are used to produce steel MMnCs and include conventional casting, liquid infiltration, squeeze casting and spray co-deposition (Fig.1). In

the casting route, the metal is heated to its molten state and reinforcements are then added and stirred to avoid the settling of reinforcements, followed by casting into a mold. The cooling rate of the casting significantly influences the distribution of reinforcements in the metal matrix [20]. The production of MMnCs by an infiltration process includes the preparation of a porous scaffold of reinforcing phase and the infiltration of a liquid metal or alloy with the help of wetting aids in a nitrogen atmosphere or with the assistance of pressure to push the liquid metal to fill the pore space in the scaffold [21]. Spray co-deposition uses the solidification of molten metal droplets containing the reinforcement particles. The resultant MMnC particles are collected on a rotating substrate where the particles are amalgamated and solidified. Typically, a consolidation step is required to prepare dense metal matrix composites [20].

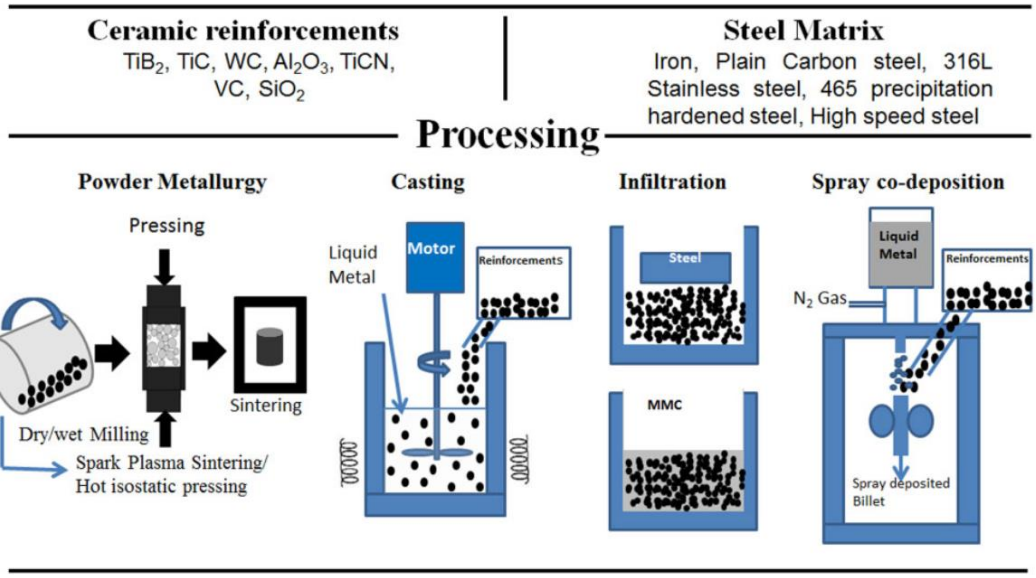

Figure 1: Ceramic reinforcements, steel matrix materials and schematic diagrams of commonly used processing routes to produce ceramic-reinforced steel matrix composites: (I) powder metallurgy; (II) casting; (III) infiltration and (IV) spray co-deposition [18].

2.3 Strengthening Mechanisms

The high mechanical resistance of MMnCs is the result of several strengthening mechanism contributions: load-transfer effect, Hall-Petch strengthening, Orowan strengthening coefficient of thermal expansion (CTE) and elastic modulus (EM) mismatch [10–13]. In the following sections, each strengthening mechanism is discussed separately.

2.3.1 Load-transfer effect

The load-transfer mechanism is based on the load-carrying capability of reinforcements in comparison to the steel matrix. The load transfer is significant in the case of fiber-reinforced composites and its effect decreases with the reduced aspect ratio of the reinforcement, but still significantly contributes to the strength [22]. A modified Shear Lag model proposed by Nardone and Prewo [23] is commonly used to predict the contribution to strengthening due to load transfer in particulate-reinforced composites [24]:

$$\Delta\sigma_{LT} = v_p \sigma_m \left[\frac{(l+t)A}{4l}\right] \tag{1}$$

Where v_p is the volume fraction of the particles in the matrix, σ_m is the yield strength of the unreinforced matrix, l is the size of the particulate parallel to the load direction, t is the thickness of the particulate, and $A = l/t$ is the particulate aspect ratio. For the case of equiaxed particles Equation (10) reduces to [24]:

$$\Delta\sigma_{LT} = \frac{1}{2} v_p \sigma_m \tag{2}$$

During the thermal treatment, dislocations are created in the metal matrix phase due to the difference in the coefficient of thermal expansion of ceramic reinforcements and the steel matrix, which causes an increase in the strength of steel MMCs, known as the matrix strengthening mechanism. The dislocation density in the matrix phase depends on the reinforcement size, the difference in the coefficient of thermal expansion and the volume fraction of the reinforcements. Thus, both the load-transfer and matrix-strengthening models are based on the transfer of the load at the interface of the reinforcement phase and the metal matrix, with the defect free and strong interfacial zone being important in achieving the strengthening effect. The interface between the ceramic reinforcements and the steel matrix is generally formed at high temperatures, involving chemical reactions and atomic transport by diffusion [25].

2.3.2 Orowan strengthening

Orowan strengthening occurs due to an artificial reduction in the spacing between the particulate reinforcements as a result of the creation of Orowan loops [25]. The so-called Orowan mechanism is based on the interaction of nano-particles with dislocations. The non-shearable ceramic reinforcement particles pin the crossing dislocations and promote dislocation bowing around the particles (Orowan loops) under an external load [26]. The Orowan effect can be expressed by the following expression:

$$\Delta\sigma_{OR} = \frac{0.13bG}{d_p\left(\sqrt[3]{\frac{1}{2}}v_p - 1\right)} ln\left(\frac{d_p}{2b}\right) \tag{3}$$

where d_p is the particle diameter (m), G is the matrix shear modulus (Pa), b is the Burger's vector (m), and v_p is the volume fraction of the particles. The Burger's vector of a dislocation is a crystal vector, specified by Miller indices, that quantifies the difference between the distorted lattice around the dislocation and the perfect lattice [27].

2.3.3 Hall-Petch strengthening

The grain size has a strong influence on metal strength since the grain boundaries can hinder dislocation movement. This is due to the different orientation of adjacent grains and to the high lattice disorder characteristic of these regions, which prevent the

dislocations from moving in a continuous slip plane [26]. The Hall-Petch equation relates the strength with the average grain size (d) [26]:

$$\Delta\sigma_{H-P} = \frac{k_y}{\sqrt{d}} \tag{4}$$

where k_y is the strengthening coefficient (characteristic constant of each material).

The particles play a fundamental role in the final grain size found in metal matrices of composites since they can interact with the grain boundaries, acting as pinning points, retarding or stopping the grain growth. The increase of v_p (volume fraction) and the decrease of d_p (particle diameter) lead to a finer structure, as theoretically modeled by the Zener equation [24]:

$$d_m = \frac{4\alpha d_p}{3v_p} \tag{5}$$

where α is a proportional constant.

2.3.4 Coefficient of thermal expansion and elastic modulus mismatch

The mismatch in the coefficient of thermal expansion (CTE) and in the elastic modulus (EM) between the reinforcements and the metal matrix is accommodated during material cooling and straining by the formation of geometrically necessary dislocations (GNDs).
The GND density due to the CTE and EM mismatch can be estimated by the following expressions [24]:

$$\rho^{CTE} = \frac{A\Delta\alpha\Delta T v_p}{bd_p(1-v_p)} \tag{6}$$

$$\rho^{EM} = \frac{6v_p}{\pi d_p^3}\varepsilon \tag{7}$$

where A is a geometric constant varying between 10 and 12 based on the geometry of the reinforcement, is the difference in CTE, ΔT is the temperature change from the processing to testing temperature and ε signifies the plastic strain of the matrix. Then, the combined strengthening due to the CTE and EM mismatch can be calculated by means of the Taylor equation [28]:

$$\Delta\sigma_{CTE+EM} = \sqrt{3}\beta Gb\left(\sqrt{\rho^{CTE}} + \sqrt{\rho^{EM}}\right) \tag{8}$$

Where β is a constant of the order of 1.25. ρ^{CTE} and ρ^{EM}represent the density of the dislocations induced by CTE and EM mismatches, respectively.

It is worth noting that as the deformation proceeds, the increase in dislocation density results in a reduced space between them, which consequently elevates the load required for further deformation.

2.3.5 Sum of contributions

The final strength of the composite, σ_c, can be evaluated by summing the above contributions related to the single strengthening effects, $\Delta\sigma_i$, with the original yield strength of the unreinforced matrix, σ_m, therefore:

$$\sigma_c = \sigma_m + \sum_i \Delta\sigma_i \tag{9}$$

Several studies proposed alternative methods to calculate σ_c, taking into account the superposition of the effects [24]. A simple approach [24] suggests calculating the final strength of the composite by summing the root of the squares of all the single strengthening contributions, as:

$$\sigma_c = \sigma_m + \sqrt{\sum_i \Delta\sigma_i^2} \tag{10}$$

Another common method that takes into account the Orowan strengthening mechanism, the CTE mismatch effect, and the load-bearing effect was proposed by Zhang and Chen [24]:

$$\sigma_c = \left(1 + 0.5v_p\right)\left(\sigma_m + A + B + \frac{AB}{\sigma_m}\right) \tag{11}$$

where A is the term relative to the CTE mismatch and B is the coefficient related to the Orowan effect:

$$A = 1.25G_m b\sqrt{\frac{12\Delta\alpha\Delta T v_p}{bd_p\left(1 - v_p\right)}} \tag{12}$$

$$B = \frac{0.13G_m b}{d_p\left[\left(\frac{1}{2v_p}\right)^{\frac{1}{3}} - 1\right]} ln\frac{d_p}{2b} \tag{13}$$

Only a few papers are available in the literature about this topic. This lack does not allow a comprehensive evaluation and comparison of the proposed methods. For this reason, the approaches are simply reported and not compared and discussed in depth.

2.4 Production Methods and Properties

The production methods can be categorized into two major groups: *ex situ* and *in situ*. The *ex situ* synthesis route consists of adding nano-reinforcements to the liquid or powdered metal, while *in situ* processes refer to those methods leading to the generation of ceramic nano-compounds by reaction during processing (a solid – solid, solid – liquid, liquid – liquid or solid – gas), for example by using reactive gases. Several methods have been developed for the *ex situ* synthesis of MMnCs over the past 30 years, such as powder metallurgy, spray deposition, mechanical alloying and casting techniques. In particular, different powder metallurgy techniques were successfully employed. Moreover, ultrasound-assisted casting plays a particularly promising role because of its high potential productivity. These methods typically require expensive and sophisticated equipment, which causes high manufacturing costs, low productivity and can also have an influence on the thermodynamic instability of the reinforcement in the metal matrix, or are not suitable for large-scale production. On the other hand, the advantages of the casting routes lie in their simplicity, flexibility, cost effectiveness and applicability to the large-quantity production of MMnCs. The casting routes employing liquid-steel metallurgy are considered the most suitable for bulk production.

For the large-scale production of metal matrix nano-composites, the main problem to face is the low wettability of ceramic nano-particles, which greatly limits the preparation of MMnCs by conventional casting processes, since the result would be an inhomogeneous distribution of particles within the matrix. The high surface energy leads to the formation of clusters of nano-particles, which are not effective in hindering the movement of dislocations and can hardly generate a physical-chemical bond to the matrix, thus reducing significantly the strengthening capability of the nano-particles [2]. Several unconventional production methods have been studied by researchers in order to overcome the wettability issue, either by the formation of the reinforcement by in situ reaction or by the ex situ addition of the ceramic reinforcement by specific techniques. Alternative methods are listed and discussed in a subsequent section by classifying them into liquid, semi-solid and solid processes.

2.4.1 Liquid processes

The production of metal-matrix composites via liquid-phase processing consists of incorporating or combining a liquid metal matrix with the reinforcement. The advantages of this technique are that a near-net-shape product can be achieved in comparison with solid-state processes (extrusion or diffusion bonding), the rate of processing is faster and related to melting most of the light metals, i.e., Al and Mg, have relatively low melting temperatures. The most common liquid-phase processing techniques can be subdivided into four major categories:

- *Casting or liquid infiltration:* The homogenous distribution of particles that are introduced directly into the melt is often achieved by stirring the molten mixture that consists of liquid metal and ceramic particles. On the other hand, in the case of centrifugal casting, a gradient in the reinforcement particle loading is obtained. In applications where the reinforcement needs to be tailored from a machining or performance perspective this can be quite advantageous.

- *Squeeze casting or pressure infiltration:* This method encompasses pressure-assisted liquid infiltration of a particulate preform. This process is particularly suited for complex

shape components, selective or localized reinforcement, and where the production speed is critical.

- *Spray co-deposition:* A granulated mixture of composite particles is produced by the atomization or spraying of liquid metal, while a particle injector introduces ceramic particles in the spray stream.

- *In situ processes:* The formation of the reinforcement phase takes place in situ, either by reaction during synthesis or by the controlled solidification of an eutectic alloy.

The major problem when using the technique of conventional liquid metallurgy process for the preparation of composites is severe aggregation of the nano-particles, even if mechanical stirring is applied prior to the casting. The reason for that lies in the high surface-to-volume ratio of ceramic nano-particles, which leads to poor wettability and high viscosity generated in the molten metal. Due to the very small size of nano-particles they are considered to be floating on the top of the molten bath of the matrix material, even though their density is relatively high compared to the density of the liquid matrix. Therefore, the density of nano-particles does not play an important role in the production process of nano-composites. This issue is of paramount importance in micron-sized particle reinforced composites. However, in nano-reinforced materials other effects such as those induced by extensive surface tension play a much more important role [29].

2.4.2 Solid-state processing

The control of reinforcement distribution and obtaining a uniform matrix microstructure is the main drawback in the production of MMnCs via liquid-phase processes. Furthermore, as the liquid-phase process involves elevated temperatures, adverse interfacial reactions between the matrix and the reinforcement are likely to occur. Because of that, the mechanical properties of the composite can be affected. The stated disadvantages and problems related to the use of the liquid-phase technique increase the interest in the solid-state processing of MMnCs. The most common solid-phase processes are based on powder-metallurgy techniques. Due to the ease of mixing and blending and the densification effectiveness, powder metallurgy techniques typically involve discontinuous reinforcements. Full density of a product that is prepared by mixing ceramic particles with a metal powder is achieved with cold isostatic compaction, followed by hot pressing. A secondary operation (extrusion or forging) is then applied to the compact that is already fully dense. Researchers are looking into new approaches like sinter forging, aiming to lower the process cost by eliminating the hot-pressing step, which already shows some promising results [30]. Solid-state processing techniques that are the most common can be subdivided into four major categories:

- *Powder-metallurgy processing:* Powder metallurgy is a branch of solid-state processing that covers the methods like pressing and conventional sintering, hot pressing or spark plasma sintering. Because of its inherent simplicity, it is also a widely investigated technique. The process of making the final product by powder metallurgy starts with blending of the reinforcement powder or precursors and metal powder, aimed at obtaining a homogenous mixture to be used for the in situ reinforcements and metal powder synthesis. The next step results in obtaining the so-called green body of the desired shape, produced by uniaxial/isostatic pressing or injection molding of the prepared homogeneous mixture through a die. The sintering process is then conducted, which can be done under different conditions (but necessary to maintain the properties of reinforcements and metallic matrix)

in order to obtain a nearly dense metal-matrix composite. Sintering is performed by exposing the green body to elevated temperatures, which depend on the materials used in the process and the sintering mechanisms to be activated. Sintering can be done without pressure applied to the sintered body or by using compressive forces in combination with elevated temperatures [18].

- *Extrusion:* Extrusion as a secondary deformation processing route for metal-matrix composites has turned out to be widely used [31]. The combination of extrusion pressure and elevated temperature presents the main advantage of the process. Because of this combination the shear between the interface of the Al/Al and Al/SiC particles in SiC reinforced aluminum occurs, which causes the fracture of the oxide layer on the Al particles and results in an enhanced bonding between the particles and the matrix. However, large strains that occur during extrusion may lead to reinforcement fracture. Therefore, the extrusion technique has been primarily used for the consolidation of composites reinforced with a discontinuous reinforcement. But even in discontinuously reinforced materials, the fracture of short fibers or particles often takes place, which can be detrimental to the properties of the composite. In Fig. 2 schematics of the three different types of extrusion processes are presented: direct, conventional, and hydrostatic extrusion [32]. In the first case, direct extrusion, deformation of the extruded material occurs by compressing it against a flat plate with a small orifice. This causes a "dead-metal zone" which consists of a region where the metal cannot flow. To minimize the so-called dead-metal zone the die is being tapered in the case of conventional extrusion. Also in this case, high deformation stresses are present at the interface between the extruded material and the die due to the die friction. In MMCs this effect is particularly exaggerated due to the presence of the particles and the large shear stresses at the metal/container interface, resulting in material discontinuities. This can result in ragged edges, called the "Christmas tree" effect. This is more predominant with an increase in reinforcement particle content, due to the increase in die friction and consequently in shear stress. Finally, the problem of die friction can be minimized by conducting the extrusion inside a high-pressure fluid. This results in a close to hydrostatic stress state and the minimal effect of billet friction due to a minimized contact area between the material and the die [32].

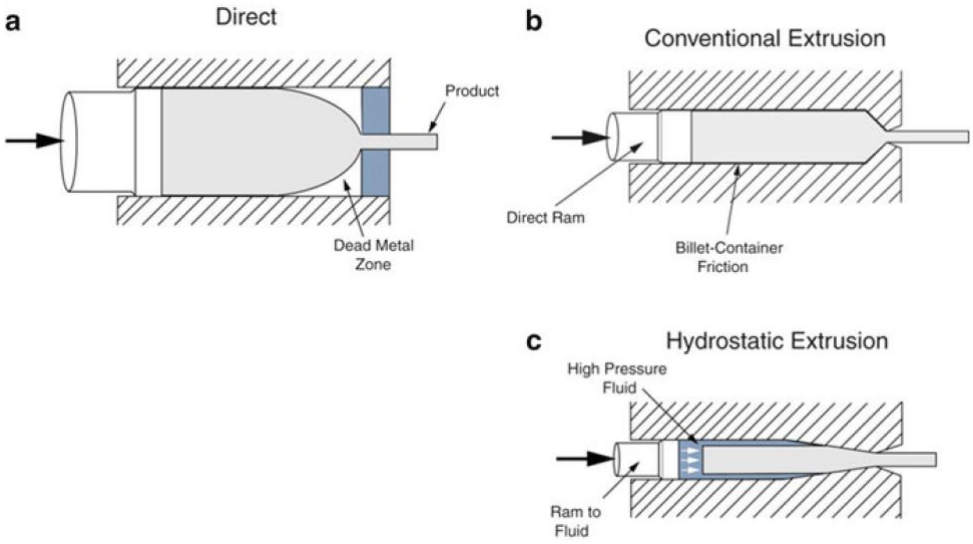

Figure 2: Three types of extrusion processing: (a) direct, (b) conventional, and (c) hydrostatic [32].

- *Forging:* The technique is mainly used for composites with discontinuous reinforcement, but nevertheless is a very common secondary deformation processing method when manufacturing metal matrix composites. There are two types of forging processes: conventional forging, where final near net-shape of the product is achieved by forging of previously hot-pressed or extruded material [32] and the novel, low-cost, sinter-forging technique. In the latter case the powder mixture of the reinforcement and the metal matrix is being processed by cold compaction, sintering and forging to a nearly full density. Machining operations and material waste are minimized as forging is conducted to produce a near-net shape material [33].

- *Pressing and Sintering:* In the production of composite materials the pressing and sintering technique represents a relatively inexpensive and simple method. Usually, the temperatures of sintering for these composite powder systems are at the level of obtaining some degree of the liquid phase. This results in better densification of the compact as the pores are filled with the liquid phase (unless an interfacial reaction takes place). In this section cemented carbides (WC–Co composites) should be specifically mentioned, which are used extensively for machining and rock- and oil-drilling operations. WC–Co composites consists of a very high-volume fraction of WC particles that are distributed in a soft cobalt matrix. The contact angle between the WC particles and cobalt matrix is 0°, meaning that cobalt, which is melted during the liquid-phase sintering, completely wets the WC particles with little or no interfacial reaction [32].

- *Diffusion Bonding:* It is a commonly used method where similar or dissimilar metals are being joined. It is conducted at elevated temperatures, with bonding occurring at the contact between the clean metal surfaces as a result of the interdiffusion of atoms. With this technique, a wide variety of matrix metals can be processed, having a control over the fiber volume fraction and orientation. However, high processing temperatures and pressures, and long processing times make the technique expensive. Also, the complexity of the shapes produced is limited. There are many variants of the basic diffusion-bonding process, although all of them involve the simultaneous application of pressure and high temperature [32].

2.4.3 Gaseous-State Processing

This type of process includes the methods by which composites are formed by deposition on the reinforcement of successive layers of matrix.

A major incentive for the use of this technique has been given by the need to achieve large adhesion at the fiber/matrix interface without generating reactions among the fibers, which can degrade the final composite properties. In particular, the PVD (Physical Vapor Deposition) technique is used for the formation of the external fiber coatings, whose purpose is to consolidate them into the composite of matrix-coated fibers.

Physical Vapor Deposition (PVD)

Plasma spraying is the primary form of gaseous-state processing. There is a continuous passage of fibers through a region in which the metal must be deposited at a high vapor pressure and where the condensation occurs in order to produce a thin coating on the fibers. The vapor production occurs directing a flow of high-energy electrons on the end of a feeding solid bar. The main application of plasma spraying is to form matrix-coated fibers, which are subsequently hot pressed to form the final product. Nanometer-scale composites that have been produced via PVD show a great deal of success. Sputter-deposition-based

processes are enabling various possibilities for the fabrication of nano-laminated microstructures with tailored chemistry, structure, and thickness of the individual layers and interfaces. However, controlling the intrinsic residual stresses can sometimes present a challenge to the synthesis of nano-laminates via PVD. This has been in some way resolved by using either in situ or post-deposition energetic particle bombardment from an ion source. During the PVD synthesis, processing parameters like reactive deposition, plasma-assisted deposition and substrate heating are also very important and have to be considered [30].

2.5 Influence of the Addition of Nano-Particles on the Mechanical and Wear Properties

2.5.1 Hardness and tensile strength

In the chapter above, various strengthening mechanisms were described that are influencing the MMnCs' mechanical properties and are contributing to the improved load-bearing capacity, i.e., ability of the material to withstand the mechanical loads that it is subjected to during its lifetime. Hardness is considered as a fast and reliable test for metals and alloys to evaluate their mechanical strength [34]. However, it was found that the correlation of hardness with the tensile strength is not linear when it comes to composites. It is not necessary that the particulate-reinforced metal material will exhibit an increased tensile strength, although the hardness will be higher. In a study by Shen et al. conducted on an aluminum alloy unreinforced and reinforced with SiC particles, it was found that a unique relationship between hardness and tensile strength does not exist, especially in cases where the matrix strength is relatively low [34]. Different deformation damage modes are occurring during the tensile and hardness tests. Fracture of the reinforcement particles, localized deformation during the hardness test and a local increase of particle concentration due to the indentation are only some of the factors influencing the material behavior. It was also observed that in the over-aged condition the composite with a higher reinforcement fraction shows a much greater hardness value, although its tensile strength may be comparable to those with lower particle fractions present in the matrix. The reinforcing phase in metal-matrix composites is generally much stiffer than the matrix. In MMCs microplasticity takes place at a fairly low stress. This is contributed to the stress concentrations in the matrix at the poles of the reinforcement and/or at the sharp corners of the reinforcing particles [35]. In another study of the Al-Cu-Mg (2080)/SiCp-T8 [36] composite an increase in the volume fraction of added particles resulted in a higher elastic modulus, macroscopic yield and tensile strength, coupled with lower ductility. The main strengthening mechanism responsible for that can be related to more load being transferred to the reinforcement. However, several researchers also proposed that relatively large particles are prone to cracking, which may take place during the composite processing by deformation (extrusion). Such cracked particles do not carry any load effectively, as observed for large SiC particles [37]. On the other hand, the size of the particles has an effect on the mechanical properties by other mechanisms. As described before, an increase in the volume fraction and a decrease of the particle size hinder the grain growth, thus resulting in a finer structure.

When dealing with metal-matrix composites reinforced with the incorporated nano-sized particles, the most favorable strengthening mechanism is considered to be Orowan strengthening [34]. Improved hardness of the nano-composite Ni/Al_2O_3 films was explained by the Orowan dislocation bowing mechanism in a study conducted by Shao et al. [38].

The Orowan loop mechanism was also observed by Thilly et al. [39], who used it to simulate and explain the good mechanical properties of the Cu/Nb nano-composites.

It was also observed that a thermal mismatch between the matrix and the reinforcing particle creates stresses around the nano-particles. These stresses are large enough to cause plastic deformation of the matrix at these sites and the generation of dislocation loops around the vicinity of the nano-particles [35]. The Orowan loops are also regarded as a source of back stress on dislocation sources [40].

2.5.2 Fatigue

Constant cyclic loading of the material degrades its mechanical properties. This phenomenon is called fatigue. During its lifetime a material can be exposed to different cyclic loadings, which may be of mechanical or thermal nature, or of the two combined. Many high-volume applications of composite materials involve cyclic-loading situations, e.g., automobile components and aircraft structures. Modulus, strength, ductility, and work-hardening characteristics of the composite constituents (reinforcement and matrix) as well as the characteristics of the interface are several of the material variables that play an important role in the fatigue of the MMCs. There are different approaches to studying fatigue and describing a material's behavior when exposed to cyclic loading. S–N curves and fatigue-crack propagation studies belong to the more conventional approaches; however, an approach involving the monitoring of the damage accumulation is also being used [32].

The fatigue behavior of particle-reinforced MMnCs is described as follows. The composite, at a given stress, undergoes a lower average strain compared to the unreinforced alloy. This is related to the fact that most of the load is carried by the high-modulus, high-strength reinforcement. In this case the fatigue behavior is influenced by various factors, which are the volume fraction of reinforcement particles and their size, the matrix and the interfacial microstructure, the inclusions or defects that are present in the matrix from processing, and the testing environment [36]. Furthermore, a fatigue-resistance increase can be obtained if the volume fraction of the particles added is increased, and at the same time decreasing their size [41][42]. Thus, a substantial increase in the fatigue resistance can be achieved by using high-stiffness particle reinforcements, while maintaining the cost at an acceptable level.

Particle-reinforced composites result in a longer fatigue life compared to the unreinforced metals, as shown in Fig. 3. These improvements are most pronounced at low cyclic stresses, i.e., in the high-cycle-fatigue regime, while at higher cyclic stresses the differences between reinforced and unreinforced materials are reduced. This has been called the "ductility exhaustion" of the composites, which takes place in the LCF regime. The higher fatigue life of the unreinforced alloy in this regime due to its better ductility is achieved compared to the composite material. At a designated volume fraction of a reinforcement present in the matrix and with decreasing particle size, the reinforcement inter-particle spacing decreases. Thus, more barriers are present to the reversible slip motion that is happening during fatigue, and because of the cyclic slip the refinement strain localization is decreased. Above a critical particle size, the reinforcement fracture is predominant and contributes to a low fatigue life, because of the increased propensity for particle cracking as the particle size increases [42]. Narrowing of the particle size distribution also results in a higher fatigue life, particularly when eliminating the larger particles that are more prone to cracking.

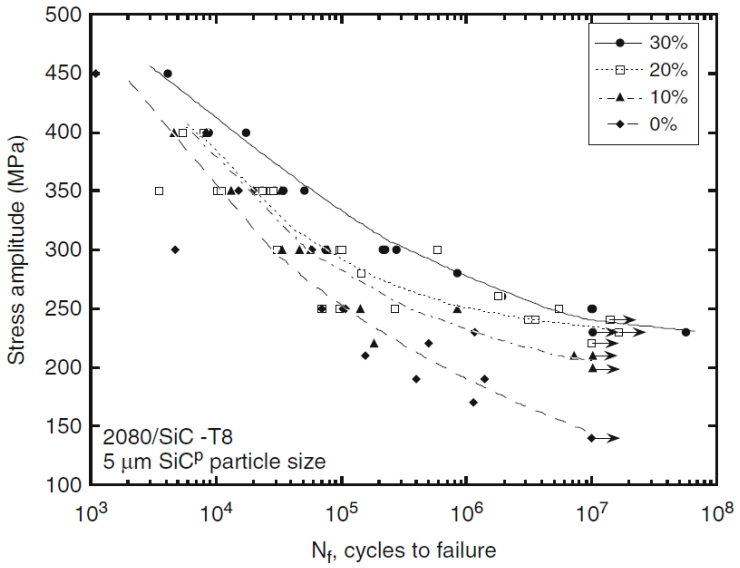

Figure 3: Effect of SiC volume fraction on the stress versus cycles fatigue behavior of 2080 Al/SiCp composites. Increasing the volume fraction results in a higher fatigue life [42].

In addition to particle reinforcement, the matrix microstructure also significantly influences the fatigue behavior of the composite. Factors affecting the matrix microstructure include the size, shape, and spacing of precipitates, the grain size, and non-reinforcement dispersoids or inclusions, such as Fe-rich inclusions in aluminum that are commonly formed during processing. It would appear that with regard to grain size, composites follow the same trend as monolithic materials, i.e., for a given matrix alloy composition and volume fraction of reinforcement, finer grain sizes generally result in improved fatigue properties. In contrast to the behavior of conventional monolithic materials, in MMnCs, a high matrix yield and ultimate tensile strength do not necessarily reflect in a high fatigue strength [32]. Vyletel et al. [43] showed that there was no significant difference in the fatigue behavior between naturally aged and artificially aged MMCs, even though the naturally aged material had a much lower yield and ultimate tensile strength. Chawla et al. [44] compared two materials with a constant reinforcement volume fraction and particle size, but very different microstructures. A thermomechanical treatment (T8) of the Al–Cu–Mg alloy produced a fine and homogeneous distribution of S' precipitates, while a single thermal treatment (T6) resulted in coarser and inhomogeneously distributed S' precipitates. Because of the finer and more closely spaced precipitates, the composite that underwent a T8 treatment exhibited a higher yield strength than the T6 material. However, despite its lower yield strength the T6-treated composites exhibited a higher fatigue resistance than the T8-treated ones. This contrasting behavior between static and cyclic loading can be attributed to the strong influence of the presence, stability, and morphology of the S' precipitates in the matrix of the composite [45]. In fatigue, failure processes are affected by a variety of microstructural factors, which include the resistance to dislocation movement and the possible dislocation pileup at precipitates and/or reinforcement particles cracking along the slip bands.

2.5.3 Creep

When exposed to a constant stress or strain for long periods of time and in the presence of increased temperature (at least half of the homologous temperature, defined as the temperature of interest divided by melting point, both in K; i.e., T/Tm) the material can

be subjected to creep. MMCs creep behavior is of great significance. Many of the structural and non-structural applications of MMCs are in an environment where they are exposed to the previously mentioned loads. There are three distinct stages of creep common to most materials. These are primary creep, where strains are relatively small, secondary or steady-state creep, and tertiary creep. The combination of hardening and recovery mechanisms during creep results in a linear relationship between the strain and the time in the secondary or steady-state regime. Finally, in the tertiary regime, the material undergoes cavitation and void growth, which is manifested in terms of a very rapid increase in the strain with the time.

The creep resistance of a material that contains high-stiffness reinforcements in the matrix is in general better than an unreinforced alloy. Reinforcements also affect the deformation mechanisms that are occurring during creep, which are changed as compared to the creep mechanisms in the non-reinforced matrix. For composite materials it was found that a higher creep resistance is accompanied by a higher sensitivity to applied stress (a much higher stress exponent). These high values of stress exponents were rationalized by the concept of a threshold stress. A detailed description is given in ref. [20], with the threshold stress being defined as the lower limiting level of stress below which there is no measurable plastic flow [46]. The threshold stress in discontinuously reinforced composites can be the result of various reasons [47][48]: (1) Orowan bowing between particles, (2) back stress associated with dislocation climb, and (3) the attractive force between dislocations and particles, resulting from the relaxation of the strain field of dislocations at the particle/matrix interface [49]. Due to the higher work-hardening rate of the matrix, i.e., the addition of particles results in a smaller volume of the matrix material, increasing the work-hardening rate relatively to the unreinforced alloy, the enhancement of dislocation/dislocation interactions can contribute to threshold stress, although this mechanism is more plausible at ambient temperature. The high stress exponents that are observed in MMCs cannot always be explained by using the threshold stress approach. Significant load transfer to the reinforcement, despite the lower aspect ratios of particles and whiskers, can occur. With increasing load transfer to the reinforcements, the resolved shear stress on the dislocations in the matrix can be lowered significantly below that required for Orowan bowing. Other aspects of creep deformation, such as grain-boundary sliding, are also considered [50]. It was shown that when the grains in the matrix are allowed to slide, incorporation of the reinforcements results in enhanced stresses in the matrix, which can result in inhomogeneous grain-boundary sliding.

The creep curves that are describing the creep behavior of the specific material are also influenced by the type of reinforcement used in the composite matrix. A schematic of typical creep curves (strain versus time) for MMCs with continuous and discontinuous reinforcement is shown in Fig. 5. A short primary creep regime is common for composites with continuous fibers, after which a long steady-state regime takes place (Fig. 5). Because the degree of load transfer in the case of a composite reinforced with discontinuous reinforcement (short fibers or particles) is not as high as compared to that for continuous fibers, the creep behavior is more typical, having all three distinct creep states (Fig. 5). The creep-behavior predictions can be made by simple viscoelastic models, such as an isostrain model, where the matrix is modeled as the viscous component and the fiber is elastic.

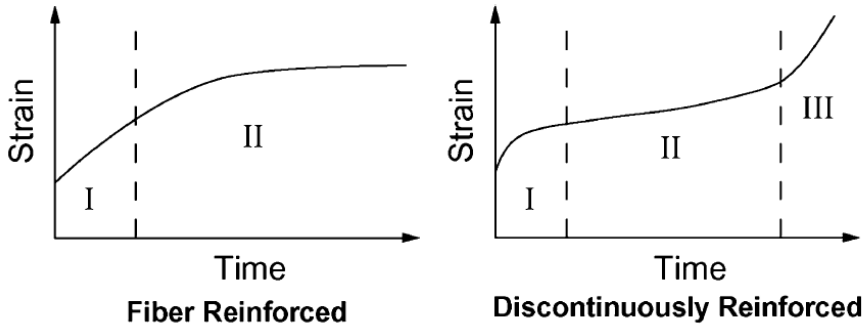

Figure 4: Schematic of creep strain versus time for fiber-reinforced and discontinuously reinforced MMCs [51]. The three stages of creep are (I) primary creep, (II) steady-state creep, and (III) fast fracture.

2.5.4 Wear

The wear and friction performance of metal-matrix composites are influenced by the amount, size, shape, and distribution of fibers and/or particles added into the matrix. The mechanical and tribological properties of MMnCs are, in addition, also affected by the interfacial bonding that is occurring between the reinforcements and the matrix. If, for instance, hard particles are used as the reinforcements in the matrix, the strength and wear resistance of the MMnCs is increased, but on the other hand the ductility of the composites is decreased and the coefficient of friction is increased. However, the coefficient of friction of the MMnCs decreases if soft particles are used, as they usually act as a solid lubricant with a reduced shear strength [52].

The wear and friction behaviors of MMnCs can be affected by various different factors. The basic tribological factors that control the wear and friction behaviors of MMnCs can be classified into three categories [52]:

1. material factors, such as the type of reinforcement, their size, shape, volume fraction and microstructure of the matrix,

2. mechanical or contact factors, such as the normal load, sliding velocity and sliding distance,

3. physical factors, such as the temperature, humidity and environmental conditions.

Wear is defined as the progressive loss of material during the relative motion between a surface and the contacting substance or substances. Various studies by different researchers [53][54][55] have been made concerning MMnCs' wear behavior and the tribological properties. The results have shown that the wear performance of MMnCs is better than that of unreinforced matrices [56], which is mainly related to the increased hardness of the composites. Fig.6 presents a comparison of the wear rates between the unreinforced alloy Al6061 and Al6061 MMnCs reinforced with SiC, which exhibits better anti-wear properties. [56]. As shown in Fig. 6, the wear rates of both the matrix alloy as well as the composite decrease linearly with the sliding distance. However, in the case of the matrix alloy a drastic increase in the wear rate can be observed after 2 km of sliding. After a certain time of sliding, high contact temperatures may develop at the sliding surface, resulting in surface softening. It may also react with the surrounding oxygen and form different oxides. With time the hard and brittle oxides formed on the surface will

become thicker, eventually covering the entire contact surface. In the case of Al alloys the aluminum oxide film partly acts as a thermal insulator, which can result in an oxide film overheating, plastic deformation and chipping off at an abnormal rate, thus increasing the overall wear rate. However, for MMnCs the wear rate was, in general, found to be lower than for the unreinforced matrices, which is especially true for severe wear regions. In these cases tribo-chemical reactions that are taking place at the contact surface significantly affect the wear rate. On one hand, tribo-chemical reactions can be altered by reinforcement particles. On the other hand, the reinforcement particles will affect the formation, hardness and thickness of a mechanically mixed layer (MML) formed between the sliding surfaces, which further controls the wear rate. MML thickness and hardness increase with increasing reinforcement fraction, thus providing improved wear resistance [57].

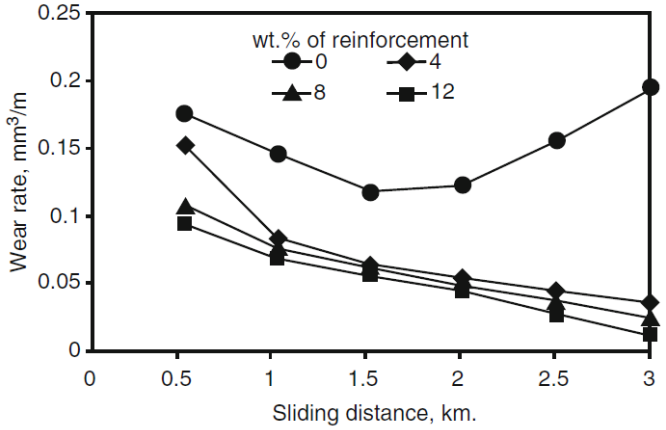

Figure 5: Variations of wear rate with sliding distance for Al6061-based MMnCs at an applied load of 10 N and a sliding velocity of 1.85 m/s [56].

When two or more surfaces are in relative motion wear mechanisms such as adhesive wear, abrasive wear, delamination wear, erosive wear, fretting wear, fatigue wear, and corrosive/oxidative wear may take place, depending on the properties of the materials being in contact. For MMnCs the most common wear mechanisms that are occurring are adhesive wear, abrasive wear, fatigue wear, and corrosive/oxidative wear [58].

Different approaches are being investigated with the aim of improving the wear and friction behavior of metallic materials. In order to achieve better wear resistance metal matrices are being reinforced with different kinds of hard reinforcement particles. In MMnCs, the most common reinforcements used are Al_2O_3, SiC, and B_4C, which are usually added to the metal to improve the mechanical properties, mainly strength and hardness of the composite. These kinds of reinforcements have been found to also improve the friction properties and wear resistance of the composites [59]. Fig. 7 shows the coefficient of friction of the aluminum alloy and the aluminum matrix composite [60]. It indicates that the coefficient of friction of the aluminum MMC is substantially lower than for the unreinforced aluminum alloy [56]. On the other hand, some of the reinforcements used, such as graphite, molybdenum disulfide, and hexagonal boron nitride, are added into the metal matrices in order to decrease the coefficient of friction of the composites, with the decrease being significant [61].

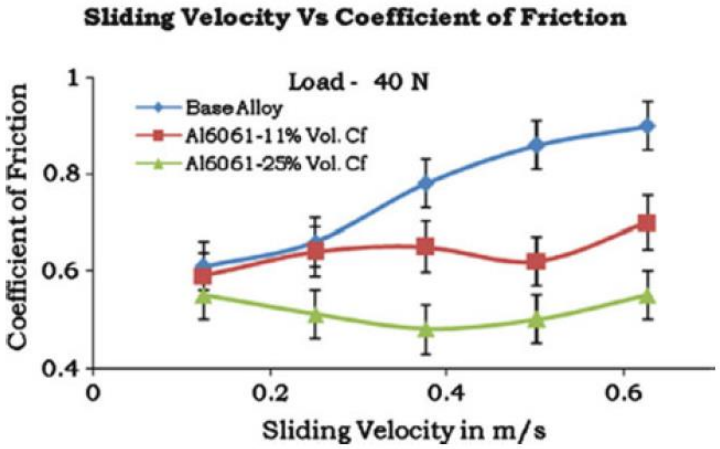

Figure 6: Variation of coefficient of friction with sliding velocity for the Al6061 alloy and its carbon fiber (C_f)-reinforced composites [60].

2.6 Applications

Metal-Matrix nano-Composites (MMnCs) are used in a numerous applications. The high strength-to-weight ratio, enhanced mechanical and thermal properties over conventional materials and the tailorability of the properties make them very attractive in a variety of applications. Increasingly, MMnCs have been used in several areas, including aerospace, transportation (automotive and railway), electronics and thermal management, filamentary superconducting magnets, electric power transmission, recreational products and sporting goods and wear-resistant materials. In this chapter we review some important applications of MMCs and point out the advantages and further possibilities of using MMCs [20].

MMnCs have been used in several applications in aerospace components. This stems in large part from the fact that materials with increased specific stiffness and strength can significantly enhance the performance of the aircraft. A simple example is stringers on aircraft skin. Stringers are often used to stabilize the skin in the fuselage. Increased skin stiffness means that there is less chance of the skin buckling. Furthermore, a large stringer can be used to stabilize the skin. Using a SiC-particle-reinforced Al matrix composite skin, the effective allowable aluminum-alloy stringer size increased, resulting in enhanced stability of the skin. In military aircraft, MMnCs have found a large number of applications [62].

In the F-16 aircraft, aluminum access doors were increasingly susceptible to fatigue cracking. The aluminum doors were replaced with particle-reinforced MMC (Al/SiCp) as a weight-neutral solution. MMnC was also used as a replacement for unreinforced aluminum in the ventral fins of the F-16. The MMnC material exhibited much lower deflection because of the higher stiffness. The incorporation of the MMC resulted in a fourfold increase in the life of the component and $26 million life-cycle cost savings [32]. Similar improvements were obtained by the incorporation of the MMnC in the F-16 fuel access door covers. Continuous fiber-reinforced MMnCs have also been used in military aircraft applications, due to their high specific strength, stiffness, and fatigue resistance. SiC monofilament-reinforced Ti-matrix composites have been used as nozzle actuator controls for the F119 engine in the F-16. The MMC replaced a heavier Inconel 718 in the actuator links and stainless steel in the piston rods [32]. Another important application in aerospace is blade sleeves in helicopters. The blade sleeve must be able to tolerate centrifugal loads from the blades to the rotor. Thus, fatigue life, fretting resistance,

toughness, and high specific strength are required. The composite providing these properties consisted of SiC particles in an Al alloy matrix. Powder metallurgy-processed billets were extruded, cut, and forged. The final component yielded only 1 % in waste. The fatigue strength of the composite was around 270 MPa (assuming a fatigue run out at 10^7 cycles), which was a 50–70 % increase over the fatigue strength of unreinforced Al. The fracture toughness was reasonable, at 25 MPa$\sqrt{\text{m}}$, and the specific strength and cost were lower than those of the initial Ti alloy used in this application [32].

The enhanced wear resistance [4] and the good thermal conductivity combined with the high specific strength make MMnCs attractive materials for aircraft brakes. Moreover, the specific strength and elastic modulus could be exploited in the sports industry, for instance for rackets or bicycle frames and other components. A further field of potential application is in electronic devices, for example, for heat sinks and solders (thanks to their thermal properties) or as antennas (thanks to their electrical properties and stiffness). Aerospace and automotive industries may exploit all the above properties for different kinds of applications, such as structural radiators, gears, aircraft fins, cylinder liners, disk brakes and calipers [30].

The improved damping capacity of MMnCs could also be exploited to reduce vibrations and the noise of structures. In Mg–Al_2O_3 samples extruded at 350 °C after powder milling, a significant damping ability was highlighted and attributed to the interface character of the MMnCs [3]. Indeed, CNT/2024 Al composites showed improved damping properties at elevated temperatures, as high as 400 °C [63].

Chapter 3

Aims and Hypothesis

3.1 Aims

The aim of the doctoral thesis is to assess the feasibility and possibilities of introducing nano-particles into a steel matrix through conventional low-cost liquid-metal casting and to determine the effect of different reinforcement nano-particles on the mechanical properties and wear resistance of the reinforced steel. Furthermore, the focus of the thesis is on the method of adding nano-particles to the steel melt with the purpose of achieving a uniform distribution of nano-particles within the steel matrix using conventional casting routes and to study the stability of the different types of nano-particles added. The particles were selected based on their high-temperature and chemical stability in the chosen steel matrix. The aim of the work is also to provide further knowledge and understanding of the incorporation and the effect of nano-particles in the steel matrix and how to obtain their homogeneous distribution, which has significant scientific importance.

The experimental work consists of various approaches to the selection, modification and addition of nano-particles and investigating their impact on the development of the microstructure and mechanical properties of steel. In order to accomplish the aims, the following goals have been established:

- determination and evaluation of thermodynamic stability of nano-particles in the steel melt with ThermoCalc software,
- altering the surface properties of nano-particles with surface plasma modification,
- evaluation of different techniques of adding nano-particles into the steel melt aimed at achieving a uniform nano-particles distribution,
- investigation of the type, concentration and size of nano-particles added in the steel matrix,
- improvement in the mechanical properties of nano-particulate-reinforced steel matrix composites (hardness, tensile strength, impact toughness, creep resistance) and
- improvement of the tribological properties of nano-particulate-reinforced steel matrix composites.

A major challenge after producing metal matrix composite samples was to determine and select the appropriate techniques for the characterization of the nano-particles in the steel matrix. Nano-particle-reinforced steel samples were characterized in terms of microstructural analysis, including identification of the nano-particles, their distribution and volume fraction. The microstructural changes and the dispersion of the nano-particles in the steel matrix were observed and analyzed by light microscopy (LM), scanning electron

microscopy (SEM) and transmission electron microscopy (TEM). The influence of the nano-particles addition type and the method of their incorporation on the mechanical properties of the metal-matrix composite were evaluated by means of mechanical testing, including tensile testing, impact toughness measurements, hardness measurements, and high-temperature creep and tribological testing.

The research on the distribution homogeneity and the incorporation of nano-particles in the steel matrix, the thermodynamic stability of particles in the steel melt, the effect of nano-particles modification, and the influence of the nano-particles type, concentration, size and addition method will allow an understanding of the process of the successful incorporation of nano-particles into the steel matrix and their influence on the mechanical properties and wear resistance. Furthermore, the focus of the doctoral thesis is on the successful production of nano-particles-reinforced steels by conventional casting methods.

3.2 Hypothesis

The main issue in the production of MMnCs is clustering and consequently the inhomogeneous distribution of the nano-particles due to their high surface energy density and low wettability with the molten metal matrix, which makes it almost impossible to produce MMnCs by a conventional casting process.

The hypotheses of the doctoral dissertation is that with a proper selection of the nano-particle type, size and concentration, modification of the nano-particles' surface properties, and an adequate introduction method a homogeneous distribution and incorporation of nano-particles in the steel MMnCs should be possible also when using conventional casting methods, thus enabling the cost-effective production of nano-particles-reinforced steel with improved mechanical properties and wear resistance. The results of the microstructural analysis and the testing of the nano-particles-reinforced steel samples will provide a reliable explanation on how the nano-particles improve the properties and, at the same time, define the mutual impact of the addition method, type, size and concentration of added nano-particles on the mechanical and anti-wear properties of the reinforced steel matrix.

Chapter 4

Materials and Methods

4.1 Material

Austenitic stainless steel AISI 316L was used for this work as a reference and matrix material, mainly due to its excellent corrosion resistance and distinctive two-phase microstructure of austenite and ferrite. The two-phase microstructure was used for the easier detection and identification of nano-particles in the steel matrix. It also belongs to the most used group of stainless steels, also when it comes to loaded parts subjected to sliding and corrosion. It is paramagnetic, has a face-centered cubic lattice and excels with a good combination of hot and cold workability, mechanical properties and corrosion resistance. The chemical composition is given in Table 1.

Table 1: Chemical composition of the base AISI 316L austenitic stainless steel in wt. %.

C	**Si**	**Mn**	**P**	**Cu**	**S**	**Cr**	**Ni**	**Mo**	**Ti**	**N**	**Co**	**V**
0.02	0.48	1.88	0.03	0.32	0.03	16.60	10.70	2.01	0.16	0.02	0.17	0.04

Preliminary tests were focused on the influence of reinforcement particle size on their distribution in the matrix of austenitic stainless steel AISI 316L. For this reason, Al_2O_3 nano-particles with a nominal mean particle size of 50 and 500 nm were selected. Based on the preliminary test results all of the following experiments were conducted using the nano-particles with a mean particle size of 50 nm.

As reinforcement nano-particles, commercial Al_2O_3, TiO_2, Y_2O_3, TiC and TiB_2 nano-powder delivered from the company US Research Nanomaterials, Inc. were used. From the transmission electron microscopy (TEM) analysis of the delivered powders, it was established that the particles are not only within one single size range, i.e. 50 nm. As shown in Fig. 7, the granule size in the case of Al_2O_3 nano-powder, declared in the 50 nm size range stands between 50 nm and 500 nm, at the same time showing agglomeration into larger particle clusters. This is true for all the nano-powders used. That is why it was decided to analyze the particles within two size ranges: < 500 nm and ≥ 500 nm.

The Al_2O_3nano-particles were selected due to their high chemical and temperature stability (melting point is 2072 $^\circ$ C), high hardness and effect on the properties of the MMCs. The addition of Al_2O_3 nano-particles into metal matrix improves the thermal fatigue resistance, fracture toughness, creep resistance and wear resistance of the metallic materials. Al_2O_3 nano-particles have also been reported to show a clean interface with the steel matrix [64]. Furthermore, in the case of steel a good wetting of Al_2O_3 was observed due to the presence of different alloying elements in the steel. A study of Howe [65] has shown that the wetting of Al_2O_3 increases with the addition of Cr, Ni, Mo and Mn to the steel.

The melting point and density of TiO_2 is 1843°C and 4.23 g/cm^3, respectively. Titanium dioxide has an elastic modulus of 228 GPa and a tensile strength of 367 MPa. It was found

that incorporated nano-sized titanium dioxide particles significantly improve the ductility, compressive yield strength and ultimate compressive strength of the metallic matrix without affecting its hardness and tensile strength [11],[66].

The main advantages of Y_2O_3 particles include a high melting point, being of approximately 2450°C, and good chemical stability. Yttrium oxide also known as yttria is mainly used for coatings that are also stable at high temperatures and resistant to many reactive molten metals [67].

TiC reinforcements show good wetting and thermodynamic stability in iron alloys and when producing steel MMCs. TiC's melting point is about 3120 °C and it has a destiny of 4.93 g/cm^3. It has an elastic modulus of approximately 440 GPa and a shear modulus of 188 GPa. TiC nano-particles are essential components of cemented carbide with a high hardness, corrosion resistance, thermal stability, etc. Also, they are often used in the manufacture of wear-resistant materials, cutting tools, molds, metal melting crucibles and in many other fields [68].

TiB_2 ceramic is a widely used reinforcement material to fabricate steel MMCs due to its high stability (melting point is 2980 °C) in steels [69]. Shurin and Panarin [70] developed the Fe-TiB_2 phase diagram, which shows a direct equilibrium between TiB_2 and ferrite and austenite phase. The phase diagram does not show the formation of the Fe_2B phase.

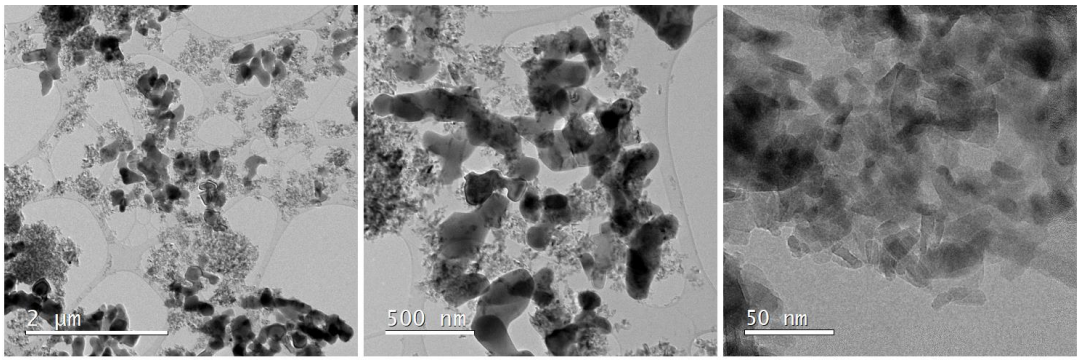

Figure 7: HAADF/STEM (high-angle annular dark-field scanning transmission electron microscopy) image of Al_2O_3 nano-powder with a mean particle size of 50 nm.

4.2 Casting Method

The material used in this investigation as a reference and starting base material was commercial AISI 316L austenitic stainless steel. The steel melt was produced under normal atmospheric conditions using a 20-kg capacity medium-frequency induction furnace.

The initial experiments were aimed at investigating the influence of different casting methods and concentrations of added Al_2O_3 particles (0.5, 1.0 and 2.5 wt.%) with mean particle sizes of 50 and 500 nm on their distribution in the austenitic stainless steel AISI 316L matrix. Different approaches were taken during conventional ingot casting in the sense of adding the particles into the melt. The methods of particle addition were the submerging method, pouring-over method and the method of insertion into the melt flow during casting, as shown in Figure 8. Nano-particles were encapsulated either in a ferritic steel tube, Al tube or Al foil and this one submerged, poured over or inserted into the melt flow. A detailed description of casting methods is given in Table 2. The final goal was to find the best incorporation method, size and concentration of nano-particles (Table 2) to achieve a uniform distribution of the particles throughout the whole ingot. Therefore, 2 kg as-cast ingots were investigated in the first stage of the research, not involving any mechanical, fatigue, creep or wear testing. Based on the results of those preliminary

experiments a final set of experiments was planned, involving 8 kg ingots, which were also hot rolled after casting. More material combined with hot rolling was needed for subsequent mechanical testing and evaluation of the influence of the added nano-particles on the mechanical, wear, creep and fatigue properties of the reinforced AISI 316L stainless steel.

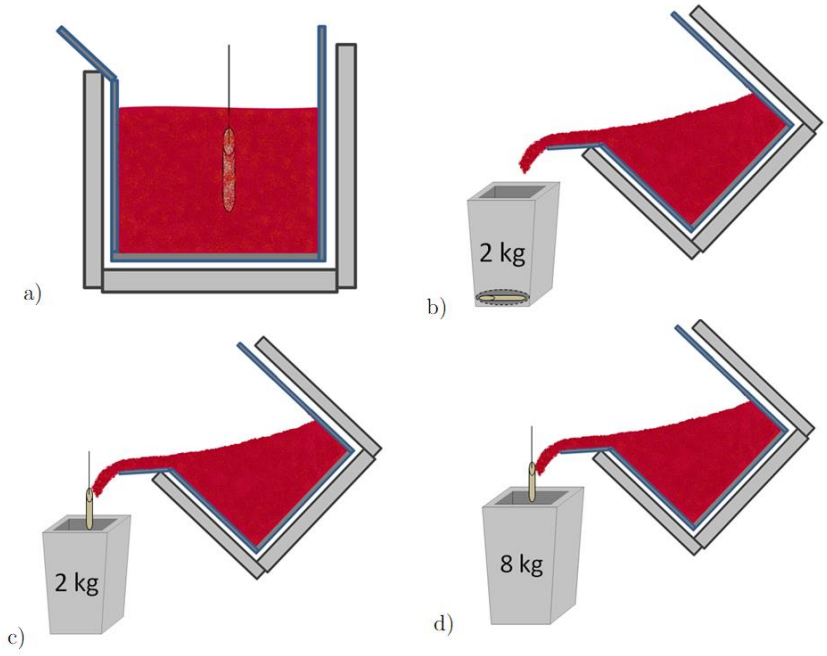

Figure 8: The methods of particle additions: a) submerging, b) pouring over method, c) insertion into the melt flow during casting (2 kg) and d) insertion into the melt flow during casting (8 kg).

The final set of experiments was focused on the method of *ex situ* introduction of the commercial Al_2O_3, TiO_2, Y_2O_3, TiC and TiB_2 nano-particles into the melt. In all cases nano-particles were added to the melt using the insertion tube method, where the nano-particles powder mixture was sealed into a thin ferritic steel tube with length of 400 mm, outer diameter 12 mm, wall thickness 0.25 mm, which had the following composition (wt.%): 0.05% C, 0.30% Si, 0.62% Mn, 16.2% Cr, 0.17% Ni and 0.18% Cu. The sealed ferritic steel tube was placed into the melt flow, with the molten metal pouring over and melting the tube. For all the experiments, the ferritic steel tube was melted and dissolved in the melt completely. The mass of each cast ingot was 8 kg. After casting, the cast ingots were hot rolled in 9 passes. The starting temperature of the ingots for hot rolling was 1150°C. The temperature after the last pass was approximately 980–1000 °C. The hot-rolled ingots were then left to cool in air to room temperature. The overall deformation rate after each pass was 12%.

Final material investigation and nano-particles effect evaluation was performed for nine different 8 kg cast and hot rolled ingots (Table 2). Firstly, remelted, cast and hot rolled 316L stainless steel ingot was used as a reference material (R). To the additionally produced ingots using 316L stainless steel were then added nano-particles with an insertion tube method, as described before. In all cases the concentration of added nano-particles was 0.5 wt. %. The A1 sample was reinforced with the addition of 50-nm-sized Al_2O_3 nano-particles. Then 50-nm-sized Al_2O_3 nano-particles were mixed with the dispersion medium CaSi in 1:1 mass ratio and added to the steel (A2). In the current work commercial CaSi was used as a dispersing agent due to the fact that it is most commonly used as a deoxidant element

in steel making, and does not cause contamination of the steel melt. In the present case, the aim of the CaSi (Ca 30%, Si 70%) addition was to facilitate dispersion (de-agglomeration) and promote the homogeneous distribution of nano-particles added in the steel melt due to the high reactivity of CaSi. The next ingot was reinforced with the addition of 50-nm-sized activated Al_2O_3 nano-particles (A3). The sample with activated Al_2O_3 nano-particles mixed with the dispersion medium CaSi in a 1:1 mass ratio added to the steel was labeled as A4. From here on, in all next cast and hot-rolled ingots nano-particles of different types were added in 0.5 wt. % and mixed with the dispersion medium CaSi in a 1:1 mass ratio. The samples were labeled as B for Y_2O_3 nano-particles addition, C for TiO_2 nano-particles added, D for TiC nano-particles and for addition of TiB_2 nano-particles as E.

Table 2: Nano-particles type, concentration, size and method of introduction.

Sample	**Base material**	**Nano-particles**	**Particles size [nm]**	**Particles concentration** [%]	**Method**	**Dispersant**
Preliminary tests (as cast)						
R	316L	-	-	-	-	-
S1		Al_2O_3	500	1.0	Submerging[2]	-
P1			500	0.5	Pouring over method [3]	-
P2				1.0		-
P3				2.5		-
P4			50	0.5		-
P5				1.0		-
P6				2.5		-
F1			500	0.5	Insertion into the melt flow during casting[4]	-
F2						CaSi (1:1)
F3			50			-
F4						CaSi (1:1)
F5			50	0.5		CaSi (1:1)

[2] Submerging of the steel tube with encapsulated nano-particles directly into the melt prior to casting.

[3] Nano-particles were placed on the bottom of the cuboid shaped steel mold wrapped in an aluminium foil and then poured over with molten steel matrix (2 kg).

[4] Nano-particles were encapsulated in an aluminium foil tube and held in the path of the melt flow when casting into the mold started (2 kg).

F6				1.0	Insertion into the melt flow during casting[5]	CaSi (1:1)
Main/Final tests (cast and hot rolled)						
R	316L	-	50	0.5	Insertion into the melt flow during casting[6]	-
A1		Al_2O_3				-
A2		Al_2O_3				CaSi (1:1)
A3		Al_2O_3 activated				-
A4		Al_2O_3 activated				CaSi (1:1)
B		Y_2O_3				CaSi (1:1)
C		TiO_2				CaSi (1:1)
D		TiC				CaSi (1:1)
E		TiB_2				CaSi (1:1)

4.3 Activation of the Surface by Oxygen Plasma

In general, the casting technique of MMCs involves producing a melt of the selected matrix material followed by the introduction of the reinforcement nano-particles into the melt in order to obtain a suitable dispersion [71]. A homogeneous dispersion of ceramic nano-particles in molten metals is hard to achieve, due to the low wettability and the large surface area of the nano-sized particles. They tend to distribute throughout the matrix non-homogeneously and agglomerate into a coarse cluster along the grain boundaries. Even more difficult is to achieve homogeneous dispersion in steel-based MMCs due to the high specific weight of the molten metal.

To avoid these problems, researchers tried to find alternative surface treatments for improving the bonding performance of ceramic nano-particles in the steel melt. Surface modification using plasma processing is a technique used to improve the bonding performance by changing functional groups and creating reactive sites on the surface. The surface modification by oxygen plasma is based on roughening the surface and increasing the wettability, which leads to mechanical and chemical bonding between the matrix and the surface of the nano-particles. In the current case the most stable Al_2O_3 nano-particles, as indicated by thermodynamic calculations using ThermoCalc software, were selected for

[5] Nano-particles were encapsulated into steel tube and held in the path of the melt flow when casting into the mold started (2 kg).

[6] Nano-particles were encapsulated into ferritic steel tube and held in the path of the melt flow when casting into the mold started (8 kg).

further plasma surface modification. Plasma surface activation by oxygen plasma (P=300 W, p=250 sccm) was carried out in an after–glow low-pressure radiofrequency (RF) plasma reactor for a time period of 10 s. The plasma treatment was performed at the Jožef Stefan Institute, Department of Surface Engineering and Optoelectronics (F4).

4.4 Thermodynamic Calculation with ThermoCalc Software

ThermoCalc software is a thermodynamic modelling tool used for exploring the equilibrium and phase relationships in complex materials. It is a very important method, which is also becoming more and more used for various kinds of calculations of thermodynamic properties in scientific investigations as well in the industry. However, the thermodynamic software calculations of phase stability as performed in our case are limited to the equilibrium state. Furthermore, thermodynamic calculations are useless without an accurate and valid database needed for the desired calculations. Therefore, the results of the thermodynamic calculations are mainly limited by the extent of the thermodynamic data that are gathered in the database used. Existing databases are being updated, but on a rather irregular basis. With the updates, the accuracy and reliability of such calculations are being improved.

ThermoCalc software is based on thermodynamic data that were obtained from experimental or theoretical tests and are listed in various databases. With the selection of the desired database we can make predictions using thermodynamic calculations of stable and metastable heterogeneous phase equilibria, calculation of transformation temperatures (liquid, solidus), design phase diagrams (binary, ternary and multicomponent), determine thermodynamic properties (enthalpy, thermal capacity and activity) of chemical reactions. In our calculations TCFE8 – TCS Steels/Fe-Alloys Database [72] was used. TCFE8 is a thermodynamic database for different kinds of steels (stainless steels, high-speed steels, tool steels, HSLA steels, cast iron, corrosion-resistant high-strength steels and more), Fe-based alloys and cemented carbides, to be used with the Thermo-Calc, DICTRA and TC-PRISMA software packages.

4.5 Characterization

4.5.1 Samples preparation

The microstructural changes and the dispersion of the ceramic particles in the steel matrix were observed and analyzed by light microscopy (LM), scanning electron microscopy (SEM), and transmission electron microscopy (TEM). Samples for the microstructure analysis and determination of the nano-particles distribution homogeneity (10 mm x 10 mm x 10 mm) were taken from different sections of the cast ingot. Multiple samples were taken from the top, middle and bottom parts of the cast ingot, as shown in Fig. 33 and 47. Additionally, samples of as-cast as well as hot-rolled ingots, taken from the middle sections were acquired for microstructural analysis and a determination of the nano-particles effect on the microstructure evolution. Metallographic samples were prepared by grinding with SiC paper, followed by polishing with a 1-µm diamond suspension and chemical etched using aqua regia (10 mL HNO_3+ 30 mL HCl +20 mL glycerol), optimally in a molar ratio of 1:3:2. Finally, all the samples were dried in hot air. Samples for the Transmission Electron Microscopy were prepared by slicing the samples into thin foils (0.5–1.0 mm) with a length of up to 3 mm. After polishing the foils down to a thickness of 100±10 µm, final milling was carried out with an Ion Slicer.

4.5.2 Particle distribution analysis

In order to determine the size distribution of nano-particles in the size range below 500 nm, SEI images from the scanning electron microscope taken at 20,000 x magnification were analyzed using FIJI (ImageJ) software. The analysis was performed so that firstly an appropriate threshold was applied and then a 3D object counter plugin was used for automatic nano-particle analysis, providing surface area and centroid coordinates for each particle. For a reliable particle analysis, all the images were taken at the same magnification with similar contrast, covering an area of about 30 μm^2 (6.0 µm x 4.8 µm). For each case at least 10 randomly selected areas were analyzed.

For a representative analysis of the particles distribution and size in the range above 500 nm, multiple surface areas of 1 mm x 1 mm were analyzed by SEM for each sample. The analysis was performed by the INCA Feature software incorporated in the SEM, which provides a high-performance automatic feature detection, analysis, and classification of the particles. In terms of particle distribution, we evaluated the results in the form of relative frequency and particles density (n*)* [mm^{-2}].

4.5.3 Light microscopy (LM)

The method enables a quick insight into the microstructure and allows microstructure characterization by revealing grain boundaries, phase boundaries, inclusions distribution, and evidence of mechanical deformation. The light microscope consists of mechanical (base, pillars, curved arm, a tube, a revolving nose-piece, stage, mechanical stage, coarse and fine adjustment) and optical (eyepiece or ocular, diaphragm, condenser or sub-stage condenser, objective) components with a built-in light source. The magnified image in the light microscope is provided by the lens and eyepiece. Modern microscopes also have a built-in camera that can capture the image [73].

The microstructure of etched test sample was analyzed by Microphot FXA, Nikon light microscope with build in 3CCD-videocamera Hitachi HV-C20A and computer software analySIS.

4.5.4 Scanning electron microscopy (SEM)

SEM allows analysis of the microstructure at a much higher magnification, i.e., sub-micron-level. However, it also enables a topography and surface-structure investigation of the samples. Modern SEMs often use a field-emission gun (FEG) with a Schottky type emitter, thus providing the ultimate performance and resolution. When the incident beam of electrons strikes the sample several electron/sample interactions occur and produce different measurable signals. Signals that are normally used for characterization are backscattered electrons (BSE), secondary electrons (SE) and characteristic X-rays that also allows the composition investigations of samples. The whole sample analysis is done under vacuum in the vacuum chamber of the microscope [74].

In our work an FE-SEM JEOL JSM 6500F field-emission scanning electron microscope (SEM) was used for the detailed microstructure analysis and investigation of the inclusions. The SEM micrographs were taken in the secondary-electron imaging (SEI) mode and backscattered electron (BSE) mode using an accelerating voltage of 15 kV, accompanied also by Energy-Dispersive X-ray Spectroscopy (EDS).

4.5.5 Transmission electron microscopy (TEM)

The TEM enables the observation and analysis of samples on a very small scale, nano and atomic scale, meaning the investigated area is very small (nanometer scale). TEM was used

for the investigation of the nano-particles' stability, incorporation and interface with the steel matrix. The investigation was made using an electron accelerating voltage of 100-300 kV, with the incident electrons being elastically and inelastically scattered. There are different methods for capturing information from the investigated sample. In the BF-bright field imaging only primary beam is being used and the contrast on the image is a result of variations in area densities. The HAADF-high-angle annular dark-field aperture shadows the primary sample and captures only a specific diffracted beam (DF image gives us information's on orientations of the crystal grains, lattice irregularities etc.) [75].

A JEOL, ARM 200 CF, AR STEM – state-of-the-art atomic-resolution scanning-transmission electron microscope was used for nano-scale microstructure investigation and investigation of the inclusions. The analyses were carried out at the National Institute of Chemistry.

4.5.6 Alicona 3D-focus variation optical measurement microscopy

Wear of the tested samples was evaluated by wear volumes measured after the tests using a 3D measurement microscope Alicona Infinite Focus G4. It is a high-resolution 3D optical device based on a variation of the focus and operates on the principle of illumination of the selected slice of the sample, which provides a great contrast and 3D image. The device enables a quantitative surface topography analysis, measurement of the roughness and profile. Computer control of the optical system enables extremely fine potentiometric focus control and image digitalization.

In wear measurements we obtained a 3D surface profile images (Fig. 9b) of the wear tracks (Fig. 9a) and determined the volume of the removed material.

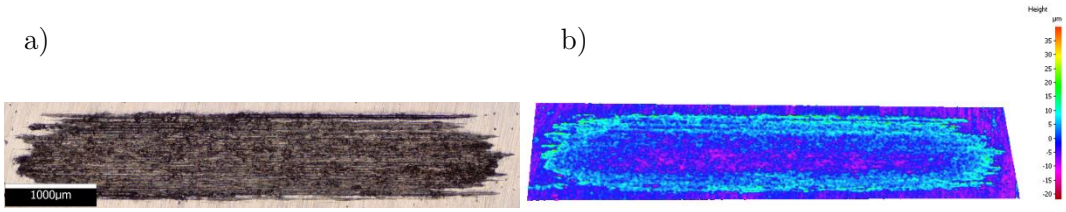

Figure 9: Identification of a) wear scar and b) 3D surface profile.

4.6 Mechanical Properties

4.6.1 Vickers hardness testing

The Vickers test is performed with different loads and in indenter, which is a square-based diamond pyramid with angles of 136 +/- 5° (Fig. 10). Indenter is forced into the material and remains applied for a specific time from 10 to 15 s and then removed. Macro-indentation (loads used are 5 to 120 kg) and micro-indentation (loads used are 1 to 1000 g) are two distinct types of Vickers testing. After the indentation the indentation diagonals are measured and averaged, and Vickers hardness number is calculated using the following equation:

$$HV = \frac{2Psin\left(\frac{136}{2}\right)}{d^2} = \frac{1.8544P}{d^2} \tag{14}$$

P…indentation load (kg), d…mean diagonal of indentation (mm).

Samples tested should be polished and flat. Each indent has to be at least 2.5 times the length of the diagonal apart from the neighboring indent as well the same distance from the edge of the sample [76].

Hardness testing of the investigated samples was carried out using standard SIST EN ISO 6507-1:2006 with an InstronTukon 2100B machine using a load of 9.807 N (HV1).

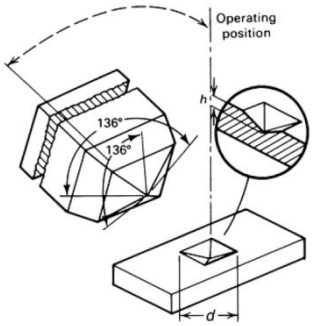

Figure 10: Diamond pyramid indenter used for the Vickers test and resulting indentation in the work piece; d, mean diagonal of the indentation in millimeters [76].

4.6.2 Impact-toughness testing

The impact toughness tests were performed using standard (SIST EN ISO 148-1:2010) Charpy V-notch test samples and the testing configuration shown in Fig. 11. The test sample in this testing procedure is supported on both ends and subjected to an impact by a single pendulum blow. Evaluation of absorbed impact energy to cause fracture is based on the potential energy of the impacting head that is transformed during the impact. The dimensions of the Charpy V-notch test sample and the whole testing setup are standardized [76].

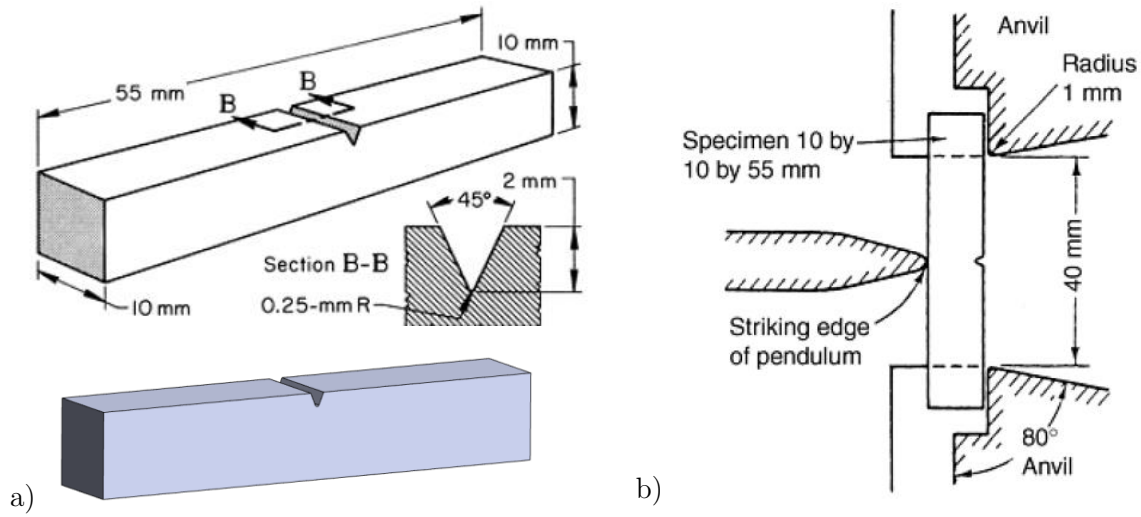

Figure 11: (a) Dimensional details of Charpy V-notch test sample and b) configuration for impact-toughness testing [76].

4.6.3 Tensile testing

Tensile tests were performed on the INSTRON 1255 test machine using the type-B standard tensile test samples (DIN 50125:2009-07). Tensile testing enables an evaluation of the ultimate tensile strength, the yield strength and the elastic and ductility properties (Young's modulus, elongation and reduction area).

During testing the force-deformation data, which is a quantitative measurement of how the test sample is deformed under applied tensile force, is being recorded and monitored. Once an external tensile loading is applied on a sample, elastic and plastic deformations will be anticipated. The applied load or force and the elongation relationship is liner in the initial portion of the test for most metallic materials. Calculation of the engineering stress and engineering strain is done using these two parameters for the purpose of yielding a relationship, as shown in Figure 12, incorporating equations 15 and 16 as follows:

$$\sigma_E = \frac{P}{A_0} \tag{15}$$

$$\varepsilon_E = \frac{L_f - L_0}{L_0} = \frac{\Delta L}{L_0} \tag{16}$$

Where:

σ_E…engineering stress, ε_E… engineering strain, P… external axial tensile load, A_0… original cross-section area of the sample, L_0… original length of the sample, L_f… final length of the sample.

Once the elastic deformation is in progress, the engineering stress-strain relationship follows Hooke's Law and slope of the curve demonstrates the Young's modulus (E):

$$E = \frac{\sigma}{\varepsilon} \tag{17}$$

Hooke's law is only valid within the elastic or proportional limit, where the relationship is linear. After that, the material behaves plastically. Yield strength is the value at which the plastic deformation of the material starts in the presence of an applied load [76]. It is also known as the proof stress and defined as the level of stress that produces a specific amount of permanent strain or deformation. In this respect, a 0.2% offset yield strength ($R_{p0.2}$) is defined as the amount of stress that will result in a plastic strain of 0.2%. Beyond yielding, an increase in the stress for permanent deformation of the sample occurs through continuous loading. At this time, the sample would be strain hardened or work hardened. Through the application of continuous loading, the maximum point will be reached for the stress-strain curve, which is the ultimate tensile strength (σ_{TS}) (equation 18). At this stage, the highest stress before necking could be borne by the sample. This is observed through a local reduction in the cross-sectional area of the sample commonly seen in the center of the gauge length.

$$\sigma_{TS} = \frac{P_{max}}{A_0} \tag{18}$$

where P_{max} is the maximum load and $A_0$is the original cross-section area of the sample.

The percentage of elongation or the percentage reduction in area represents the tensile ductility of the sample, as shown in the following equations:

$$\%\, Elongation = \frac{\Delta L}{L_0} x100 \tag{19}$$

$$\%RA = \frac{A_0 - A_f}{A_0}\, x100 = \frac{\Delta A}{A_0}\, x\, 100 \tag{20}$$

where, Af is the cross-sectional area of sample at fracture.

In Fig. 13 the tensile test sample used in the current investigation is shown.

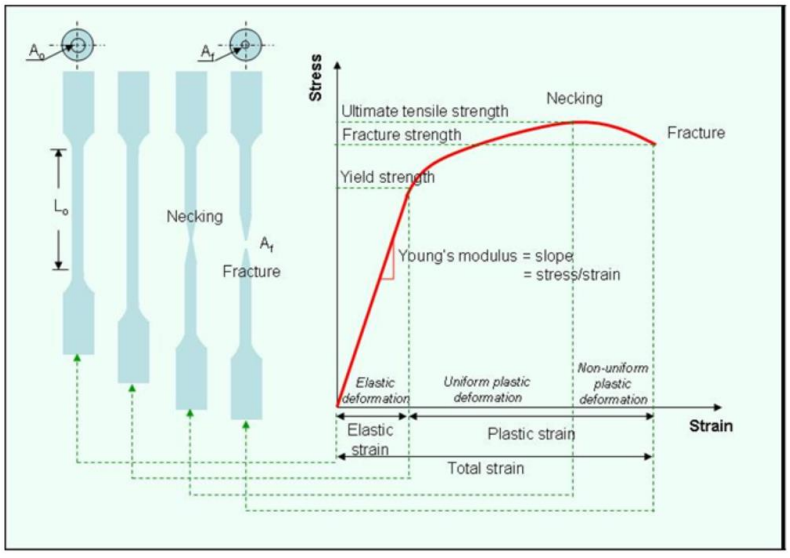

Figure 12: Stress-strain relationship under uniaxial tensile loading.

Figure 13: Tensile test sample used for mechanical properties evaluation.

4.7 Fatigue and Creep Testing

4.7.1 Fatigue testing

The fatigue tests were performed on a Rumul Cracktronic resonant test machine using standard Charpy V-notch test samples (Fig. 11) and bending loading. In the testing the stress ratio R (max. vs. min. stress) was set to 0.1 and the materials were tested at three maximum stress levels, 250, 300 and 350 MPa, until sample failure by cracking or fracture. Due to the low power consumption (approx. 5 W) and the high testing frequencies (~180 Hz) the Cracktronic is well suited for high-cycle fatigue testing. The total number of cycles a sample sustains before failure is called the "fatigue (cyclic) life", noted by N. The graph plotting values of stress level (S) and number of cycles until failure (N) is called the "S-N curve" or "Wöhler diagram" (Fig. 14). The S-N curve is obtained by conducting several fatigue tests. In each test, the sample is loaded to a certain level of stress (S) and loaded until it fractures. When the sample fractures, the level of stress applied (S) and the number of cycles (N) to fracture are noted. The results of tests are represented by a point on the curve. On the other hand, the stress level, where the samples do not fail, reaching a number of cycles above several millions of cycles is called the fatigue limit.

Fatigue is the progressive, localized, permanent structural change that occurs in materials subjected to alternating stresses and strains that may result in cracks or fractures after a sufficient number of loading and unloading cycles. The cyclic stresses are normally well below the Yield strength of the material [76].

A typical S-N curve [77] corresponding to this type of material is shown as Curve A in Figure 14. Many non-ferrous metals and alloys, such as aluminum, magnesium, and copper alloys, do not exhibit well-defined endurance limits. These materials instead display a continuously decreasing S-N response, similar to Curve B in Figure 14. In such cases, a *fatigue strength* $\mathbf{S_f}$ for a given number of cycles must be specified. An effective endurance limit for these materials is sometimes defined as the stress that causes failure at $1x10^8$ or $5x10^8$ loading cycles.

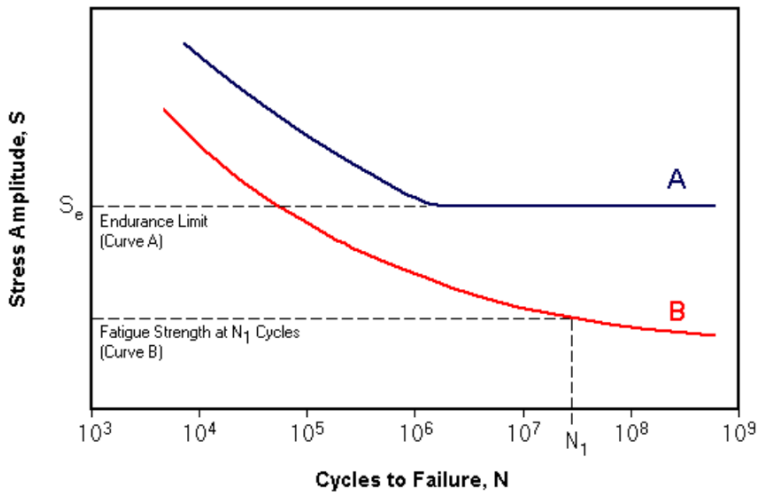

Figure 14: Typical S-N Curves [77].

4.7.2 Creep test

The design of components that are subjected to loads at increased temperatures for a long period of time must show appropriate creep properties or creep-resistance that affects

component behavior over time. Creep properties are obtained by conducting high-temperature creep tests. In such tests, there are two quantities of interest. First, is the measurement of the deformation of the material subjected to a constant load at a specified temperature in a given amount of time, called the creep rate. The second is a measurement of the life of a material at a specified temperature and specified loading, which we conduct until material failure, called the creep rapture time [76].

Creep tests were performed under a constant load corresponding to the stress level of 300 MPa, and an elevated temperature of 650°C. In order to ensure a firm sample to grip fixture, a preload of 26 kg was applied prior to elevating the temperature to 650°C. The time needed to reach the testing temperature (650°C) from room temperature was approximately 2:30 h. The temperature was measured at three points, i.e., in the middle part and both ends of the sample. The testing time was up to 300 hours, resulting in the rupture of the test sample. The creep sample used in the investigation is shown in Fig. 15.

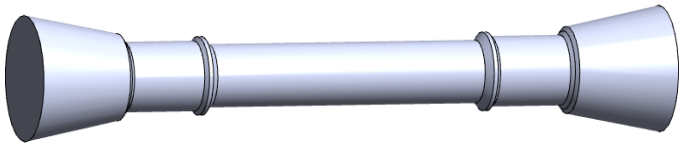

Figure 15: Schematic representation of creep-test sample.

4.8 Tribological Testing

Tribological testing was carried out in a dry reciprocating sliding contact in the normal room atmosphere (T = 20°C, RH = 45 %) using a TRIBOtechnic Pin-on-Disc TRIBOtester (Fig. 16a). Three sets of test conditions in terms of load and sliding speed were selected in order to determine how the material behaves under different contact conditions. A hardened stainless-steel ball (X47Cr14) with a diameter of 10 mm and hardness of 490 HV1 was used as a loading counter-body, loaded against the oscillating disc/plate sample. All the test parameters are presented in Table 3. In order to establish the test-to-test repeatability, each friction/wear test was repeated at least three times. The coefficient of friction was measured continuously during the test and the wear volume determined using the 3D optical profilometer (Alicona Infinite Focus G4) after the completion of the test. For each test a new ball was used and both samples (the disc representing tested MMnC material and the steel ball representing counter-body) were washed in high-purity acetone and dried in air prior to the testing.

The wear rate k, was calculated according to eqn. 21 for the investigated composite samples tested at two different loads (1 N, 3 N) and two sliding speeds (2 mm/s, 20 mm/s) for a total sliding distance of 6 m.

$$k = \frac{W}{F_N \cdot s} \left[{}^{mm^3}/_{Nm} \right] \tag{21}$$

where W is the wear volume, F_N is the normal load and s is the sliding distance.

Table 3: Wear-test parameters used.

Test number	**1**	**2**	**3**
Counter body	hardened stainless-steel ball (X47Cr14)		
Contact load F_N (N)	1	3	3
Hertz contact pressure [MPa]	470	675	675
Sliding speed [mm/s]	20	20	2
Amplitude [mm]	5		
Frequency [Hz]	2	2	0.2
Test time [s]	300	300	3000
Sliding distance [m]	6		

a)  b) 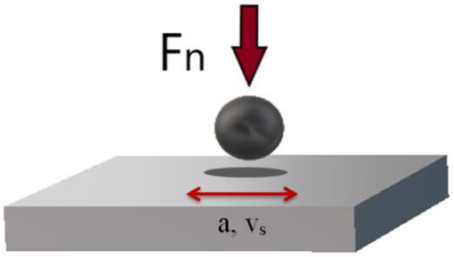

Figure 16: a) Tribotechnic unidirectional and oscillating Pin-on-Disc TRIBOtester and b) schematic illustration of the reciprocating contact between the ball and the investigated material.

Chapter 5

Thermodynamic Calculations

Before the casting of the nano-particles-reinforced 316L stainless steel the thermodynamic calculations of the phase stability with the amount (in mass fraction) of phases and amount of components in phases for AISI 316L steel and added nano-particles were simulated using the ThermoCalc software. The purpose was to get an insight into the casting process, mainly from the point of determining which phases are occurring during the solidification of the melt and the stability of the added nano-particles. The database used for the thermodynamic calculations was TCFE8-TCS Steels/Fe-Alloys.

A lot of phases have been identified in austenitic stainless steel in different studies during the years from various authors, some of them occurring during the solidification and some being secondary phases as a result of further treatment of the austenitic stainless steel (solution annealing). Among austenite and δ -ferrite, some of the secondary phases can be present in the microstructure of austenitic stainless steel. The most common secondary phases are: σ phase (tetrag.), Laves (hexag.), χ-phase (b.c.c.), M_6C (f.c.c.), $M_{23}C_6$ (f.c.c.), MX (f.c.c.), Cr_2N (hexag.), Z-phase (tetrag.), π-phase (cub. pr.), R-phase (hexag.) [78]. In addition to these phases, the orthorhombic M_7C_3 carbide can occur in austenitic stainless steel with a higher bulk carbon content mass fraction of 0.3-0.6 %. Most common phases occurring during the solidification are nicely presented in the work of J. Janovec et al [78], focused on the austenitic stainless-steel ASTM A351 in the as-cast condition. In general, stainless steels are solution treated. However, in some cases austenitic stainless steels are also used in the as-cast condition (elbows for pipe lines systems, centrifugally cast or sand-cast large tubes), with the following phases being present during the solidification:

- Basic (polymorphous) phases: liquid, FCC (austenite), BCC (α - and/or δ -ferrite)
- Carbides: M_3C, M_7C_3, $M_{23}C_6$, M_6C
- Intermetallic phases: laves phase, chi (χ), sigma (σ) [78].

In current thermodynamic calculations stable as well as unstable phases that are available in the used database were considered in the calculations, including some of the phases that can occur only in special austenitic stainless steels with higher amounts of silicon or phosphorous, like silicides (G-phase) and phosphides (M_3P). A list of all the phases present in the equilibrium calculations for the investigated AISI 316L austenitic stainless steel with the given composition (Table 1) and without added nano-particles is shown in the legend of the thermodynamic calculations of the phase-stability diagram of Fig. 17. From thermodynamic analysis, it can be concluded that in the AISI 316L steel many phases will be present in the equilibrium. However, most of them are present in very small quantities, since there are little impurities present, i.e., phosphorus and sulfur. The selected temperature area from 50 to 1500 °C covers the whole solidification and cooling region from the liquid phase of the AISI 316L steel. Although all the diagrams are presenting a very wide temperature range, in reality a lot of equilibrium phases will not be

present in the microstructure. The cooling rates to room temperature are too fast for the formation of all the equilibrium phases with which the diffusion and migration of the atoms is disabled. Therefore, the phases that are indicated to occur below 500 °C are unlikely to be present in reality in the experimentally produced material. The following graphs are therefore shown with phases that are important for the experimental work and the presence of which can actually be expected. These are for AISI 316L steel: FCC_A1 (austenite), BCC_A2 (ferrite), liquid phase and sigma phase. As we were focused on the thermodynamic behavior of the added nano-particles and the stability of the particular types of nano-particles used, property diagrams for the Fe –16.60Cr – 0.02C – 0.48Si – 1.88Mn – 10.70Ni – 2.01Mo system and added nano-particles were calculated in the temperature range from 50 to1500 °C, with the results being presented in Figures 17 to 32 and discussed in detail for each specific nano-particle type added.

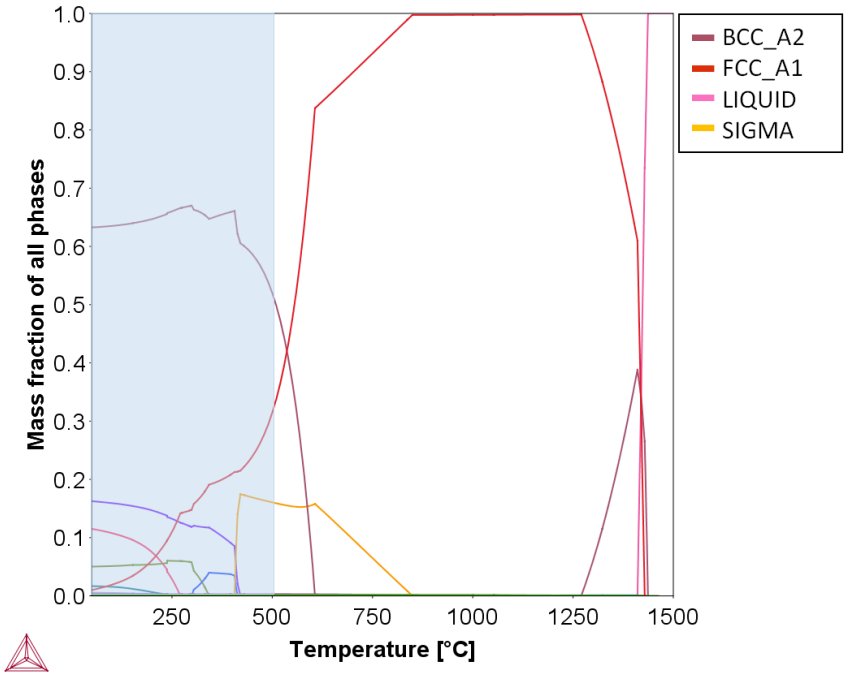

Figure 17: ThermoCalc calculations of phase stability: FCC_A1 (austenite), BCC_A2 (ferrite), liquid phase and sigma phase; mass fraction of all phases present from 0 to 1.0 for non-modified AISI 316L stainless steel.

The calculated thermodynamic calculations of phase stability with mass fraction of all phases for AISI 316L steel with the addition of 0.5 wt. % Al_2O_3 nano-particles is shown in Fig. 18 and Fig. 19. In the present thermodynamic calculations corundum represents the stable phase of Al_2O_3. The addition of nano-particles in the melt was simulated by the addition of aluminum and oxygen in the mass concentrations corresponding to the selected concentration of added nano-particles (i.e., 0.5 wt% of Al_2O_3 nano-particles corresponds to 0.265 wt% Al and 0.235 wt% O). This results in the formation of thermodynamically stable particles, i.e., Al_2O_3, which remains undissolved also in the liquid region of the AISI 316L austenitic stainless steel matrix, as the melting temperature of oxide particles is much higher (2072° C for Al_2O_3) compared to the steel matrix (1400°C) [18]. As the chosen nano-particles are already by their intrinsic properties very stable and inert the addition of the constituent elements in the thermodynamic calculations resulted in the formation of phases corresponding to the type of simulated nano-particles addition. However, in some cases thermodynamic calculations gave results that are not completely consistent with the

literature by means of the phase stability, which should stay unchanged above the melting point of the matrix. Partial dissolution of those phases at higher temperatures or their reaction with the other elements present in the melt was indicated by the calculations. Fig. 20 represents the phase stability diagram for the corundum phase when the addition of 0.5 wt. % of Al_2O_3 nano-particles into the AISI 316L steel was simulated. As can be seen, the oxygen content stays almost unchanged up to the matrix melting temperate of approximately 1400 °C. However, the aluminum content is constant up to a temperature of approx. 500 °C, followed by a slight drop, which coincides with the increase in titanium concentration in the corundum phase. This trend is present up to about 1400 °C, when the aluminum content again increases to the previous value and is balanced by the titanium concentration drop. As indicated by the thermodynamic calculations, the Al_2O_3 phase, although declared as a high-temperature stability phase, may start reacting with some of the other elements (in this case with titanium). However, this is not changing the phase itself significantly.

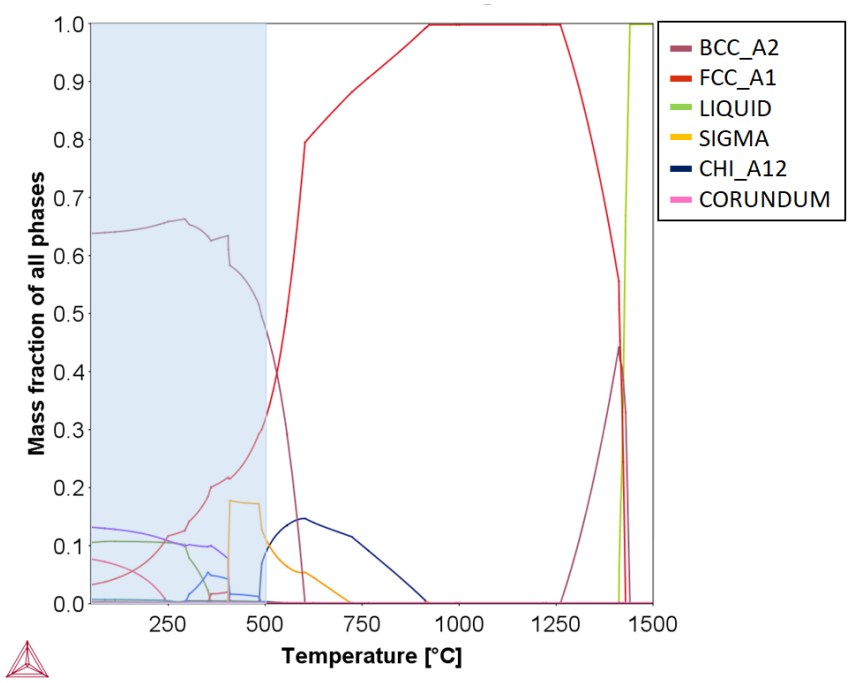

Figure 18: ThermoCalc calculations of phase stability: FCC_A1 (austenite), BCC_A2 (ferrite), liquid phase, sigma phase, chi phase and corundum (Al_2O_3) phase; mass fraction of all phases present from 0 to 1.0 for AISI 316L with the addition of 0.5 wt. % Al_2O_3 nano-particles.

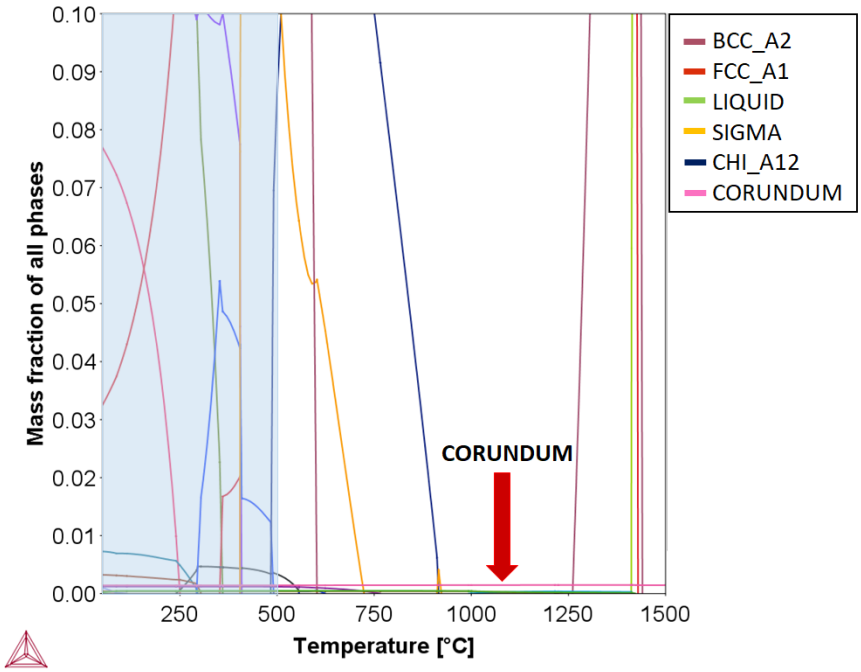

Figure 19: ThermoCalc calculations of phase stability: FCC_A1 (austenite), BCC_A2 (ferrite), liquid phase, sigma phase, chi phase and corundum (Al_2O_3) phase; enlarged area of the mass fraction of all phases present from 0 to 0.1 for AISI 316L with the addition of 0.5 wt. % Al_2O_3nano-particles.

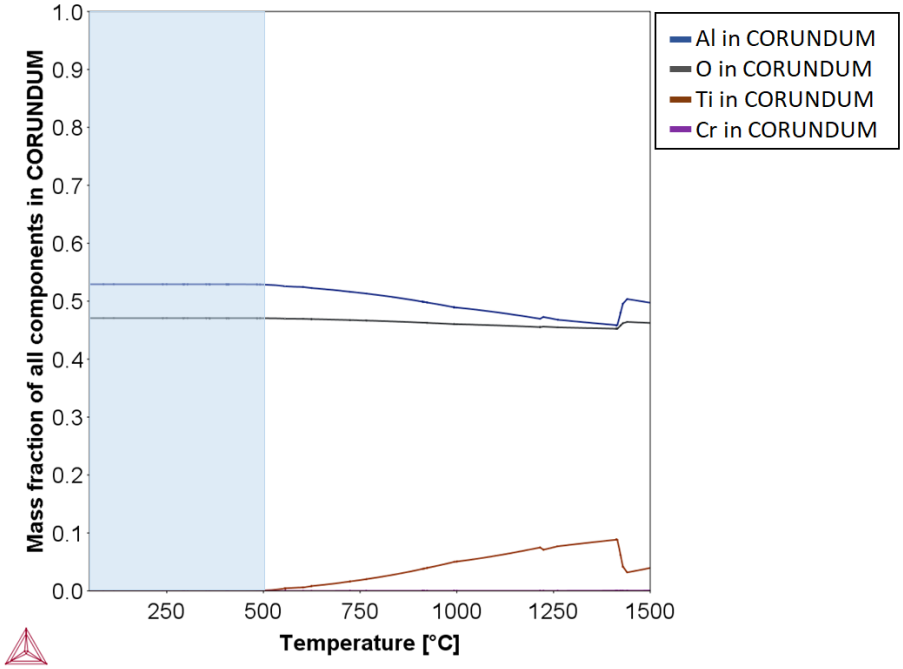

Figure 20: ThermoCalc calculations of elemental composition of CORUNDUM phase for the addition of 0.5 wt. % Al_2O_3 nano-particles into the AISI 316L stainless-steel matrix.

In the case of the addition of 0.5 wt. % TiO_2 nano-particles to the base composition (AISI 316L) the TiO_2 phase is again presented as the corundum phase type on the graphs of the thermodynamic calculations of phase stability (Fig. 21 and Fig. 22). Fig. 23

represents the phase-stability diagram upon the temperature range with a mass fraction of the components in the corundum phase when TiO_2 was added to the AISI 316L in 0.5 wt. %. It can be seen that this phase type is enriched in titanium throughout the whole calculated temperature range. It also indicates the presence of chromium in the mentioned phase. These two elements are showing a slight concentration fluctuation through the calculated temperature range in contrast to oxygen, which is being practically constant. Based on the thermodynamic calculations it can be concluded that in the case of the addition of TiO_2 particles ($\rho_{TiO_2} = 4.23\ g/cm^3$) more stable complex oxides of the M_2O_3 phase type can be formed with M taking into consideration both elements titanium and chromium. Because Cr_2O_3 has a lower Gibbs energy (at 1500°C is $\Delta G_f = -453\ kJ/mol$) than TiO_2 (at 1500°C is $\Delta G_f = -377.09\ kJ/mol$) and there is large activity of chromium due to its wt. % in the steel, the TiO_2 nano-particles could become the basis for the formation of the complex oxides $xTiO_2 \cdot yCr_2O_3$ or M_2O_3.

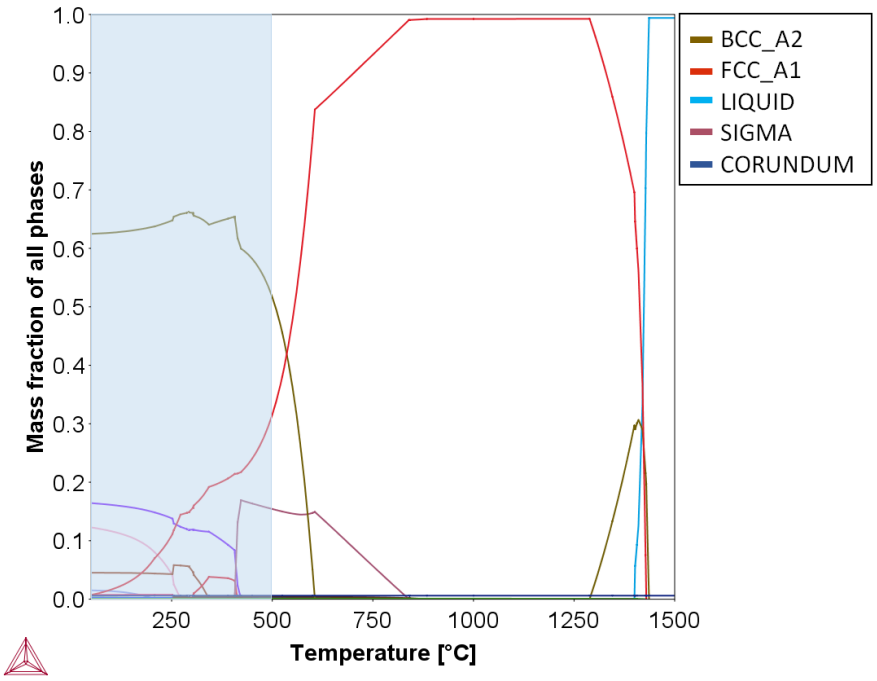

Figure 21: ThermoCalc calculations of phase stability: FCC_A1 (austenite), BCC_A2 (ferrite), liquid phase, sigma phase and corundum (TiO_2) phase; mass fraction of all phases present from 0 to 1.0 for AISI 316L with the addition of 0.5 wt. % TiO_2 nano-particles.

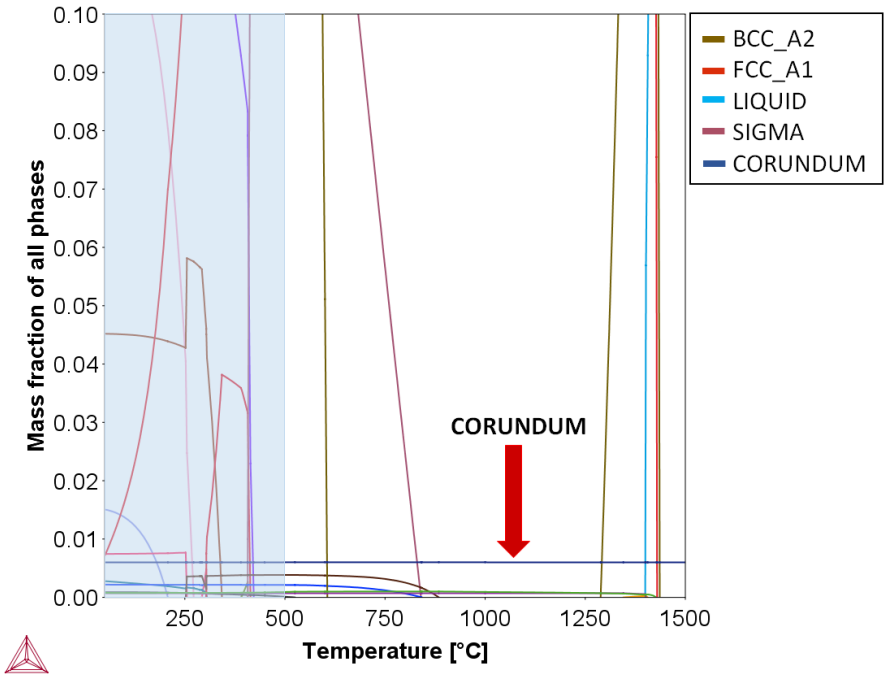

Figure 22: ThermoCalc calculations of phase stability: FCC_A1 (austenite), BCC_A2 (ferrite), liquid phase, sigma phase and corundum (TiO_2) phase; enlarged area of the mass fraction of all phases present from 0 to 0.1 for AISI 316L with the addition of 0.5 wt. % TiO_2nano-particles.

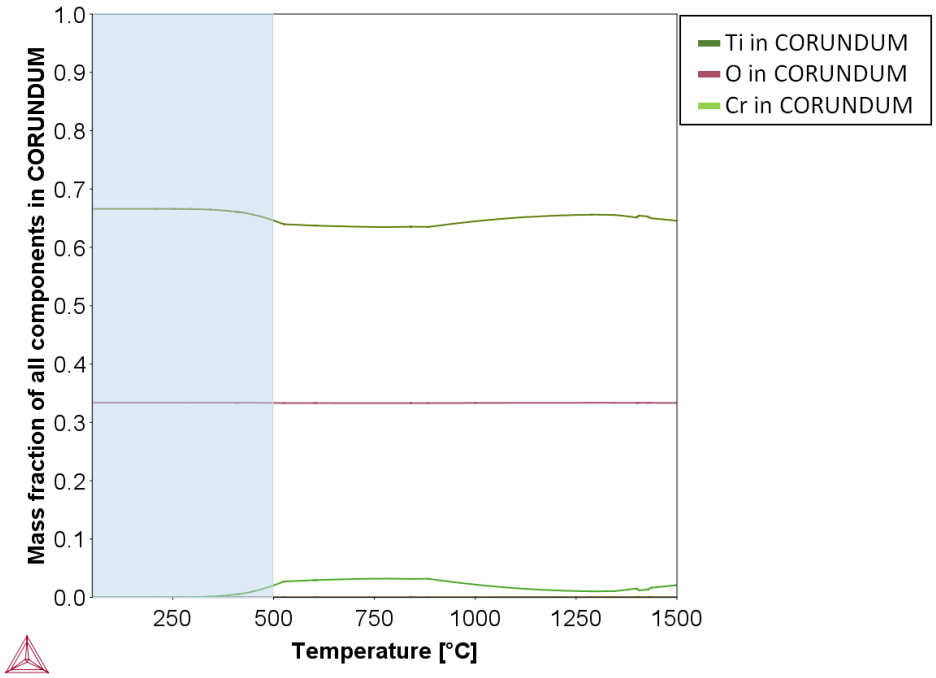

Figure 23: ThermoCalc calculations of elemental composition of CORUNDUM phase for the addition of 0.5 wt. % TiO_2 nano-particles into the AISI 316L stainless-steel matrix.

The Fig. 24 and Fig. 25 represent thermodynamic calculations of the phase stability for AISI 316L with the addition of 0.5 wt. % Y_2O_3 nano-particles, with Fig. 25 showing the enlarged area from 0 to 0.1 mass fraction of all the occurring phases. The Y_2O_3 is

represented with the M2O3C phase. Fig. 26 represents the phase-stability diagram in the temperature range with a mass fraction of the components in the M2O3C phase when Y_2O_3 was added to the AISI 316L in 0.5 wt. %. Calculations showing a stable concentration of yttrium and oxygen content in the M2O3C phase suggest that yttrium oxide particles are stable throughout the whole temperature range being calculated. However, this should be taken with a certain degree of caution since the database might be lacking some information about the thermodynamic descriptions of phases and elements (enthalpies of formation, enthalpies of mixing, Gibbs free energies, etc.). As can be seen from Fig. 26 the calculations of the elemental composition of the M2O3C phase are made to a temperature of 1500 °C even though this phase is shown to be stable only to 1150 °C (Fig. 25). This suggests that in this case the calculations are not so accurate. The equilibrium condition at 1400 °C shows that at this point only 4 phases are stable: liquid phase (L), which practically contains all the Y, austenite FCC_A1, ferrite BCC_A2 and corundum. Above approximately 1450 °C it is only liquid phase left, with the thermodynamic calculations indicating that Y_2O_3 is already dissolved above that temperature.

Yttrium forms a very stable oxide Y_2O_3 [67], which has a very high negative Gibbs energy ($\Delta G_f \approx -1400\ kJ/mol$ at 1500 ° C), a high melting point (T_m=2425 ° C) and a high density ($\rho_{Y_2O_3} = 5.01\ g/cm^3$). Because of yttrium's high affinity for the oxygen it takes most of the oxygen present from the melt and during the cooling forms a fine dispersion of Y_2O_3 particles, which are presenting heterogeneous nucleation sites for the grains' growth. However, the performed thermodynamic calculations and phase diagrams shown in Figs. 24 and 25 indicate that the phase M2O3C, representing Y_2O_3, dissolves already at a temperature of about 1150 °C.

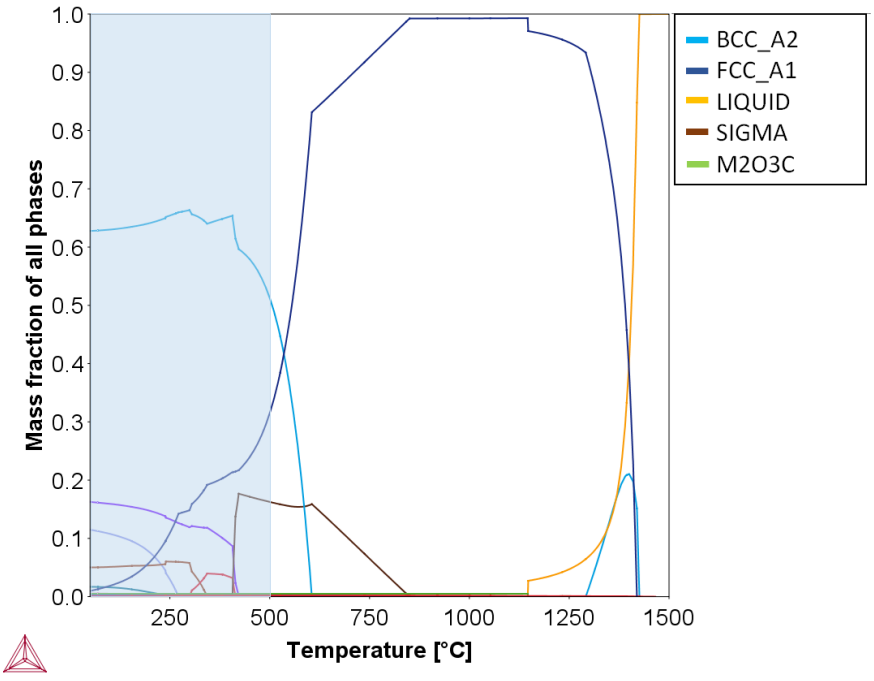

Figure 24: ThermoCalc calculations of phase stability: FCC_A1 (austenite), BCC_A2 (ferrite), liquid phase, sigma phase and M2O3C (Y_2O_3) phase; mass fraction of all phases present from 0 to 1.0 for AISI 316L with the addition of 0.5 wt. % Y_2O_3 nano-particles.

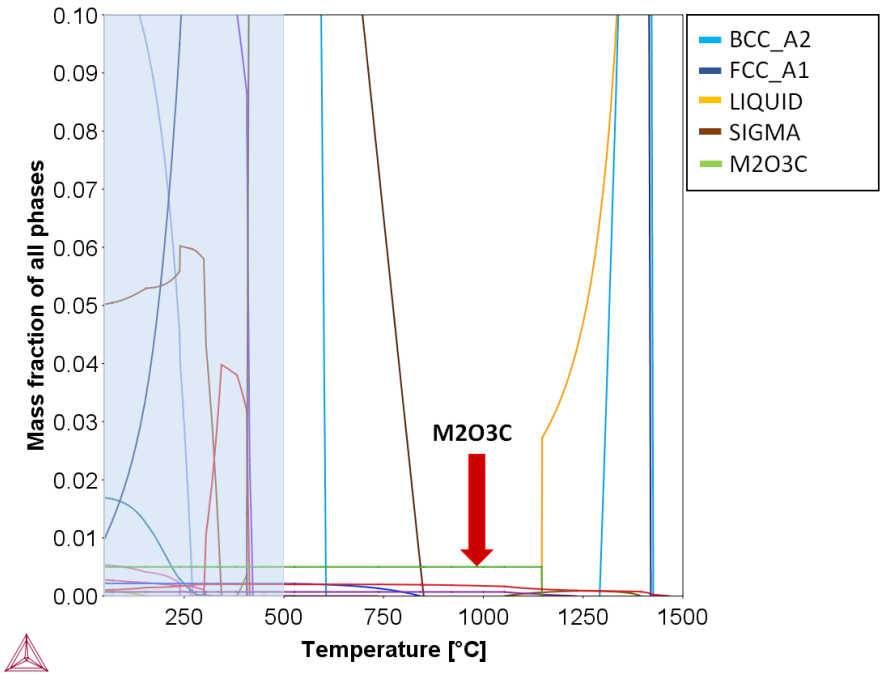

Figure 25: ThermoCalc calculations of phase stability: FCC_A1 (austenite), BCC_A2 (ferrite), liquid phase, sigma phase and M2O3C (Y_2O_2) phase; enlarged area of the mass fraction of all phases present from 0 to 0.1 for AISI 316L with the addition of 0.5 wt. % Y_2O_3 nano-particles.

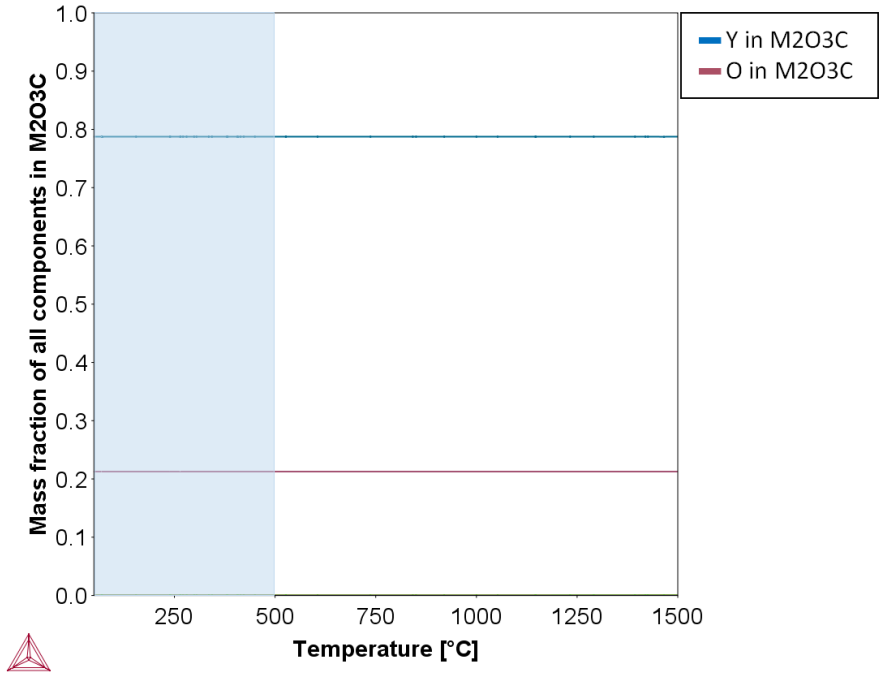

Figure 26: ThermoCalc calculations of elemental composition of M2O3C phase for the addition of 0.5 wt. % Y_2O_3nano-particles into the AISI 316L stainless-steel matrix.

Thermodynamic calculations of the phase stability with the mass fraction of all the phases for AISI 316L steel with the addition of 0.5 wt. % TiC nano-particles is shown in Fig. 27 and an enlarged part in Fig. 28. Fig. 29 represents the phase-stability diagram for

the temperature range with the mass fraction of the components in the FCC A1#2 phase when TiC was added to the AISI 316L in 0.5 wt. %. The performed thermodynamic calculations show that in the case of the addition of TiC nano-particles in the melt of austenitic stainless steel the titanium-rich particles containing carbon and nitrogen, thus forming M(C,N) type phase, i.e., titanium carbo-nitride, are present. When temperature is reaching the melting point of the steel fraction of the FCC A1#2 phase, representing the Ti-rich particles slightly decreases, meaning that some of them are being slowly dissolved into the melt. Also, the concentration of nitrogen in the FCC A1#2 phase increases with respect to the drop of the carbon concentration when the liquid region of the steel is achieved. This suggests that above the melting point only nitrogen-containing particles (TiN) co-exist with the liquid phase. From the analysis, it can be concluded that the added TiC nano-particles will dissolve in the steel melt, with the titanium being used for the formation of more stable TiN particles, if there is enough nitrogen available. During cooling the presence of carbon will lead to the formation of Ti(C,N).

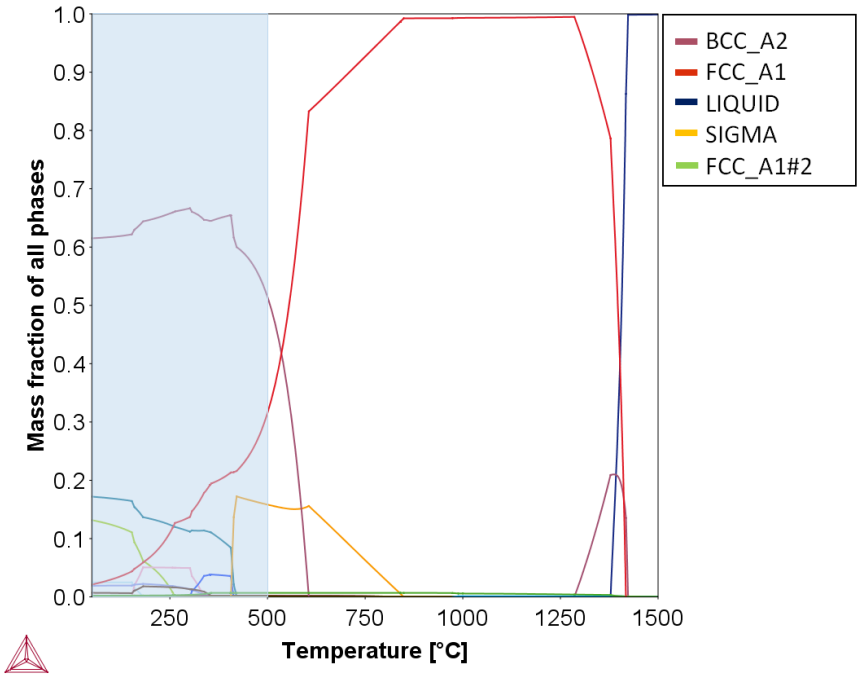

Figure 27: ThermoCalc calculations of the phase stability: FCC_A1 (austenite), BCC_A2 (ferrite), liquid phase, sigma phase and FCC_A1#2 (TiC) phase; mass fraction of all phases present from 0 to 1.0 for AISI 316L with the addition of 0.5 wt. % TiC nano-particles.

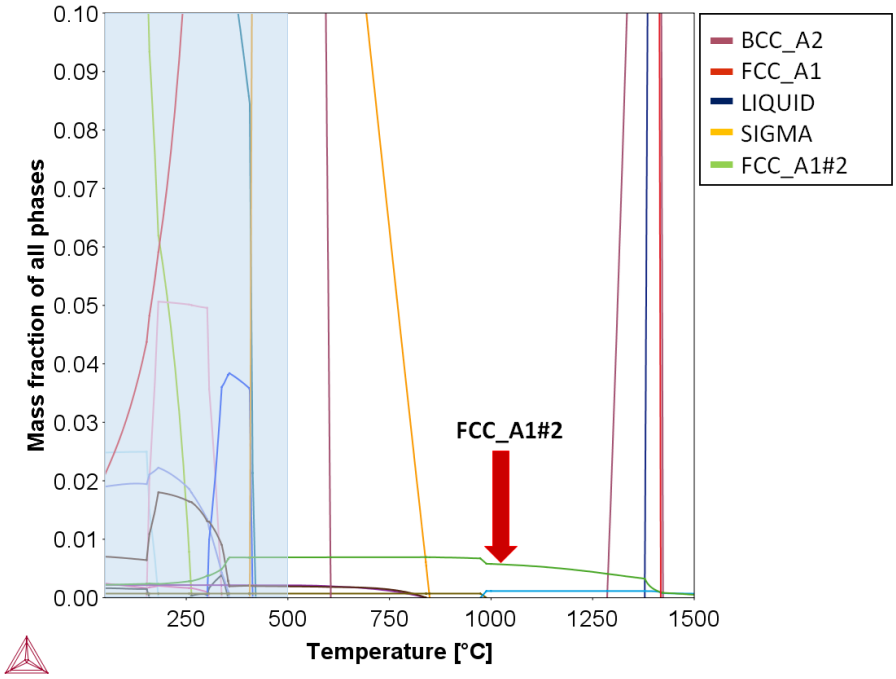

Figure 28: ThermoCalc calculations of phase stability: FCC_A1 (austenite), BCC_A2 (ferrite), liquid phase, sigma phase and FCC_A1#2 (TiC) phase; enlarged area of the mass fraction of all phases present from 0 to 0.1 for AISI 316L with the addition of 0.5 wt. % TiC nano-particles.

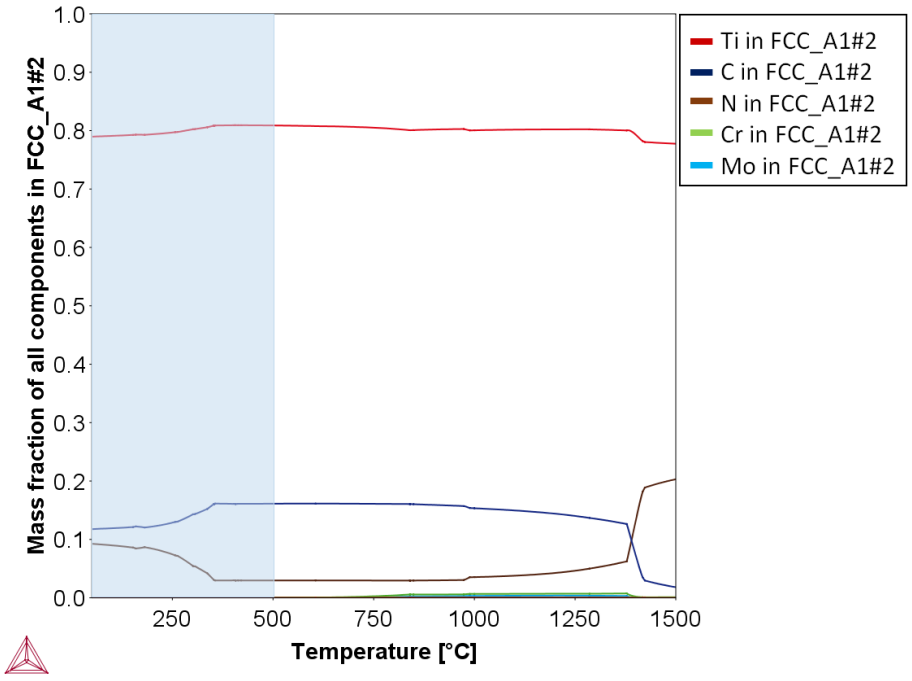

Figure 29: ThermoCalc calculations of elemental composition of FCC_A1#2 phase for the addition of 0.5 wt. % TiC nano-particles into the AISI 316L stainless-steel matrix.

The Fig. 30 and Fig. 31 represent thermodynamic calculations of the phase stability with the mass fraction of all the phases for AISI 316L with the addition of 0.5 wt. % TiB_2 nano-particles. It can be seen that TiB_2 is present in the form of the B2M phase. Fig. 32

represents the phase-stability diagram in the temperature range with a mass fraction of the components in the B2M phase when TiB_2 was added to the AISI 316L in 0.5 wt. %. In this case, the fraction of boron and titanium is not changed throughout the whole calculated temperature range. It should be pointed out that Ti forms a stable boride (TiB_2), which has a high melting point of T_m=2980 ° C and a density of $\rho_{TiB_2} = 4.52\ g/cm^3$[69]. However, in the present calculations the TiB_2 phase was found to be stable only up to a temperature of approximately 1350 °C, as indicated by the stability of the B2M phase in the thermodynamic calculations of phase stability (Fig. 30). Thermodynamic calculations thus suggest that above 1350 °C the TiB_2 nano-particles are being dissolved in the melt. Again, the thermodynamic calculations might be limited by the data that are available in the ThermoCalc database used.

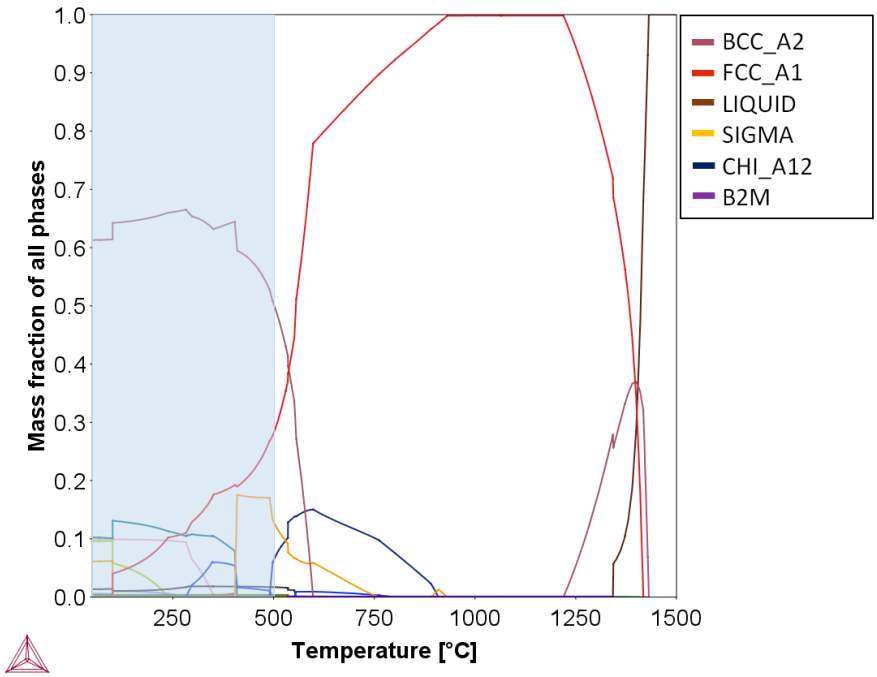

Figure 30: ThermoCalc calculations of the phase stability: FCC_A1 (austenite), BCC_A2 (ferrite), liquid phase, sigma phase, chi phase and B2M (TiB_2) phase; mass fraction of all phases present from 0 to 1.0 for AISI 316L with the addition of 0.5 wt. % TiB_2 nano-particles.

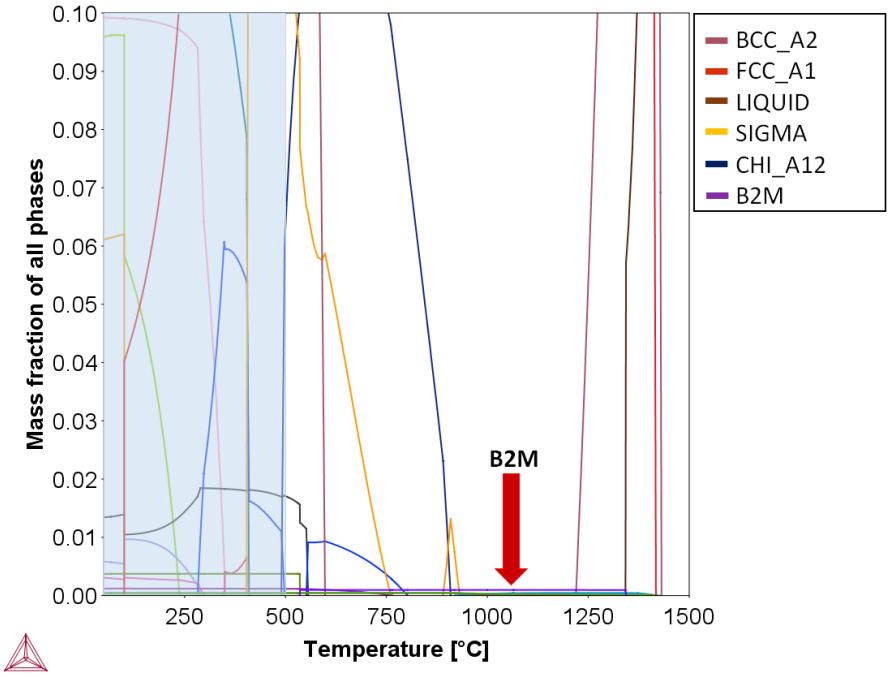

Figure 31: ThermoCalc calculations of the phase stability: FCC_A1 (austenite), BCC_A2 (ferrite), liquid phase, sigma phase, chi phase and B2M (TiB_2) phase; enlarged area of the mass fraction of all phases present from 0 to 0.1 for AISI 316L with the addition of 0.5 wt. % TiB_2 nano-particles.

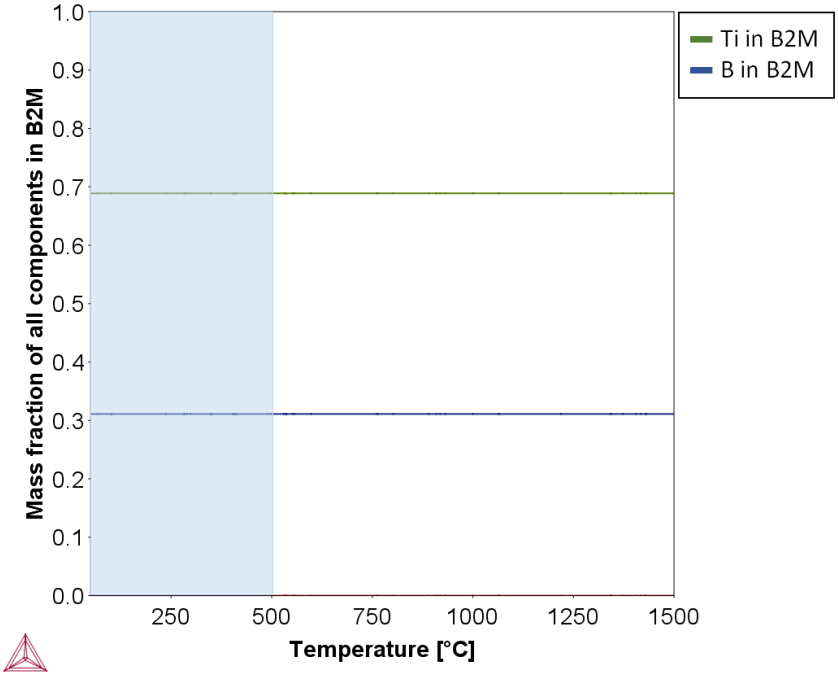

Figure 32: ThermoCalc calculations of elemental composition of B2M phase for the addition of 0.5 wt. % TiB_2 nano-particles into the AISI 316L stainless-steel matrix.

Chapter 6

Experimental Results

6.1 Preliminary Experiments

Preliminary experiments were focused on different approaches in terms of casting methods and the effect of concentration (0.5, 1.0 and 2.5 wt.%) and size (50 and 500 nm) of the added Al_2O_3 particles on their distribution in the as-cast austenitic stainless steel AISI 316L matrix. The goal was to find the best incorporation method, concentration and size of nano-particles to achieve a uniform distribution of the particles throughout the whole volume of the cast ingot. During preliminary tests, the nano-particles-reinforced steel samples were characterized in terms of microstructural analysis, including identification of the nano-particles, their distribution and volume fraction. The methods of production were submerging, pouring over method and introduction into the melt flow during casting. All the LM and SEM micrographs were made by analyzing samples taken from the top (T), middle (M) and bottom (B) portions of the as-cast ingot (Fig. 33). For a representative analysis all the micrographs of the microstructure shown are from the middle portion of the as-cast ingot. This is true for all the samples investigated.

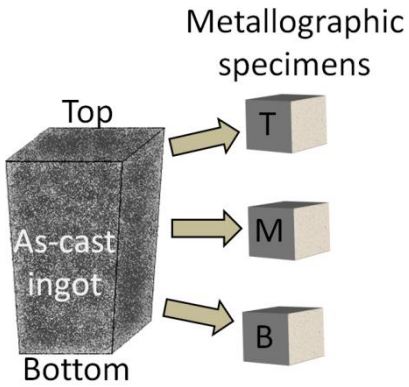

Figure 33: Schematic diagram of the subtraction of the metallographic as-cast samples.

6.1.1 Submerging

In the case of submerging the steel tube with encapsulated Al_2O_3 particles with a size of 500 nm directly into the steel melt prior to casting, no particles were found in the as-cast ingot microstructure. One of the problems of adding Al_2O_3 nano-particles (and also other types of nano-particles) in the melt during the process of steel casting is the density ($\rho_{Al_2O_3} = 3.95\ g/cm^3$) of the nano-particles added in comparison to the density of iron ($\rho_{Fe} = 7.85\ g/cm^3$). Due to the big difference in the density, they can be easily agglomerated and transformed into the slag on the surface of the melt.

6.1.2 Pouring over method

In the preliminary experiments six different batches (P1-P6) where molten metal was poured over the nano-particles (Fig. 13b) were prepared using two different particle sizes (500 nm and 50 nm) and three different concentrations (0.5 wt%, 1.0 wt% and 2.5 wt%) of Al_2O_3, as shown in Table 1. The Al_2O_3 particles powder was wrapped in an aluminum foil, placed on the bottom of the cuboid-shaped steel mold and poured over with the molten steel matrix. During casting the aluminum foil melts and dissolves in the metal.

Figure 34 shows a LM and SEM micrograph of the as-cast microstructure of pure 316L austenitic stainless steel with a distinctive two-phase microstructure of austenite and ferrite, with about 6% of delta ferrite (δ-ferrite) phase. Depending on the chemical composition of the melt, more precisely depending on the relationship between the alpha-gens (Cr, Al, V, Mo, Si, W) and gamma-gens (Ni, Cu, Mn, Co, C, N) elements in the steel, solidification can start with the crystallization of δ-ferrite or austenite. For a chromium content above 13% a two-phase microstructure consisting of austenite and δ-ferrite is formed at a temperature of 1050 °C. The fraction of delta ferrite is higher when increasing the chromium content in the steel. In Fig. 33 the micrograph shows the arrangement of the two microstructure constituents (δ-ferrite and austenite). It shows that δ-ferrite has solidified from the interdendritic melt.

a) 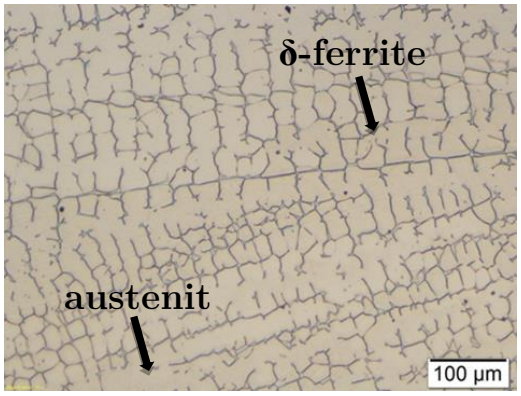

b) 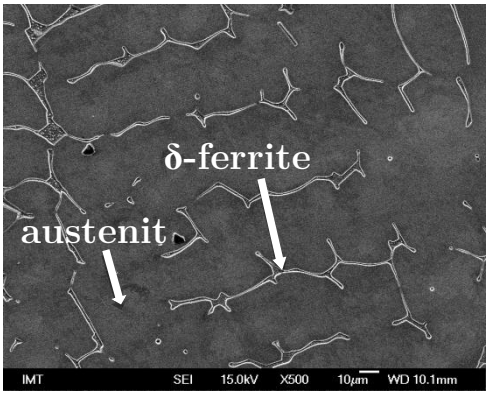

Figure 34: As-cast microstructure of AISI 316L austenitic stainless steel at a a) 50x magnification and b) 500x magnification for sample R (reference material) without the addition of nano-particles.

In order to confirm the incorporation/presence of Al_2O_3 of particles in the microstructure and to analyze the particle distribution the samples were subjected to SEM analysis. For a representative analysis of the particles distribution ten random micrographs were taken and analyzed for each sample taken from the bottom, middle and top portion of the as-cast piece. In order to do the particle analysis efficiently, all the images were taken at the same magnification of 1000x with similar contrast.

As shown in Figs. 35-38 the microstructure of the austenitic stainless steel is modified after the addition of Al_2O_3 particles, being incorporated into the metal matrix with the pouring over method. However, the distribution of Al_2O_3 particles is non-homogeneous and concentrated in certain areas, with an increased particles concentration and size leading to more pronounced agglomeration. From the SEM/EDS elemental mapping analysis, shown in Figure 35 b) it was confirmed that the bright, small spot-like features represent the Al_2O_3 particles, which are incorporated, but non-uniformly distributed, in the steel matrix.

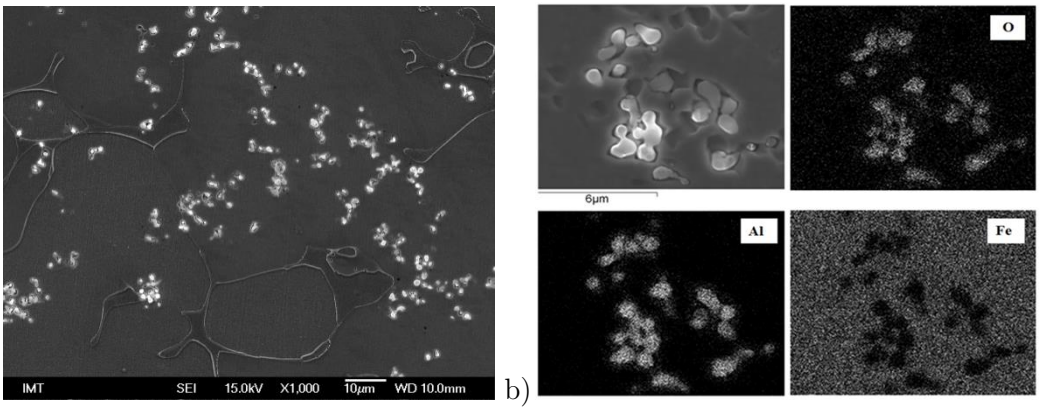

Figure 35: As-cast microstructure of AISI 316L austenitic stainless steel with the addition of a) 0.5 wt. % Al_2O_3 nano-particles (sample P1) for a particle size of 500 nm and (b) SEM/EDS elemental mapping; sample taken from the middle part of the as-cast ingot.

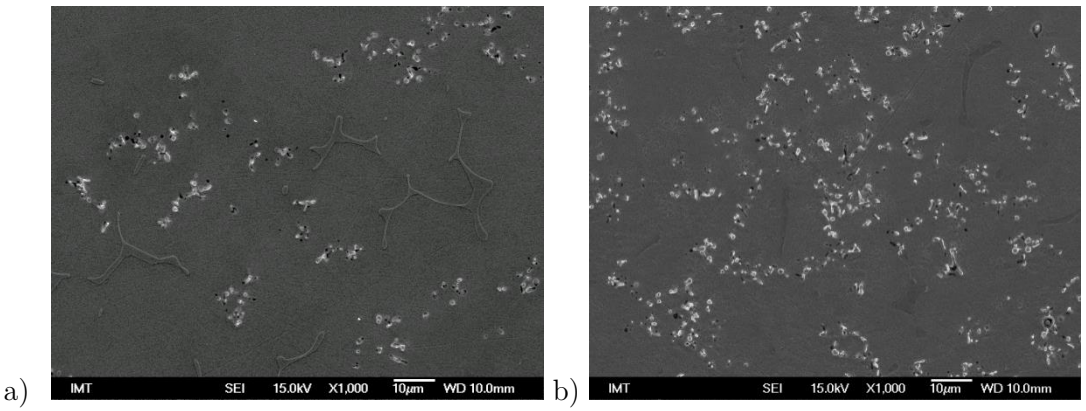

Figure 36: As-cast microstructure of AISI 316L austenitic stainless steel with the addition of a) 0.1 wt. % Al_2O_3 nano-particles (sample P2) and b) 2.5 wt.% Al_2O_3 nano-particles (sample P3) for a particle size of 500nm at a 1000x magnification; sample taken from the middle part of the as-cast ingot.

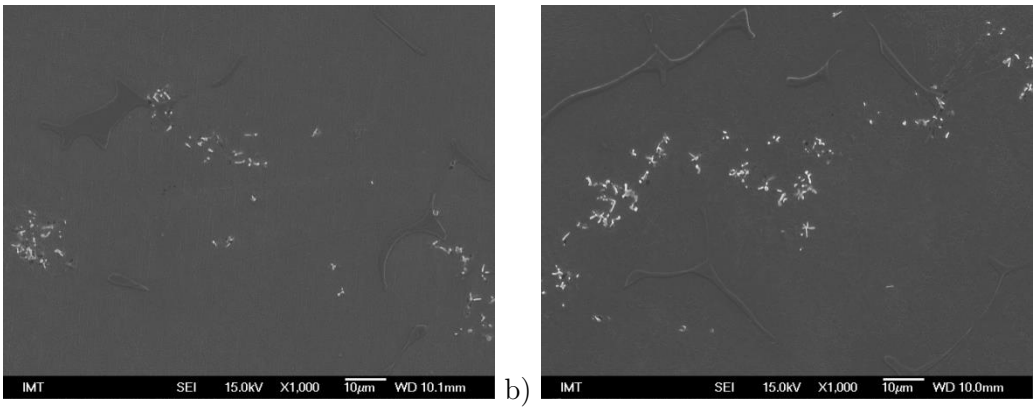

Figure 37: As-cast microstructure of AISI 316L austenitic stainless steel with the addition of a) 0.5 wt. % Al_2O_3 nano-particles (sample P4) and b) 1.0 wt.% Al_2O_3 nano-particles (sample P5) for a particle size of 50 nm at a 1000x magnification; sample taken from the middle part of the as-cast ingot.

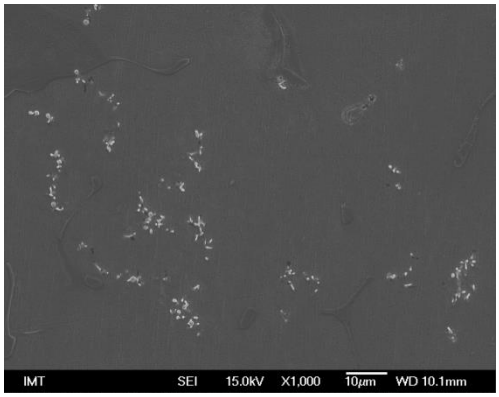

Figure 38: As-cast microstructure of AISI 316L austenitic stainless steel with the addition of 2.5 wt. % Al_2O_3 nano-particles (sample P6) for a particle size of 50 nm at a 1000x magnification; sample taken from the middle part of the as-cast ingot.

A concentration-dependent analysis (Fig. 39) shows that at 0.5 to 1.0 wt% the distribution of particles is more homogeneous throughout the cast ingot than in the case of 2.5 wt%, which is true for the 2D-area (Fig. 36) as well as the 3D-volume analysis. The particles-distribution analysis performed on the samples from the first set of experiments revealed that the addition of Al_2O_3 particles in 0.5 to 1.0 wt%, regardless of the mean particle size (50 or 500 nm), results in a relatively similar number of Al_2O_3 particles per unit area [μm^2] throughout the whole volume of the as-cast ingot with very small deviations. Nevertheless, metallographic observations show the agglomeration of nano-particles. For a low particles weight percent between 0.5 and 1.0 % the distribution of Al_2O_3 particles in the cast ingot was found to be more or less independent of the position, concentration and size of particles, resulting in about 0.01 particles/μm^2. However, as the weight percent increased to 2.5 % the particles concentration ratio starts to decrease towards the bottom of the cast ingot (Fig. 39). Furthermore, with the increased particle mass fraction, also their concentration in the cast ingot increased by up to 3 times, with the size of particles starting to play a role. The larger the particles, the larger is the volume fraction of the incorporated particles. A size-dependent analysis showed that Al_2O_3 powder with a mean particle size of 50 nm is more homogeneously distributed than the 500 nm one.

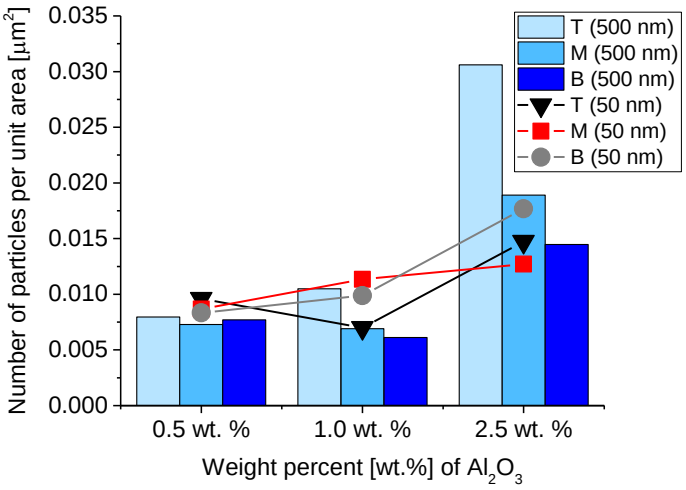

Figure 39: Influence of different concentrations and sizes of Al_2O_3 particles on their distribution in the cast ingots.

In the context of the microstructural changes characterization and the analysis of the ceramic particles incorporation into the steel matrix, transmission electron microscopy (TEM) was also employed. With STEM/EDS elemental mapping shown in Fig. 40 and the STEM line-profile analysis shown in Fig. 41 the successful incorporation and coherent bonding of the Al_2O_3 nano-particles in the steel matrix was confirmed. No discontinues at the particle/matrix interface, modification of the metal matrix or the formation of intermetallic phases could be observed.

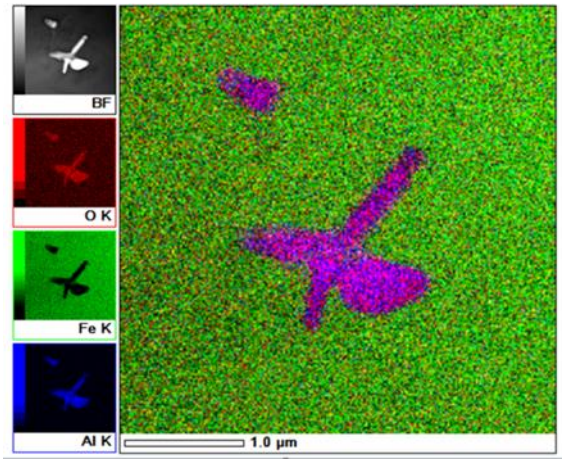

Figure 40: STEM/EDS elemental mapping of Al_2O_3 ultrafine particles (500 nm, 0.5 wt. %) in the as-cast microstructure of 316L austenitic stainless steel, without using the CaSi.

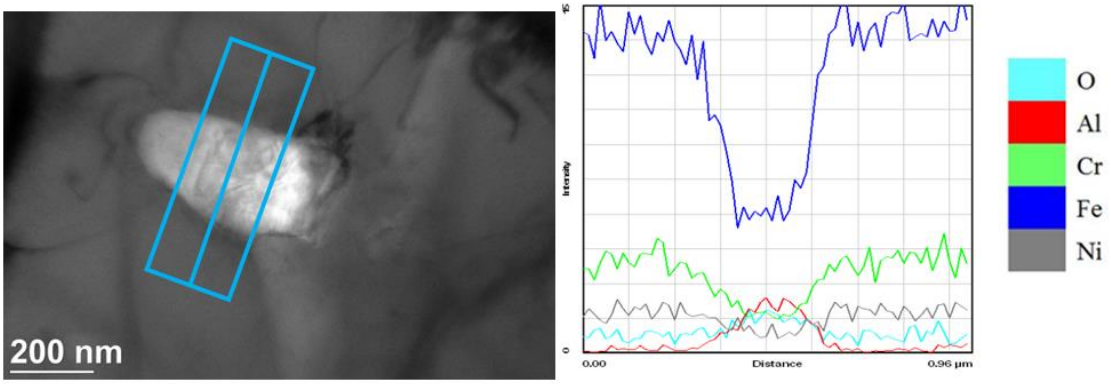

Figure 41: STEM - line profile of Al_2O_3 ultrafine particles (500 nm, 0.5 wt%) in the as-cast microstructure of 316L austenitic stainless steel, without using the CaSi.

6.1.3 Insertion into the melt flow during casting

The third set of experiments comprised four batches (F1-F4) shown in Figs. 42-43 where two different Al_2O_3 particle sizes (500 nm and 50 nm) in 0.5 wt. % were used. In two cases the Al_2O_3 particles powder was mixed with the same amount of dispersion medium, i.e., CaSi, in a 1:1 mass ratio and encapsulated into an aluminum foil tube and inserted/held in the path of the melt flow when the casting into the mold started. For the comparison, two additional batches were prepared where only Al_2O_3 powder was encapsulated into the aluminum foil tube, Table 1. The aluminum foil tube had a length of 400 mm, outer diameter of 12 mm and wall thickness of 0.4 mm. The ends of the tube were sealed with pliers and the aluminum foil tube was held in the path of the melt flow when casting into the mold started. The aluminum tube melts and dissolves in the melt.

By using CaSi as a dispersion medium and introducing an Al_2O_3/CaSi mixture through a sealed aluminum foil tube a reduced particles clustering and a more homogeneous distribution of reinforcement nano-particles in the steel matrix was obtained, as shown in Figs. 42 and 43. CaSi was used because it is highly reactive and most commonly used as a de-oxidant element in steelmaking, thus not causing contamination of the steel melt. During calcium treatment, the Al_2O_3 inclusions are converted to molten calcium aluminates, which are globular in shape because of the surface tension effect. The change in the inclusion composition and shape is known as inclusion morphology control. With the addition of CaSi to liquid steel we could control the distribution of the oxide particles added in the steel melt and potentially also their shape and size.

a) 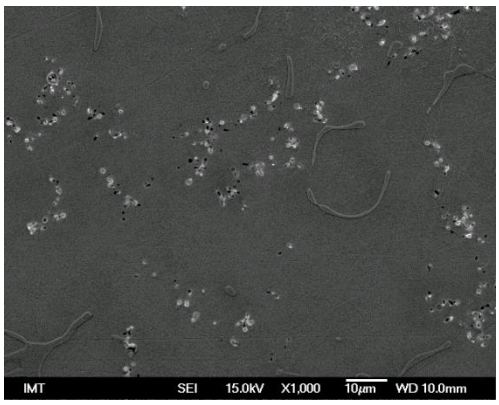

b) 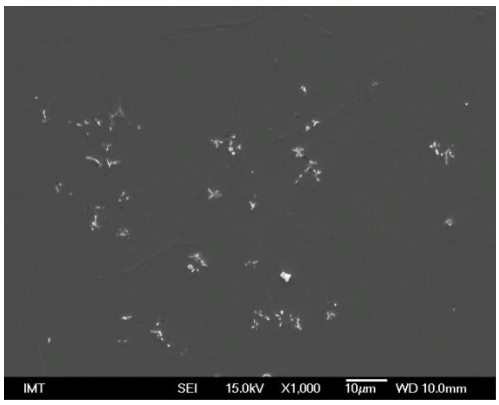

Figure 42: As-cast microstructure of AISI 316L austenitic stainless steel with a) the addition of 0.5 wt. % Al_2O_3 nano-particles (sample F1) and b) 0.5 wt. % Al_2O_3 nano-particles mixed with the dispersion medium CaSi in a 1:1 mass ratio(sample F2) for a particle size of 500nm at a 1000x magnification; sample taken from the middle part of the as-cast ingot.

a) 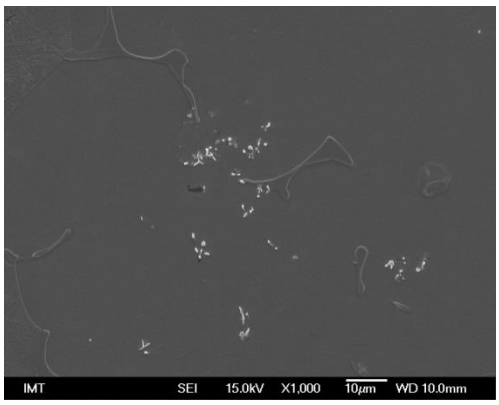

b) 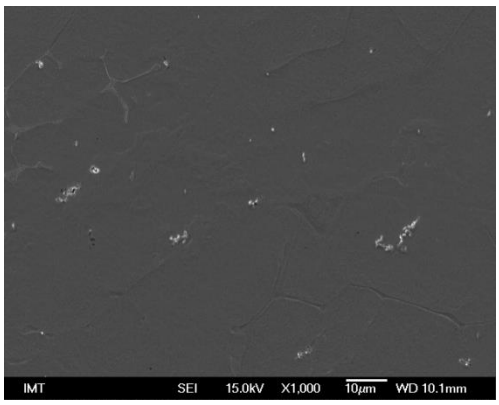

Figure 43: As-cast microstructure of AISI 316L austenitic stainless steel with a) the addition of 0.5 wt. % Al_2O_3 nano-particles (sample F3) and b) 0.5 wt. % Al_2O_3 nano-particles mixed with the dispersion medium CaSi in a 1:1 mass ratio (sample F4) for a particle size of 50nm at a 1000x magnification; sample taken from the middle part of the as-cast ingot.

The particles-distribution analysis (Fig. 44) shows that the use of a dispersion agent reduces the influence of particles size (500 nm or 50 nm) on the particles distribution homogeneity in the steel matrix. It results in a difference in the particles concentration throughout the ingot being reduced from more than 0.01 particles/μm^2 to less than 0.002 particles/μm^2.

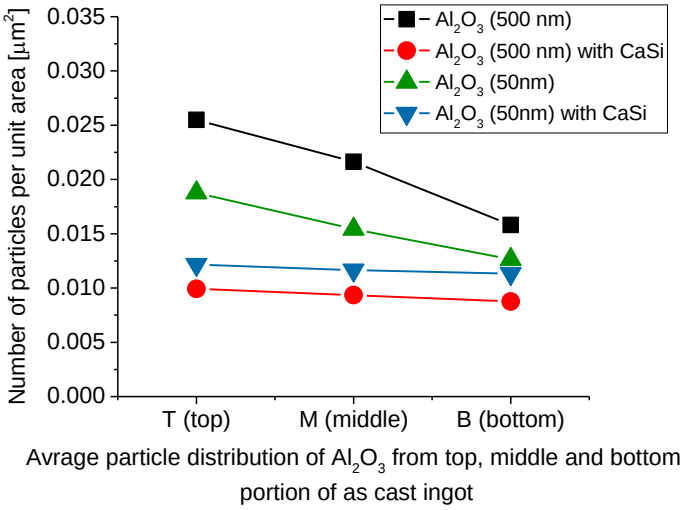

Figure 44: Influence of different sizes (500 and 50 nm) of Al_2O_3 particles and the addition of CaSi on the distribution of Al_2O_3 particles (0.5 wt. %).

In the fourth set of experiments two batches were prepared by the method of adding Al_2O_3 nano-particles to the melt flow during casting using a particle size of 50 nm and two different concentrations (0.5 wt. % and 1.0 wt. %). The nano-particles were encapsulated into the steel tube and held in the path of the melt flow when casting into the mold started. The aluminum foil tube was replaced by a steel one in order to eliminate any potential influence of melted aluminum foil on the formation of non-metallic inclusions, i.e., aluminates.

Using CaSi as a dispersion medium and introducing the Al_2O_3/CaSi mixture through a sealed steel tube reduced the particle clustering and gave a more homogeneous distribution of the reinforcement nano-particles in the steel matrix, as shown in Fig. 45. A concentration-dependent analysis presented in Fig. 46 shows that at the nano-particle mass fraction of 0.5 wt.% the number of Al_2O_3 nano-particles per unit area (μm^2) is between 0.011 and 0.012 and for 1.0 wt% between 0.014 and 0.016. The analysis shows that Al_2O_3 nano-particles are more homogeneously distributed through the whole ingot in the case of the 0.5 wt. % concentration.

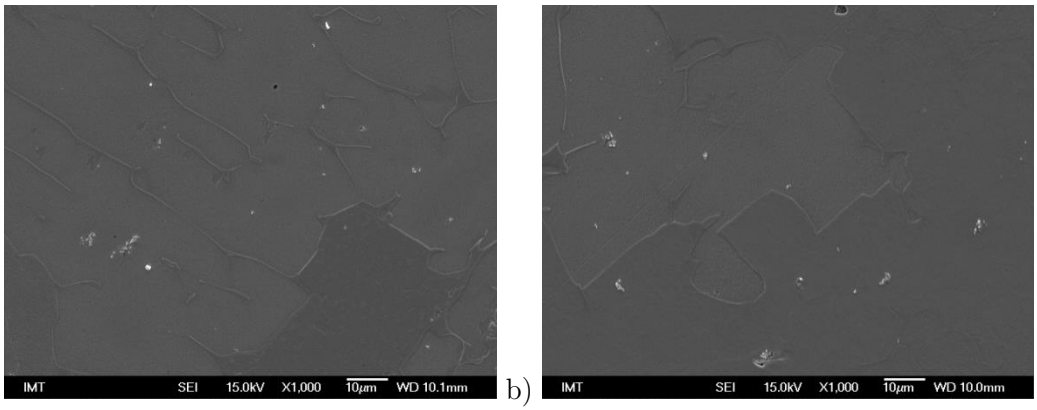

Figure 45: As-cast microstructure of AISI 316L austenitic stainless steel at 1000x magnification with the addition of a) 0.5 wt. % Al_2O_3 nano-particles (sample P5) and b) 1.0 wt.% Al_2O_3 nano-particles (sample P6). In both cases Al_2O_3 particles of 50 nm were

mixed with the dispersion medium CaSi in a 1:1 mass ratio; sample taken from the middle part of the as-cast ingot.

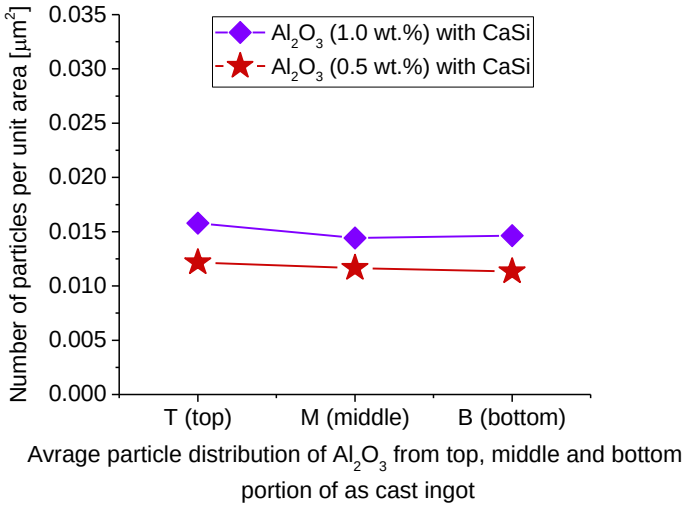

Figure 46: Influence of different concentrations (0.5 wt.% and 1.0 wt.%) of Al_2O_3 particles with a mean particle size of 50nm and the addition of CaSi on the particles distribution.

Based on the results from the preliminary tests the method of introducing 50-nm-sized nano-particles in a 0.5 wt% concentration into the melt flow during casting was selected. The nano-particles were encapsulated into a ferritic steel tube and held in the path of the melt flow when casting into the mold started. As compared to the preliminary experiments using 2 kg as-cast ingots, in the main experiments 8-kg ingots modified by nano-particles were prepared, with the casting being followed by hot rolling.

6.2 Main Experiments

6.2.1 Metallographic analysis

6.2.1.1 Light microscopy (LM)

A microstructure investigation of the samples was carried out for the as-cast condition as well as after the hot-rolling process. A certain degree of thermomechanical processing is required to achieve a suitable final microstructure, which might require even further heat treatment. However, the aim of the research was not to evaluate the effect of nano-particles on the final properties of AISI 316L steel, but on the possibility of successfully incorporating nano-particles into the steel matrix and how they influence the material performance. Therefore, the investigation was performed on as-cast and hot-rolled ingots without a final annealing treatment. The as-cast microstructure analysis was performed to determine the effect of the concentration, size and method of nano-particle addition on their distribution. On the other hand, hot-rolled samples were used to determine the stability of the nano-particles and their distribution after the hot-rolling process.

Optical micrographs were made by analyzing samples taken from the top (T), middle (M) and bottom (B) portion of the cast and hot-rolled ingot (Fig 47). As there was no significant difference between the three mentioned regions analyzed and for a representative analysis all the micrographs of the microstructure shown are from the middle portion of the as-cast and additionally hot-rolled ingot. This is true for all the samples investigated. The microstructure evolution of the samples with the addition of different nano-particles,

analyzed using the light microscope is shown in Figs. 48 to 52. A metallographic analysis shows that alloys produced with different additions of nano-particles contain different amounts of recrystallized and un-recrystallized grains of austenite with a distribution of δ-ferrite ranging from 0.3 to 1.0 %. The total volume fraction of recrystallized and un-recrystallized grains was not evaluated in detail and is described only based on light microscope images. The detailed effect of the nano-particles on the recrystallization process was not the focus of this investigation and might be the basis for further studies.

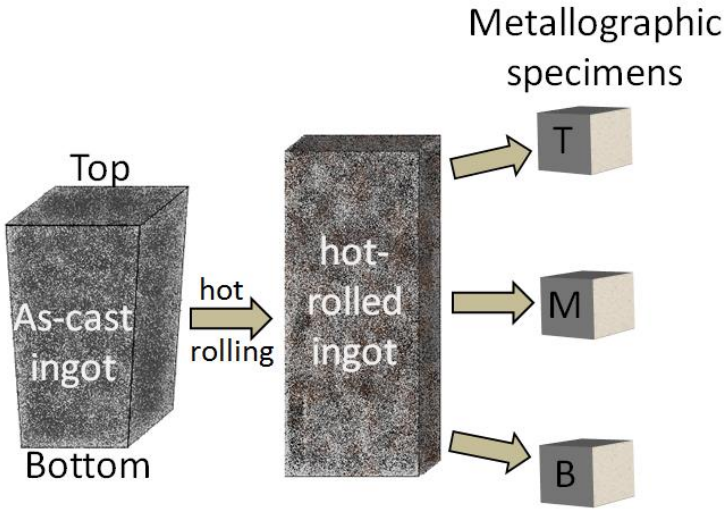

Figure 47: Schematic diagram of the subtraction of the metallographic samples.

Generally, austenitic stainless steels are assumed to be in the class of materials exhibiting a relatively low stacking-fault energy, which favors recrystallization over recovery during conventional hot-working processes. Highly alloyed austenitic stainless steels, e.g., 316L, are expected to exhibit progressively more sluggish recrystallization because of the accelerated recovery processes [79]. In the current case, experimental mold cast ingots were heated to 1200 °C prior to hot rolling, hot rolled and then left to be air cooled. It was established from the LM micrographs that the matrix consists of a distinctive two-phase microstructure of recrystallized and un-recrystallized grains of austenite and δ-ferrite, which was measured using a Feritoscope MP30 according to ISO 9001 and found to be below 1% for all the samples investigated, regardless of whether the nano-particles were added or not. In the case of the reference sample (R) the volume fraction of δ-ferrite was 0.98 % (Fig. 48). The amount of δ-ferrite in the samples (A1-A4) with the addition of 0.5 wt. % of Al_2O_3 nano-particles was in a very narrow range, between 0.91 and 0.99 % (Figs. 49 and 50). In the case of the samples involving oxide nano-particles (A2, B, C) the δ-ferrite values showed a larger variation. For the A2 sample with Al_2O_3 nano-particles (Fig. 49 b)) the δ-ferrite volume faction was 0.91 %, for sample B (Y_2O_3; Fig. 51 a)) 0.71 % and for sample C (TiO_2; Fig. 51 b)) 0.36 %. The addition of Ti-based nano-particles resulted in a reduced amount of δ-ferrite, which in the case of sample C with TiO_2 nano-particles (Fig. 51 b)) was 0.36 %, for sample sample D (TiC; Fig. 52 a)) 0.42 % and for sample E (TiB_2; Fig. 52 b)) 0.31 %.

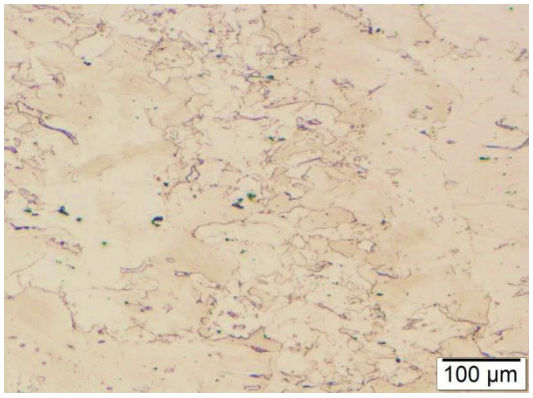

Figure 48: Cast and hot-rolled microstructure of the reference AISI 316L austenitic stainless-steel sample (R) with 0.98 % of δ -ferrite.

a) 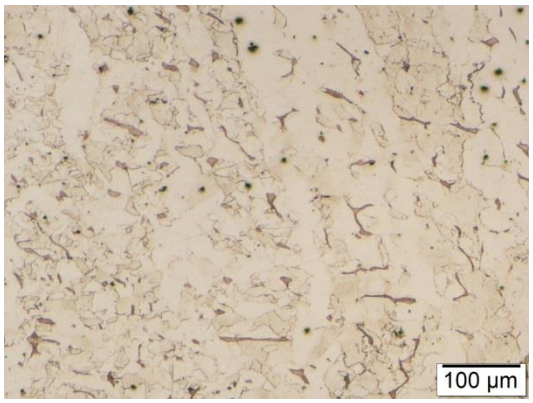

b) 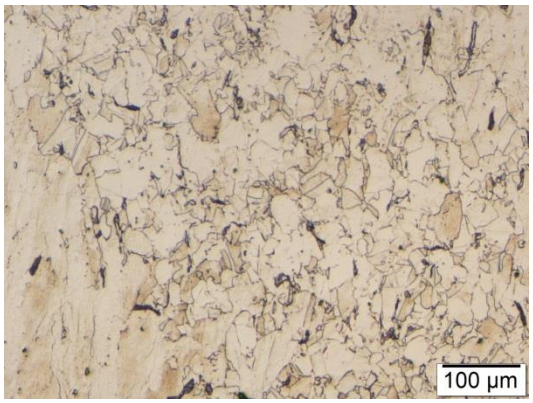

Figure 49: Cast and hot-rolled microstructure of AISI 316L austenitic stainless steel; a) sample A1(addition of 0.5 wt. % Al_2O_3 nano-particles) - 0.98 % of δ-ferrite, b) sample A2 (addition of 0.5 wt. % Al_2O_3 nano-particles mixed with the dispersion medium CaSi in 1:1 mass ratio) - 0.91 % of δ-ferrite.

a) 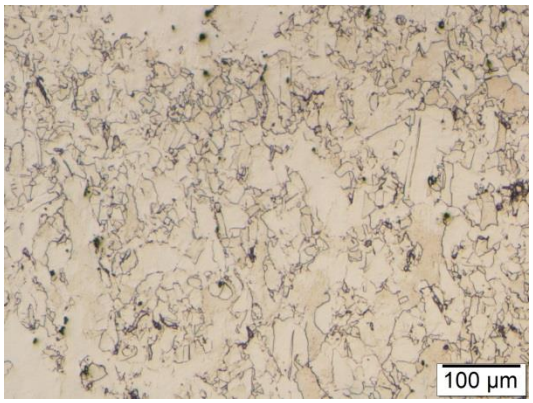

b) 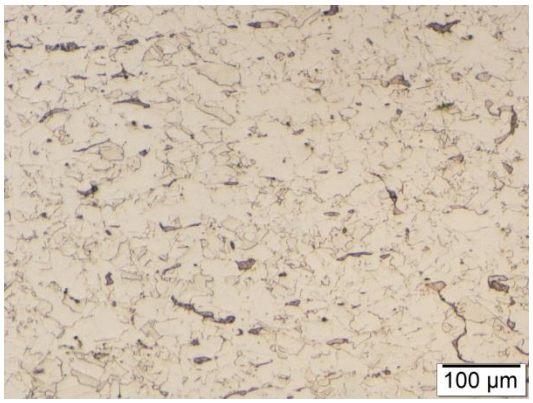

Figure 50: Cast and hot-rolled microstructure of AISI 316L austenitic stainless steel; a) sample A3(addition of activated 0.5 wt. % Al_2O_3 nano-particles)- 0.99 % of δ-ferrite, b) sample A4 (addition of activated 0.5 wt. % Al_2O_3 nano-particles mixed with the dispersion medium CaSi in 1:1 mass ratio)- 0.93 % of δ-ferrite.

a) 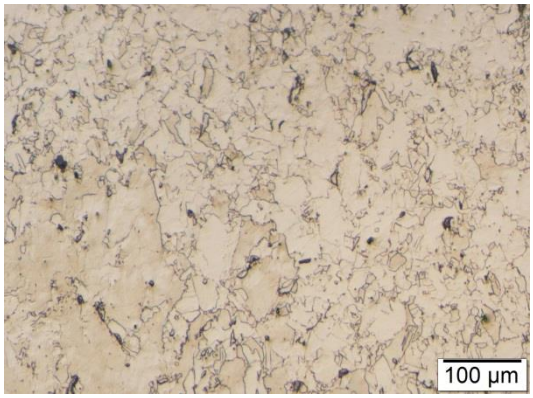

b) 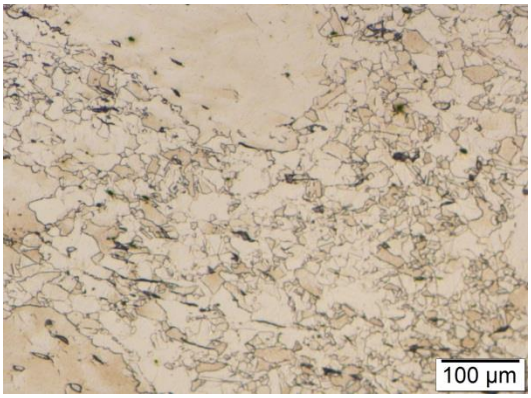

Figure 51: Cast and hot-rolled microstructure of AISI 316L austenitic stainless steel; a) sample B (addition of 0.5 wt. % Y_2O_3 nano-particles mixed with the dispersion medium – CaSi in 1:1 mass ratio)- 0.71 % of δ-ferrite, b) sample C (addition of 0.5 wt. % TiO_2nano-particles mixed with the dispersion medium CaSi in 1:1 mass ratio)- 0.36 % of δ-ferrite.

a) 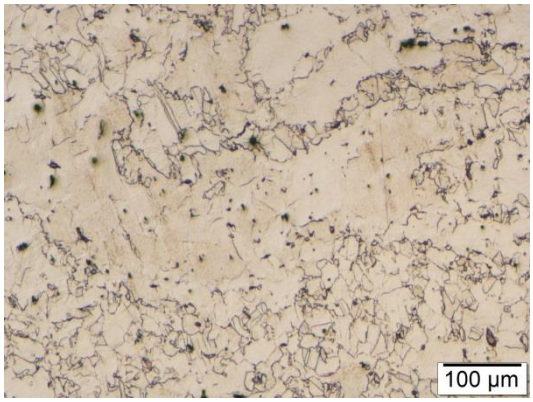

b) 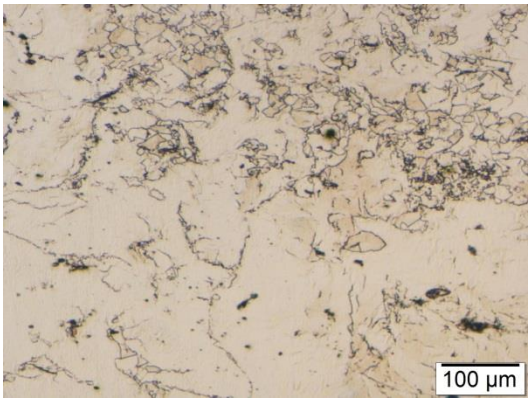

Figure 52: Cast and hot-rolled microstructure of AISI 316L austenitic stainless steel; a) sample D (addition of 0.5 wt. % TiC nano-particles mixed with the dispersion medium CaSi in 1:1 mass ratio)- 0.42 % of δ-ferrite, b) sample E (addition of 0.5 wt. % TiB_2 nano-particles mixed with the dispersion medium CaSi in 1:1 mass ratio)- 0.31 % of δ-ferrite.

6.2.1.2 Scanning electron microscopy (SEM) and energy-dispersive X-ray spectroscopy (EDS) analysis

To analyze the obtained microstructure of cast and hot-rolled material in detail, especially to show the morphology and size of different nano-particles clearly, the etched samples of AISI 316L austenitic stainless steel reinforced with nano-particles (50 nm, 0.5 wt% concentration) were further examined by SEM and EDS analysis at larger magnifications. For analyzing purposes, up to 10 images were acquired at different locations of each sample, taken at magnifications of 5000× and 20,000×.

In order to confirm the type of reinforced nano-particle for particle sizes larger than 500 nm, the investigated samples were also characterized by energy-dispersive X-ray spectroscopy (EDS) analysis. Smaller particles could not be analyzed due to the limitation of the EDS technique and were subjected to more sensitive TEM examination. Fig. 53 represents the microstructure of the cast and hot-rolled reference AISI 316L austenitic stainless steel without the addition of any nano-particles. The image shows a partially recrystallized microstructure with recrystallized grains. The recrystallized grains are clean (largely free from defects), whereas the deformed regions show a large concentration of defects, such as dislocations and cell boundaries, as seen in Figure 70.

a) 

b) 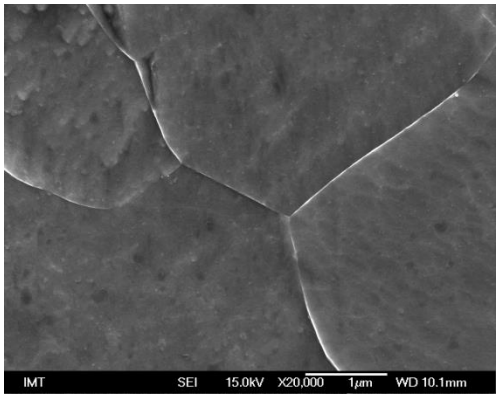

Figure 53: Cast and hot-rolled microstructure of AISI 316L austenitic stainless steel at a a) 5000x magnification and b) 20,000x magnification for sample R (reference material) without the addition of nano-particles.

As can be clearly seen from Figs. 54–61, and confirmed by EDS analysis (Figs. 55, 57, 59, 61) the addition of 0.5 wt. % of Al_2O_3 nano-particles leads to the effective incorporation of nano-particles in the steel matrix without any evident intermetallic reactions. In Figs. 55, 57, 59, 61 spectrum 1 represents Al_2O_3 nano-particle EDS analysis and spectrum 2 represents the matrix. However, in the case of "pure" Al_2O_3 nano-particles, not being mixed with the dispersion medium (A1), the particles are non-uniformly distributed in the matrix, with pronounced particles clustering taking place. Activating the Al_2O_3 nano-particles in oxygen plasma (A3) did not have any evident effect, neither on the way how the nano-particles are incorporated into the steel matrix, nor on the distribution homogeneity and clustering (Figs. 58 and 59). On the other hand, when Al_2O_3 nano-particles are mixed with the CaSi de-oxidant agent (experiment A2 and A4), they are much more uniformly distributed in the matrix with reduced clustering, as shown in Figs. 56 and 60. By using CaSi as a dispersion medium and introducing the nano-particles/CaSi mixture through a sealed ferritic steel tube, reduced particles clustering and more homogeneous distribution of reinforcing nano-particles in the steel matrix is obtained. This also made the automatic analysis of the particles size distribution using the INCA Feature (1mm × 1mm surface) possible. INCA Feature classifies features by morphology, chemistry and position.

a) 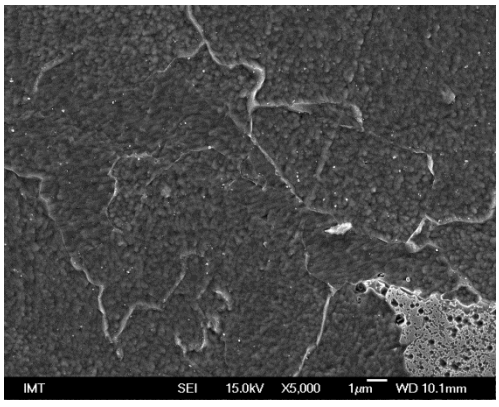

b) 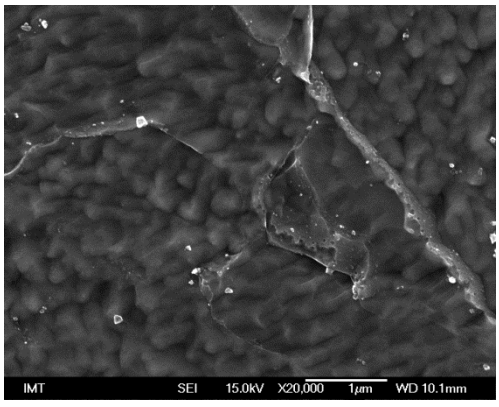

Figure 54: Cast and hot-rolled microstructure of AISI 316L austenitic stainless steel with the addition of 0.5 wt. % Al_2O_3 nano-particles (sample A1) at a a) 5000x magnification and b) 20,000x magnification.

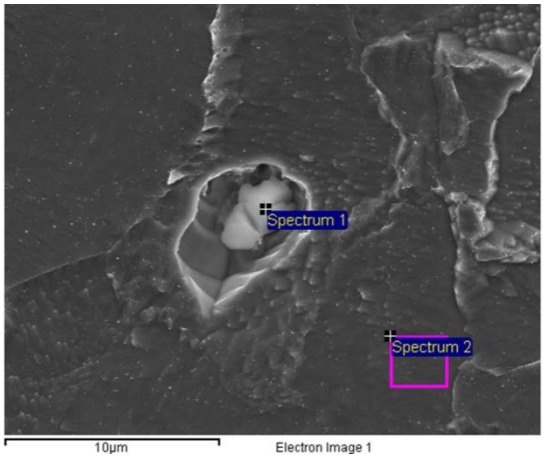

Element \ Spectrum	1 [wt%]	2 [wt%]
O	49.18	1.07
Al	36.64	0.00
Si	0.00	0.56
Ca	3.82	0.00
Ti	0.54	0.00
Cr	2.39	16.00
Mn	0.00	1.43
Fe	6.20	66.41
Ni	1.23	11.83
Mo	0.00	2.69

Figure 55: SEI image of incorporated particle larger than 500 nm at 5000x magnification for sample A1 and corresponding EDS analysis in weight %.

a) 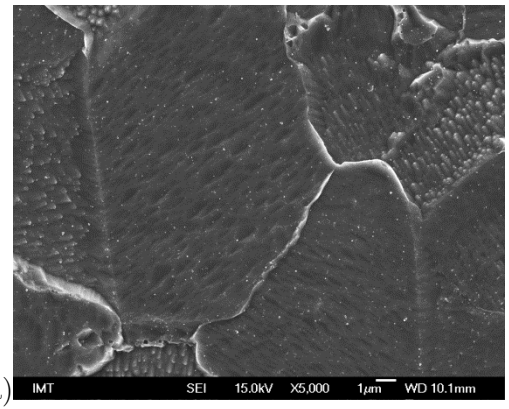

b) 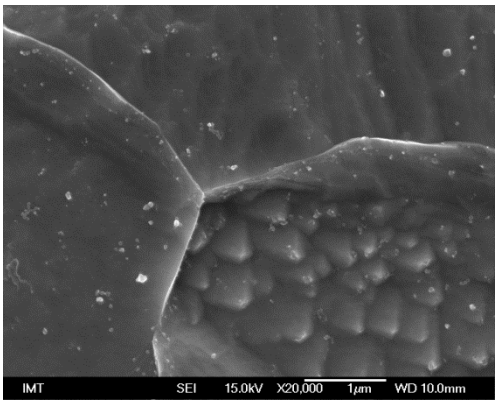

Figure 56: Cast and hot-rolled microstructure of AISI 316L austenitic stainless steel at a) 5000x magnification and b) 20,000x magnification for sample A2 with the addition of 0.5 wt. % Al_2O_3nano-particles mixed with the dispersion medium CaSi in 1:1 mass ratio.

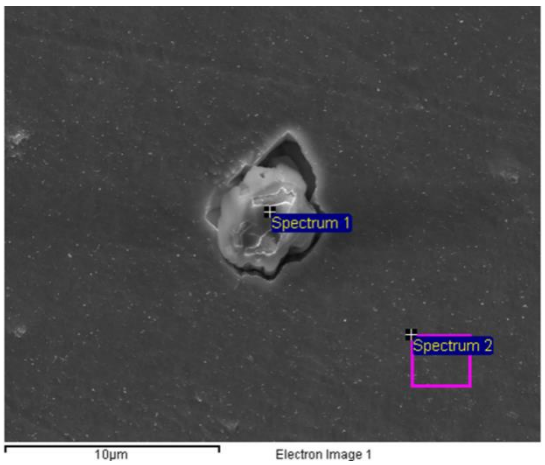

Element \ Spectrum	1 [wt%]	2 [wt%]
O	41.62	0.00
Al	37.48	0.00
Si	0.00	0.52
Ti	3.94	0.00
Cr	3.93	18.02
Mn	0.00	2.06
Fe	11.45	67.96
Ni	1.57	11.44

Figure 57: SEI image of incorporated particle larger than 500 nm at 5000x magnification for sample A2 and corresponding EDS analysis in weight %.

a) 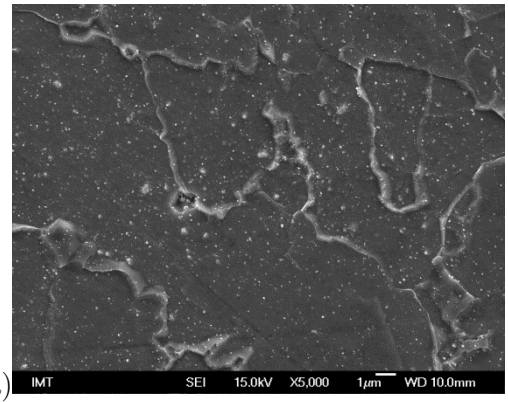

b) 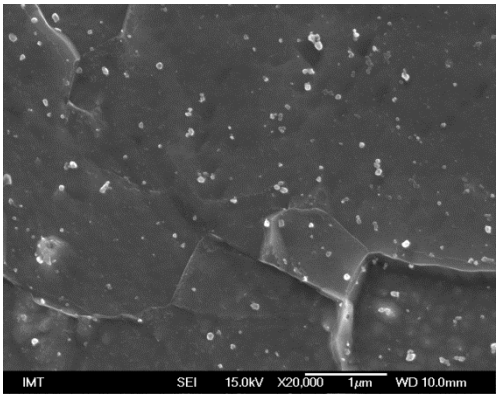

Figure 58: Cast and hot-rolled microstructure of AISI 316L austenitic stainless steel at a) 5000x magnification and b) 20,000x magnification for sample A3 with the addition of activated 0.5 wt. % Al_2O_3 nano-particles in weight %.

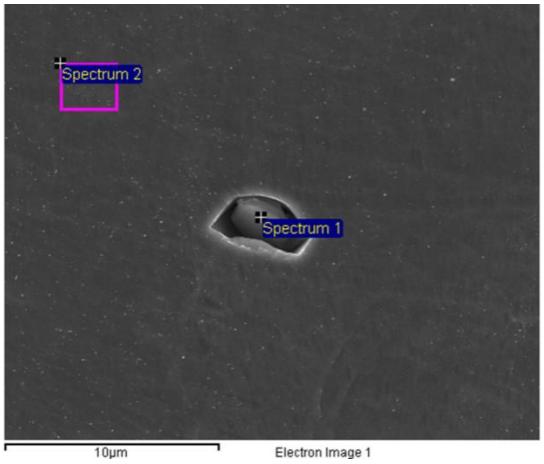

Element \ Spectrum	1 [wt%]	2 [wt%]
O	50.88	0.00
Al	36.77	0.00
Si	0.00	0.55
Ca	4.04	0.00
Cr	1.81	17.13
Mn	0.00	1.96
Fe	5.82	68.98
Ni	0.67	11.38

Figure 59: SEI image of incorporated particle larger than 500 nm at 5000x magnification for sample A3 and corresponding EDS analysis in weight %.

a) 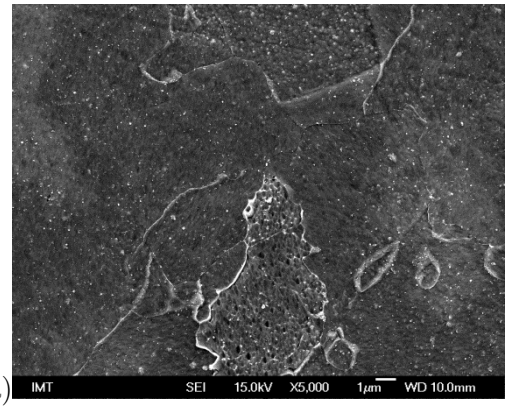

b) 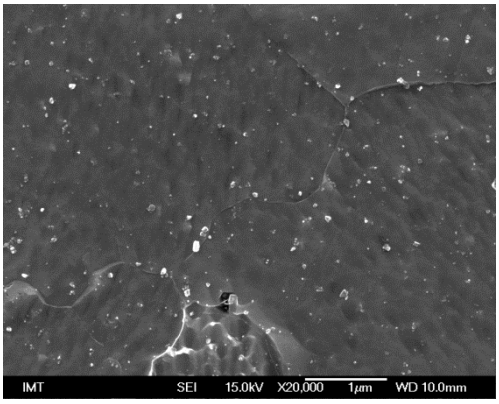

Figure 60: Cast and hot rolled microstructure of AISI 316L austenitic stainless steel at a a) 5.000x magnification and b) 20.000x magnification for sample A4 with addition of activated 0.5 wt. % Al_2O_3 nano-particles mixed with the dispersion medium CaSi in 1:1 mass ratio.

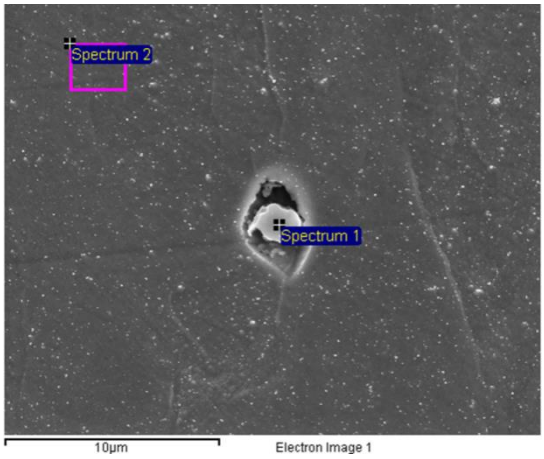

Element \ Spectrum	1 [wt%]	2 [wt%]
O	35.38	0.00
Al	46.64	0.00
Si	0.00	0.37
Mo	1.03	2.27
Cr	5.61	17.44
Mn	4.75	2.17
Fe	5.33	67.41
Ni	1.25	10.34

Figure 61: SEI image of incorporated particle larger than 500 nm at 5000x magnification for sample A4 and corresponding EDS analysis in weight %.

In the case of sample B (with the addition of Y_2O_3 nano-particles) the nano-particles are effectively introduced into the steel matrix and, as can be seen from Fig. 62, they are uniformly distributed in the matrix without obvious clustering, obtained by the addition of CaSi in the nano-particles mixture. From the energy-dispersive X-ray spectroscopy (EDS) analysis shown in Fig. 63 we have confirmed that the type of reinforcing particles larger than 500 nm are Y_2O_3 (spectrum 1). In spectrum 1 also the elements from the background (matrix; spectrum 2) can be seen, such as Cr, Mn, Ni and Fe, which is due to the analyzing volume exceeding the size of the analyzed particle.

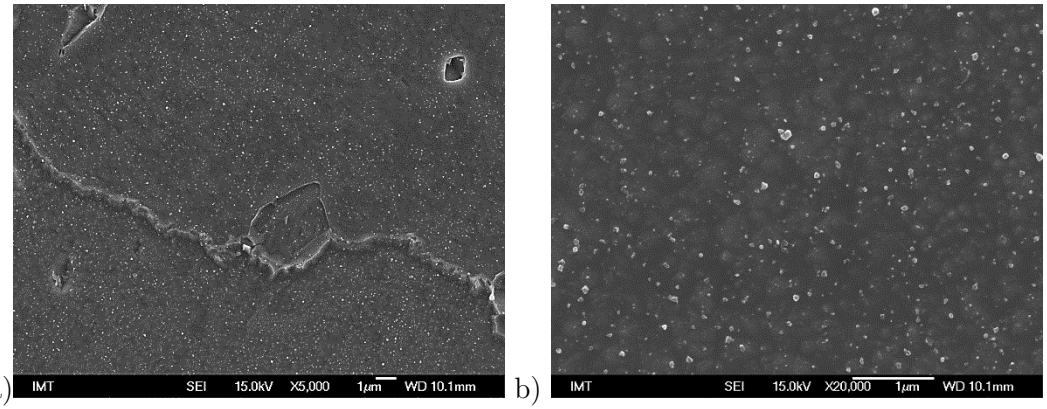

a) b)

Figure 62: Cast and hot-rolled microstructure of AISI 316L austenitic stainless steel at a) 5000x magnification and b) 20,000x magnification for sample B with the addition of 0.5 wt. % Y_2O_3 nano-particles mixed with the dispersion medium CaSi in 1:1 mass ratio.

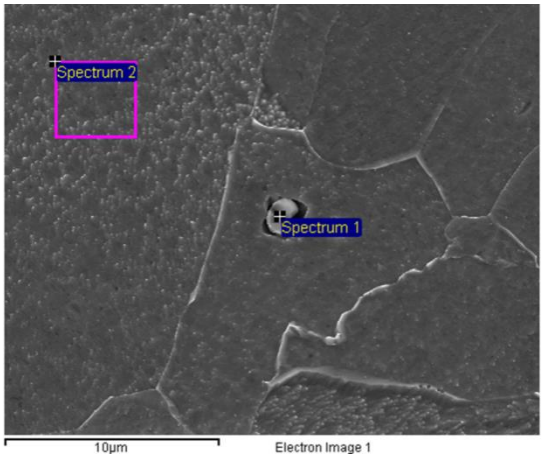

Element \ Spectrum	1 [wt%]	2 [wt%]
O	33.81	0.00
Al	5.13	0.00
Si	4.44	0.38
Ca	5.61	0.00
Ti	5.42	0.00
Mo	0.00	2.33
Cr	3.33	17.06
Mn	1.05	2.29
Fe	17.81	66.62
Ni	1.34	11.32
Y	22.05	0.00

Figure 63: SEI image of incorporated particle larger than 500 nm at 5000x magnification for sample B and the corresponding EDS analysis in weight %.

The same observation as for Al_2O_3 and Y_2O_3 nano-particles can be made for the addition of TiO_2 nano-particles mixed with the CaSi dispersion medium, as shown in Figs. 64 and 65. They are uniformly distributed and for particles larger than 500 nm it was confirmed they represent the TiO_2 (spectrum 1), originating from the TiO_2 nano-particles added to the AISI 316L austenitic stainless steel (spectrum 2). In spectrum 1 we see elements from the background (matrix; Cr, Mn and Fe) that are present due to the small particle size.

a) 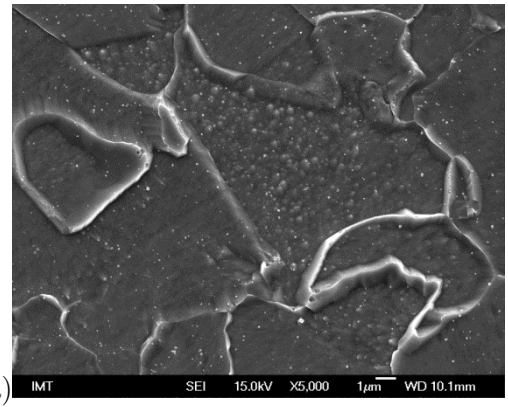

b) 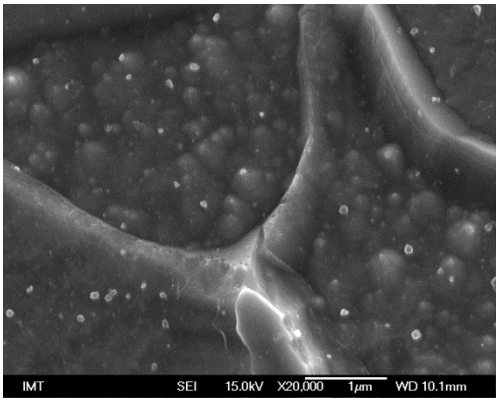

Figure 64: Cast and hot-rolled microstructure of AISI 316L austenitic stainless steel at a) 5000x magnification and b) 20,000x magnification for sample C with the addition of 0.5 wt. % TiO_2 nano-particles mixed with the dispersion medium CaSi in 1:1 mass ratio.

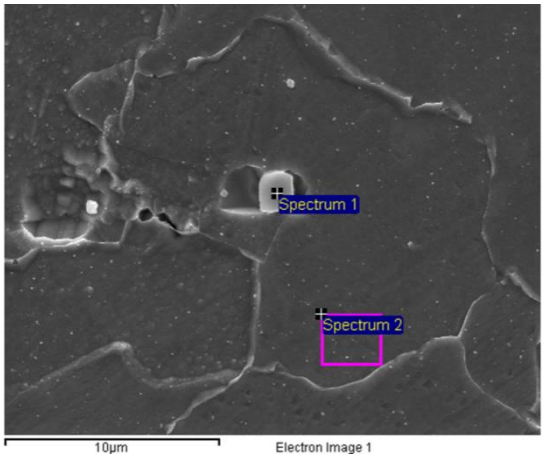

Element \ Spectrum	1 [wt%]	2 [wt%]
O	32.47	0.00
Al	0.89	0.00
Si	0.00	0.53
Ti	19.89	0.00
Mo	0.00	2.14
Cr	17.28	17.34
Mn	2.80	1.76
Fe	26.68	66.56
Ni	0.00	11.68

Figure 65: SEI image of incorporated particle larger than 500 nm at 5000x magnification for sample C and corresponding EDS analysis in weight %.

Figs. 66 and 67 show SEM analyses for TiC nano-particles-reinforced AISI 316L stainless steel. The EDS analysis of the particles present in the microstructure and larger than 500 nm (spectrum 1) shows that by eliminating the effect of the matrix the particles mostly contain O and Ti. This suggests that above the melting point TiC nano-particles have dissolved followed by the formation of more stable titanium inclusions, i.e., titanium oxides. This is also true for the addition of TiB_2 nano-particles, with the SEM/EDS analysis being shown in Figs. 68 and 69. As confirmed by the EDS analysis (Fig. 69) larger particles ($\geq$ 500 nm) present in the matrix contain Ti and O elements, at the same time having a circular shape typical for TiO_2 particles. This is in the agreement with the thermodynamic calculations indicating that phase B2M, representing TiB_2, dissolves already at a temperature of about 1350 °C.

a) 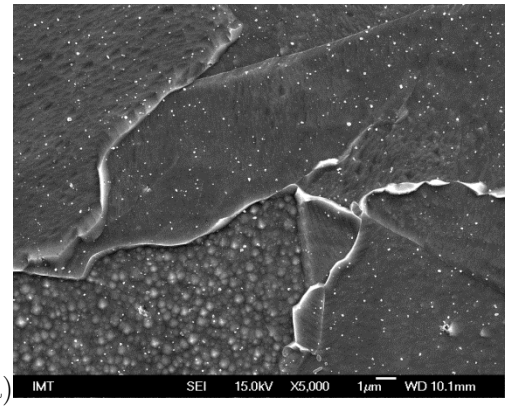

b) 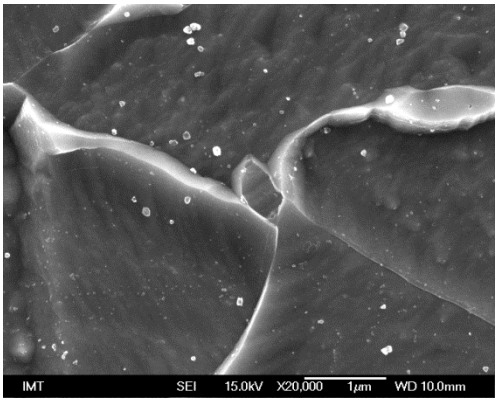

Figure 66: Cast and hot-rolled microstructure of AISI 316L austenitic stainless steel at a a) 5000x magnification and b) 20,000x magnification for sample D with the addition of 0.5 wt. % TiC nano-particles mixed with the dispersion medium CaSi in 1:1 mass ratio.

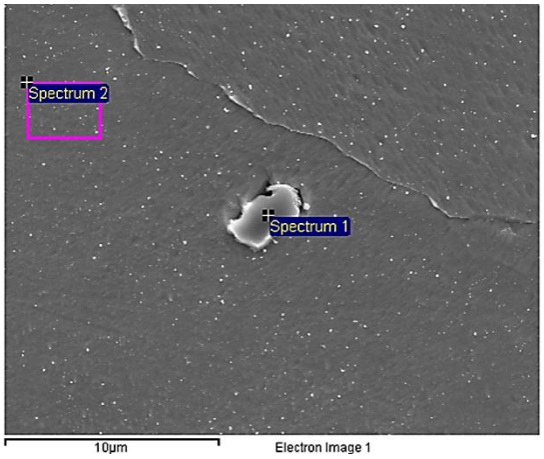

Element \ Spectrum	1 [wt%]	2 [wt%]
O	31.44	0.00
Al	0.78	0.00
Si	0.00	0.48
Ti	41.84	0.00
V	1.23	0.00
Mo	0.00	2.57
Cr	6.58	18.07
Mn	5.07	1.96
Fe	11.02	66.33
Ni	2.03	10.60

Figure 67: SEI image of incorporated particle larger than 500 nm at 5000x magnification for sample D and corresponding EDS analysis in weight %.

a) 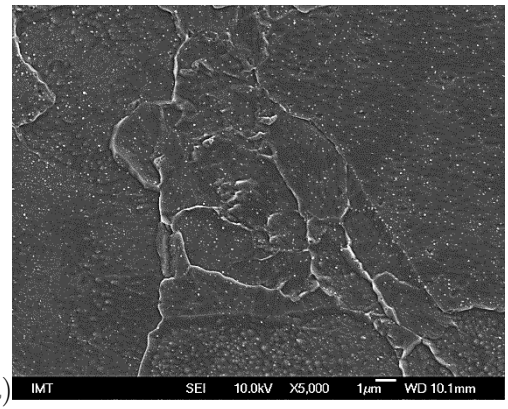

b) 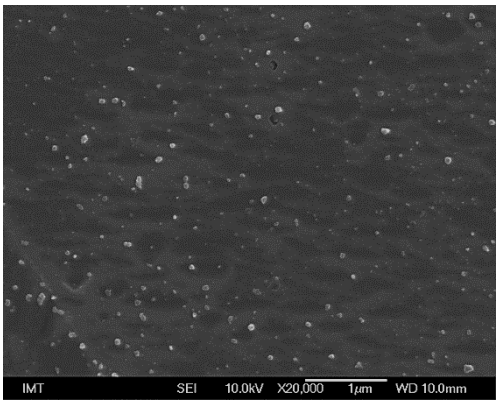

Figure 68: Cast and hot-rolled microstructure of AISI 316L austenitic stainless steel at a) 5000x magnification and b) 20,000x magnification for sample E with addition of 0.5 wt. % TiB_2 nano-particles mixed with the dispersion medium CaSi in 1:1 mass ratio.

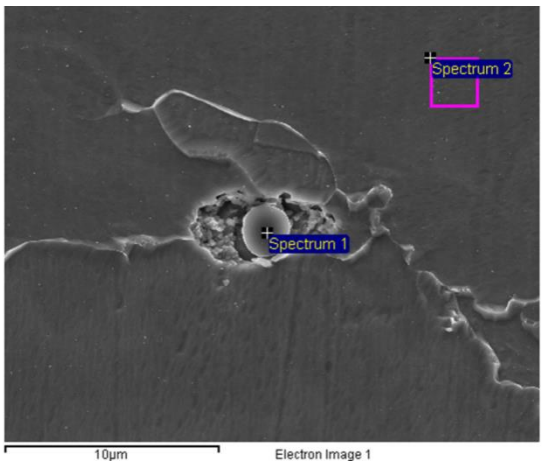

Element \ Spectrum	1 [wt%]	2 [wt%]
O	37.49	0.00
Al	0.43	0.00
Ti	47.73	0.00
Mo	0.00	1.63
Cr	4.88	16.94
Mn	6.30	2.11
Fe	3.17	68.19
Ni	0.00	11.13

Figure 69: SEI image of incorporated particle larger than 500 nm at 5000x magnification for sample E and corresponding EDS analysis in weight %.

6.2.1.3 Transmission electron microscopy (TEM) analysis

In the context of the characterization of microstructural changes and the dispersion of the nano-particles in the size range smaller than 500 nm when incorporated in the steel matrix, the samples were finally analyzed by transmission electron microscopy (TEM). Fig. 70 shows a HAADF/STEM image displaying the nano-particles in the microstructure of the austenitic stainless steel AISI 316L.

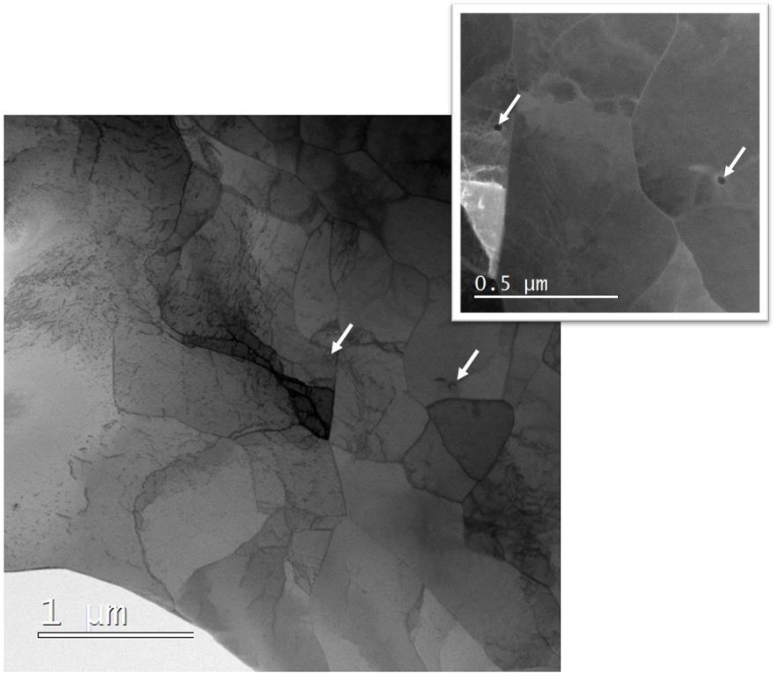

Figure 70: HAADF/STEM image of AISI 316L austenitic stainless steel with incorporated nano-particles (indicated by arrows).

With STEM/EDS elemental mapping shown in Fig. 71 and the STEM line-profile analysis shown in Fig. 72 the successful incorporation and coherent bonding of the Al_2O_3 nano-particles in the steel matrix was confirmed. TEM/EDS elemental mapping was used to find and confirm the presence of nano-particles in the range < 500 nm that were incorporated into the matrix. Furthermore, the STEM line-profile analysis was also employed in order to confirm the clean interface between the nano-particles and the matrix. A STEM line-profile analysis is an appropriate and accurate method for a reliable determination of the nano-particle/matrix interface. No intermetallic phases could be detected at the nano-particle/matrix interface (Fig. 72). With the STEM/EDS elemental mapping and the STEM line-profile analysis it was confirmed that the thermodynamically stable Al_2O_3 nano-particles stayed undissolved in the steel matrix. Some of the other elements could also be detected around the Al_2O_3 nano-particle, like titanium, nitrogen, manganese and sulfur, which means that some of the titanium could react with the Al_2O_3 nano-particles, resulting in the formation of complex oxides. Another explanation could be that the formation/nucleation of TiN and MnS started on the added nano-particle. The whole system is in the approximately 50-nm size range. The ThermoCalc calculations for the elemental composition of the most stable corundum phase also predicted that some of the titanium would be present in the mentioned phase (Fig.20). This is true for all the analyzed samples being alloyed/reinforced with Al_2O_3 nano-particles, either activated or not and mixed with CaSi or not (samples A1 to A4).

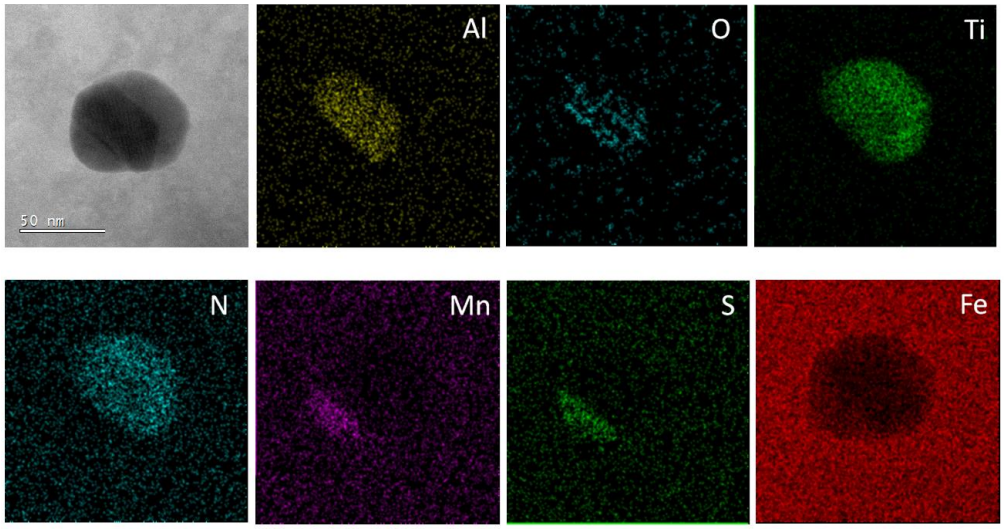

Figure 71: STEM/EDS elemental mapping of Al_2O_3 nano-particle in the microstructure of AISI 316L austenitic stainless steel; sample A2.

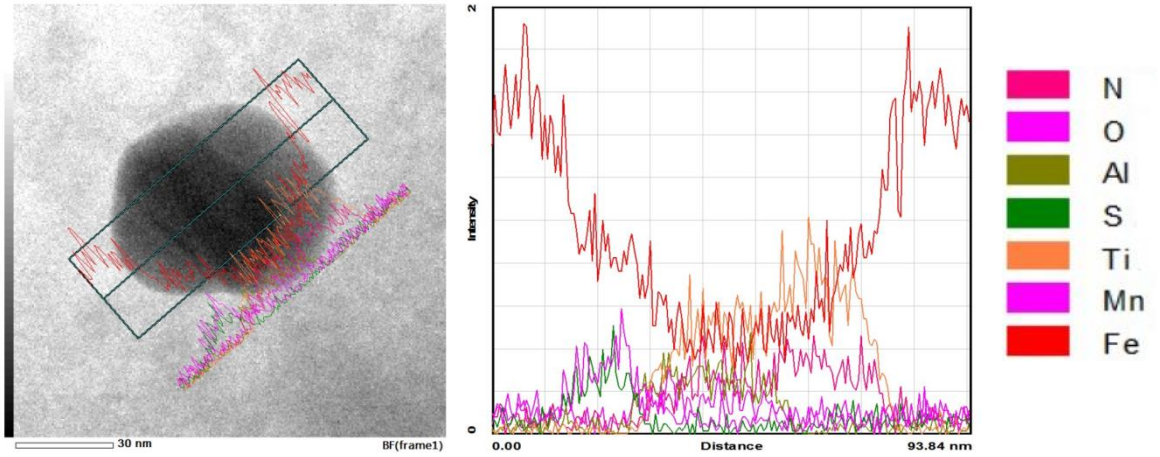

Figure 72: STEM line-profile analyses of Al_2O_3 nano-particle in the microstructure of AISI 316L austenitic stainless steel; sample A2.

In the thermodynamic calculations of the phase stability for the case of adding Y_2O_3 nano-particles (Fig.25) the M2O3C phase that represents Y_2O_3 dissolves already at a temperature of about 1150 °C. The TEM analysis confirms that the yttrium oxide has dissolved, followed by the reaction of yttrium with the surrounding elements, like Ti, Mn and S, forming new non-oxide-based complex particles (Fig. 73) with a clear interface toward the steel matrix (Fig. 74).

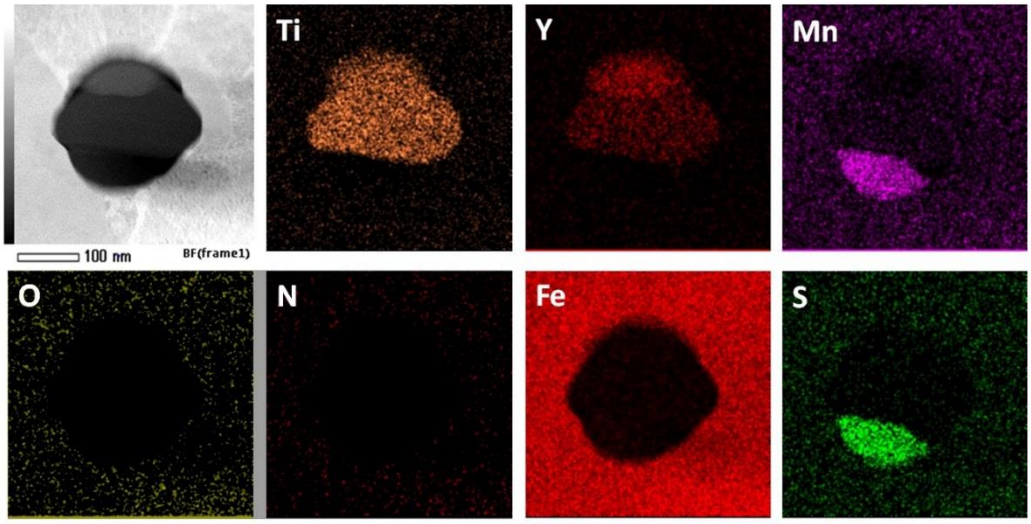

Figure 73: STEM/EDS elemental mapping of Y_2O_3 nano-particles in the microstructure of AISI 316L austenitic stainless steel (sample B).

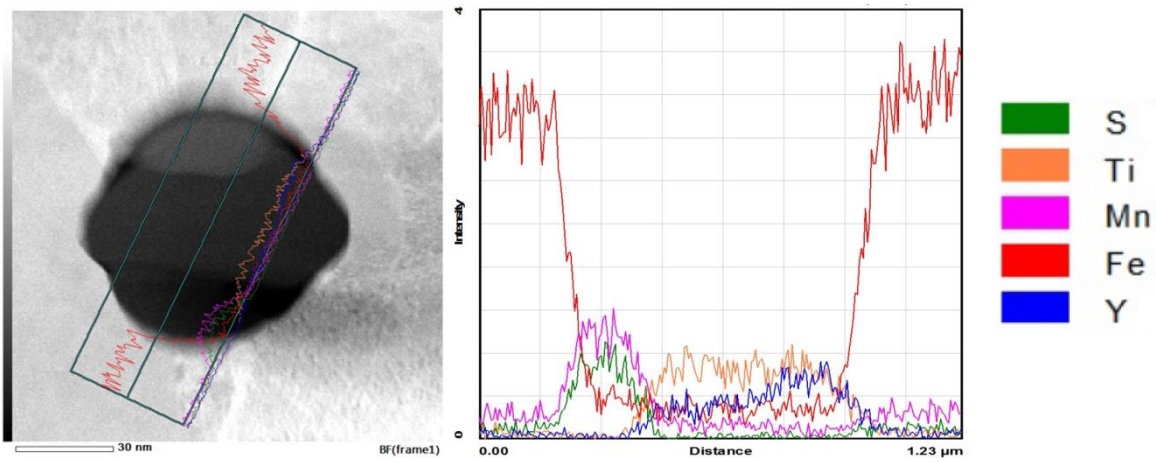

Figure 74: STEM line-profile analyses of Y_2O_3 nano-particles in the microstructure of AISI 316L austenitic stainless steel (sample B).

In the case of the added TiO_2 nano-particles (sample C) also particles smaller than 500 nm found in the metal matrix were confirmed by STEM/EDS elemental mapping (Fig. 75) to be titanium oxide, evidently originating from the added powder. Furthermore, from the STEM line-profile analysis shown in Fig. 76 no discontinues at the particle/matrix interface, modification of metal matrix or formation of intermetallic phases could be observed.

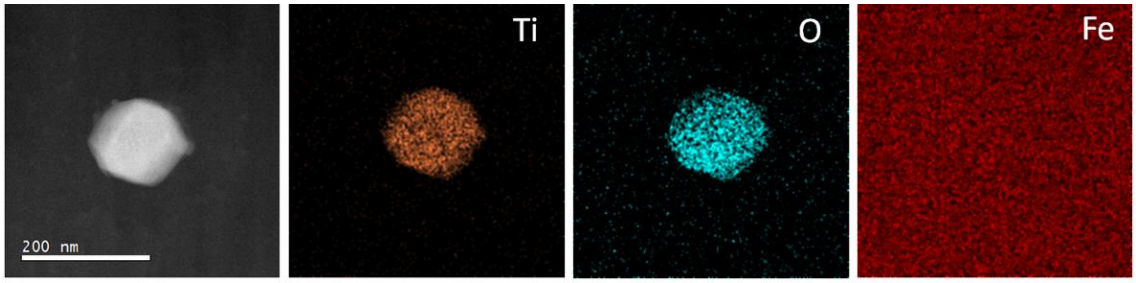

Figure 75: STEM/EDS elemental mapping of TiO_2 nano-particles in the microstructure of AISI 316L austenitic stainless steel (sample C).

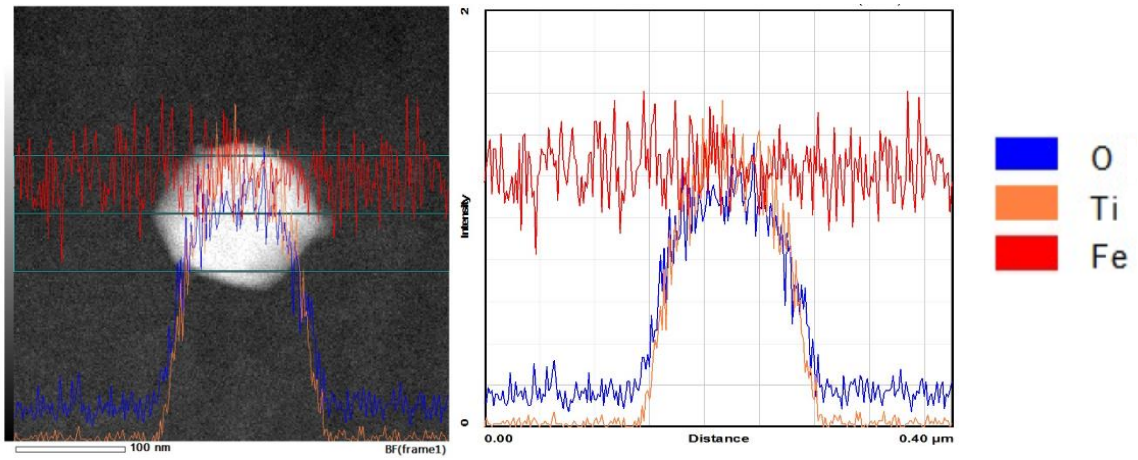

Figure 76: STEM line-profile analyses of TiO_2 nano-particles in the microstructure of AISI 316L austenitic stainless steel (sample C).

The STEM/EDS elemental mapping and the STEM line-profile analysis for the TiC nano-particles alloyed AISI 316L stainless steel are shown in Figs. 77 and 78. In the case of the TiC nano-particles the thermodynamic calculations indicate that above the melting point only nitrogen-containing particles can co-exist with the liquid phase. This means that the added TiC nano-particles will dissolve in the steel melt, followed by the formation of the more stable TiN and Ti(C,N) precipitates, if there is enough nitrogen and carbon available. This is confirmed by the TEM analysis shown in Figs. 79 and 61. As manifested by the STEM/EDS elemental mapping of the particles observed in the AISI 316L steel alloyed with TiC nano-particles (Fig. 79), the particles are titanium nitrides with a typical quadratic shape and a very clear interface, normally found for precipitates (Fig. 80).

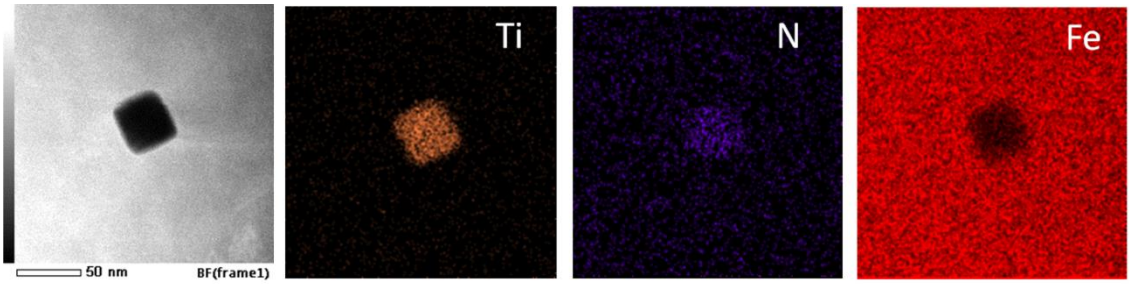

Figure 77: STEM/EDS elemental mapping of TiC nano-particles in the microstructure of AISI 316L austenitic stainless steel (sample D).

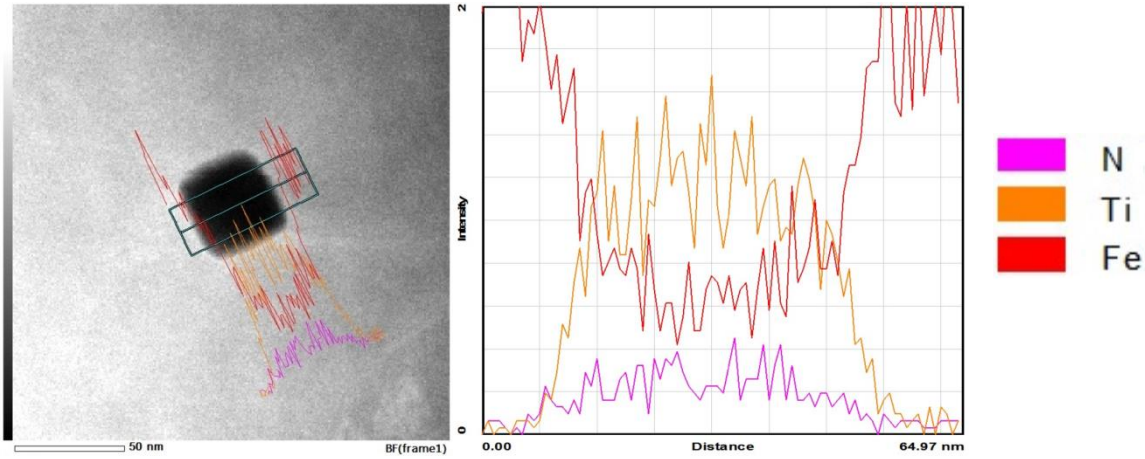

Figure 78: STEM line-profile analyses of TiC nano-particles in the microstructure of AISI 316L austenitic stainless steel (sample D).

The STEM/EDS elemental mapping and the STEM line-profile analysis for TiB_2 nano-particles alloyed AISI 316L stainless steel, focused on the analysis of the particles found, are shown in Figs. 73 and 74. From the analysis of the typical nano-particle found we can conclude that the TiB_2 nano-particles remain undissolved in the melt, followed by an effective integration into the steel matrix during the solidification. Based on the shape of the particles and absence of a nitrogen or oxide signal, titanium nitrides and titanium oxides can be excluded, respectively. Furthermore, also the formation of TiC is unlikely, as already shown by the ThermoCalc calculation and the results for the added TiC nano-particles. Finally, since the boron signal is very difficult to detect, it is the only feasible explanation that the nano-particles found are undissolved TiB_2 nano-particles, which theoretically should be stable in the steel melt.

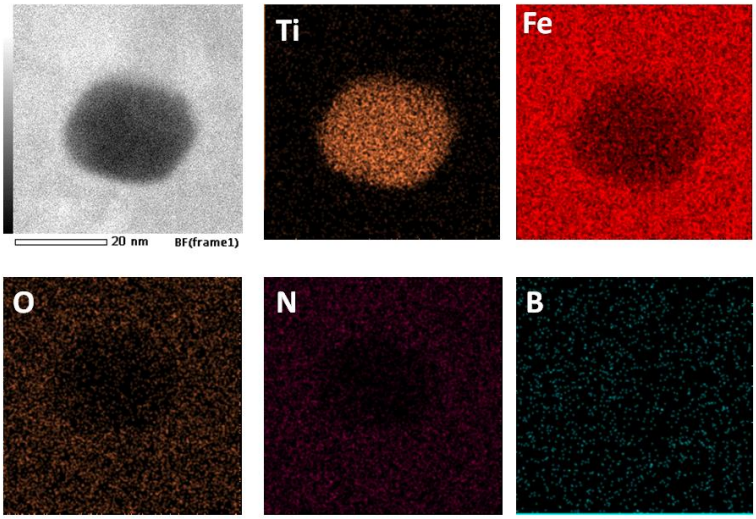

Figure 79: STEM/EDS elemental mapping of TiB_2 nano-particles in the microstructure of AISI 316L austenitic stainless steel (sample E).

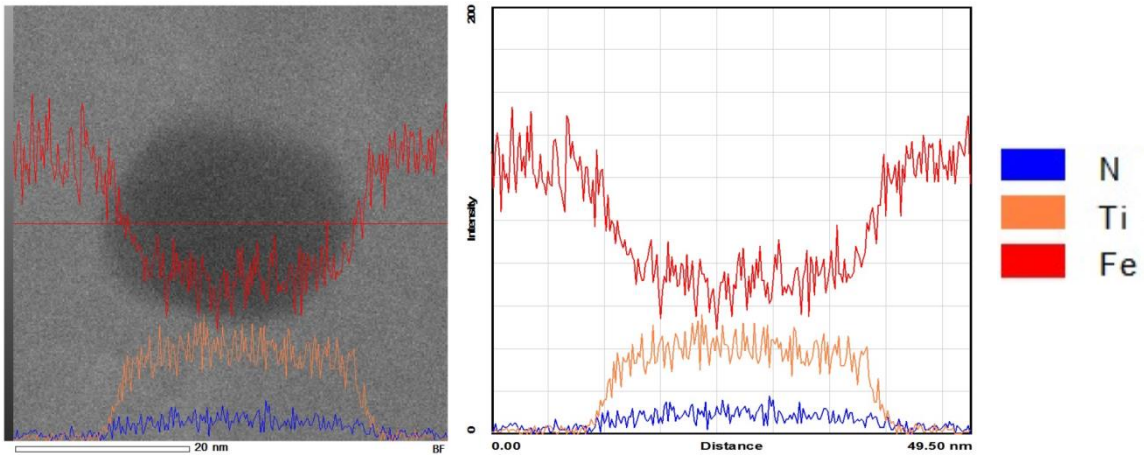

Figure 80: STEM line-profile analyses of TiB_2 nano-particles in the microstructure of AISI 316L austenitic stainless steel (sample E).

6.2.2 Particles distribution

The particle distribution results for the reinforced austenitic stainless steel 316L are summarized in Figs. 81 to 87. The particles distribution was determined for nano-particles in the range < 500 nm and ≥ 500 nm. They were chemically and morphologically detected (INCA Feature), including the chemical composition, size and position analysis of each particle. This was determined for both particle size ranges, providing information on the size and spatial distribution of the particles. Since all steels contain non-metallic inclusions (oxide inclusions can contain aluminum, silicon and/or calcium, sulfides typicality contain manganese) [80], the reference material was first examined for the type of inclusions, where chromium-rich oxides also containing manganese were mainly identified as well as some manganese sulfides. In this way, typical non-metallic inclusions were eliminated from the nano-particles distribution analysis.

The particles distribution analysis in the AISI 316L stainless-steel matrix for the nano-particles added in a 0.5 wt. % concentration is presented in the form of relative frequency and particles density per mm^2. A separate analysis was performed for the particles larger

than or equal to 500 nm and for those smaller than 500 nm. In the case when pure the Al_2O_3 nano-particles powder with a nominal size of 50 nm and without any dispersion agent (sample A1) was used, a non-homogeneous distribution and particle agglomeration was observed. The situation was very similar for the Al_2O_3 nano-particles, being oxide plasma activated, but still used without any dispersion agent (sample A3). Therefore, an accurate particles distribution analysis by applying the INCA Feature was not possible, because it cannot perform the automatic segmentation of agglomerated particles. In these cases (sample A1 and A3) particles distribution analysis for both particle sizes (larger and smaller than 500 nm) was analyzed using FIJI (ImageJ) software based on manual counting and measurements. The size distribution of the nano-particles is presented with an equivalent circular dimeter (ECD).

In the case of adding Al_2O_3 nano-particles without using any dispersion agent (sample A1), the relative frequency of the particles smaller than 500 nm is the highest (~15 %) for the smallest particles with their size ranging below 200 nm, which then exponentially drops toward larger sizes. Also, for particles larger than 500 nm most of the particles (<15 %) are in the lower size range (<800 nm), as shown in Fig. 81 a). The general particle size distribution follows the distribution shown by the starting powder analysis, with the particles ranging from 50 nm up to over 1 µm. By mixing Al_2O_3 nano-particles with a dispersion agent (sample A2) the relative frequency of the smallest particles increased, for particles smaller than 500 nm to about 25 % and for particles larger than 500 nm to over 15 % (Fig. 81 b). This indicates that the dispersion medium improves the homogeneity of the particles distribution within the steel matrix, helps to maintain smaller particles sizes and reduces the particle clustering. As shown in Fig. 82, the Al_2O_3 nano-particles activation by oxide plasma had no positive effect on the relative frequency of the nano-particles size distribution within the steel matrix. In addition, lower relative frequency values indicate a less-homogeneous particles distribution and more pronounced clustering for the activated Al_2O_3 nano-particles, which is true for both cases, without (sample A3; Fig. 82 a) and with the addition of the CaSi dispersion agent (sample A4; Fig. 82 b).

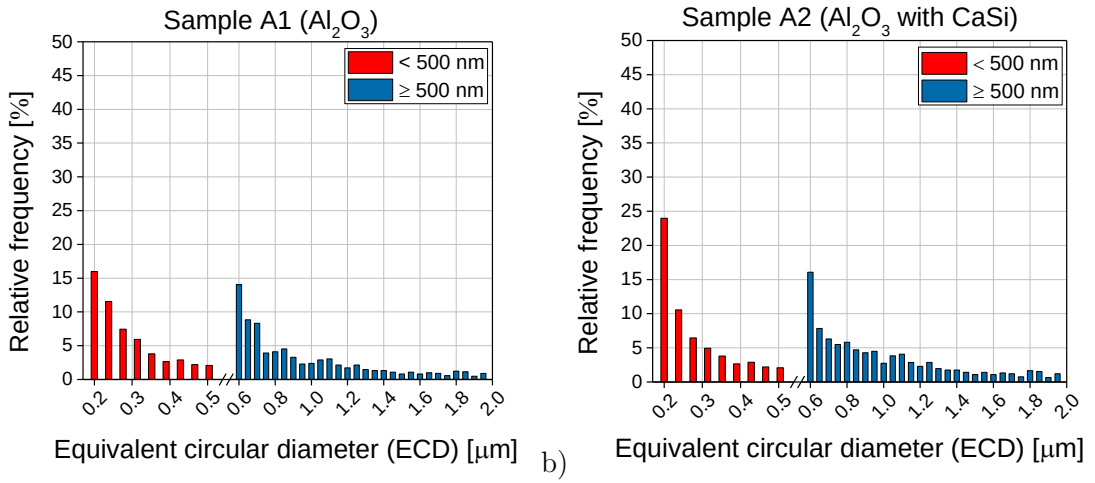

a) b)

Figure 81: Relative frequency of the particles size distribution in the steel matrix for a) sample A1(addition of 0.5 wt. % Al_2O_3 nano-particles) and b) sample A2 (addition of 0.5 wt. % Al_2O_3 nano-particles mixed with the dispersion medium CaSi in 1:1 mass ratio).

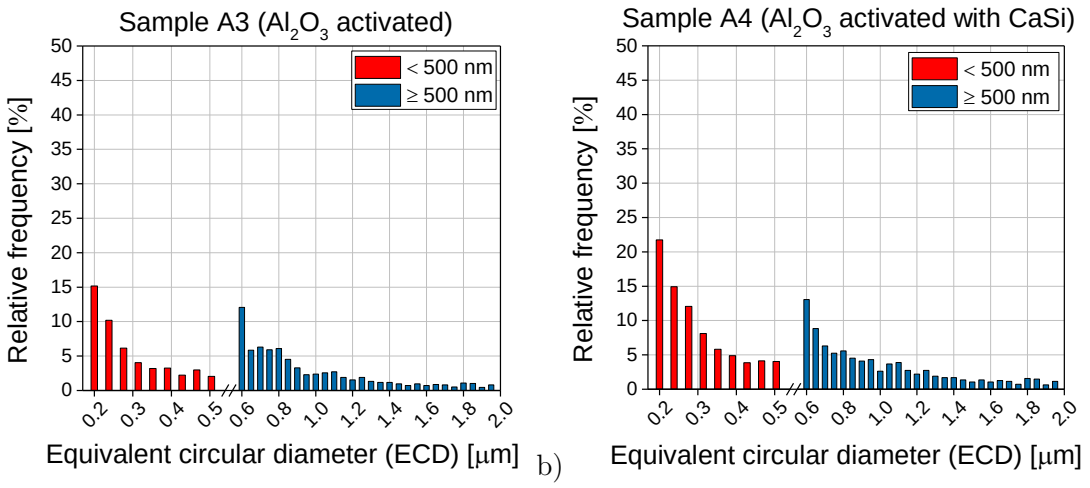

a) b)

Figure 82: Relative frequency [%] of particles for a)- sample A3(addition of activated 0.5 wt. % Al_2O_3 nano-particles), b)- sample A4 (addition of activated 0.5 wt. % Al_2O_3 nano-particles mixed with the dispersion medium CaSi in 1:1 mass ratio).

In the case of samples B–E, the relative frequency of particles < 500 nm is the highest (27–46 %) for the particle size range ≤ 200 nm and it drops in a similar fashion. The highest relative frequency of 46% was measured for sample C with the addition of TiO_2 nano-particles, which indicates their higher stability at higher temperatures as well as lower tendency for agglomeration. This behavior is also evident, although to a lesser extent for TiC (38 %), Y_2O_3 (31 %), and TiB_2 (27 %) nano-particles as compared to the samples reinforced with Al_2O_3 nano-particles (sample A2 and A4). The latter seems to be the least thermodynamically stable, as compared to the others. For particles ≥ 500 nm, the highest frequency corresponds to particles size around 500 nm (10–15 %). It should be noted that the peak of the lognormal distribution of the relative frequency of particles is at the particles size around 400 nm, i.e., the frequency of particles range < 300 nm is smaller. This is probably due to the initial nano-particle size distribution in the powder. Also, for samples C, D, and E, the relative frequency of particle sizes above 1 µm shows additional peaks, indicating the presence of larger particles and/or agglomerates. In the case of sample B (Y_2O_4 with CaSi), the decrease of the relative frequency is smooth, which may indicate the presence of larger particles but no agglomerates.

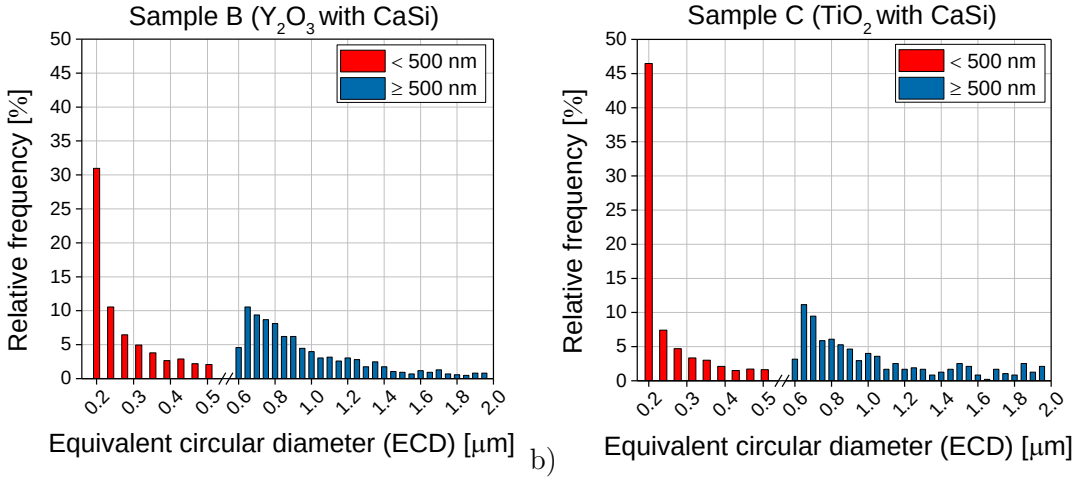

a) b)

Figure 83: Relative frequency [%] of particles for a)- sample B (addition of 0.5 wt. % Y_2O_3 nano-particles mixed with the dispersion medium CaSi in 1:1 mass ratio), b)- sample C

(addition of 0.5 wt. % TiO_2 nano-particles mixed with the dispersion medium CaSi in 1:1 mass ratio).

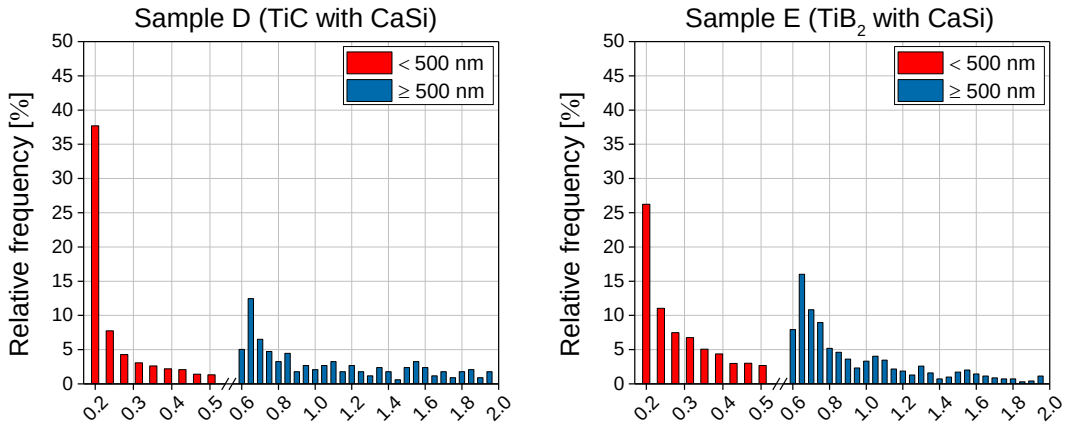

a) b)

Figure 84: Relative frequency [%] of particles for a)-sample D (addition of 0.5 wt. % TiC nano-particles mixed with the dispersion medium – CaSi in 1:1 mass ratio), b)- sample E (addition of 0.5 wt. % TiB_2nano-particles mixed with the dispersion medium CaSi in 1:1 mass ratio).

Also, the particles density per mm^2 was analyzed separately, for particles smaller than 500 nm and those larger than 500 nm. The density of Al_2O_3 nano-particles added in the concentration of 0.5 wt. % is shown in Fig. 85. In the case of Al_2O_3 nano-particles added without any dispersion agent (samples A1), the density of particles smaller than 500 nm is $8.5\times10^6/mm^2$, which is four orders of magnitude higher than for particles larger than 500 nm, with a density of about $1.3\times10^3/mm^2$. Mixing the Al_2O_3 nano-particles with the CaSi dispersion agent (sample A2) resulted in a strongly increased number of small particles (< 500 nm) with a density $12\times10^6/mm^2$ and a corresponding decrease in larger particles (> 500 nm) with a density below $1\times10^3/mm^2$. In the case of activated Al_2O_3 nano-particles (samples A3 and A4) the positive effect of the dispersion agent is similar; however, the activation shows a negative effect on the small vs. large particles density ratio, i.e., reducing the density of smaller particles by about 35 %. These results confirm the positive effect of the dispersion agent on the distribution homogeneity and the ability to reduce nano-particles clustering and agglomeration. Particles activation, on the other hand, has a rather negative effect.

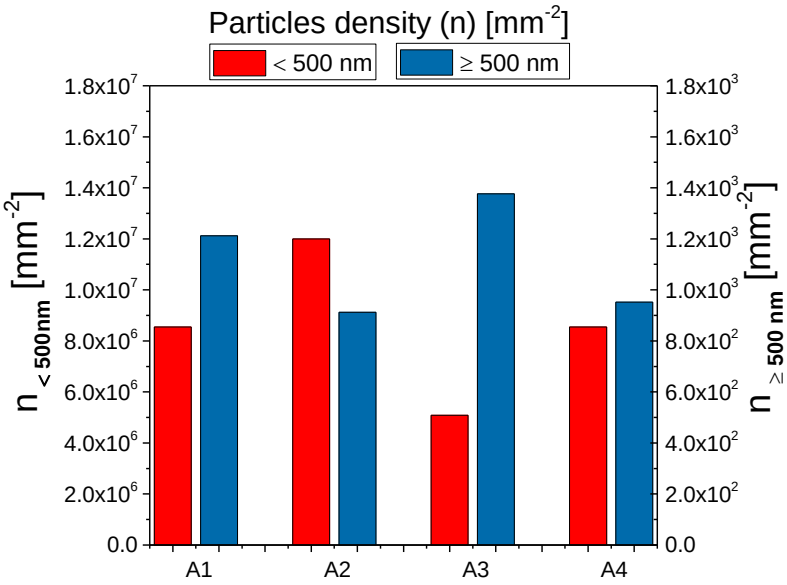

Figure 85: Particles density of Al_2O_3 nano-particles in the steel matrix for the particles size range < 500 nm and ≥ 500 nm.

In the case of adding different oxide nano-particles (samples A2, B, C) shown in Fig. 86, the density of the particles smaller than 500 nm linearly increases from 1.2×10^7 to 1.4×10^7 and 1.8×10^7/mm^2 for samples with Al_2O_3 (A2), Y_2O_3 (B), and TiO_2 (C) nano-particles, respectively. The opposite behavior is evident for particles larger than 500 nm, with the density decreasing from 9×10^2 to 8.5×10^2 and 5×10^2/mm^2. Even though the density of particles smaller than 500 nm is five orders of magnitude higher than the density of those larger than 500 nm, we can see an inversely proportional trend, i.e., increasing density of smaller particles and decreasing density of larger ones. In the case of more stable Y_2O_3 nano-particles (B) more particles smaller than 500 nm and a reduced degree of complex nano-particles formation as compared to the Al_2O_3 nano-particles (A2) is indicated by the particle density analysis (Fig. 86). The highest particle density was detected for the TiO_2 nano-particles (C), confirming the best stability of the TiO_2 nano-particles in the experimental batches without complex nano-particles formation.

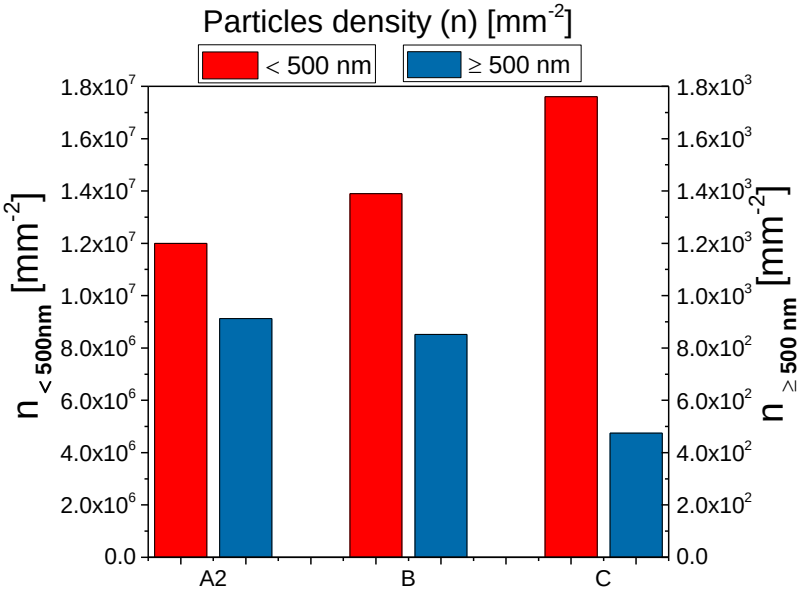

Figure 86: Particles density of oxide nano-particles for the particles size range < 500 nm and ≥ 500 nm (A2 – Al_2O_3, B – Y_2O_3, C – TiO_2).

The particles density analysis for samples C, D, and E, where titanium-based nano-particles were added, is shown in Fig. 87. It can be seen that for particles smaller than 500 nm, the density is between 9×10^6 and $1.8\times10^7/mm^2$, which is five orders of magnitude higher than the density of particles larger than 500 nm, being between 3×10^2 and $7\times10^2/mm^2$. It should be noted that the density of the particles smaller than 500 nm for sample D (TiC with CaSi) is about 50 % lower as compared to samples C (TiO_2 with CaSi) and E (TiB_2 with CaSi), both showing very similar densities. However, sample D has also the smallest density of particles larger than 500 nm. The TiC nano-particles are dissolved in the steel melt, which is followed by the formation of other precipitates, thus resulting in a lower particle density of the TiC nano-particles. In the case of the TiB_2 nano-particles a slightly higher particle density is shown than for the TiO_2 (E). This corresponds with the slightly increased number of larger particles in the case of sample E (TiB_2 nano-particles), with a higher probability for the formation of more complex inclusions.

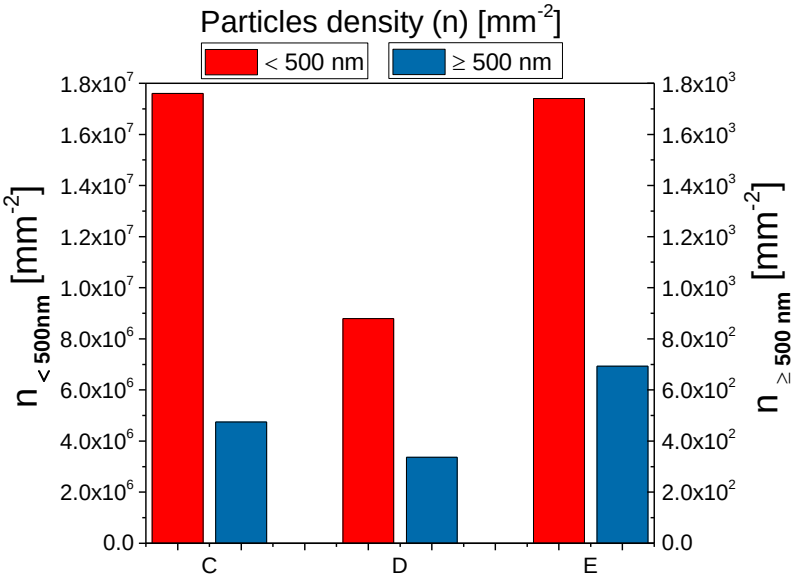

Figure 87: Particles density of Ti-based nano-particles for the particles size range < 500 nm and ≥ 500 nm (C – TiO_2, D – TiC, E – TiB_2).

6.2.3 Influence of added nano-particles on the mechanical properties

This chapter addresses the influence of different nano-particles added in a 0.5 wt. % concentration using the ferritic steel tube insertion method on the mechanical properties of AISI 316L austenitic stainless steel. All the properties were determined for the cast and hot-rolled condition and compared to the reference AISI 316L steel in the same cast and hot-rolled condition. The mechanical properties investigated were analyzed in terms of the particle type and comprised hardness, impact toughness, yield and ultimate tensile strength.

6.2.3.1 Hardness and impact-toughness results

The hardness and impact-toughness results for the reference austenitic stainless steel AISI 316L and the ones reinforced with different nano-particles are summarized in Figs. 88 to 90.

In the case of the reference cast and hot-rolled austenitic stainless steel AISI 316L (sample R) a hardness of 161 HV1 and an impact toughness of 161 J were obtained. By adding 0.5 wt. % of Al_2O_3 nano-particles with a nominal size of 50 nm (sample A1) no change in the hardness could be detected. However, due to the non-homogeneous distribution of the nano-particles the impact toughness also decreased to about 155 J, as shown in Fig. 88. On the other hand, mixing the Al_2O_3 nano-particles powder with the CaSi dispersion agent, which promotes more homogeneous nano-particles distribution and diminishes particles agglomeration and clustering, a hardness increase without a loss in impact toughness was detected. In the case of sample A2 a hardness increase from 161 to 185 HV1 was observed (Fig.88), which is provided by the homogeneously distributed reinforcing secondary phase of the Al_2O_3 nano-particles. Although the Al_2O_3 nano-particles activation by oxygen plasma was aimed at changing the surface energy and facilitating more homogeneous particles distribution in the steel matrix, this was not the case, as proven by the microstructural analysis. Consequently, reinforcing the austenitic stainless steel AISI 316L with activated Al_2O_3 nano-particles resulted in an increased hardness (165 – 180 HV1), but in a considerable drop in the impact toughness. As shown in Fig. 88, in

the case of samples A3 and A4 the impact toughness was reduced by almost 20 %, even down to 135 J.

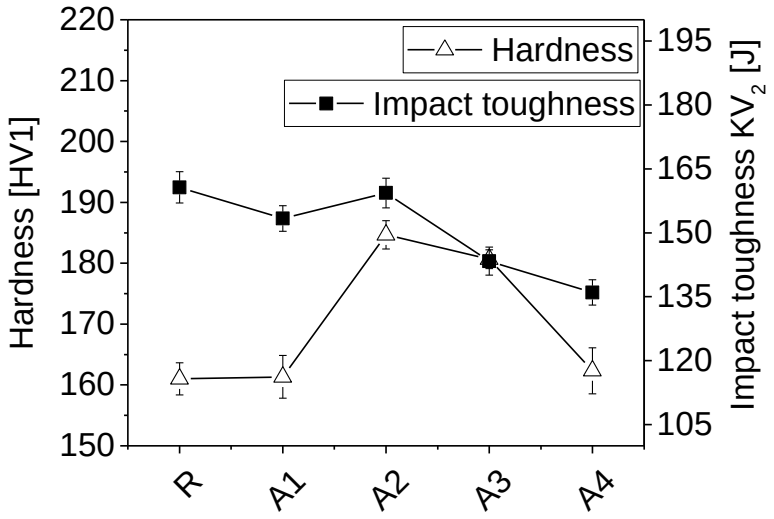

Figure 88: Effect of Al_2O_3 nano-particles on the hardness and impact toughness of AISI 316L stainless steel in the cast and hot-rolled condition.

The results for different oxide nano-particles (Al_2O_3 A2, Y_2O_3–B and TiO_2–C) mixed with the CaSi dispersion agent and added in a 0.5 wt. % concentration are shown in Fig. 89. In this case a hardness increase was observed for all the oxide nano-particles tested, with the largest hardness increase (192 HV1) being obtained by the addition of the more stable Y_2O_3 nano-particles (sample B), followed by the Al_2O_3 (sample A2; 185 HV1) and the finest TiO_2 nano-particles (sample C; ~175 HV1). In the agreement with the more homogeneous distribution and increased density of the finer nano-particles, the addition of Y_2O_3 and TiO_2 nano-particles mixed with the CaSi dispersion agent also resulted in an improved impact toughness, being increased from about 160 J to 167 J, as shown in Fig. 89.

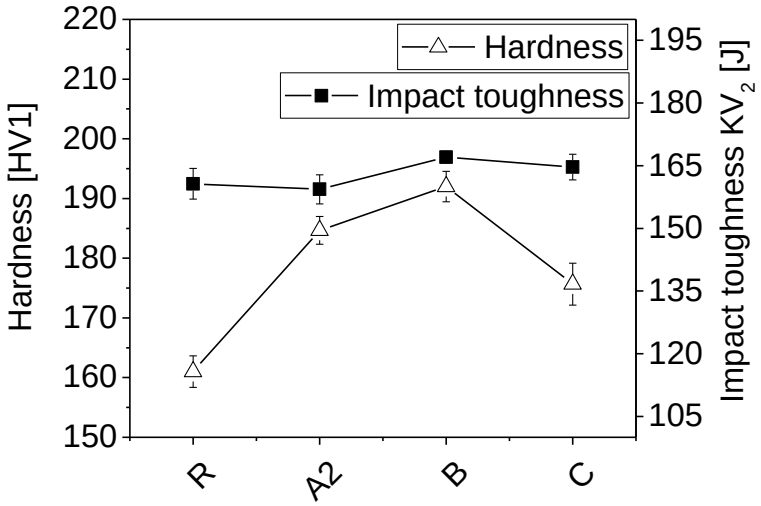

Figure 89: Effect of oxide nano-particles on the hardness and impact toughness of reinforced AISI 316L stainless steel in the cast and hot-rolled condition.

In the case of Ti-based nano-particles added to the AISI 316L stainless steel, the highest hardness was obtained for the most stable TiB_2 nano-particles with a high number density (sample E), showing the highest hardness among all the investigated nano-particles of almost 200 HV1 (improvement of more than 20 %). The hardness increase of the TiB_2 nano-particles-reinforced AISI 316L stainless steel is followed by the TiC nano-particles. However, in the case of the TiC nano-particles a hardness increase of ~175 HV1 is not the result of direct nano-particles integration into the metal matrix, but caused by the TiC dissolution and the formation of TiN precipitates. However, in both cases a high number density of reinforcing particles, although being quite uniformly distributed, led to a drop in the impact toughness, as shown in Fig. 90. In the case of the added TiC nano-particles the impact toughness was reduced to about 150 J and for the TiB_2 nano-particles even below 135 J.

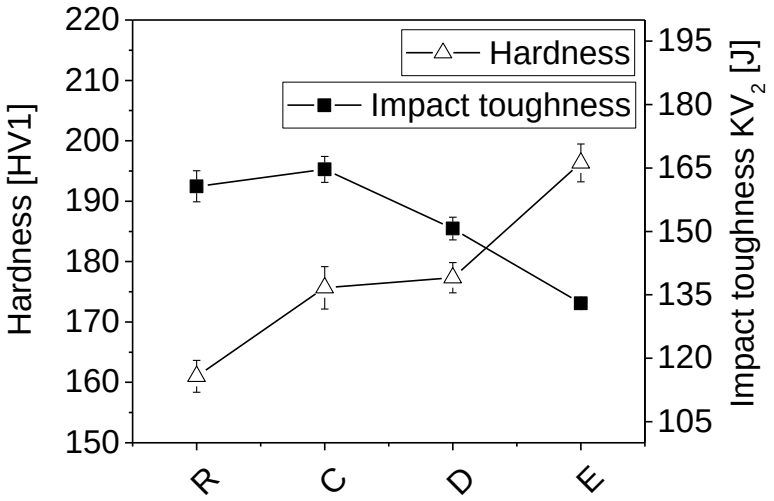

Figure 90: Effect of Ti-based nano-particles on the hardness and impact toughness of AISI 316L stainless steel in the cast and hot-rolled condition.

6.2.3.2 Tensile-test results

The yield and ultimate tensile strength results for the reference austenitic stainless steel AISI 316L and the ones reinforced with different nano-particles are summarized in Figs. 91 to 93.

In the case of the reference cast and hot-rolled austenitic stainless steel AISI 316L (sample R) a yield strength of 387 MPa, an ultimate tensile strength of 593 MPa and an elongation at fracture of 43 % were obtained. By adding 0.5 wt. % of Al_2O_3 nano-particles with a nominal size of 50 nm (sample A1) no major changes in the tensile properties were detected. A yield strength of 390 MPa, an ultimate tensile strength of 598 MPa and an elongation at fracture of 42 % were obtained for sample A1. In the case of sample A2 where Al_2O_3 nano-particles were mixed with CaSi dispersion agent, which promotes more homogeneous distribution of nano-particles, a slight increase in the yield strength, but a drop in the ultimate tensile strength and elongation were detected. In this case, the yield strength increased from 387 MPa to 396 MPa, while the ultimate tensile strength dropped from 593 MPa to 586 MPa (Fig. 91). Reinforcing the austenitic stainless steel AISI 316L with activated Al_2O_3 nano-particles (sample A3) resulted in a slight increase in the yield strength to 397 MPa, without a loss in the ultimate tensile strength (587 MPa), but some impairment of the elastic properties (A = 37 %). Finally, by combining Al_2O_3 nano-particles activation and the addition of the CaSi dispersion agent (sample A4) the yield strength

dropped to 383 MPa, while the ultimate tensile strength increased to 600 MPa and elongation at fracture to 40 %.

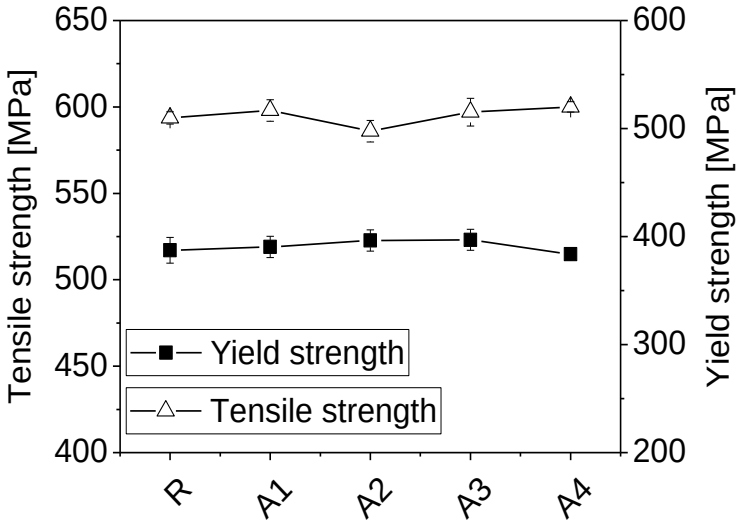

Figure 91: Effect of Al_2O_3 nano-particles on the yield and ultimate tensile strength of AISI 316L stainless steel in the cast and hot-rolled condition.

The results for different oxide nano-particles (Al_2O_3 – A2, Y_2O_3 – B and TiO_2 – C) mixed with the CaSi dispersion agent and added in a 0.5 wt. % concentration are shown in Fig. 92. In this case the yield strength increase obtained by the addition of the Al_2O_3 nano-particles (sample A2; 396 MPa) was followed by the TiO_2 nano-particles (sample C; 393 MPa), while the addition of Y_2O_3 nano-particles (sample B) resulted in a considerable drop in the yield strength (369 MPa). In terms of the ultimate tensile strength all the oxide nano-particles-reinforced samples show reduced values. For the TiO_2 nano-particles (sample C) the ultimate tensile strength dropped to 588 MPa and for the Y_2O_3 nano-particles (sample B) even down to 579 MPa. The best combination of high strength and good elastic properties was shown by the stainless steel reinforced with TiO_2 nano particles (sample C), combining a high yield and ultimate tensile strength and a high elongation of about 45 %. On the other hand, the addition of Y_2O_3 nano-particles (sample B) results in a considerable drop in the strength, as well as a drop in the elastic properties (A = 41 %).

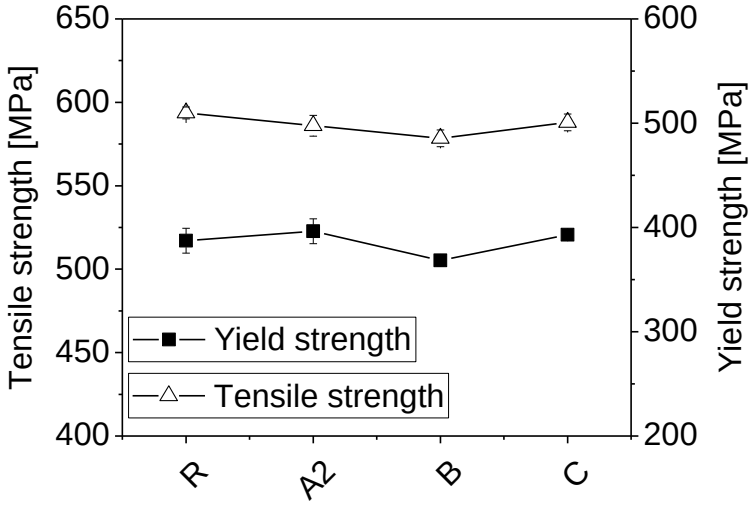

Figure 92: Effect of oxide nano-particles on the yield and ultimate tensile strength of the reinforced AISI 316L stainless steel in the cast and hot-rolled condition.

In the case of Ti-based nano-particles (TiO_2 – C, TiC – D and TiB_2 – E) added to the AISI 316L stainless steel an increase in the yield strength was obtained for all the investigated samples (Fig. 93). The highest yield strength of 426 MPa and ultimate tensile strength of 606 MPa were obtained for the TiC nano-particles, with an elongation at fracture of 41 %. The yield strength increase of the TiC nano-particles-reinforced AISI 316L stainless steel is followed by the TiB_2 nano-particles (sample E), being in the range of 415 MPa, with a more or less unaltered ultimate tensile strength (591 MPa) and elongation (43 %). As already mentioned, the TiO_2 nano-particles (sample C) provided a minor improvement in the yield strength (393 MPa) and elongation (44 %), compensated for by a slight drop in the ultimate tensile strength (588 MPa).

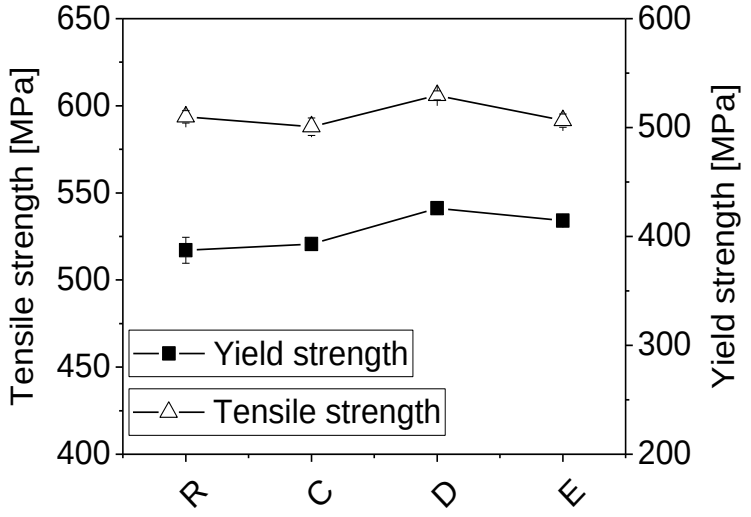

Figure 93: Effect of Ti-based nano-particles on the yield and ultimate tensile strength of AISI 316L stainless steel in the cast and hot-rolled condition.

6.2.4 Influence of added particle on the fatigue resistance and high-temperature creep resistance

This chapter addresses the influence of different nano-particles added in a 0.5 wt. % concentration using the ferritic steel tube insertion method on the fatigue and high-temperature creep resistance of the stainless steel. All the properties were determined for the cast and hot-rolled condition and compared to the reference AISI 316L steel in the same cast and hot-rolled condition.

6.2.4.1 Fatigue resistance

The fatigue resistance of the nano-particles-reinforced AISI 316L stainless steel evaluated in terms of the number of cycles till failure, obtained at three different bending stress levels (250 MPa, 300 MPa, 350 MPa), is shown in Figs. 94-96. Fig. 94 shows the Al_2O_3 nano-particles mixed with or without the CaSi dispersion agent and being activated by oxygen plasma or not. The effect of different oxide particles (Al_2O_3, Y_2O_3 and TiO_2) on the fatigue resistance is shown in Fig. 95, and the effect of Ti-based nano-particles (TiO_2, TiC and TiB_2) in Fig. 96.

In the case of the reference cast and hot-rolled AISI 316L austenitic stainless steel (sample R) failure took place after about 85,000, 160,000 and 580,000 loading cycles when loaded to a stress level of 350, 300 and 250 MPa, respectively. The addition and reinforcing of AISI 316L stainless steel with Al_2O_3 nano-particles led to an improved fatigue resistance (Fig. 94) with the number of loading cycles till failure being increased to 100,000–130,000 cycles at a high stress level (350 MPa), to 250,000 300,000 loading cycles at a middle stress level (300 MPa) and to about 1,000,000 loading cycles at a low stress level (250 MPa). No obvious difference could be observed between the activated and non-activated Al_2O_3 nano-particles, while the addition of the dispersion agent, in general, gave better results (sample A2 and A4), as shown in Fig. 94.

The results of the fatigue bending test for samples reinforced with different oxide nano-particles (samples A2, B, C) are shown in Fig. 95. In terms of fatigue resistance the Al_2O_3 (sample A2) and TiO_2 nano-particles (Sample C) provide a similar level of improvement as compared to the reference non-modified AISI 316L austenitic stainless steel. On the other hand, the Y_2O_3 nano-particles (sample B), which were found to lead to the formation of more complex particles in the metal matrix, resulted in a slightly lower fatigue resistance, especially when it comes to a high loading stress (350 MPa), as shown in Fig. 95.

The most noticeable increase in the fatigue properties, as compared to the reference stainless steel, was found for the titanium-based nano-particles-reinforced austenitic stainless steel (samples C, D, E), with the highest density of very fine particles, as shown in Fig. 96. In this case all three nano-particle types (sample C - TiO_2, sample D - TiC and sample E - TiB_2) show a similar level of improvement, with the number of bending cycles till failure being increased to over 1,000,000 cycles at 250 MPa, to about 300,000 at 300 MPa and to about 140,000 at 350 MPa (Fig. 96).

Fine stable nano-particles and inclusions in the metal matrix create obstacles for dislocation sliding and climbing movements, thus resulting in improved fatigue properties. However, if non-homogeneously distributed and agglomerated into clusters they may also act as a defect in the matrix [32]. In the current case the fatigue properties of the cast and hot-rolled stainless steel were improved through the reinforcement with nano-particles added in 0.5 wt. %, regardless of the type of nano-particles used. Furthermore, a homogeneous distribution of the nano-particles obtained by mixing the nano-particles with the CaSi dispersion agent provided superior results.

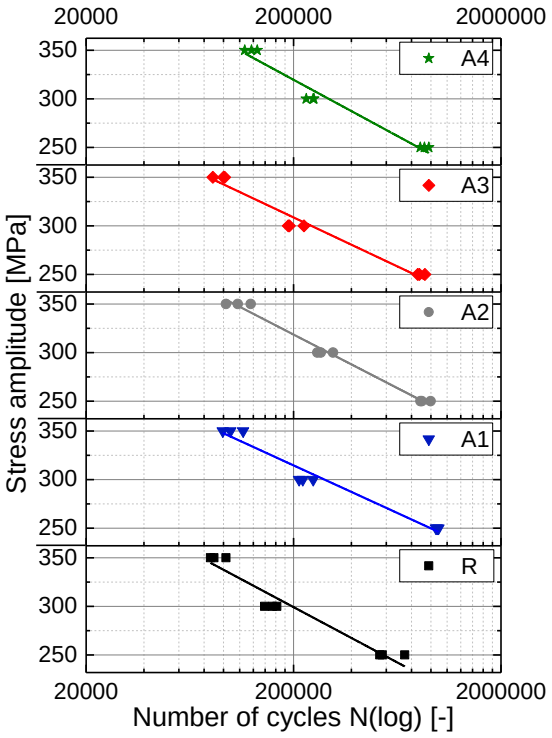

Figure 94: Effect of Al_2O_3 nano-particles on the bending-fatigue resistance of reinforced AISI 316L stainless steel in the cast and hot-rolled condition.

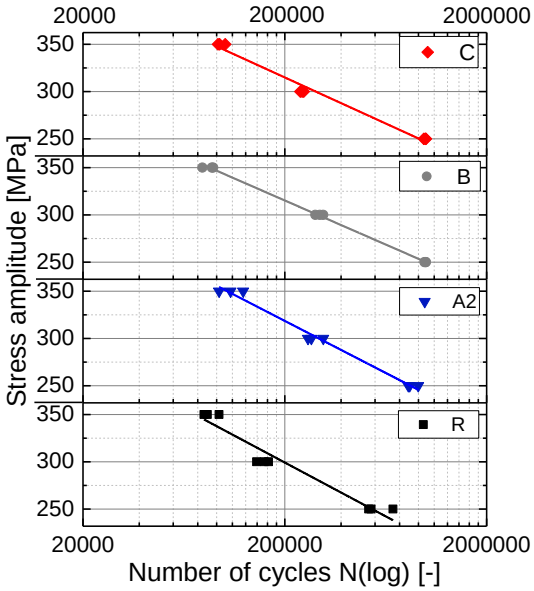

Figure 95: Effect of oxide nano-particles on the bending-fatigue resistance of reinforced AISI 316L stainless steel in the cast and hot-rolled condition.

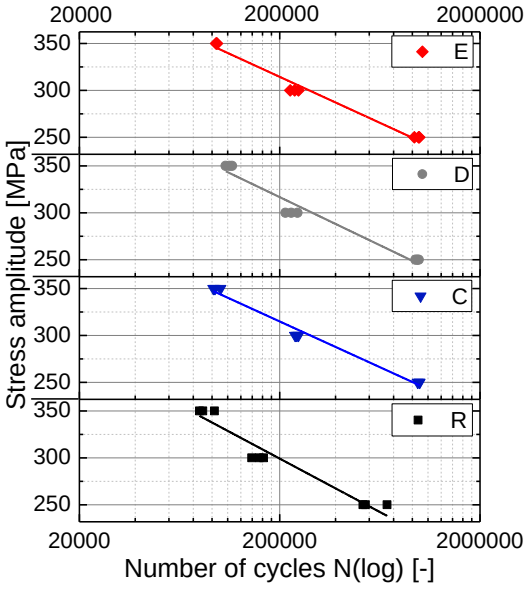

Figure 96: Effect of Ti-based nano-particles on the bending-fatigue resistance of reinforced AISI 316L stainless steel in the cast and hot-rolled condition.

6.2.4.2 High-temperature creep resistance

The high-temperature creep resistance of nano-particle-reinforced AISI 316L stainless steel was evaluated in terms of the microstructure modification and the minimum (steady-state) creep rate $d\varepsilon/dt$, obtained at a stress level of 300 MPa, and an elevated temperature of 650°C.

To analyze the microstructure modification in detail, especially to show the morphology and size of the different nano-particles after the creep test, the etched samples of AISI 316L

austenitic stainless steel reinforced with nano-particles were examined by SEM and EDS analysis at magnifications of 500x and 3000x. Energy-dispersive X-ray spectroscopy was employed to confirm the type of reinforced nano-particles for a particle size larger than 500 nm. Fig. 97 represents the microstructure of the reference AISI 316L austenitic stainless steel after a creep test without the addition of any nano-particles. In the deformed microstructure, we observed the precipitated σ phase. The σ phase is formed with the phase transformation from δ-ferrite to σ phase, occurring in a high Cr-concentration region of δ-ferrite and is formed directly from the δ-ferrite particles [81]. It has a detrimental effect on the properties of stainless steel (decrease of toughness and elongation, formation of brittle region, reduction of corrosive resistance). The σ phase is a tetragonal crystal structure that is rich in chromium, molybdenum and nickel, with its precipitation temperature being in the range 600 to 1000 °C [81]. In our case, the creep tests' temperature was within this region. Besides the temperature, plastic deformation has a considerable influence on the precipitation of the σ phase. The σ phase is formed on grain boundaries, especially at triple points, on incoherent boundaries of twins and next to non-metallic inclusions. To further confirm the precipitation of the σ phase after creep testing, measurements of the δ-ferrite using the Feritoscope MP30 (according to ISO 9001), performed before and after creep tests, was carried out

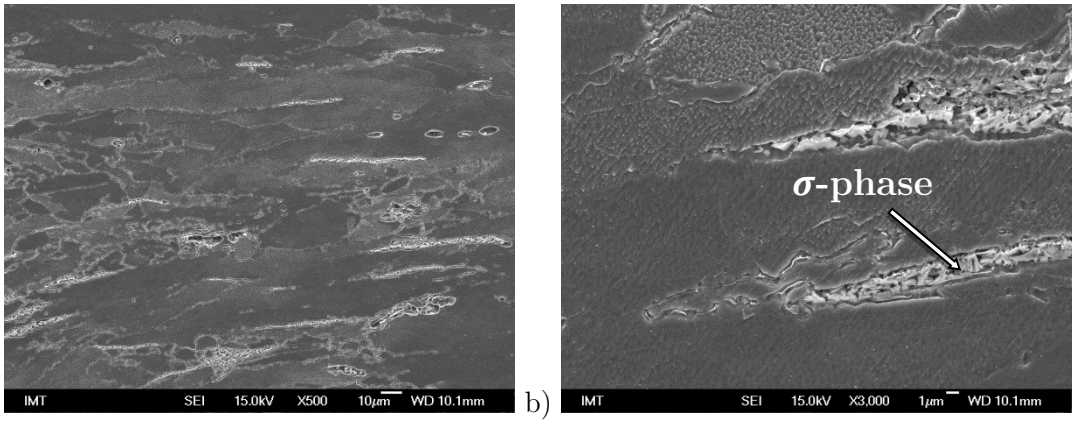

Figure 97: Microstructure of AISI 316L austenitic stainless steel after creep test at a) 500x magnification and b) 3000x magnification for sample R (reference material) without the addition of nano-particles.

As can be clearly seen from Figs. 98-105 and was confirmed by EDS analysis, Al_2O_3 nano-particles larger than 500 nm embedded in the steel matrix did not show any evident intermetallic reaction during or after the creep test at an elevated temperature of 650°C. In Fig. 98, showing the EDS analysis of specimen A1, spectrum 1 represents the Al_2O_3 nano-particle, spectrum 2 the σ phase rich in chromium, molybdenum and nickel and spectrum 3 the matrix. Similar analyses were made and observations recorded for the samples A2, A3 and A4 with Al_2O_3 nano-particles being surface activated and/or mixed with the CaSi dispersion agent before being introduced into the melt. Therefore, the same conclusions without any evident intermetallic reactions of Al_2O_3 nano-particles during high-temperature creep tests can be drawn for all the Al_2O_3 reinforced samples.

a) 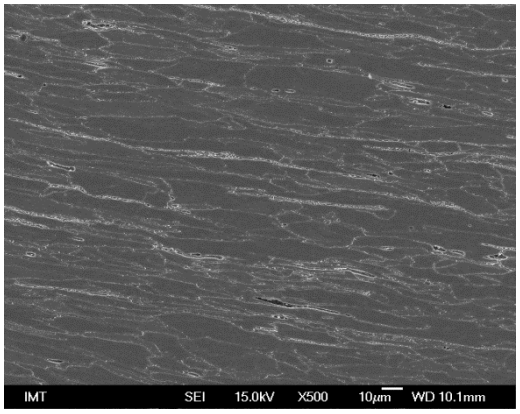

b) 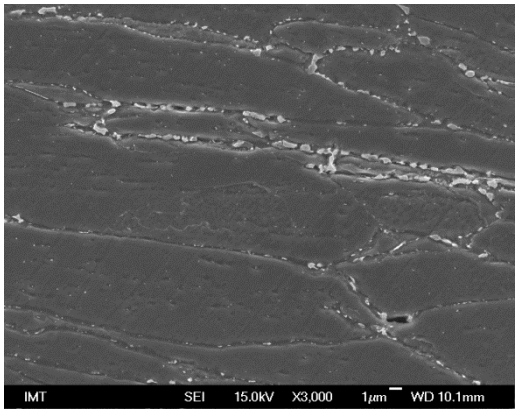

Figure 98: Microstructure of AISI 316L austenitic stainless steel reinforced with 0.5 wt. % of Al_2O_3 nano-particles (sample A1) after creep test at a) 500x magnification and b) 3000x magnification.

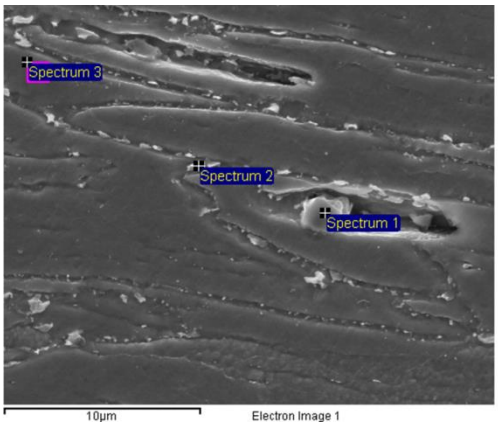

Spectrum / Element	1 [wt%]	2 [wt%]	3 [wt%]
O	31.21	0.00	0.00
Al	54.30	0.00	0.00
Ti	0.35	0.00	0.00
Cr	4.73	25.06	16.69
Mn	3.09	1.46	1.71
Fe	6.22	59.36	68.69
Ni	0.00	8.41	11.06
Mo	0.00	5.71	1.85

Figure 99: SEI image of incorporated Al_2O_3 particle larger than 500 nm after creep test at 5000x magnification for sample A1 and corresponding EDS analysis in weight %.

a) 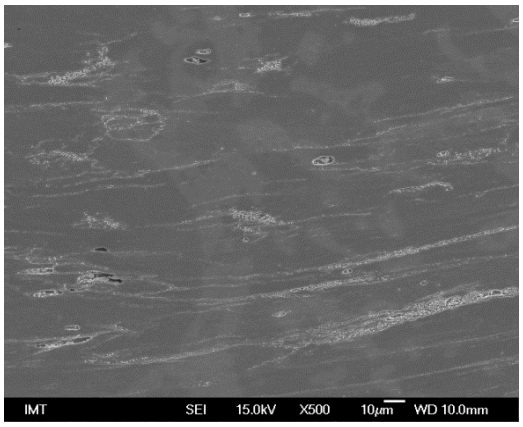

b) 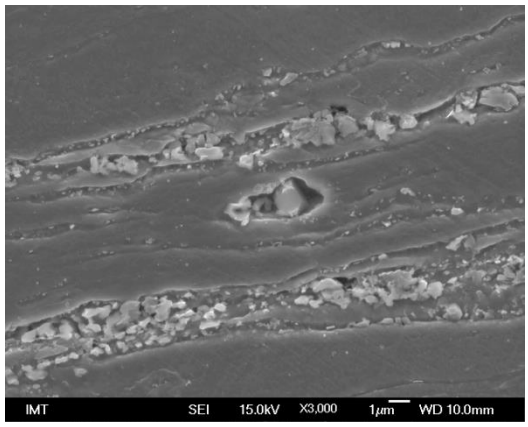

Figure 100: Microstructure of reinforced AISI 316L austenitic stainless steel after creep test at a) 500x magnification and b) 3000x magnification for sample A2 with the addition of 0.5 wt. % Al_2O_3 nano-particles mixed with the dispersion medium CaSi in 1:1 mass ratio.

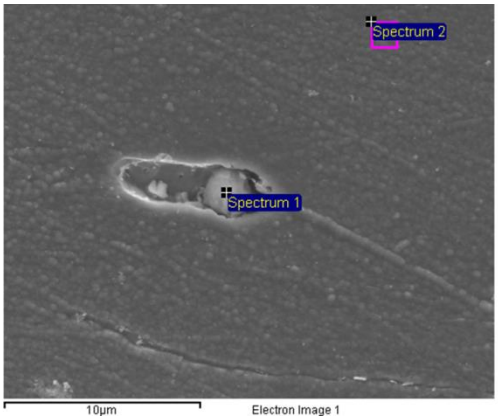

Element \ Spectrum	1 [wt%]	2 [wt%]
O	46.40	0.00
Al	33.45	0.00
Ti	0.91	0.54
Cr	1.30	16.97
Mn	3.84	1.86
Fe	12.60	68.17
Ni	0.71	10.39
Mo	0.80	2.07

Figure 101: SEI image of incorporated Al_2O_3 particle larger than 500 nm after creep test at 5000x magnification for sample A2 and corresponding EDS analysis in weight %.

a) 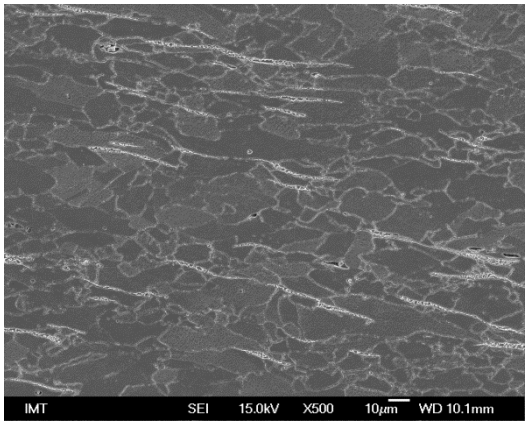

b) 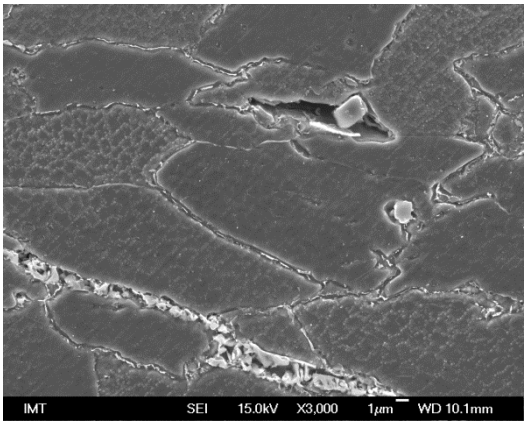

Figure 102: Microstructure of reinforced AISI 316L austenitic stainless steel after creep test at a) 500x magnification and b) 3000x magnification for sample A3 with the addition of 0.5 wt. % of activated Al_2O_3 nano-particles.

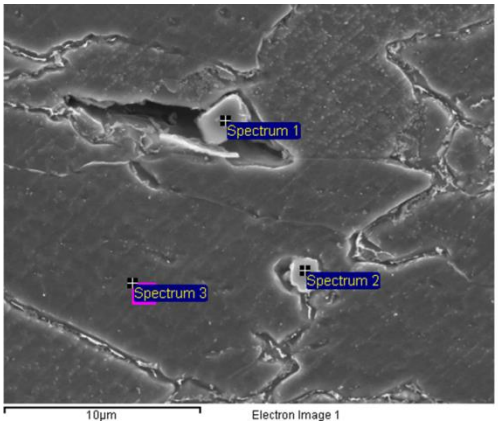

Element \ Spectrum	1 [wt%]	2 [wt%]	3 [wt%]
O	35.58	32.27	0.00
Al	48.18	43.54	0.00
Ti	0.84	0.74	0.46
Cr	6.55	5.82	17.14
Mn	3.37	6.03	1.50
Fe	4.09	10.38	68.62
Ni	1.40	1.22	9.79
Mo	0.00	0.00	2.48

Figure 103: SEI image of incorporated Al_2O_3 particle larger than 500 nm after creep test at 5000x magnification for sample A3 and corresponding EDS analysis in weight %.

a) 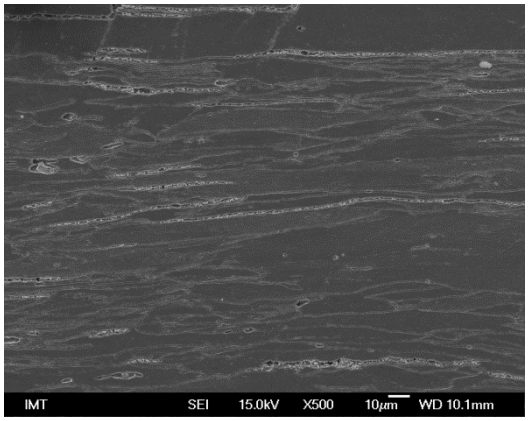

b) 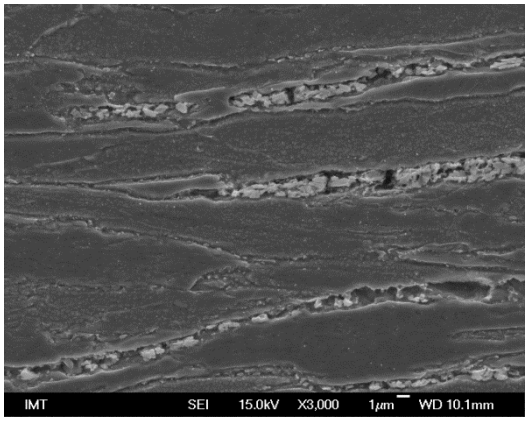

Figure 104: Microstructure of reinforced AISI 316L austenitic stainless steel after creep test at a) 500x magnification and b) 3000x magnification for sample A4 with the addition of 0.5 wt. % of activated Al_2O_3 nano-particles mixed with the dispersion medium CaSi in 1:1 mass ratio.

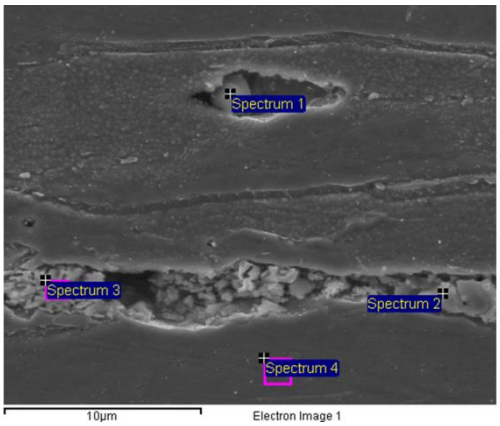

Spectrum / Element	1 [wt%]	2 [wt%]	3 [wt%]	4 [wt%]
O	49.43	0.00	0.00	0.00
Al	38.73	0.00	0.00	0.00
Ti	1.14	0.85	0.66	0.58
Cr	2.97	38.98	38.48	16.83
Mn	0.00	0.96	1.70	1.45
Fe	6.39	41.64	42.15	66.96
Ni	0.62	2.83	3.97	11.74
Mo	0.72	14.74	13.04	2.43

Figure 105: SEI image of incorporated Al_2O_3 particle larger than 500 nm after creep test at 5000x magnification for sample A4 and the corresponding EDS analysis in weight %.

In the case of sample B (added Y_2O_3 nano-particles, Fig. 106) nano-particles introduced into the steel matrix were unaffected by the elevated temperature and plastic deformation taking place during the creep test. Energy-dispersive X-ray spectroscopy (EDS) analysis shown in Fig. 107 confirms that the particles larger than 500 nm are of the Y_2O_3 type (spectrum 1). In spectrum 1 elements from the background (steel matrix; spectrum 2) can also be seen, such as Cr, Mn, Ni and Fe, which is due to the analyzing volume exceeding the size of the analyzed particle.

a) 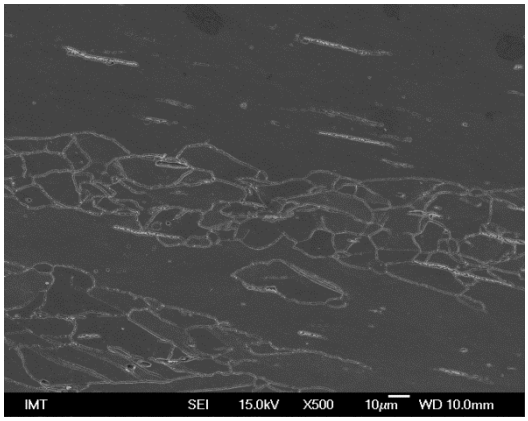

b) 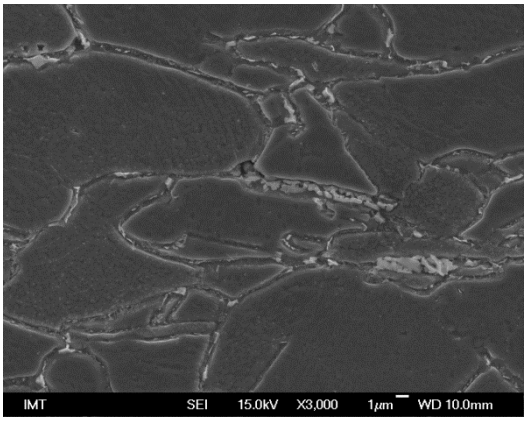

Figure 106: Microstructure of AISI 316L austenitic stainless steel reinforced with 0.5 wt. % of Y_2O_3 nano-particles (sample B) after creep test at a) 500x magnification and b) 3000x magnification.

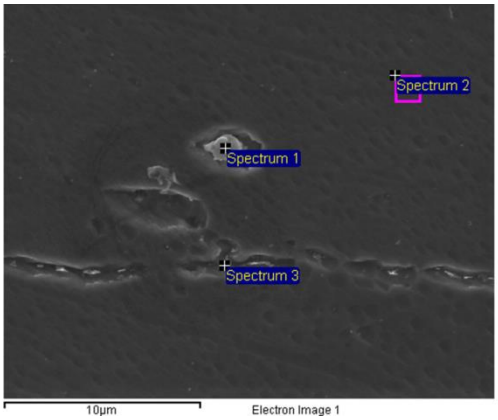

Spectrum / Element	1 [wt%]	2 [wt%]	3 [wt%]
O	45.43	1.16	2.51
Y	38.01	0.00	0.39
Ti	0.84	0.52	0.66
Cr	3.88	17.65	17.86
Mn	0.86	2.23	1.37
Fe	9.37	66.03	62.86
Ni	1.53	10.38	8.86
Mo	0.90	2.04	5.49

Figure 107: SEI image of incorporated Y_2O_3 particle larger than 500 nm after creep test at 5000x magnification for sample B and corresponding EDS analysis in weight %.

The same observations as for the Al_2O_3 and Y_2O_3 nano-particles can also be made for the addition of TiO_2 nano-particles mixed with the CaSi dispersion medium, as shown in Figs. 108 and 109. It was confirmed that TiO_2 (spectrum 1) nano-particles do not show any evident intermetallic reaction with the matrix after the high-temperature creep test.

a) 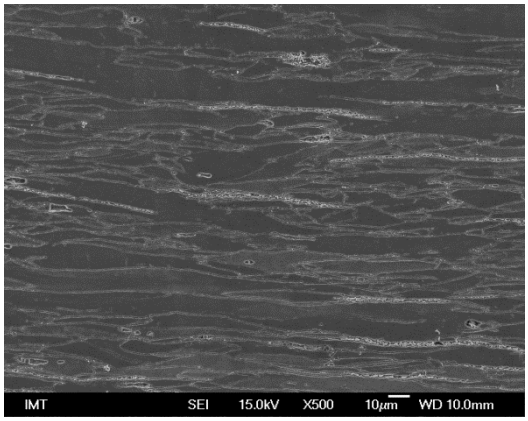

b) 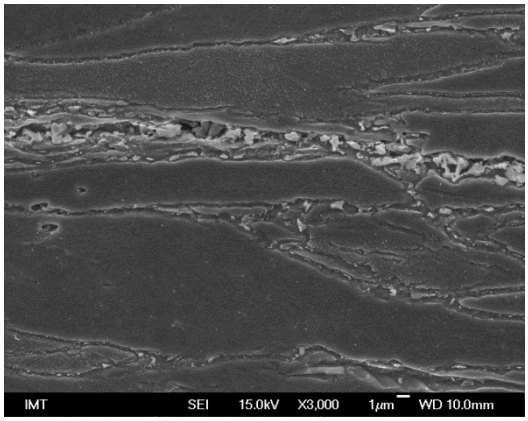

Figure 108: Microstructure of AISI 316L austenitic stainless steel reinforced with 0.5 wt. % of TiO_2 (sample C) after creep test at a) 500x magnification and b) 3000x magnification.

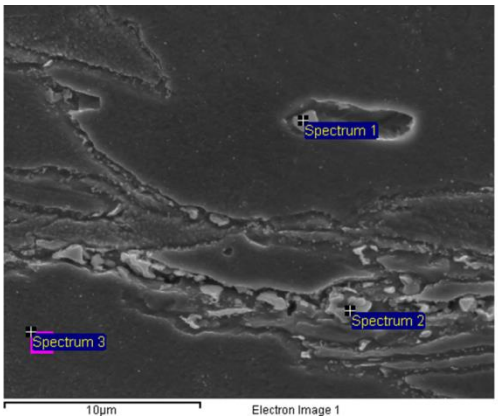

Spectrum / Element	1 [wt%]	2 [wt%]	3 [wt%]
O	18.87	0.00	0.00
Si	0.31	0.00	0.49
Ti	10.40	0.00	0.00
Cr	16.17	54.86	17.44
Mn	14.96	1.62	1.62
Fe	30.64	31.78	67.57
Ni	3.99	2.62	10.55
Mo	4.67	9.12	2.33

Figure 109: SEI image of incorporated TiO_2 particle larger than 500 nm after creep test at 5000x magnification for sample C and the corresponding EDS analysis in weight %.

Figs. 110-113 show an SEM analysis for the TiC- and TiB_2-nano-particles-reinforced AISI 316L stainless steel. The EDS analysis performed before creep testing (Chapter 6.2.1.2) shows that the particles present in the microstructure and larger than 500 nm mostly consist of O and Ti. This was also observed after the creep test, with the SEM/EDS analyses being shown in Figs. 111 and 113. The analysis confirmed that larger particles ($\geq$ 500 nm) present in the matrix contain Ti and O and do not show any noticeable changes after the creep test. However, as shown in Fig. 112, large bands/clusters of precipitated σ phase were observed for sample E, reinforced with the TiB_2 nano-particles.

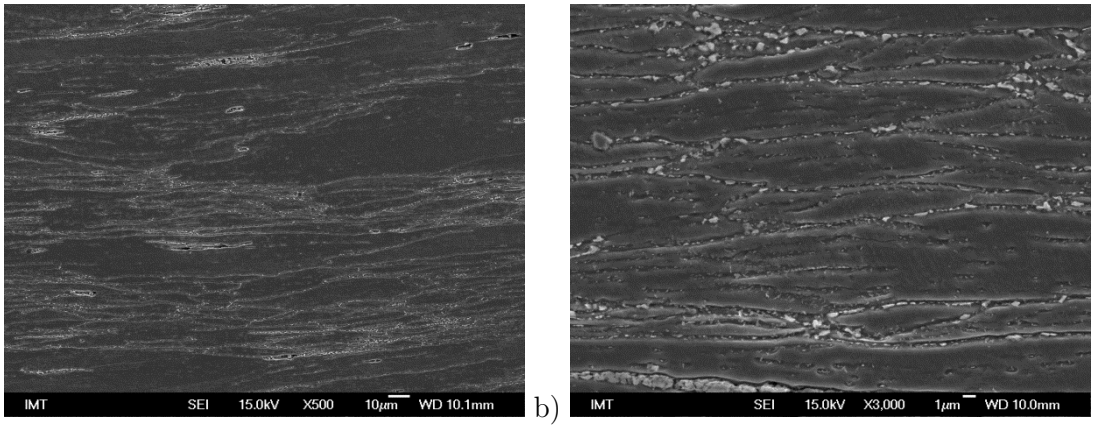

Figure 110: Microstructure of AISI 316L austenitic stainless steel reinforced with 0.5 wt. % of TiC nano-particles (sample D) after creep test at a) 500x magnification and b) 3000x magnification.

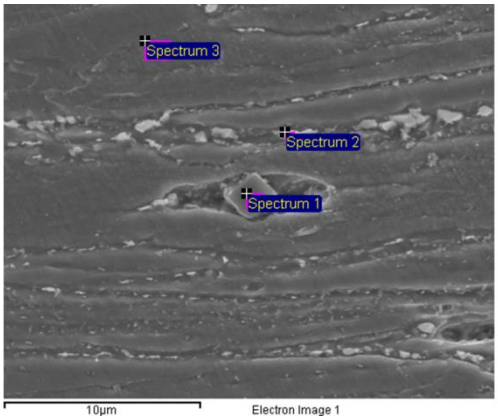

Element \ Spectrum	1 [wt%]	2 [wt%]	3 [wt%]
O	36.17	0.00	0.00
Al	0.62	0.00	0.00
Ti	44.55	0.00	0.00
Cr	4.72	45.56	16.61
Mn	7.09	1.27	1.61
Fe	6.84	39.05	68.36
Ni	0.00	3.70	11.62
Mo	0.00	10.43	1.79

Figure 111: SEI image of incorporated particle larger than 500 nm after creep test at 5000x magnification for sample D and corresponding EDS analysis in weight %.

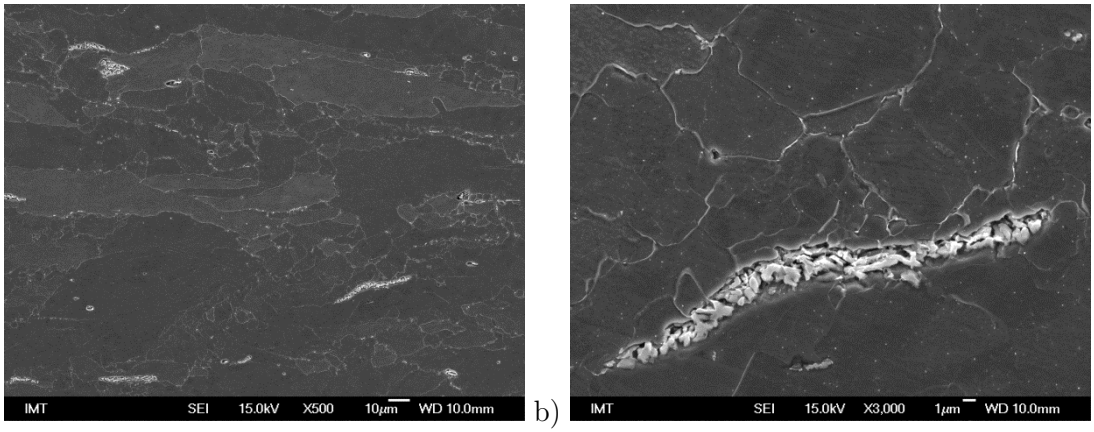

Figure 112: Microstructure of AISI 316L austenitic stainless steel reinforced with 0.5 wt. % of TiB_2 nano-particles (sample E) after creep test at a) 500x magnification and b) 3000x magnification.

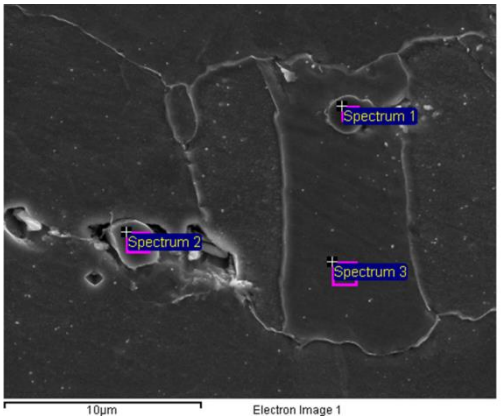

Element \ Spectrum	1 [wt%]	2 [wt%]	3 [wt%]
O	33.44	34.23	0.00
Al	0.64	1.28	0.00
Ti	43.14	47.62	0.33
Cr	5.75	5.71	16.99
Mn	6.33	5.96	1.85
Fe	9.40	5.20	68.27
Ni	1.31	0.00	9.75
Mo	0.00	0.00	2.81

Figure 113: SEI image of incorporated TiB_2 particle larger than 500 nm after creep test at 5000x magnification for sample E and corresponding EDS analysis in weight %.

The high-temperature creep resistance of nano-particle-reinforced AISI 316L stainless steel evaluated in terms of the minimum (steady-state) creep rate $d\varepsilon/dt$ is shown in Figs. 114-116. Fig. 114 shows the Al_2O_3 nano-particles mixed with or without the CaSi dispersion agent and being activated by oxygen plasma or not. Effect of different oxide particles (Al_2O_3, Y_2O_3 and TiO_2) on the high-temperature creep resistance is shown in Fig. 115 and the effect of Ti-based nano-particles (TiO_2, TiC and TiB_2) in Fig. 116. In the case of the reference cast and hot-rolled AISI 316L austenitic stainless steel (sample R) the minimum creep rate $d\varepsilon/dt$ was 1.39 x 10^{-7} s^{-1} when exposed to a stress level of 300 MPa and an elevated temperature of 650°C. The addition and reinforcing of AISI 316L stainless steel with Al_2O_3 nano-particles led to a higher minimum creep rate $d\varepsilon/dt$ (Fig. 114), increasing it from 1.39 x 10^{-7} s^{-1} to 5.26 x 10^{-7} s^{-1}. However, the creep-rate difference between the reference material and the reinforced samples is not significant, with all the values being of the same order of magnitude. In addition, no significant difference was observed between samples A1, A2, A3 and A4, employing the CaSi dispersion agent and/or the nano-particles' surface activation. According to the literature, the creep resistance of the material containing high-stiffness reinforcements in the matrix should, in general, be better than the unreinforced alloy [82]. However, in the present case, the addition of Al_2O_3 nano-particles resulted in a reduced creep resistance compared to the reference (R) material. This might be due to the fact that the added nano-particles are increasing the number of nucleation sites for the formation of the σ phase [83]. The volume fraction of sigma phase will therefore increase in the material, thus having a detrimental effect on the high-temperature properties of the stainless steel. Sigma-phase precipitation is occurring via the transformation reaction from δ-ferrite to σ phase. In order to perform a quantitative analysis of the δ-ferrite to σ phase transformation the difference in the δ-ferrite before and after the creep test was also determined (Fig. 114b). All the reinforced samples show an increased δ-ferrite drop, which is consistent with the higher creep rate of those samples. The exception is sample A4, where more condensed areas of σ phase precipitation were observed, leading to a further deterioration in the creep resistance.

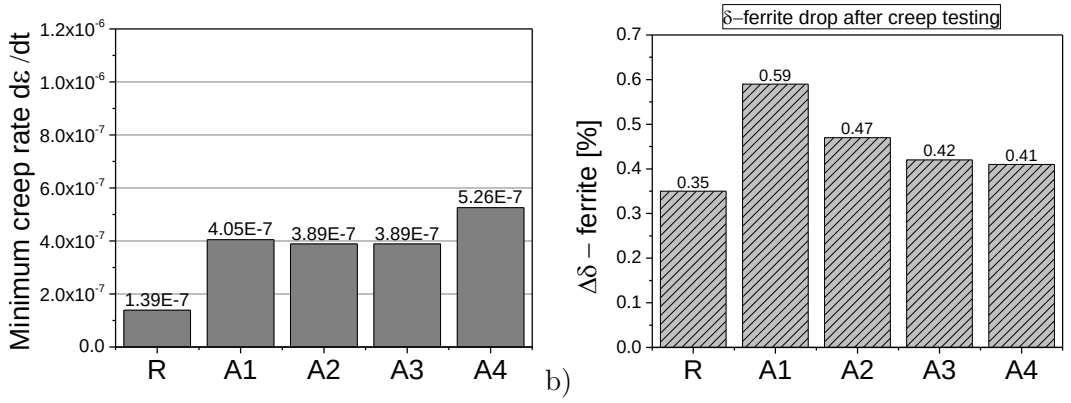

Figure 114: Effect of Al_2O_3 nano-particles, particles' surface activation and the presence of CaSi dispersion agent on the a) minimum (steady-state) creep rate and b) δ -ferrite drop after the creep test for reinforced AISI 316L stainless steel in the cast and hot-rolled condition.

When comparing the oxide nano-particles group (samples A2 - Al_2O_3, B -, C - TiO_2) the creep rate is again of the same order of magnitude, thus it is hard to talk about a significant difference between the reinforced and non-reinforced material. The creep rate is just slightly increased with the addition of oxide nano-particles, being the largest for sample C, reinforced with TiO_2 nano-particles (Fig.115), followed by Al_2O_3 (A2) and Y_2O_3 (B) nano-particles. A slight increase in the δ -ferrite drop was found for samples A2 and B when compared to the reference material, suggesting that more σ phase was formed. However, the lowest difference in the amount of δ -ferrite before and after the creep testing was found for the C sample showing the lowest creep resistance (Fig.115). Anyway, in this case the smallest value of δ - ferrite was also measured before the creep testing, with the microstructure analysis after the test showing condensed precipitation of the σ phase in the form of larger clusters and bands. Furthermore, when comparing the creep resistance of specimens A2 (Al_2O_3) and B (Y_2O_3), the latter had a greater density of large and more complex particles before the high-temperature testing, thus resulting in higher creep rate.

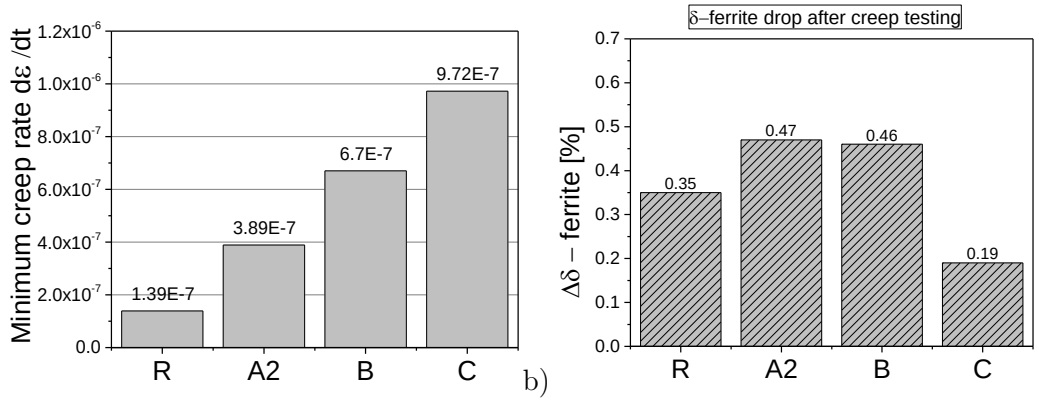

Figure 115: Effect of oxide nano-particles on the a) minimum (steady-state) creep rate and b) δ-ferrite drop after the creep test for reinforced AISI 316L stainless steel in the cast and hot-rolled condition.

The creep rate in the case of Ti-based nano-particles was of the same order of magnitude as observed for the oxide nano-particles-reinforced stainless steel (Fig. 116). However, in this case an improvement in the creep rate was observed for sample D (TiC reinforcement),

which also exhibits the smallest difference in the δ-ferrite change. The difference in the δ-ferrite for samples C and E is higher and very similar, but still lower than for the reference material, although displaying the highest creep rate. In this group the lowest destiny of the large and small particles is shown by sample D, also displaying the lowest creep rate. This indicates that the best creep resistance is achieved when the optimal density of large and small particles is reached in the matrix material.

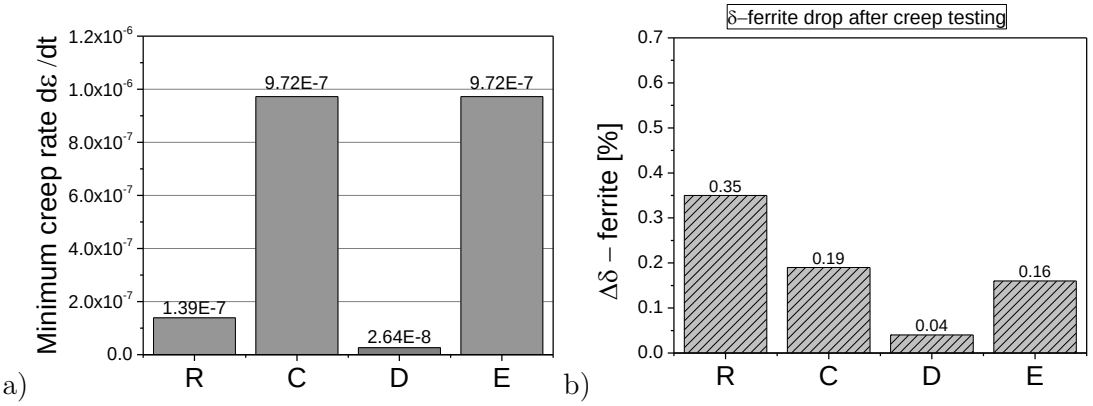

Figure 116: Effect of Ti-based nano-particles on the a) minimum (steady-state) creep rate and b) the δ-ferrite drop after the creep test for the reinforced AISI 316L stainless steel in the cast and hot-rolled condition.

6.2.5 Influence of added particles on the tribological properties

This chapter highlights the influence of the nano-particle type and the use of the dispersion agent on the wear and friction behavior of the cast and hot-rolled AISI 316L stainless steel reinforced with the addition of 0.5 wt. % of nano-particles. To fully examine the potential of the nano-particles reinforcement, stainless-steel samples were tested under three different contact conditions, i.e., low-load, high-sliding-speed, high-load, high-sliding-speed and high-load, low-sliding-speed conditions. In all three cases, the total sliding distance was 6 m and the testing was done under dry reciprocating sliding conditions.

6.2.5.1 Low-load, high-sliding-speed conditions

The variation in the wear rate and the hardness for the cast and hot-rolled AISI 316L austenitic stainless steel reinforced with different nano-particles, tested under low-load, high-sliding-speed conditions (1N, 20 mm/s) are shown in Figs. 117 and 118.

As shown in Fig. 117, the wear rate for the AISI 316L stainless steel decreases with the addition of Al_2O_3 nano-particles from $2.3 \cdot 10^5$ μm^3/Nm down to about $1.1 \cdot 10^5$ μm^3/Nm. It is evident that the addition of the Al_2O_3 particles is beneficial in terms of improving the wear resistance of the AISI 316L steel due to the increased hardness and better scratching resistance of the hard reinforcing Al_2O_3 ceramic particles phase. Furthermore, by obtaining a more homogeneous distribution of Al_2O_3 nano-particles, facilitated by mixing nano-particles with dispersive medium (samples A2 and A4), a further 25 % reduction in the wear rate was observed, reaching vales as low as $1.1 \cdot 10^5$ μm^3/Nm. On the other hand, the activation and surface properties-modification of the reinforcing Al_2O_3 nano-particles had no beneficial effect on the wear resistance of the AISI 316L stainless steel, as shown in Fig. 117.

In the case of the addition of different oxide nano-particles (samples A2, B, C; Fig. 118a) the most distinctive decrease in the wear rate was obtained in the case of the Y_2O_3

nano-particles being mixed with the CaSi (sample B) and added to the AISI 316L austenitic stainless steel. The wear rate decreased by more than 50 %, from $2.3 \cdot 10^5$ μm^3/Nm down to $8.9 \cdot 10^4$ μm^3/Nm. The wear-resistance improvement obtained with the addition of Y_2O_3 nano-particles, resulting in the formation of fine complex particles in the metal matrix and a large hardness increase, is followed by Al_2O_3 (sample A2) and the finest TiO_2 nano-particles (sample C), as shown in Fig. 118a.

The wear testing results for the AISI 316L stainless steel reinforced with Ti-based nano-particles are shown in Fig. 118b. Also, in the case of Ti-based nano-particles, the wear-rate reduction from $2.3 \cdot 10^5$ μm^3/Nm down to $1.2 \cdot 10^5$ μm^3/Nm was achieved for the cast and hot-rolled AISI 316L stainless steel. The most distinctive wear-rate reduction was obtained by the reinforcement with the most stable TiB_2 nano-particles (sample E), also providing the largest hardness increase. In line with the smaller hardness increase the wear-rate improvement is followed by the reinforcement with TiC (sample D) and TiO_2 (sample C) nano-particles, in all cases mixed with the CaSi dispersion agent.

Generally speaking, the wear rate of the cast and hot-rolled AISI 316L stainless steel was reduced in all cases when reinforced with the addition of nano-particles, regardless of the nano-particle type used. In the case of abrasive wear, being the main wear component in the current case (Fig. 117-118), the improvement can be ascribed to the hardness increase and the improved scratching resistance provided by the hard reinforcing phase.

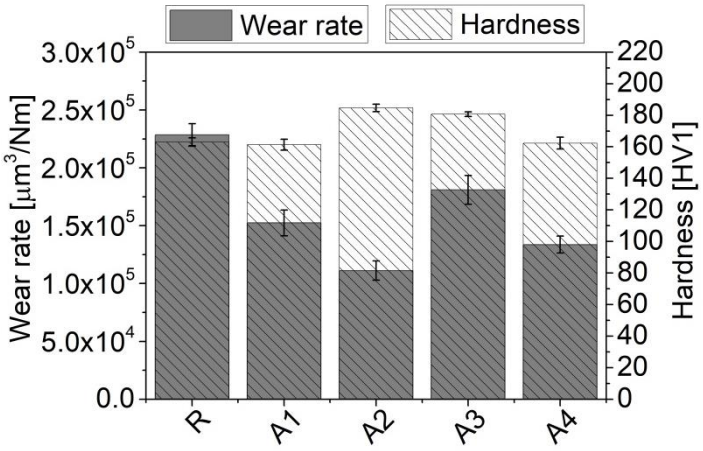

Figure 117: Wear rate and hardness values for AISI 316L stainless steel reinforced with Al_2O_3 nano-particles investigated under low-load, high-sliding-speed conditions.

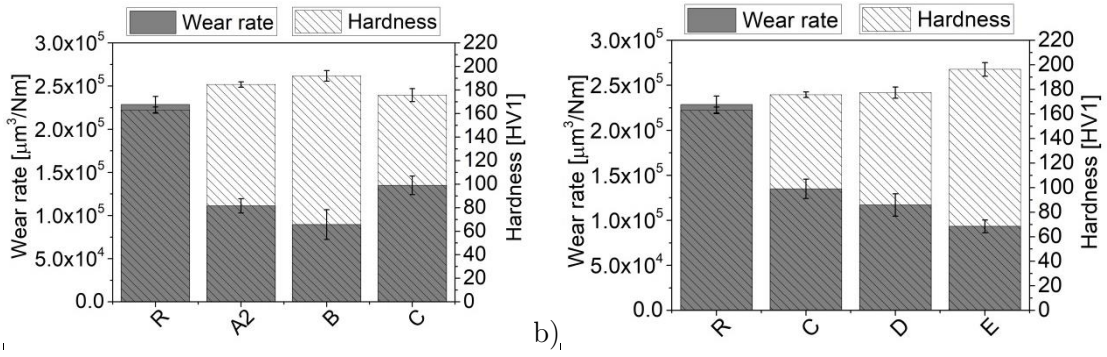

Figure 118: Wear rate and hardness values for AISI 316L stainless steel reinforced with (a) oxide nano-particles (A2-Al_2O_3, Y_2O_3-B, TiO_2-C) and (b) Ti-based nano-particles (TiO_2-C, TiC-D, TiB_2-E) investigated under low-load, high-sliding-speed conditions.

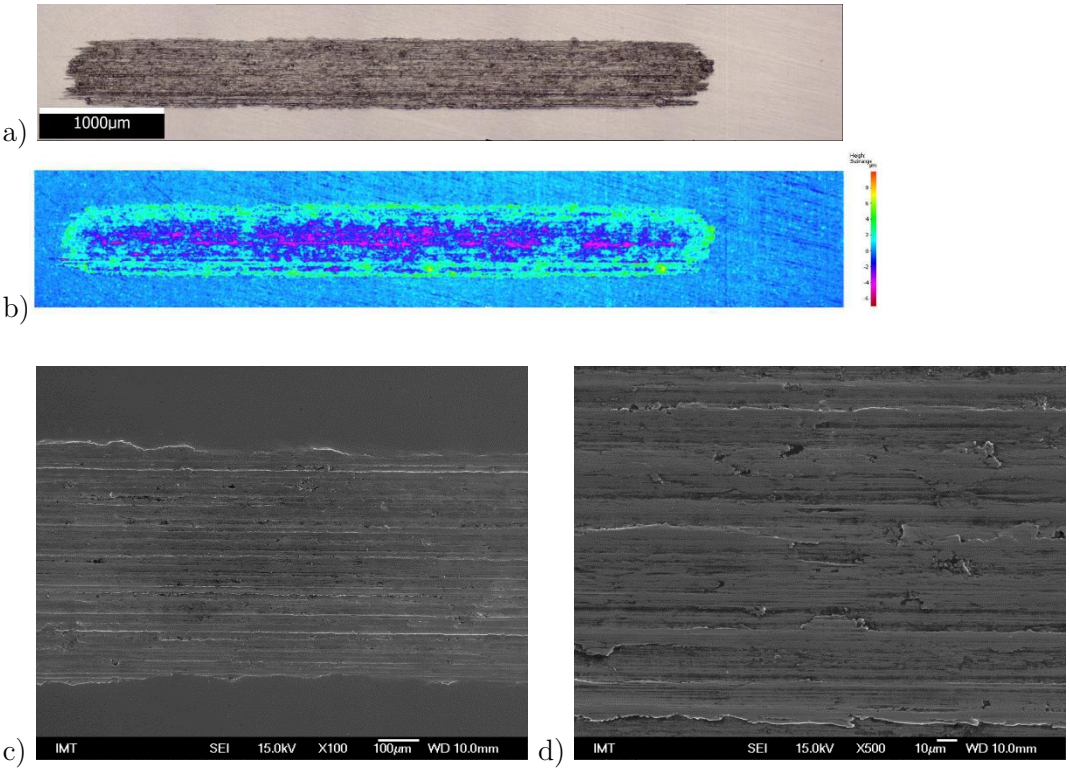

Figure 119: Worn surface of sample R (reference material) without the addition of nanoparticles; a) LM image, b) 3D surface profile, and SEI images at the magnification c) 100x and d) 500x.

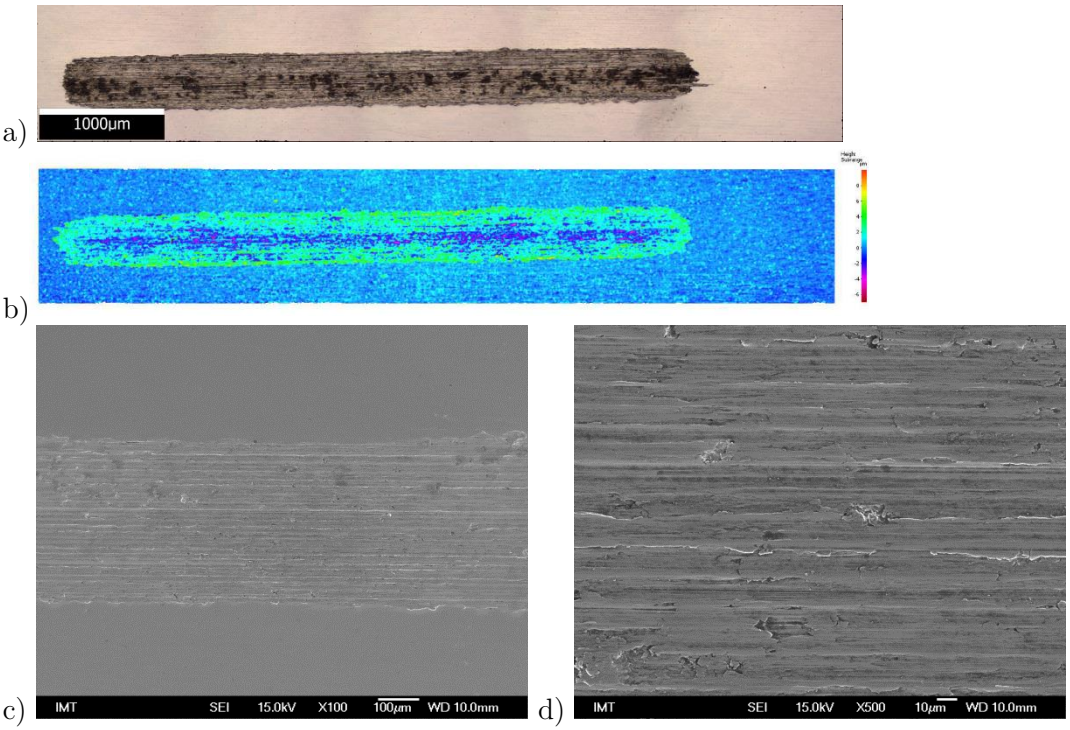

Figure 120: Worn surface of sample A2 with the addition of 0.5 wt. % of Al_2O_3 nanoparticles mixed with the dispersion medium CaSi in 1:1 mass ratio; a) LM image, b) 3D surface profile, and SEI images at the magnification c) 100x and d) 500x.

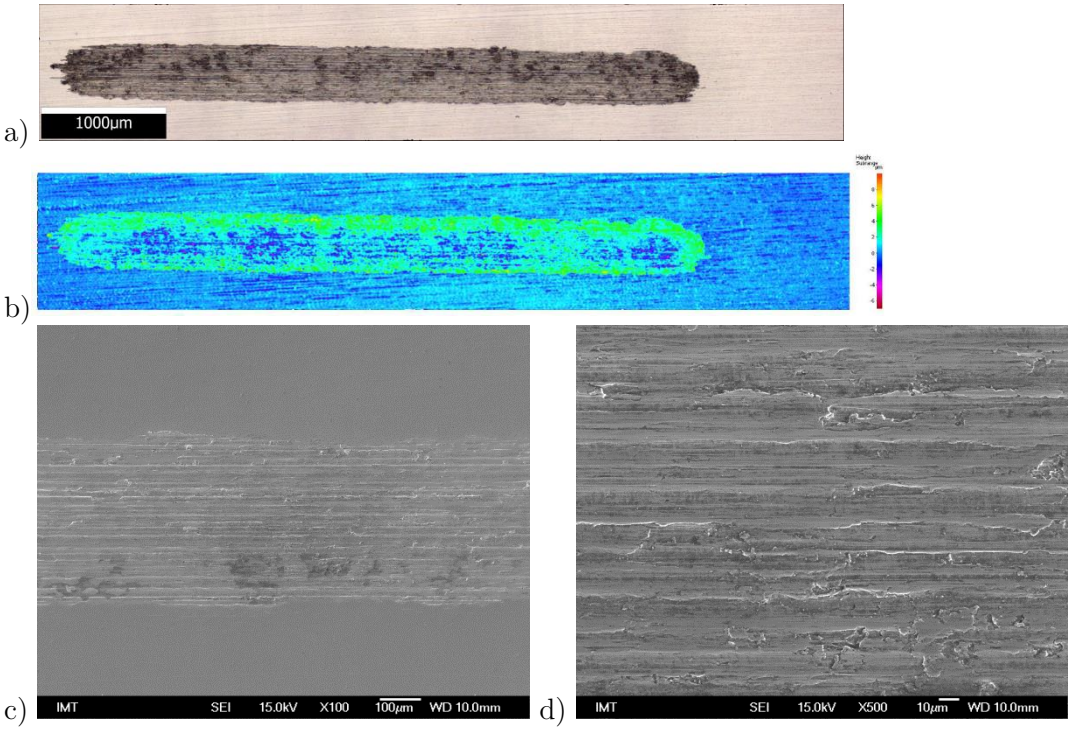

Figure 121: Worn surface of sample B with the addition of 0.5 wt. % of Y_2O_3 nano-particles mixed with the dispersion medium CaSi in 1:1 mass ratio; a) LM image, b) 3D surface profile, and SEI images at the magnification c) 100x and d) 500x.

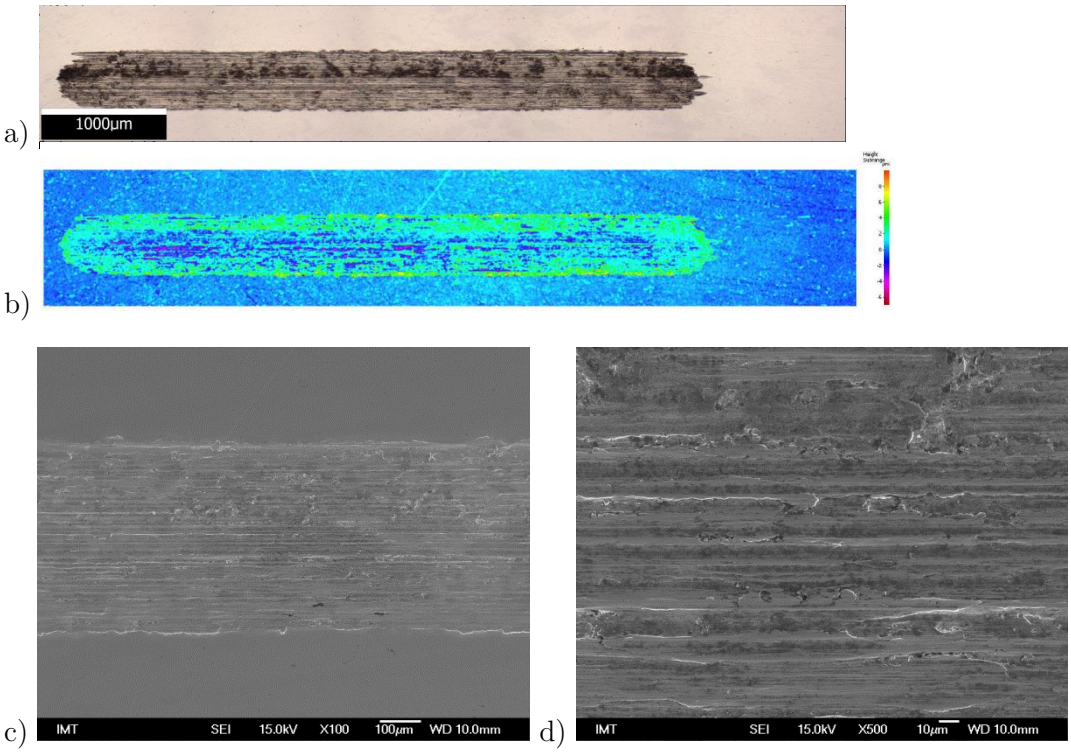

Figure 122: Worn surface of sample E with the addition of 0.5 wt. % of TiB_2 nano-particles mixed with the dispersion medium CaSi in 1:1 mass ratio; a) LM image, b) 3D surface profile, and SEI images at the magnification c) 100x and d) 500x.

Variation in the steady-state coefficient of friction for the reference AISI 316L austenitic stainless steel investigated under low-load, high-sliding-speed contact conditions is shown in Figs. 123 and 124. The average steady-state coefficient of friction for the reference cast and hot-rolled AISI 316L stainless steel under dry sliding is ~ 0.5. Also in the case of reinforcing AISI 316L stainless steel with nano-particles, the level of the coefficient of friction remained more or less the same (~0.5), regardless of the nano-particles type and the particles preparation method used. The only exception with an approx. 10 % higher average friction were the samples B and D, AISI 316L stainless steel reinforced with Y_2O_3 and TiC nano-particles, respectively, as shown in Fig. 124.

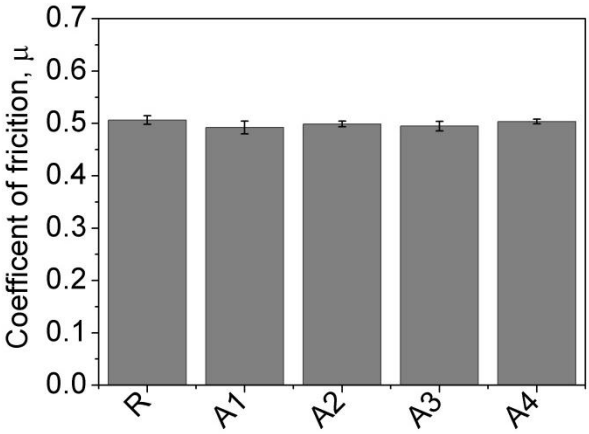

Figure 123: Steady-state coefficient of friction for AISI 316L austenitic stainless steel reinforced with Al_2O_3 nano-particles, investigated under low-load, high-sliding-speed conditions.

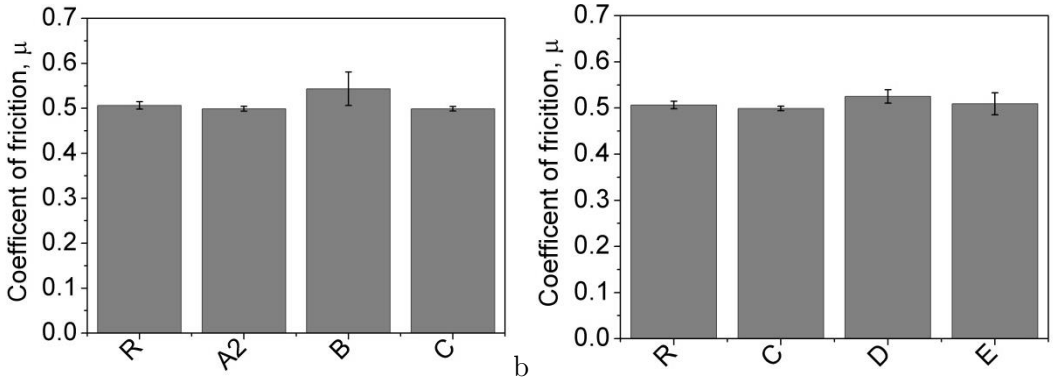

Figure 124: Steady-state coefficient of friction for AISI 316L austenitic stainless steel reinforced with (a) oxide nano-particles (A2-Al_2O_3, Y_2O_3-B, TiO_2-C) and (b) Ti-based nano-particles (TiO_2-C, TiC-D, TiB_2-E) investigated under low-load, high-sliding-speed conditions.

6.2.5.2 High-load, high-sliding-speed conditions

The same trends and similar wear-rate reductions, with abrasive wear being the main wear mechanism (Fig. 127), were also observed for the tribological testing under high-load, high-sliding-speed conditions (load of 3N and sliding speed of 20 mm/s), as shown in Figs. 125 and 126. In this case the wear rate for the cast and hot-rolled AISI 316L stainless steel was reduced from $1.5 \cdot 10^6$ μm^3/Nm down to about $6.7 \cdot 10^5$ μm^3/Nm, as the steel matrix was reinforced with the Al_2O_3 nano-particles added in 0.5 wt. %. Again, better wear-rate results

were obtained for the samples A2 and A4, where Al_2O_3 nano-particles were mixed with the CaSi dispersive medium, as shown in Fig. 125. However, under high-load, high-sliding-speed conditions the very best wear resistance of the AISI 316L stainless steel ($k = 1.4 \cdot 10^4$ $\mu m^3/Nm$) was observed if the Al_2O_3 nano-particles were prior-activated by an oxygen plasma (sample A4).

Also for the reinforcement with oxide nano-particles (Fig. 126 a) and Ti-based nano-particles (Fig. 126 b), the improvement in the austenitic stainless steel's wear resistance follows the same trends as observed in the case of the low-load, high-sliding-speed conditions. For the oxide nano-particles the lowest wear rate of $6.8 \cdot 10^5$ $\mu m^3/Nm$ was obtained when reinforcing the AISI 316L stainless steel with Y_2O_3 nano-particles (sample B; Fig. 81a) and for Ti-based nano-particles when TiB_2 nano-particles (sample E) are used as the reinforcement phase. In agreement with the largest hardness increase the TiB_2 nano-particles reinforcement provides the lowest wear rate of $6.2 \cdot 10^5$ $\mu m^3/Nm$, as shown in Fig. 126. Hardness is defined as the resistance to plastic deformation, which means a diminished effect of micro scratching and ploughing and consequently less material removal. The reduced amount of plastic deformation and scratching, obtained by reinforcing the steel matrix with nano-particles, especially Y_2O_3 (sample B) and TiB_2 (sample E), is confirmed by the wear track microscopic analysis, shown in Fig. 126.

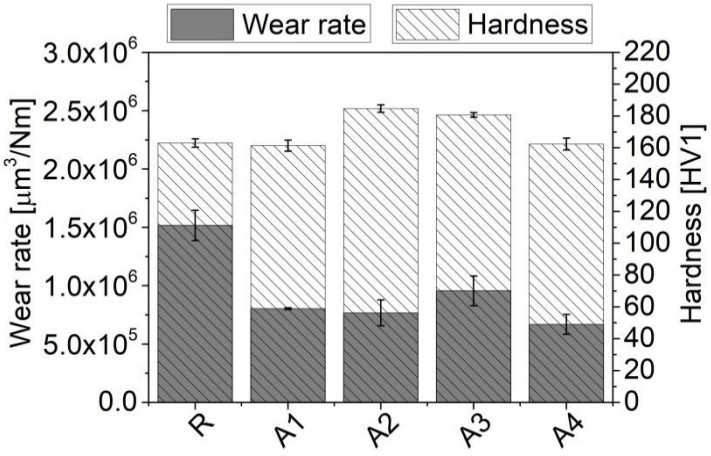

Figure 125: Wear rate and hardness values for the AISI 316L stainless steel reinforced with Al_2O_3 nano-particles, investigated under high-load, high-sliding-speed conditions.

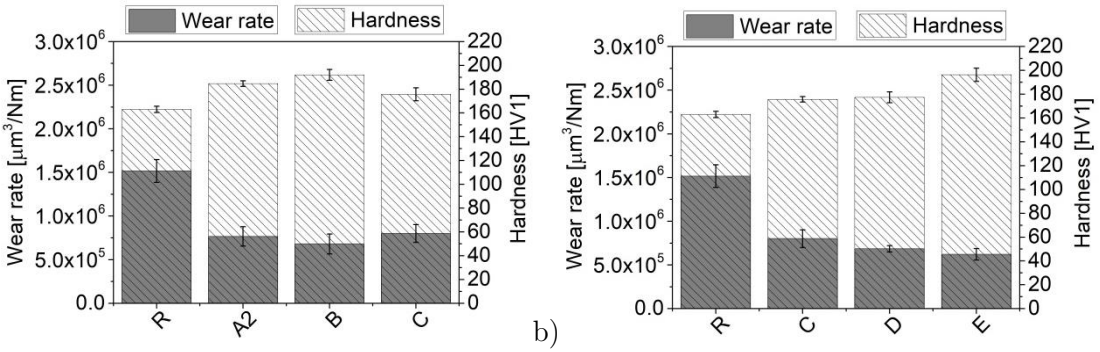

Figure 126: Wear rate and hardness values for AISI 316L stainless steel reinforced with (a) oxide nano-particles (A2-Al_2O_3, Y_2O_3-B, TiO_2-C) and (b) Ti-based nano-particles (TiO_2-C, TiC-D, TiB_2-E) investigated under high-load, high-sliding-speed conditions.

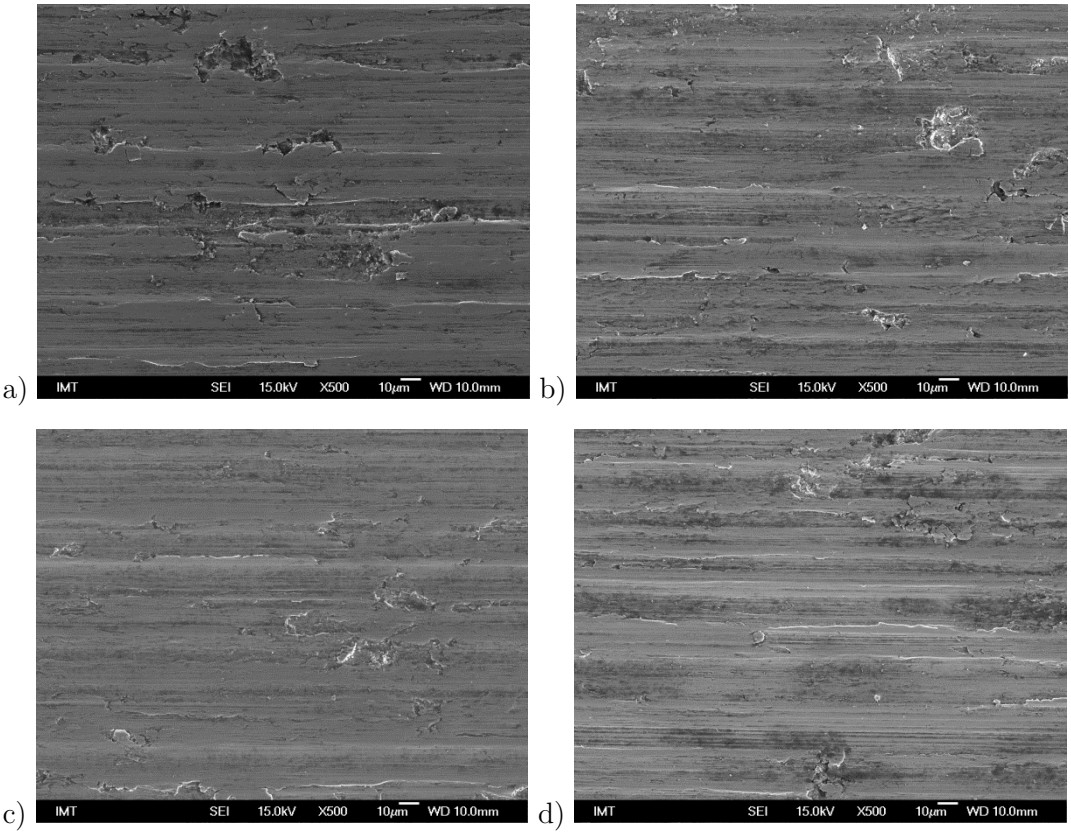

Figure 127: SEM micrographs (500x magnification) of the wear tracks for the high-load, high-sliding-speed conditions; a) reference material (sample R) without addition of nano-particles, b) sample A4 with Al_2O_3 nano-particles, c) sample B with Y_2O_3 nano-particles and d) sample E with TiB_2 nano-particles.

Under high-load, high-sliding-speed contact conditions the steady-state coefficient of friction of the cast and hot-rolled AISI 316L stainless steel was reduced to ~0.45, with all the investigated samples, being reinforced with different nano-particles or not, displaying similar friction behavior and average friction vales, as shown in Figs. 128 and 129. However, due to the reduced micro scratching and ploughing component the reinforcement with nano-particles will provide some beneficial effect.

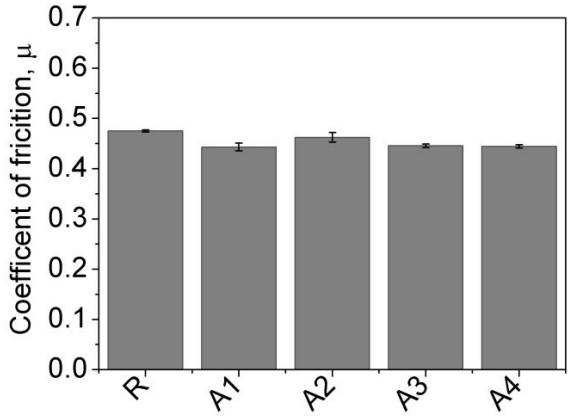

Figure 128: Steady-state coefficient of friction for AISI 316L austenitic stainless steel reinforced with Al_2O_3 nano-particles, investigated under high-load, high-sliding-speed conditions.

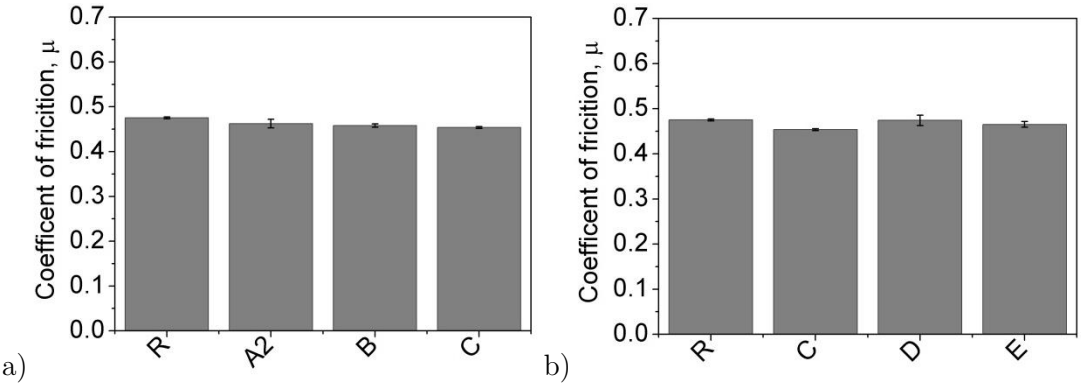

Figure 129: Steady-state coefficient of friction for AISI 316L austenitic stainless steel reinforced with (a) oxide nano-particles (A2-Al_2O_3, Y_2O_3-B, TiO_2-C) and (b) Ti-based nano-particles (TiO_2-C, TiC-D, TiB_2-E) investigated under high-load, high-sliding-speed conditions.

6.2.5.3 High-load, low-sliding-speed conditions

The wear test results for the low-load, high-sliding-speed contact conditions (load of 3N and sliding speed of 0.2 mm/s) are shown in Figs. 130 and 131. In compliance with the high-load, low-sliding-speed and high-load, high-sliding-speed contact conditions, also in the case of the high-load, low-sliding-speed condition the wear rate of the cast and hot-rolled AISI 316L stainless steel was reduced from $1.5 \cdot 10^6$ $\mu m^3/Nm$ down to about $4.7 \cdot 10^5$ $\mu m^3/Nm$ when reinforced with Al_2O_3 nano-particles (Fig. 130). A further improvement is obtained when the Al_2O_3 nano-particles are mixed with the CaSi dispersion agent (sample A2), providing a more homogeneous distribution of the Al_2O_3 nano-particles in the metal matrix with an increased hardness and toughness.

In terms of the type of reinforcement nano-particles the best results for the oxide nano-particles are shown by the Y_2O_3 nano-particles (sample B), providing a superior wear resistance with the the wear rate being reduced even down to $3.4 \cdot 10^5$ $\mu m^3/Nm$ (Fig. 131a). In the case of the Ti-based nano-particles slightly higher wear rates of about $4.4 \cdot 10^5$ $\mu m^3/Nm$ are provided by the reinforcement with the TiO_2 (sample C) and TiC (sample D) nano-particles. The exception in terms of higher hardness providing lower wear rates is the AISI 316L stainless steel reinforced with TiB_2 nano-particles. Although providing the largest increase in hardness reinforcement, with the TiB_2 nano-particles this results in one of the highest wear rates of about $6.1 \cdot 10^5$ $\mu m^3/Nm$, as shown in Fig. 131b. The reason presumably lies in the very fine TiB_2 nano-particles not providing the same level of abrasive resistance as the larger ones, with the wear mechanism being shifted from predominantly abrasive to a combination of abrasive wear, plastic deformation and fatigue, as also observed for the reference material (Fig. 132).

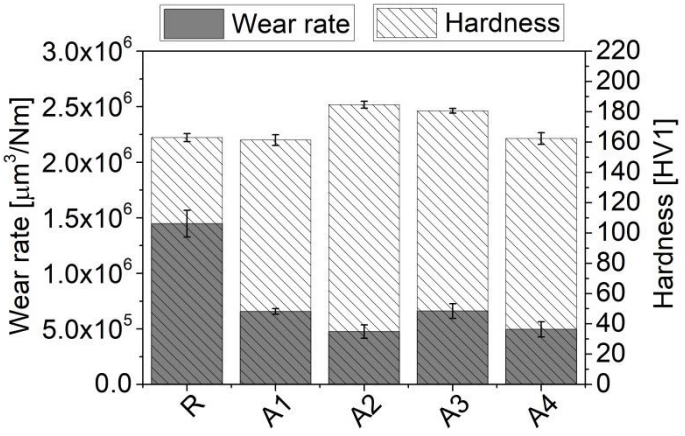

Figure 130: Wear rate and hardness values for AISI 316L stainless steel reinforced with Al_2O_3 nano-particles, investigated under high-load, low-sliding-speed conditions.

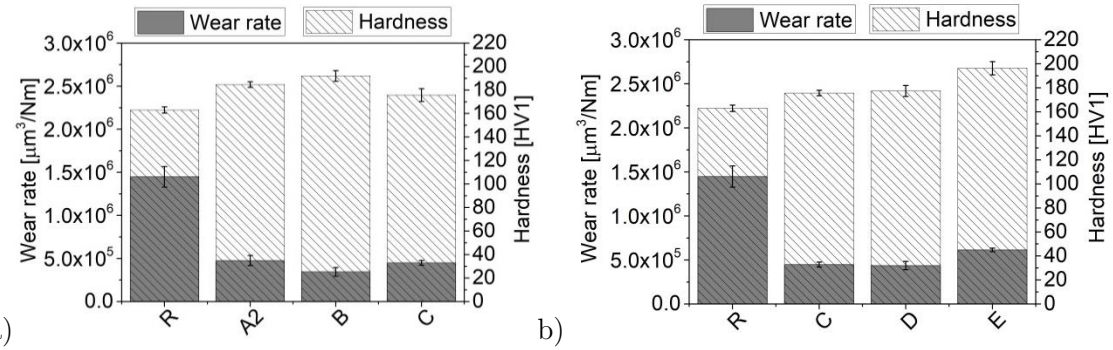

Figure 131: Wear rate and hardness values for AISI 316L stainless steel reinforced with (a) oxide nano-particles (A2-Al_2O_3, Y_2O_3-B, TiO_2-C) and (b) Ti-based nano-particles (TiO_2-C, TiC-D, TiB_2-E) investigated under high-load, low-sliding-speed conditions.

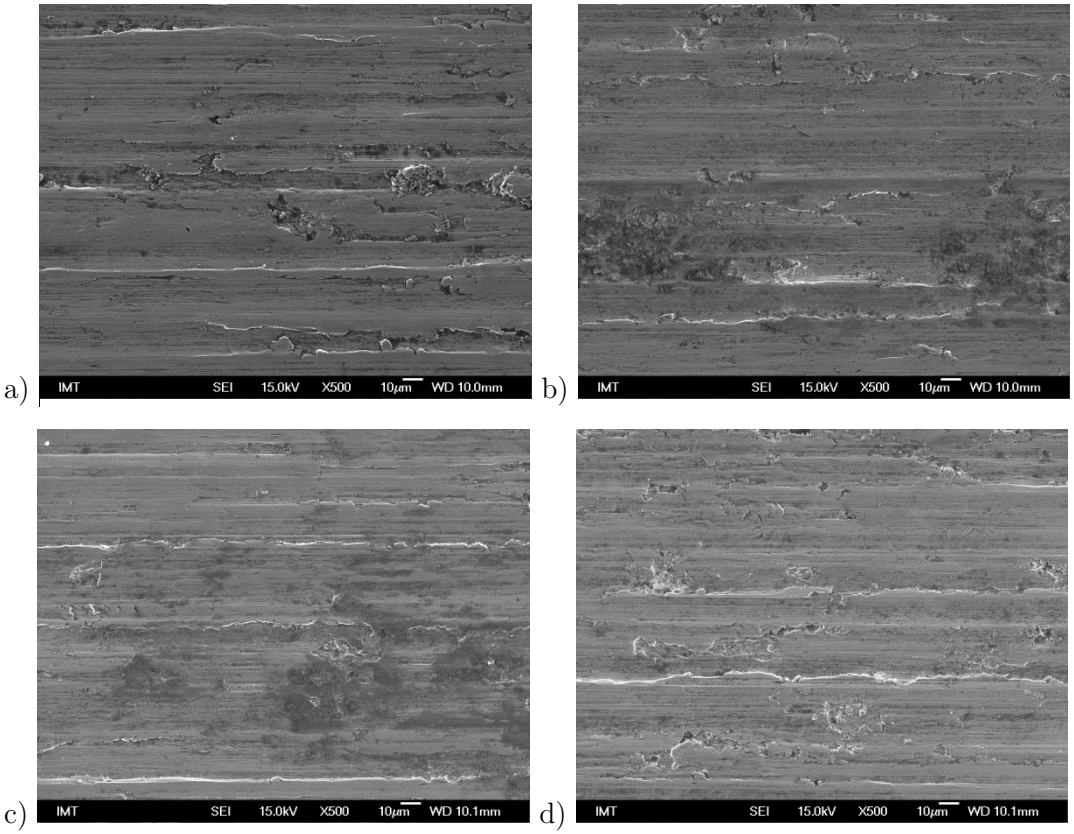

Figure 132: SEM micrographs (500x magnification) of the wear tracks for the high-load, low-sliding-speed conditions; a) reference material (sample R) without the addition of nano-particles, b) sample A4 with the Al_2O_3 nano-particles, c) sample B with Y_2O_3 nano-particles and d) sample E with TiB_2 nano-particles.

In the case of the high-load, low-sliding-speed contact conditions the steady-state coefficient of friction for the reference cast and hot-rolled AISI 316L stainless steel was 0.55. Under these conditions the reinforcement with nano-particles did not only improve the wear resistance, but it also resulted in a lower steady-state friction, as shown in Figs. 133 and 134. For the oxide and TiC nano-particles the steady-state coefficient of friction during 50 min of sliding was reduced to 0.5, and for TiB_2 even below 0.5 (Fig. 134b) due to the reduced ploughing component.

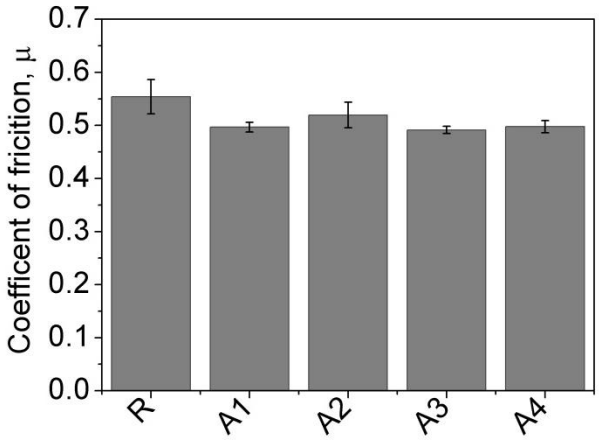

Figure 133: Steady-state coefficient of friction for AISI 316L austenitic stainless steel reinforced with Al_2O_3 nano-particles, investigated under high-load, low-sliding-speed conditions.

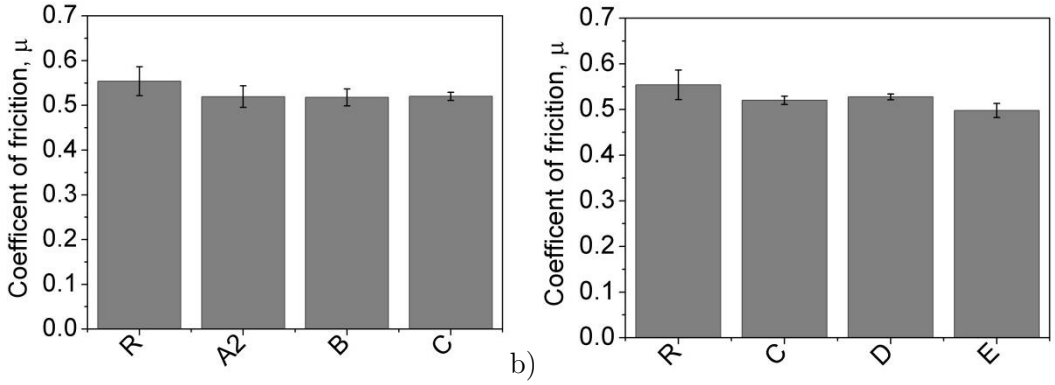

Figure 134: Steady-state coefficient of friction for the AISI 316L austenitic stainless steel reinforced with (a) oxide nano-particles (A2-Al_2O_3, Y_2O_3-B, TiO_2-C) and (b) Ti-based nano-particles (TiO_2-C, TiC-D, TiB_2-E) investigated under high-load, low-sliding-speed conditions.

Chapter 7

Discussion

7.1 Preliminary Results

Preliminary tests were focused on different approaches to homogeneously introducing nano-particles into the metal matrix and how the concentration (0.5, 1.0 and 2.5 wt.%) and size of the added Al_2O_3 nano-particles effect their distribution in the as-cast austenitic stainless steel matrix. The purpose was also to determine the methodology and analyzing techniques suitable for the analysis and identification of the nano-particles incorporated into the steel matrix. The methods of production were submerging, the pouring over method and insertion into the melt flow during the conventional ingot-casting route.

In the case of the submerging method there were no nano-particles found in the as-cast microstructure. The problem is the large difference in the density of the Al_2O_3 nano-particles added to the melt in comparison to the density of the iron. The density of the Al_2O_3 nano-particles is 3.95 g/cm^3 and that of iron, 7.85 g/cm^3. Due to the large difference in the density they can be easily agglomerated and transformed into the slag on the surface of the melt.

Based on the experimental results from the pouring over method the Al_2O_3 nano-particles with different sizes (500 and 50 nm) were found to be successfully incorporated into the steel matrix. However, the distribution in the steel matrix is non-homogeneous and concentrated in certain areas, forming reinforcement-particle clusters. On the other hand, the results of the particle distribution analysis showed that the addition of Al_2O_3 nano-particles in 0.5 to 1.0 wt. % concentrations provides an even distribution of particles through the whole volume of the as-cast ingot, with very small deviations in the distribution over the ingot height of about 0.01 particles/μm^2, regardless of whether we used 50-nm or 500-nm sized particles. Nevertheless, metallographic observations show the agglomeration of nano-particles. When the mass fraction was increased to 2.5 wt. % the particles distribution became non-uniform, with the nano-particles concentration decreasing towards the bottom region of the as-cast ingot. In this case, also the size of the particles starts to play a role, with the larger particles being more easily incorporated into the steel matrix. Furthermore, the size-dependent analysis showed that the Al_2O_3 nano-particles with a mean particle size of 50 nm are more homogeneously distributed than the 500-nm particles. With the STEM/EDS and STEM-line profile analysis the successful incorporation and coherent bonding of the Al_2O_3 nano-particles in the steel matrix were confirmed.

By adding nano-particles using the insertion method, where nano-particles sealed in a steel tube are inserted into the melt flow during the casting and by using CaSi as a dispersion medium, reduced particles clustering and a more homogeneous distribution were obtained. The particle distribution analysis also showed that the use of a dispersion agent reduces the influence of the particle size (500 or 50 nm) on the particles distribution in the steel matrix. CaSi is believed to act as a dispersion medium when added to the molten steel together with the nano-particles (nano-particles/CaSi mixture). When the CaSi comes into contact with molten steel a turbulent reaction scatters the particles through the whole volume of the melt, thus providing more effective particles dispersion, reduced particles

clustering and a more homogeneous distribution in the metal matrix. This hypothesis was proven, as a uniform distribution in the cases when CaSi was used was obtained. Therefore, all the additional experiments with other types of nano-particles were conducted in the same manner, using a nano-particles/CaSi mixture in a 1:1 mass ratio and the steel tube insertion method.

7.2 Thermodynamic Calculations and Microstructure Analysis

Knowledge of the phases and the microstructural components formed during solidification of the alloys under the equilibrium condition is essential for the production of materials. Thermodynamic calculations using different software tools, such as ThermoCalc, are nowadays an important step prior to the experimental production of alloys. Our goal was mainly to achieve a uniform distribution and the incorporation of different nano-particles into the steel matrix via a conventional ingot-casting route without particles dissolution or intermetallic reactions taking place. Therefore, the theoretical determination of the stability of the different types of the added nano-particles to the AISI 316L austenitic stainless steel matrix was performed and afterwards compared with the experimental results. The thermodynamic calculations might be limited by the data that are available in the database used and may differ from the experimental results. However, it is still the best choice for the thermodynamic calculations made for this study.

The thermodynamic calculations revealed that in the AISI 316L steel many phases will be present under equilibrium conditions; however, some of them exist in very small quantities due to the very small amount of impurities. Furthermore, the real-life conditions in production are non-equilibrium, with the times for diffusion and the formation of all the predicted phases simply being too short. Nevertheless, the calculations were mainly focused on the thermodynamic behavior of the added nano-particles and the stability of the particular types of nano-particles used. Other studies show [11],[64],[65],[66],[67],[68],[70] that the nano-particles used in this work (oxide and Ti-based nano-particles) have a high temperature stability range and low Gibbs formation energy, and therefore should not react with the melt or dissolve even at the temperatures of the liquid steel.

Optical microscope images of the microstructure of the cast and hot-rolled AISI 316L austenitic stainless steel without and with the addition of different nano-particles display a distinctive two-phase microstructure of recrystallized and un-recrystallized grains of austenite and δ-ferrite, with the δ-ferrite fraction being below 1 %. Furthermore, the effect of the nano-particles addition on the microstructure or the grain size could not be identified, regardless of the type of nano-particles used. However, alloys produced with the addition of different types of nano-particles show different amounts of recrystallized and unrecrystallized austenite grains as well as the δ-ferrite fraction, ranging from 0.3 to 1.0 %.

In all cases, when the nano-particles were added to the matrix material using the conventional ingot casting method, regardless of the particles type used and either using dispersion medium CaSi or not, the microstructure observations reveal the presence of nano-particles, visible as white dots scattered throughout the whole volume of the AISI 316L austenitic stainless steel matrix. These were not observed for the reference material, indicating that these are indeed the added nano-particles. However, their stability and the inertness in the steel differed depending on the nano-particle type.

According to the thermodynamic calculations of the phase stability performed for the AISI 316L steel with the addition of 0.5 wt. % of Al_2O_3 nano-particles, the Al_2O_3 nano-

particles should stay stable and undissolved also in the liquid region of the matrix material as the Al_2O_3 melting temperature is much higher (2072° C) than the matrix (1400°C). This is in agreement with the particle distribution analysis, showing the highest frequency for particles below 200 nm (particle size range < 500 nm) and around 500 nm (particle size range ≥ 500 nm), being consistent with the size distribution of the Al_2O_3 powder used. The particle distribution in terms of the relative frequency and the particles density was evaluated for two particles sizes, < 500 nm and ≥ 500 nm, since particles of different sizes (from 50–100 nm up to 1 μm) were found to be present in the as-delivered powders.

The used insertion-tube method of incorporating the Al_2O_3 nano-particles during the conventional ingot casting in terms of the particles stability was found to be successful; however, not all the samples showed a uniform distribution of the added nano-particles. Al_2O_3 nano-particles were observed in all four cases (samples A1–A4), but in the case when only nano-particles were used without any dispersion medium (samples A1 and A3) the particles were found to be non-uniformly distributed in the matrix, accompanied by pronounced particles clustering. The density of the nano-particles ($\rho_{Al_2O_3} = 3.95\ g/cm^3$), being lower than the density of iron ($\rho_{Fe} = 7.85\ g/cm^3$), could represent a problem during production with conventional ingot-casting methods. It could cause floating of nano-particles to the surface of the molten metal. However, it was established [31] that the density of the nano-particles does not play an important role in the process of nano-composites production. The problem lies in the size of the nano-particles added. Such small particles are supposed to float on top of the molten bath, even if their density would be higher than the density of the liquid metal. Plasma surface modification of the Al_2O_3 nano-particles (sample A3) did not show any signs of improvement in terms of the particles uniform distribution, which is in the agreement with the negative particle-size effect. However, when the Al_2O_3 nano-particles were mixed with the CaSi de-oxidant (samples A2 and A4), a uniform distribution of nano-particles within the matrix was obtained. The CaSi is believed to act as a dispersion medium when added to the molten steel together with the nano-particles (nano-particles/CaSi mixture sealed into a ferritic iron tube). When the CaSi comes into contact with molten steel a turbulent reaction scatters the particles through the whole volume of the melt, thus reducing the particles clustering, providing a more homogeneous particles distribution and an increased particles incorporation rate, as proven by the experiment and the particles density analysis. The highest particles density for particles size < 500 nm was obtained for sample A2, involving the CaSi dispersant.

The STEM and STEM-EDS analyses confirmed the successful incorporation and coherent bonding of the nano-sized Al_2O_3 particles (50–100 nm) with the steel matrix. Furthermore, the STEM/EDS elemental mapping and the STEM line-profile analysis showed that the thermodynamically stable Al_2O_3 nano-particles remained undissolved in the steel matrix. However, some of the other elements were also detected around the Al_2O_3 nano-particles, including titanium, manganese, nitrogen and sulfur, which indicates that the formation of some complex oxides and a reaction with titanium might also have taken place. Another explanation could be that the formation of TiN as well as the nucleation of MnS started on the added nano-particle itself, with the whole system being in the 50-nm size range. The ThermoCalc calculations of the most stable corundum phase also predict that some of the titanium could be present in the corundum (Al_2O_3) phase above 500 °C, with the aluminum content showing a slight drop at the same temperature. The content of oxygen, on the other hand, stays almost unchanged up to the steel matrix melting temperature of approximately 1400 °C. The free energies of the Al_2O_3 and TiO_2 formation are very close [84], and thus some of the titanium present it the steel might react with the Al_2O_3 nano-particle added and start forming complex oxides.

In the case of the Y_2O_3 nano-particles the stability of particles in the molten steel is not as good, as indicated by the thermodynamic calculations. Under equilibrium conditions

the Y_2O_3 nano-particle would start to dissolve at a temperature of about 1150°C and would be completely gone above 1400 °C. However, the experiments were not done under equilibrium conditions, thus the diffusion times for such reactions are too slow. Furthermore, according to reference [51] the main advantages of Y_2O_3 (as well as for the other particle types investigated) are a high melting point (2450 °C) and good chemical stability. The experimental batch of the cast and hot-rolled stainless steel with added Y_2O_3 nano-particles confirms the presence of yttrium-rich particles, which were found to be uniformly distributed in the steel matrix. This shows that the CaSi dispersant was also effective in this case. The particles larger than 500 nm were confirmed to contain a large fraction of yttrium and oxygen, thus proving that they are indeed Y_2O_3 particles that stayed undissolved in the AISI 316L steel matrix and survived the production route. There were also other elements found in the spectrum of the Y_2O_3 particles, but we have to take into consideration that due to the very small size of the particles and EDS analyzing volume, the surroundings and background are also included in the chemical analysis. When performing the STEM and STEM/EDS analysis of the nano-particles smaller than 500 nm the spherical-shaped yttrium-rich nano-particles were found. However, in this case also a titanium signal increase was observed across the particle, as well as an increase in manganese and sulfur on the outer area of the particle, suggesting that the MnS inclusions start to nucleate on the particle.

The thermodynamic simulation for TiO_2 nano-particles predicts that these particles are not thermodynamically favored when added to the AISI 316L austenitic stainless steel. In the equilibrium calculations the corundum (M_2O_3) phase enriched in titanium is shown. This indicates that complex oxides might form with the M_2O_3 type phase, with M considering both elements titanium and chromium. Because Cr_2O_3 has a lower Gibbs energy than the TiO_2 and there is large activity of chromium due to its high wt. % in the steel, the TiO_2 nano-particles added to the steel could become the basis for the formation of complex oxides xTiO2 • yCr2O3 or M2O3. The thermodynamic results differ slightly from the experimental ones, as the SEM and EDS analysis of the distributed nano-particles larger than 500 nm did confirm it to be TiO_2 particles originally added to the AISI 316L austenitic stainless steel. This is also supported by the particles distribution analysis, with the samples reinforced with TiO_2 nano-particles showing the highest relative frequency for 500-nm- and <-200-nm-sized particles, being also the most common among all the nano-particle types used. The STEM/EDS elemental mapping and the STEM line-profile analysis of the smaller particles (below 500 nm) further indicate the stability of TiO_2 nano-particles when added to the steel melt, with only titanium and oxygen being present in the analyzed data. The STEM line-profile analysis also showed no discontinued regions at the particle/matrix interface or the presence of any intermetallic phases around the TiO_2 nano-particle, ultimately confirming that the TiO_2 nano-particles are very stable in the steel and do not react with the matrix, thus disproving the thermodynamic simulations.

Thermodynamic calculations made for the addition of the 0.5 wt. % TiC to the AISI 316L steel matrix suggest that the TiC nano-particles will dissolve in the steel melt. However, they would exist in the matrix at lower temperatures, also containing some of the nitrogen available in the steel. For the larger particles the SEM and EDS analysis showed that the majority of the particles consists of titanium and oxygen. This implies that some of the larger TiC particles being present in the nano-particles powder were reduced by the oxygen, followed by the formation of the more stable titanium oxide inclusions. However, in the case of the smaller nano-particles, the titanium reacted with the nitrogen in the steel, forming more stable TiN nano-precipitates, as shown by the STEM and STEM/EDS analyses.

For the TiB_2 nano-particles their thermal stability up to 1350 °C was predicted by ThermoCalc. Therefore, at the casting temperatures of the steel matrix they would start

dissolving when in contact with the melt, but still stable at lower temperatures. The composition of the phase representing TiB_2 (B2M) does not show any variation in the constituent elements with the temperature. This might be due to the limited or inadequate thermodynamic information database and incorrect calculations. The SEM and EDS analyses of the nano-particles present in the stainless-steel matrix (sample E) showed that particles above 500 nm mainly consist of titanium and oxygen, similar as in the case of the TiC nano-particles. Similar reactions probably take place, by oxygen reducing the particles and forming a more stable titanium oxide. For the smaller nano-particles, the STEM/EDS elemental mapping and the STEM line-profile analyses revealed titanium-rich particles to be present in the steel. However, no boron was detected in the particles as well as no other non-metallic elements when performing the analysis. Since boron is an element that is very difficult to detect, the only feasible explanation for the nano-particles is that they are undissolved TiB_2 nano-particles, which theoretically should be stable in the steel melt.

7.3 Mechanical Properties

The volume fraction, type, size, shape, and distribution of the particles added into the matrix have a decisive effect on the mechanical properties of the MMC. The right combination(s) of mentioned factors can provide superior mechanical strength, while maintaining or even improving other important engineering properties, such as toughness, damping capacity, wear resistance, creep behavior as well as the electrical and thermal properties. However, for an optimal exploitation of the strengthening potential a homogeneous distribution of the reinforced particles in the metal matrix first needs to be obtained. In this work the influence of different nano-particles added in a 0.5 wt. % concentration using the ferritic steel tube insertion method on the mechanical properties of AISI 316L austenitic stainless steel was addressed. The mechanical properties discussed include hardness, impact toughness, yield strength (YS) and ultimate tensile strength (UTS), and elongation.

After alloying austenitic stainless steel with Al_2O_3 nano-particles, although adding only 0.5 wt. % of nano-powder, a hardness increase was obtained, being in accordance with the strengthening mechanism in MMnCs. For the reference material a hardness of about 160 HV1 and an impact toughness of about 160 J were measured. No change in the hardness could be detected in the case when the as-delivered, non-modified Al_2O_3 nano-particles were used (sample A1). However, due to the non-homogeneous distribution of the nano-particles the impact toughness decreased to about 155 J. The highest hardness (185 HV1) was obtained with sample A2, where the Al_2O_3 nano-particles were mixed with a CaSi dispersive medium, which facilitates a more homogeneous and uniform distribution of nano-particles in the steel matrix. In this case the hardness increase without a loss in impact toughness was detected. Reinforcing austenitic stainless steel AISI 316L with activated Al_2O_3 nano-particles (sample A3 and A4) resulted in an increased hardness, but also in a considerable drop in the impact toughness, with the nano-particles activation not providing any positive results in terms of the particles distribution uniformity and clustering. In the case of the different oxide nano-particles being tested, the largest hardness increase was obtained with the addition of the Y_2O_3 nano-particles (sample B; ~190 HV1), followed by the Al_2O_3 (sample A2; 185 HV1) and the TiO_2 (sample C; 175 HV1). A more homogeneous distribution and an increased density of finer nano-particles observed in the case of Y_2O_3 and TiO_2 nano-particles also resulted in an improved impact toughness, being increased from about 160 J up to about 170 J. In the case of the Ti-based nano-particles added to the steel matrix, the highest hardness was obtained for the most stable TiB_2 nano-particles (sample E), which also showed the highest particle density. The hardness was improved by more than 20 %. However, the increased hardness obtained by the high particles density

was accompanied by the impact toughness being reduced to below 135 J. The addition of TiC nano-particles (sample D) showed a hardness increase of 175 HV1, which is not the result of direct nano-particles integration into the steel matrix, but caused by TiC dissolution and the formation of TiN precipitates. In this case the impact toughness was reduced by not more than 5 %, down to about 150 J. The beneficial effect of the nano-particles on the hardness is mainly the result of the interaction of nano-particles in the steel matrix with dislocations. The effect is similar to those of the nano-sized precipitates, by which they hinder the mobile dislocations, known as precipitation strengthening [85]. When dislocations glide through the matrix, they encounter the particle/matrix interface and the stress required for the dislocation to overcome the particle pinning effect is increased. In the case of hard nano-particles the stress required for shearing the particles can be greater than the stress to loop it. In such a case the dislocation loop around the particle is generated, which further enhances the precipitation-strengthening effect. This mechanism is known as fine precipitation strengthening, and can be described using the Ashby-Orowan relation [85].

In the case of the reference cast and hot-rolled austenitic stainless steel (sample R) the yield strength (YS) of 387 MPa and the ultimate tensile strength (UTS) of 593 MPa with an elongation at fracture (A) of 43% were obtained. In the case when adding as-delivered, non-modified Al_2O_3 nano-particles (sample A1) no major changes in YS and UTS, but a drop-in elongation due to non-homogeneous distribution of nano-particles, were observed. However, for a more homogeneous distribution, obtained by mixing the Al_2O_3 nano-particles with CaSi (sample A2), which reduces the particles agglomeration and promotes the dispersion of particles, also a slight increase in YS of about 3 % was found with only a very minor effect on the elongation. Furthermore, the activation of nano-particles by the oxygen plasma (samples A3 and A4) resulted in an increased YS and UTS, but in an almost 15 % reduced elongation. In the case of different oxide nano-particles (A - Al_2O_3, B - Y_2O_3, C - TiO_2) mixed with CaSi, the nano-particles have different stabilities in the molten metal, with the Al_2O_3 nano-particles being supposed to be more stable in the steel melt as well as in the steel. Therefore, the most evident combination of both strengthening effect and the hindering of dislocation movements can be expected for the most stable and resistant Al_2O_3 nano-particles, thus resulting in the highest improvement in tensile properties. However, in the current case also TiO_2 nano-particles showed an improvement in the tensile as well as the elastic properties, where a homogeneous distribution and the highest density of very fine nano-particles was obtained. Smaller and more uniformly distributed nano-particles are required in terms of good tensile properties combined with a good elongation. On the other hand, Y_2O_3 nano-particles, which were found to lead to the formation of more complex particles in the metal matrix, resulted in impaired elastic and tensile properties as compared to the reference material. In the case of the Ti-based nano-particles added to the AISI 316L stainless steel, the TiC nano-particles showed the largest improvement in tensile properties from among all the nano-particle types used, which is due to the formation of TiN precipitates, caused by TiC dissolution, and followed by TiB_2 nano-particles. In both cases no major impact on the elastic properties could be detected, as a result of the absence of the complex particles formation.

7.4 Fatigue Resistance and High-Temperature Creep Resistance

In terms of fatigue resistance, the reinforcement of AISI 316L steel with nano-particles had a beneficial effect. According to the literature, material reinforced with homogeneously distributed nano-particles will have far superior fatigue properties to that of micro-particles

and clustered nano-particles strengthened material with a similar volume content of the reinforcement phase. Thermodynamically stable nano-particles and inclusions create obstacles for dislocation sliding and climbing movements, thus providing improved fatigue resistance. From the experimental results, it can be concluded that with the addition of 0.5 wt. % of Al_2O_3 nano-particles improved fatigue resistance of austenitic stainless steel is obtained. No obvious difference could be observed between the activated and non-activated Al_2O_3 nano-particles (samples A1 and A3), while the addition of a dispersion agent in general gives better results (samples A2 and A4). In the case of different oxide nano-particles (A - Al_2O_3, B - Y_2O_3, C - TiO_2) added to the steel matrix a similar level of fatigue resistance improvement of about 20 % was obtained for the Al_2O_3 and TiO_2 nano-particles. However, in the case of the Y_2O_3 nano-particles a lower fatigue resistance, especially at high stress levels, was obtained, which can be ascribed to the formation of more complex particles. The most noticeable increase in fatigue resistance, even up to 50 %, was obtained with the Ti-based nano-particles, having the highest density of very fine particles. Fine, stable, nano-particles and precipitates in the metal matrix create obstacles for dislocation sliding and climbing movements, thus resulting in improved fatigue resistance. In the current case the fatigue properties were improved by the addition of different nano-particles in 0.5 wt. % to AISI 316L austenitic stainless steel, as long as the formation of more complex particles is avoided. Furthermore, the homogeneous distribution of nano-particles obtained by mixing nano-particles with the CaSi dispersion agent provided superior results.

The results for the high-temperature creep resistance of the nano-particle-reinforced AISI 316L stainless steel evaluated in terms of minimum (steady-state) creep rate indicate that the creep resistance at 650 °C is in general lower than for the reference material. However, the difference is not considered major, with all the investigated specimens showing results of the same order of magnitude. In the deformed microstructure the precipitated σ phase was observed, besides the non-modified nano-particles introduced during the casting, being the result of the phase transformation from δ-ferrite to σ phase. The transformation/precipitation temperature is between 600 and 1000 °C, which coincides with the performed creep experiments. Besides the temperature, also the plastic deformation during creep testing has an influence on the σ phase precipitation. In the current case, the addition of Al_2O_3 nano-particles (samples A) resulted in a reduced creep resistance when compared to the reference material. This can be related to the fact that with the addition of nano-particles (representing non-metallic inclusions) the number of nucleation sites for the formation of the σ phase is increasing, being one route for its precipitation. A higher fraction of σ phase is therefore present in the nano-particles-reinforced material, thus having a detrimental effect on the high-temperature properties of the steel. A similar effect on creep rate and creep resistance was observed with the addition of different oxide nano-particles (A - Al_2O_3, B - Y_2O_3, C - TiO_2) to the austenitic stainless steel matrix, with the Y_2O_3 nano-particles further reducing the creep resistance due to the formation of larger, more complex inclusions and TiO_2 nano-particles triggering the more condensed precipitation of σ phase in the form of larger clusters and bands. Almost identical results were observed for the TiB_2 nano-particles (sample E), showing a smaller fraction of σ phase, but its precipitation in the form of larger clusters, as well as bands and a further drop in creep resistance. However, some improvement in creep resistance and the smallest creep rate was observed for the AISI 316L steel reinforced with TiC nano-particles (sample D), which also exhibited the smallest difference in δ-ferrite change and the volume fraction of σ phase. This is consistent with the lowest particle destiny and the finest particles shown by the stainless steel reinforced with TiC nano-particles (sample D).

7.5 Tribological Properties

Finally, the effect of the nano-particles on the wear resistance and coefficient of friction of AISI 316L austenitic stainless steel at room temperatures was investigated and compared to the reference, non-modified AISI 316L steel. To fully examine the potential of nano-particles reinforcement, testing was performed under three different contact conditions, i.e., low-load, high-sliding-speed, high-load, high-sliding-speed and high-load, low-sliding-speed conditions.

At room temperature the average coefficient of friction for the reinforced AISI 316L austenitic stainless steel sliding against a hardened stainless steel ball (X47Cr14) was ~ 0.5, regardless of whether or which of the nano-particles type and particles preparation was used. The high-sliding-speed (20 mm/s) steady-state conditions were reached after about 1 m of sliding. However, for a low sliding speed (2 mm/s) a faster running-in, with the steady-state conditions being reached after about 0.6 m, was observed.

For all the samples abrasive wear (material removed from the surface) was found to be the prevailing wear mechanism accompanied by plastic deformation and adhesive wear (material adhered), observed especially at the edges of the wear scar. The improvement in the wear resistance of more than two fold, observed for nano-particles reinforced AISI 316L austenitic stainless steel, can be ascribed to the hardness increase and improved scratching and ploughing resistance provided by the hard reinforcing phase. By obtaining a more homogeneous distribution of Al_2O_3 nano-particles, achieved by mixing the nano-particles powder with a dispersive medium (samples A2 and A4), the wear rate was further reduced by 25%. In the case of different oxide nano-particles the highest wear resistance in the low-load, high-sliding-speed conditions was obtained with the addition of Y_2O_3 nano-particles (sample B), resulting in the formation of more resistant, complex particles in the metal matrix and in a large hardness increase. In terms of abrasive wear resistance, reinforcement with Y_2O_3 nano-particles is followed by Al_2O_3 (samples A) and TiO_2 nano-particles (sample C). However, the most distinctive wear-rate reduction, being in the range 100–150 % when compared to the reference AISI 316L steel, was obtained by using a reinforcement with the most stable TiB_2 nano-particles (sample E), also providing the highest hardness increase. In the case of TiO_2 (sample C) and TiC (sample D) nano-particles the wear resistance improvement was comparable to the reinforcement with Al_2O_3 nano-particles.

The same trends and similar wear-rate reductions, with abrasive wear being the main wear mechanism, were observed for all three contact conditions investigated: low-load, high-sliding-speed, high-load, high-sliding-speed and high-load, low-sliding-speed conditions. However, the improvement obtained using the nano-particles reinforcement is intensifying as the contact conditions become more demanding (shift from low-load, high-sliding-speed towards high-load, low-sliding-speed conditions). In all cases, better results were obtained when nano-particles were mixed with the CaSi dispersive medium, providing a more homogeneous particles distribution. Furthermore, the Y_2O_3 nano-particles were found to be superior when it comes to reinforcement with oxide nano-particles and TiB_2, among the Ti-based ones, which for milder contact conditions even outperformed the Y_2O_3 nano-particles. The exception were the high-load, low-sliding-speed conditions, where very fine TiB_2 nano-particles cannot provide the same level of abrasive resistance as the larger more complex ones, with the wear mechanism being shifted from predominantly abrasive to a combination of abrasive wear, plastic deformation and fatigue.

Chapter 8

Conclusion

The results of this investigation indicate that the nano-particles reinforcement of steel is feasible even when using simple liquid-metal casting routes. The most promising and homogenous distribution of nano-particles in the steel matrix is obtained when the nano-particles are mixed with the CaSi dispersion medium, sealed into a steel tube and added into the melt flow during conventional ingot casting. The dispersion agent also reduces the influence of the particle size on the particles distribution in the steel matrix. Through the ex-situ introduction of nano-particles into the steel melt, nano-particles were successfully incorporated into the steel matrix, which then improved the mechanical and tribological properties of the steel through precipitation strengthening and dislocation hardening. However, the degree of improvement greatly depends on the nano-particle type and distribution. The results of this investigation can be summarized in the following conclusions:

1. The thermodynamic calculations reveal that in the AISI 316L stainless steel many phases are present under equilibrium conditions. However, the calculations were mainly focused on the thermodynamic behavior of the added nano-particles, i.e., Al_2O_3, Y_2O_3, TiO_2, TiC and TiB_2, and the stability of the particular types of nano-particles when used to produce nano-particulates-reinforced AISI 316L steel. According to the thermodynamic calculations for phase stability the Al_2O_3 nano-particles should stay undissolved when added in 0.5 wt. % to the AISI 316L steel. However, in other cases, where Y_2O_3, TiO_2, TiC and TiB_2 were added, the thermodynamic calculation suggests that the nano-particles dissolve or react with other elements when added to the liquid steel, which results in the formation of different precipitates or phases. Thermodynamic calculation predictions in some cases do not coincide with our experimental results obtained, which might be because of the limited data available in the database.

2. The plasma surface modification of thermodynamically stable Al_2O_3 nano-particles, selected due to the highest stability indicated by the thermodynamic calculations, did not show any signs of improvement in terms of the uniform distribution or prevention of agglomeration and clustering.

3. Using the proper incorporation method, involving the addition of nano-particles through the tube insertion method, nano-particles can be successfully introduced into the steel matrix using the conventional casting route and improve the steel properties. By using CaSi as a dispersion medium and introducing nano-particles/CaSi mixture through a sealed ferritic steel tube, reduced particles clustering and the homogeneous distribution of the reinforcing nano-particles in the steel matrix is obtained. CaSi in contact with molten steel

causes a turbulent reaction and scatters the particles throughout the whole volume of the melt. In all cases, regardless of the particles type used, CaSi provided an intense and more homogeneous distribution of nano-particles throughout the whole volume of the AISI 316L austenitic stainless steel matrix, as confirmed by the particles distribution analysis. However, the rate of incorporation, stability and inertness of the nano-particles in the steel matrix differed, depending on the nano-particles type. The best results were obtained in the case of the Al_2O_3 nano-particles mixed with the CaSi, followed by the TiO_2 and TiB_2 nano-particles, both mixed with CaSi.

4. No effect of nano-particles addition on microstructure or grain size of the investigated stainless steel could be identified, regardless of the type of nano-particles used. However, reinforced AISI 316L steel batches produced with the addition of different types of nano-particles show different amount of recrystallized and unrecrystallized austenite grains but mainly δ-ferrite fraction, ranging from 0.3 to 1.0 wt %. The decrease of δ-ferrite triggered by the nano-particles addition is strongly depended on the type of the nano-particles. In the case of Al_2O_3 nano-particles δ-ferrite fraction was in a similar range as observed in the non-modified reference material. However, the addition of other oxide nano-particles (i.e. Y_2O_3) and especially Ti-based nano-particles had a much bigger effect, reducing the δ-ferrite fraction down to 0.3 %.

5. Results clearly show that the dispersion medium improves the homogeneity of the particles distribution within the steel matrix. At the same time, it helps in maintaining the smaller particles sizes and reduces the particles clustering. Furthermore, detailed microstructural analysis confirmed that the nano-particles were successfully incorporated into the AISI 316L steel matrix, with a clear interface and no intermetallic reactions, especially when it comes to TiO_2 nano-particles displaying high stability at high temperatures, as well as low affinity to agglomeration. However, in the case of Al_2O_3, Y_2O_3 and TiC nano-particles, particles start to react with the elements in the melt and form new complex nano-particles or serve as nucleation sites.

6. The thermodynamically stable Al_2O_3 nano-particles remaine undissolved in the steel matrix, which in some cases become nucleation sites for formation of TiN and MnS. However, also in such cases the whole system remains in the 50-nm size range. Similar goes for small Y_2O_3 nano-particles, where traces of other elements are detected (titanium, manganese and sulphur), while the larger ones stay undissolved in the AISI 316L steel matrix. High stability was shown also by TiO_2 nano-particles, which did not react with the matrix, thus disproving the thermodynamic simulations. On the other hand, large TiC and TiB_2 nano-particles were reduced by the oxygen and formed more stable titanium oxide inclusions. However, in the case of the smaller nano-particles, TiB_2 remained unchanged without any other non-metallic element being detected and TiC dissolving, with titanium reacting with the nitrogen in the steel and forming more stable TiN nano-precipitates.

7. Through nano-particles reinforcement, the mechanical properties of AISI 316L steel were improved; however, the degree of improvement depended on the nano-particles type and distribution. A considerable hardness increase of about 20 % was obtained with the addition of Al_2O_3, Y_2O_3 and especially TiB_2 nano-

particles. A more homogeneous distribution and increased density of finer nano-particles obtained in the case of the Y_2O_3 and TiO_2 nano-particles provided also an improved impact toughness. The most evident combination of both strengthening effect and the hindering of dislocation movement was achieved for the most stable and resistant Al_2O_3 nano-particles, resulting in the greatest improvement in tensile properties. In the case of Ti-based nano-particles the TiC nano-particles showed the largest improvement in tensile properties among the nano-particles types used, which is due to the formation of very fine TiN precipitates, caused by the TiC dissolution, and followed by the TiB_2 nano-particles. In both cases, no major impact on the elastic properties could be detected.

8. Through nano-particles reinforcement, also the fatigue resistance of the AISI 316L steel was improved. An improvement of about 20 % was obtained for the oxide nano-particles. However, the most noticeable increase in the fatigue resistance, even up to 50 %, was obtained with the Ti-based nano-particles, providing the highest density of very fine particles. On the other hand, the high-temperature creep resistance of nano-particles-reinforced AISI 316L stainless steel was in general found lower than for the reference material. This is mainly attributed to the formation of the σ phase, which starts to form above 600 °C and is promoted by the presence of nano-particles, acting as additional nucleation sites. Exception is TiC nano-particles reinforced AISI 316L steel exhibiting the smallest volume fraction of σ phase. This is consistent with the lowest particle destiny and the finest particles shown by stainless steel reinforced with TiC nano-particles.

9. In terms of tribological properties, beneficial results are obtained for all the reinforced AISI 316L steel batches. The nano-particles were found to improve the abrasive wear resistance, which is further improved for up to 25 % if the nano-particles are mixed with the CaSi dispersive medium, providing a more homogeneous particles distribution. The Y_2O_3 nano-particles were found to be superior in terms of wear resistance improvement when it comes to the reinforcement with oxide nano-particles and TiB_2 among the Ti-based ones. The exception are the high-load, low-sliding-speed conditions, where very fine TiB_2 nano-particles cannot provide the same level of abrasive resistance as the larger, more complex ones, with the wear mechanism being shifted from predominantly abrasive to a combination of abrasive wear, plastic deformation and fatigue.

References

[1] S. Chen, P. Seda, M. Krugla, and A. Rijkenberg, "High-modulus steels reinforced with ceramic particles through ingot casting process," *Mater. Sci. Technol.*, vol. 32, no. 10, pp. 992–1003, 2016.

[2] S. R. Bakshi, D. Lahiri, and a Agarwal, "Carbon nanotube reinforced metal matrix composites - a review," *Int. Mater. Rev.*, vol. 55, no. 1, pp. 41–64, 2010.

[3] Z. Trojanová, P. Lukáč, H. Ferkel, and W. Riehemann, "Internal friction in microcrystalline and nanocrystalline Mg," *Mater. Sci. Eng. A*, vol. 370, no. 1–2, pp. 154–157, 2004.

[4] F. Shehata, A. Fathy, M. Abdelhameed, and S. F. Moustafa, "Preparation and properties of Al2O3 nanoparticle reinforced copper matrix composites by in situ processing," *Mater. Des.*, vol. 30, no. 7, pp. 2756–2762, 2009.

[5] H. Ferkel and B. L. Mordike, "Magnesium strengthened by SiC nanoparticles," *Mater. Sci. Eng. A*, vol. 298, no. 1–2, pp. 193–199, 2001.

[6] N. Natarajan, V. Krishnaraj, and J. P. Davim, *Metal Matrix Composites Synthesis, Wear Characteristics, Machinability Study of MMC Brake Drum*. 2015.

[7] K. Purazrang, P. Abachi, and K. U. Kainer, "Mechanical behaviour of magnesium alloy MMCs produced by squeeze casting and powder metallurgical techniques," *Compos. Eng.*, vol. 3, no. 6, pp. 489–505, 1993.

[8] H. Dieringa, "Properties of magnesium alloys reinforced with nanoparticles and carbon nanotubes: A review," *J. Mater. Sci.*, vol. 46, no. 2, pp. 289–306, 2011.

[9] R. Dasgupta, "Aluminium Alloy-Based Metal Matrix Composites: A Potential Material for Wear Resistant Applications," *ISRN Metall.*, vol. 2012, pp. 1–14, 2012.

[10] C. R. Crowe, R. A. Gray, and D. F. Hasson, "MICROSTRUCTURE CONTROLLED FRACTURE TOUGHNESS OF SiC/Al METAL MATRIX COMPOSITES.," no. Warrendale, PA, USA. pp. 843–866, 1985.

[11] J. W. Kaczmar, K. Pietrzak, and W. Wlosinski, "The production and application of metal matrix composite materials," *J. Mater. Process. Technol.*, vol. 106, no. 1–3, pp. 58–67, 2000.

[12] J. R. Davis, *Copper and Copper Alloys,ASM International*. 2001.

[13] P. K. Deshpande, J. H. Li, and R. Y. Lin, "Infrared processed Cu composites

reinforced with WC particles," *Mater. Sci. Eng. A*, vol. 429, no. 1–2, pp. 58–65, 2006.

[14] P. K. Deshpande and R. Y. Lin, "Wear resistance of WC particle reinforced copper matrix composites and the effect of porosity," *Mater. Sci. Eng. A*, vol. 418, no. 1–2, pp. 137–145, 2006.

[15] W. F. Gale and T. C. Totemeier, "Mechanical Properties of Titanium and Titanium Alloys," *Smithells Met. Ref. B.*, no. 1, pp. 22–83, 2004.

[16] T. Saito, "A Cost-Effective P / M Titanium Matrix Composite for Automobile Use," *Adv. Perform. Mater.*, vol. 2, pp. 121–144, 1995.

[17] R. Casati and M. Vedani, "Metal Matrix Composites Reinforced by Nano-Particles—A Review," *Metals (Basel).*, vol. 4, no. 1, pp. 65–83, 2014.

[18] F. Akhtar, "Ceramic reinforced high modulus steel composites: processing, microstructure and properties," *Can. Metall. Q.*, vol. 53, no. 3, pp. 253–263, 2014.

[19] I. Hussainova, "Effect of microstructure on the erosive wear of titanium carbide-based cermets," *Wear*, vol. 255, no. 1–6, pp. 121–128, 2003.

[20] "Metal Matrix Composites," pp. 1–2, 2014.

[21] K. U. Leuven, "Wetting of solids by molten metals and its relationship to the preparation of metal matrix composites," *Composites*, vol. 18, no. 3, p. 265, 1987.

[22] K. I. Parashivamurthy, R. K. Kumar, S. Seetharamu, and M. N. Chandrasekharaiah, *Review on TiC reinforced steel composites*, vol. 36, no. 18. 2001.

[23] V. C. Nardone and K. M. Prewo, "On the strength of discontinuous silicon carbide reinforced aluminum composites," *Scr. Metall.*, vol. 20, no. 1, pp. 43–48, 1986.

[24] A. Sanaty-Zadeh, "Comparison between current models for the strength of particulate-reinforced metal matrix nanocomposites with emphasis on consideration of Hall-Petch effect," *Mater. Sci. Eng. A*, vol. 531, pp. 112–118, 2012.

[25] E. Pagounis and V. . Lindroos, "Processing and properties of particulate reinforced steel matrix composites," *Mater. Sci. Eng. A*, vol. 246, no. 1–2, pp. 221–234, 1998.

[26] D. Hull and D. J. Bacon, "Introduction to Dislocations," *Butterworth-Heinemann.* 2011.

[27] W. Callister and D. Rethwisch, *Materials science and engineering: an introduction*, vol. 94. 2007.

[28] R. Smallman and A. Ngan, "Physical metallurgy and advanced materials," 2011.

[29] D. Zhou, F. Qiu, H. Wang, and Q. Jiang, "Manufacture of nano-sized particle-reinforced metal matrix composites: A review," *Acta Metall. Sin. (English Lett.*, vol. 27, no. 5, pp. 798–805, 2014.

[30] F. C. Campbell, *Metal Matrix Composites*. 2006.

[31] D. J. Lloyd, *Composites Engineering Handbook*. P.K. Mallick, ed., 1997.

[32] K. K. Nikhilesh, Chawla and Chawla, *Metal Matrix Composites*. Springer: New York, NY, USA, 2006.

[33] N. Chawla, J. J. Williams, and R. Saha, "Mechanical behavior and microstructure characterization of sinter-forged SiC particle reinforced aluminum matrix composites," *J. Light Met.*, vol. 2, no. 4, pp. 215–227, 2002.

[34] Z. Zhang and D. L. Chen, "Consideration of Orowan strengthening effect in particulate-reinforced metal matrix nanocomposites: A model for predicting their yield strength," *Scr. Mater.*, vol. 54, no. 7, pp. 1321–1326, 2006.

[35] H. A. Seong-Min Choi, "Nanocomposites—a new material design concept," *Sci. Technol. Adv. Mater.*, vol. 6, pp. 2–10, 2005.

[36] B. N. Chawla and Y. Shen, "Mechanical Behavior of Particle Reinforced Metal Matrix Composites **," *Adv. Eng. Mater.*, vol. 3, no. 6, pp. 357–370, 2001.

[37] N. Chawla, C. Andres, L. C. Davis, J. E. Allison, and J. W. Jones, "The interactive role of inclusions and SiC reinforcement on the high-cycle fatigue resistance of particle reinforced metal matrix composites," *Metall. Mater. Trans. A*, vol. 31, no. 3, pp. 951–957, 2000.

[38] R. C. Shao, I., Vereecken, P. M., Chien, C. L., Searson, P. C., & Cammarata, "Synthesis and characterization of particle-reinforced Ni/Al2O3 nanocomposites," *J. Mater. Res.*, vol. 17, no. 06, pp. 1412–1418, 2002.

[39] L. Thilly, M. Veron, O. Ludwig, and F. Lecouturier, "Deformation mechanism in high strength Cu/Nb nanocomposites," *Mater. Sci. Eng. A*, vol. 309, pp. 510–513, 2001.

[40] D. J. Dieter, G. E., & Bacon, *Mechanical Metallurgy (Vol.3)*. New York: McGraw-hill., 1986.

[41] J. Llorca, "Fatigue of particle-and whisker-reinforced metal-matrix composites," *Prog. Mater. Sci.*, vol. 47, pp. 283–353, 2002.

[42] N. Chawla, J. W. Jones, C. Andres, and J. E. Allison, "Effect of SiC volume fraction

and particle size on the fatigue resistance of a 2080 Al/SiC p composite," *Metall. Mater. Trans. A*, vol. 29, no. 11, pp. 2843–2854, 1998.

[43] and J. E. A. G. M. Vyletel, D. C. Van Aken, "EFFECT OF MICROSTRUCTURE ON THE CYCLIC RESPONSE AND FATIGUE BEHAVIOR OF AN XD TM ALUMINUM METAL MATRIX COMPOSITE," *Scr. Metall. Mater.*, vol. 25, no. LC, pp. 2405–2410, 1991.

[44] N. Chawla, U. Habel, Y. L. Shen, C. Andres, J. W. Jones, and J. E. Allison, "The Effect of Matrix Microstructure on the Tensile and Fatigue Behavior of SiC Particle-Reinforced 2080 AI Matrix Composites," *Metall. Mater. Trans. A Phys. Metall. Mater. Sci.*, vol. 31, no. 2, pp. 531–540, 2000.

[45] C. Calabrese and C. Laird, "Cyclic stress-strain response of two-phase alloys Part I. Microstructures containing particles penetrable by dislocations," *Mater. Sci. Eng.*, vol. 13, no. 2, pp. 141–157, 1974.

[46] Y. Huang and T. G. Langdon, "The creep behavior of discontinuously reinforced metal-matrix composites," *Jom*, vol. 55, no. 1, pp. 15–20, 2003.

[47] D. C. Dunand and B. Derby, "Fundamentals of Metal-Matrix Composites," *Bost. Butterworth-Heinemann*, p. 191, 1993.

[48] A. B. Pandey, R. S. Mishra, and Y. R. Mahajan, "Steady state creep behaviour of silicon carbide particulate reinforced aluminium composites," *Acta Metall. Mater.*, vol. 40, no. 8, pp. 2045–2052, 1992.

[49] E. Arzt and D. S. Wilkinson, "Threshold stresses for dislocation climb over hard particles: the effect of an attractive interaction," *Acta Metall.*, vol. 34, no. 10, pp. 1893–1898, 1986.

[50] S. B. Biner, "An analysis of grain boundary sliding and grain boundary cavitation in discontinuously reinforced composites," *Acta Mater.*, vol. 44, no. 5, pp. 1813–1829, 1996.

[51] H. Lilholt, "Aspects of deformation of metal matrix composites," *Materials Science and Engineering A*, vol. 135, no. C. pp. 161–171, 1991.

[52] P. L. Menezes, S. P. Ingole, M. Nosonovsky, S. V. Kailas, and M. R. Lovell, *Tribology for scientists and engineers: From basics to advanced concepts*. 2013.

[53] A. P. Sannino and H. J. Rack, "Dry sliding wear of discontinuously reinforced aluminum composites: review and discussion," *Wear*, vol. 189, no. 1, pp. 1–19, 1995.

[54] A. Riahi and A. Alpas, "The role of tribo-layers on the sliding wear behavior of graphitic aluminum matrix composites," *Wear*, vol. 251, no. 1–12, pp. 1396–1407, 2001.

[55] L. Jinfeng, J. Longtao, W. Gaohui, T. Shoufu, and C. Guoqin, "Effect of Graphite Particle Reinforcement on Dry Sliding Wear of SiC/Gr/Al Composites," *Rare Met. Mater. Eng.*, vol. 38, no. 11, pp. 1894–1898, 2009.

[56] S. C. Sharma, "The sliding wear behavior of Al6061garnet particulate composites," *Wear*, vol. 249, no. 12, p. 1036, 2001.

[57] A. Wang and H. J. Rack, "Transition wear behavior of SiC-particulate-and SiC-whisker-reinforced 7091 Al metal matrix composites," *Mater. Sci. Eng. A*, vol. 147, no. 2, pp. 211–224, 1991.

[58] P. L. Menezes, S. P. Ingole, M. Nosonovsky, S. V Kailas, and M. R. Lovell, *Tribology for scientists and engineers*. Springer, 2013.

[59] A. Shafiei-Zarghani, S. F. Kashani-Bozorg, and A. Zarei-Hanzaki, "Microstructures and mechanical properties of Al/Al2O3surface nano-composite layer produced by friction stir processing," *Mater. Sci. Eng. A*, vol. 500, no. 1–2, pp. 84–91, 2009.

[60] C. S. Ramesh, H. Adarsha, S. Pramod, and Z. Khan, "Tribological characteristics of innovative Al6061-carbon fiber rod metal matrix composites," *Mater. Des.*, vol. 50, pp. 597–605, 2013.

[61] J. L. Li and D. S. Xiong, "Tribological properties of nickel-based self-lubricating composite at elevated temperature and counterface material selection," *Wear*, vol. 265, no. 3–4, pp. 533–539, 2008.

[62] B. N. Chawla and Y. Shen, "Mechanical Behavior of Particle Reinforced Metal Matrix Composites **," no. 6, pp. 357–370, 2001.

[63] C. F. Deng, D. Z. Wang, X. X. Zhang, and Y. X. Ma, "Damping characteristics of carbon nanotube reinforced aluminum composite," *Mater. Lett.*, vol. 61, no. 14–15, pp. 3229–3231, 2007.

[64] E. Pagounis and V. Lindroos, "Processing and properties of particulate reinforced steel matrix composites," *Mater. Sci. Eng. A*, vol. 246, no. 1, pp. 221–234, 1998.

[65] J. M. Howe, "Bonding, structure, and properties of metal/ceramic interfaces: Part 1 Chemical bonding, chemical reaction, and interfacial structure," *Int. Mater. Rev.*, vol. 38, no. 5, pp. 233–256, 1993.

[66] S. F. Hassan, O. O. Nasirudeen, N. Al-Aqeeli, N. Saheb, F. Patel, and M. M. A. Baig, "Processing, microstructure and mechanical properties of a TiO_2 nanoparticles reinforced magnesium for biocompatible application," *Metall. Res. Technol.*, vol. 114, no. 2, p. 214, 2017.

[67] V. Swamy, H. J. Seifert, and F. Aldinger, "Thermodynamic properties of Y2O3 phases and the yttrium–oxygen phase diagram," *J. Alloys Compd.*, vol. 269, no. 1–

2, pp. 201–207, 1998.

[68] M. Kiviö, L. Holappa, T. Yoshikawa, and T. Tanaka, "Interfacial phenomena in Fe-TiC systems and the effect of Cr and Ni," *High Temp. Mater. Process.*, vol. 31, no. 4–5, pp. 645–656, 2012.

[69] H. Y. Wang, Q. C. Jiang, B. X. Ma, Y. Wang, and F. Zhao, "Reactive infiltration synthesis of TiB2-TiC particulates reinforced steel matrix composites," *J. Alloys Compd.*, vol. 391, no. 1–2, pp. 55–59, 2005.

[70] A. K. Shurin and V. E. Panarin, "Phase diagrams for iron with interstitial phases as a basis for developing wear-resistant and eutectic steels," *Met. Sci. Heat Treat.*, vol. 26, no. 2, pp. 166–169, 1984.

[71] J. Hashim, L. Looney, and M. S. J. Hashmi, "Metal matrix composites: production by the stir casting method," *J. Mater. Process. Technol.*, vol. 92–93, pp. 1–7, 1999.

[72] "Thermo-Calc Software: Thermo-Calc." [Online]. Available: http://www.thermocalc.com/products-services/software/thermo-calc/.

[73] A. society of Metals, *ASM handbook Volume 10:Materials Characterization*. 1986.

[74] D. E. Newbury, D. C. Joy, P. Echlin, C. E. Fiori, and J. I. Goldstein, *Advanced Scanning Electron Microscopy and X-ray microanalysis*. 1986.

[75] D. B. Williams and C. B. Carter, *Transmission Electron Microscopy*, vol. 5, no. 721. 2009.

[76] J. A. Bailey, *ASM Handbook Volume 08-Mechanical Testing and Evaluation*. .

[77] "Total Materia," *https://www.totalmateria.com/*. .

[78] J. Janovec, J. Medved, and M. Jenko, "Phases in austenitic stainless steels," *Mater. Tehnol. 37*, vol. 37, no. 6, pp. 307–312, 2003.

[79] M. C. Mataya, E. R. Nilsson, E. L. Brown, and G. Krauss, "Hot working and recrystallization of As-Cast 316L (1)," *Metall. Mater. Trans. A*, vol. 34, no. 8, pp. 1683–1703, 2003.

[80] Sandvikens Tryckeri, "Handbook of Stainless Steel," *Outokumpu*, pp. 1–89, 2013.

[81] C.-C. Hsieh and W. Wu, "Overview of Intermetallic Sigma () Phase Precipitation in Stainless Steels," *ISRN Metall.*, vol. 2012, no. 4, pp. 1–16, 2012.

[82] N. Q. Vo, C. H. Liebscher, M. J. S. Rawlings, M. Asta, and D. C. Dunand, "Creep properties and microstructure of a precipitation-strengthened ferritic Fe-Al-Ni-Cr alloy," *Acta Materialia*, vol. 71. pp. 89–99, 2014.

[83] C. Hsieh and W. Wu, "Overview of intermmtallic sigma phase precipitation in stainless steels," pp. 361–382, 2014.

[84] N. Birks, G. H. Meier, and F. S. Pettit, *Introduction to the high temperature oxidation of metals*. Cambridge University Press, 2006.

[85] J. Adamczyk, "Development of the microalloyed constructional steels," *J. Achiev. Mater. Manuf. Eng.*, vol. 14, no. 1–2, pp. 9–20, 2006.

Bibliography

Journal Articles

A. Kračun, M. Torkar, J. Burja, B. Podgornik, Bojan,"Microscopiccharacterization and particle distribution in a cast steel matrix composite," *Materiali in tehnologij*e, vol. 50, no. 3, pp. 451-454, 2016.

A. Kračun, B. Podgornik, F. Tehovnik, F. Kafexhiu, D. Jenko, "Distribution of Al_2O_3 reinforcement particles in austenitic stainless steel depending on their size and concentration, " *Materiali in tehnologije*, vol. 51, no. 6, pp. 973-980 , 2017.

A. Kračun, D. Jenko, M. Godec, S. V. Savilov, G. Prieto, W. Tuckart, B. Podgornik,"Nanoparticles reinforcement for the improved strength and high-temperature wear resistance of Mn-Cr steel," *Metallurgical and materials transactions A*, vol. 49, no. 11, pp. 5683-5694, 2018.

Conference Paper

A. Kračun, M. Torkar, J. Burja, B. Podgornik. Distribution of oxide nanoparticles in stainless steel, " in book of abstracts of the Cutting edge 2015 : scientific conference, Ljubljana, September 2015.

B. Podgornik, F. Tehovnik, M. Torkar, A. Kračun, D. Jenko, I. Paulin, B. Šetina, M. Godec, B. Senčič, W. Tuckart, "Improving properties of steel through nanoparticles allloying," Program and book of abstracts, 23rd International Conference on Materials and Technology, Portorož, September 2015.

A. Kračun, M. Torkar, J. Burja, B. Podgornik, "Microscopic characterization of nanoparticles in steel," Program and book of abstracts, 23rd International Conference on Materials and Technology, Portorož, September 2015.

B. Podgornik, A. Kračun, M. Godec, W. Tuckart, "Altering steel properties by alloying with carbon nanotubes and nanoparticles," V: Abstracts & Programme Book : AMPT 2016. Kuala Lumpur: ASM International. 2016.

A. Kračun, F. Tehovnik, F. Kafexhiu, B. Podgornik, "Distribution of Al_2O_3 Reinforcement Particles in Austenitic Stainless Steel Depending on Their Size and Concentration," Program and book of abstracts, 24th International Conference on Materials and Technology, Portorož, September 2016.

A. Kračun, F. Tehovnik, F. Kafexhiu, B. Podgornik, “Influence of concentration and size of Al_2O_3 particles on their distribution in reinforced austenitic stainless steel,”Proceedings, Mednarodna podiplomska šola Jožefa Stefana. 2016.

A. Kračun, “Influence of concentration and size of Al_2O_3particles on their distribution in reinforced austenitic stainless steel,” Proceedings : part 2. Ljubljana: Mednarodna podiplomska šola Jožefa Stefana. 2016.

A. Kračun, F. Tehovnik, F. Kafexhiu, T. Kosec, B. Podgornik, “Effect of Al_2O_3 nano-particles on the tribological properties of stainless steel,” Program and book of abstracts, 25th International Conference on Materials and Technology, Portorož, 2017.

B. Podgornik, A. Kračun, D. Jenko, G. Prieto, W. Tuckart, “Fatigue and wear properties of nano-particles alloyed steels,” Proceedings : TRIBaires2017. Buenos Aires: Asociación Argentina de Tribología. 2017.

B. Podgornik, M. Sedlaček, A. Kračun, F. Kafexhiu,“Sliding and impact wear resistance of tool steel after deep cryogenic treatment,” WTC 2017, 6th World Tribology Congress, Beijing, China, 2017.

U. Cvelbar, A. Jurov, A. Kračun, G. Filipič, B. Mušič, B. Podgornik, “Plasma-enabled catalytic properties of nanostructures for applications,” V: International Workshop on Plasma Synthesis of Nanomaterials and its Applications for Sensor Devices, Gifu, Japan, 2018.

Other Publications (optional)

B. Podgornik, A. Kračun. Meritev debeline cinkanega sloja. Ljubljana: IMT, 2015. 5 f., ilustr. [COBISS.SI-ID 1169834]

B. Podgornik, F. Kafexhiu, A. Kračun. Določitev obrabne odpornosti orodnih jekel. Ljubljana: IMT, 2016. 26 str., ilustr. [COBISS.SI-ID 1295530], Naročnik: Metal Ravne, Ravne na Koroškem

A. Kračun, F. Kafexhiu, B. Podgornik. Analiza DB35 - HBCP glave z vtisnjenimi PTFE ležaji. Ljubljana: IMT, 2017. 12 str., ilustr. [COBISS.SI-ID 1374378], Naročnik: Iskra Mehanizmi d.o.o.

A. Kračun, F. Kafexhiu, B. Podgornik. Meritev debeline galvanskega nanosa. Ljubljana: IMT, 2017. 15 str., ilustr. [COBISS.SI-ID 1332394], Naročnik: Iskra Mehanizmi d.o.o., 4245 Kropa

A. Kračun, F. Kafexhiu, B. Podgornik. Meritev debeline galvanskega nanosa: base cone & plunger zone. Ljubljana: IMT, 2017. 30 str., ilustr. [COBISS.SI-ID 1335466], Naročnik: Iskra Mehanizmi d.o.o., Kropa

A. Kračun, B. Podgornik. Meritev debeline Zn sloja na ohišju BCP_GGB_B3. Ljubljana: IMT, 2017. 11 str., ilustr. [COBISS.SI-ID 1364394], Naročnik: Iskra Mehanizmi d.o.o., Kropa

A. Kračun, B. Podgornik. Merjenje debeline Zn sloja z analizo. Ljubljana: IMT, 2017. 12 str., ilustr. [COBISS.SI-ID 1357738], Naročnik: Iskra Mehanizmi d.o.o., Kropa

A. Kračun, F. Kafexhiu, B. Podgornik. Primerjalna analiza debeline galvanskega nanosa. Ljubljana: IMT, 2017. 9 str., ilustr. [COBISS.SI-ID 1334954], Naročnik: Iskra Mehanizmi d.o.o., Kropa

Biography

Ana Kračun has a Bachelor's degree in Ecology with nature conservation from the Faculty of Natural science and Mathematics, University of Maribor (2008-2011). She continued her studies at the Faculty of Mechanical Engineering, University of Maribor (2011-2014) where she got her Master's degree from Technical environmental conservation. During her studies, she joined Talum Institute, where she worked on research projects involving material and environmental research areas where she also did her Master's thesis.

After her Masters in 2014, she enrolled in a Ph.D. at the Jožef Stefan International Postgraduate School, program Nanosciences and Nanotechnologies as a young researcher at the Institute of Metals and Technology. During her study, she visited the Universidad Nacional del Sur, University in Bahia Blanca in Argentina, where she worked with a group of Prof. Dr. Walter Tuckart. The goal of the visit done in the frame of bilateral project was to study the wear resistance of steel reinforced with nanoparticles and C-nanotubes.

During her Ph.D. work she was also involved in research activities and analyses for Slovenian industry and attended several regional and international conferences.